

HZDR-122

ANNUAL REPORT 2022

Institute of Resource Ecology



Wissenschaftlich-Technische Berichte
HZDR-122 2023 . ISSN 2191-8708

HZDR

HELMHOLTZ ZENTRUM
DRESDEN ROSSENDORF

Wissenschaftlich-Technische Berichte
HZDR-122

Annual Report 2022

Institute of Resource Ecology

Editorial board:

Prof. Dr. Thorsten Stumpf

Dr. Harald Foerstendorf

Dr. Frank Bok

Dr. Anke Richter

Impressum

Print edition: ISSN 2191-8708

Electronic edition: ISSN 2191-8716

The electronic edition is published under Creative Commons License (CC BY-NC-ND):

<https://www.hzdr.de/publications/Publ-36635>

<https://nbn-resolving.org/urn:nbn:de:bsz:d120-qucosa2-838570>

Published by Helmholtz-Zentrum Dresden–Rossendorf e.V.

Contact

Helmholtz-Zentrum Dresden–Rossendorf e.V.
Institute of Resource Ecology
Bautzner Landstraße 400
D-01328 Dresden
Germany

Phone: +49 (0) 351 260 3210

Fax: +49 (0) 351 260 3553

e-mail: contact.resourceecology@hzdr.de

<https://www.hzdr.de/fwo>

This report is also available at <https://www.hzdr.de/fwo>

Cover picture

After the invasion of the Russian army into the Ukraine, the HZDR started efforts to support Ukrainian scientists. Mrs. Inna Iarmosh from Kiiiv (second from right) successfully applied for a grant from the Volkswagen-Stiftung to continue her PhD work at the Institute of Resource Ecology. The photo was taken at the welcome reception of Mrs. Iarmosh at HZDR showing the scientific director of HZDR, Prof. Dr. S. M. Schmidt (on the right), Dr. C. Franzen from the management board (on the left), and Prof. Dr. V. Brendler, head of the department Actinide Thermodynamics at the Institute of Resource Ecology (second from left).

Cover photo taken by Dr. B. Schroeder, HZDR.

Preface

DEAR INTERESTED READERS,
DEAR COLLEAGUES,

There is war in Europe again. Russia's invasion of Ukraine also had an impact on the institute's life. Eight colleagues with Ukrainian citizenship are part of our institute. Our thoughts and sympathy are with them. In response to the Russian war of aggression, funds were spontaneously collected in the Institute, which were used for aid deliveries to Ukraine. I would like to take this opportunity to thank you again for your great willingness to donate! Furthermore, thanks to the financial support of the Volkswagen Foundation, we were able to employ a colleague who had to flee her home, Ms. Inna Iarmosh, as a PhD student. You can find a picture of her on the cover of the annual report. Despite the frightening developments in Europe, the Institute of Resource Ecology (IRE) has continued to fulfill its scientific tasks successfully in 2022. The following pages of the report provide comprehensive information on this.

The IRE is one of the ten institutes of the Helmholtz-Zentrum Dresden-Rossendorf (HZDR). Our research activities are mainly integrated into the program "Nuclear Waste Management, Safety and Radiation Research (NUSAFE)" of the Helmholtz Association (HGF) and focus on the topics "Safety of Nuclear Waste Disposal" and "Safety Research for Nuclear Reactors". The program NUSAFE, and therefore all work which is done at IRE, belong to the research field "Energy" of the HGF.

The IRE conducts applied basic research to protect humans and the environment from the effects of radioactivity. For this purpose, we develop molecular process understanding using state-of-the-art methods of microscopy, spectroscopy, diffraction, numerical simulation, theoretical chemistry and systems biology. We implement this in a cross-institutional research environment at the HZDR. Our active interdisciplinarity combines radiochemistry, actinide chemistry, geo- and biosciences, as well as material science and reactor physics. We provide knowledge that is applied in particular to reactor and repository safety as well as in radioecology.

We achieve this goal with a unique infrastructure comprising chemical and biological laboratories as well as hot cells in corresponding radiation and biological safety laboratories in Dresden, Leipzig, and Grenoble. In Grenoble, at the European Synchrotron Radiation Facility (ESRF), the institute operates the only German beamline with four experimental stations for advanced X-ray spectroscopy and diffraction of radioactive samples, which is also made available to external users.

Although the Corona pandemic reached into 2022, 98 original papers were published in peer-reviewed international scientific journals with an average impact factor of 7.35. The extraordinary broadness of research topics and activities is illustrated by some selected highlights below:

Over the last years, the HZDR reactor dynamics core simulator coupled with the German advanced thermal hydraulic system code ATHLET has been extended towards safety analyses of sodium cooled fast reactors (→ p. 82). Last year, the first verification and validation calculations using the coupled code system DYN3D/ATHLET on measurement data from two French sodium cooled fast reactors have been successfully conducted.

Ion irradiations, as a surrogate for poorly accessible neutron irradiations, are an indispensable tool for the investigation of

the behavior of materials for nuclear environments. However, the ion-induced microstructural damage is limited to the first few micrometer below the surface and exhibits intricate depth dependencies, e.g. (→ p. 72), posing a challenge for the derivation of bulk-equivalent mechanical properties. An important advancement of the concept to extract bulk-equivalent mechanical properties from the nanoindentation response of ion-irradiated layers has been made by combining a modified Nix-Gao model of the indentation size effect with the composite hardness of the layer-substrate system (→ p. 74). The work helps to sharpen the tool of ion irradiation as a means for both fast materials screening of candidate nuclear materials for their behavior under reactor-relevant conditions as well as for more fundamental studies.

The institute was intensively involved in the generation, critical assessment and compilation of thermodynamic data. Both our HZDR database RES³T and the joint project THEREDA took profit from that by significantly expanding the range of covered ligands, minerals, and elements. Respective high-ranked publications were issued together with the Departments of f-Element Chemistry and of Surface Processes. Within the huge EURAD project, essential milestones with respect to laying the foundations for a Europe-wide Knowledge Management System dedicated to Radioactive Waste Management together with BGE (the German implementer) and SSTC NRS from Ukraine were achieved.

Europium has been used for decades as an analog for describing the mobility of trivalent actinides in nuclear waste disposal. Despite the large amount of available data for Eu(III), no internationally recommended thermodynamic database exists for this element. Closing this gap has been started in collaboration with the Paul Scherrer Institute (PSI) and the Swedish Nuclear Fuel and Waste Management Company (SKB), by critically evaluating all thermodynamic data including complexation constants, solubility products, and thermodynamic functions so far published. This resulted in the first comprehensive, self-consistent, critically assessed, transparent, and openly accessible thermodynamic database of chemical and thermodynamic aspects of europium with the inorganic ligands SO_4^{2-} , Cl^- , and PO_4^{3-} . Currently, this work is being extended to other ubiquitous inorganic ligands such as OH^- and CO_3^{2-} (→ p. 48).

How does the compositional heterogeneity of rocks affect the migration properties of radionuclides? One heterogeneous rock type of interest for the nuclear repository are the sandy facies of the Opalinus Clay (→ p. 42). Diffusion experiments with the positron emission tomography (PET) tracer ^{22}Na showed that sandy laminae and carbonate concretions cause a remarkably heterogeneous migration. Calculations based on the new PET data show, which constituents and what geometries of the sandy facies are responsible for the overall lower diffusivity compared to the argillaceous facies (→ p. 44). In addition, such quantitative PET results are enormously useful because they allow for validation of transport simulations at the pore scale (→ p. 41). They thus form the basis for robust large-scale predictions.

Magnetotactic bacteria are a special group of microorganisms. In addition to their ability to orient themselves in the earth's magnetic field, they also grow under microaerophilic conditions at low nutrient concentrations. Therefore, they are found in all types of water bodies. We studied their interaction with uranium, which is of importance as a geogenic pollutant or major component of nuclear waste (→ p. 55). For *Magnetospirillum magneticum* AMB-1, we found stable

and strong U(VI) binding *via* carboxyl groups of the peptidoglycan and almost complete immobilization over a wide pH range.

Metal-organic frameworks (MOFs) are an interesting group of compounds characterized by three-dimensional structures with flexible cavities, which allow for a wide range of chemistry. The pores can be used for storage and separation of contaminants, gases, or organic molecules. Moreover, MOFs have been suggested as sensors for ionizing radiation as well as contaminations and as potential tailor-made waste matrices. Actinide-MOFs are however hitherto almost unknown, especially when it comes to transuranic-bearing MOFs. We were able to synthesize and characterize a series of Actinide-MOFs bearing Th(IV), U(IV), Np(IV), and Pu(IV) using anthracene dicarboxylic acid as a linker. These MOFs are highly symmetrical, which enables an unusually high coordination number of 12 for each actinide center, which goes along with a high stability. In addition, the materials are large band-gap semiconductors, which suggests potential application in sensing (→ p. 14).

DNA forms the longest and most densely negatively charged biopolymer of a cell. It is the target of many organic ligands and metal cations, including radionuclides. Negatively charged anions such as chloride or sulfate cannot interact directly with DNA. We have shown by correlative spectroscopy, microscopy and molecular dynamics simulations that the unexpected effects of anions on the stability of tightly packed DNA superstructures originates in the alteration of DNA hydration by anion-specific solvation structures. Their consideration will be required in future analyses of radionuclide DNA interactions (→ p. 65).

All four experimental stations of ROBL were heavily requested and produced scientific highlights. For the direct determination of anomalous dispersion parameters at XRD-2, Florian Meurer received the Lieselotte-Templeton-Award 2023 of the German Crystallographic Society. At XRD-1, we used for the first time a diamond anvil cell to study the structure of actinide-hosting ceramics at elevated pressure for improved predictions of radwaste under more extreme conditions (→ p. 35). Atomistic calculations were combined with EXAFS to elucidate the reduction and early condensation steps of $\text{TcO}_2 \times \text{H}_2\text{O}$ chains into a 3D network (→ p. 21). Multi-edge HERFD-XANES at the U L_{1, L_3} and M_4 edges have been used for the first-time in combination with electronic structure calculations to assess the uranium valence electronic structure.

Beside these highlights, we obtained many other new scientific results in the past year, some of which are presented in this annual report.

In the last year, more than 180 scientists and technicians were employed at the Institute of Resource Ecology. Thereof, 49 Ph.D. students worked at the institute in 2022.

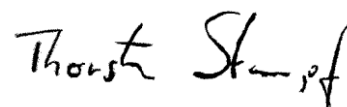
As special highlights, the Institute organized two international scientific workshops. The conference "Actinides Revisited" took place in Dresden and the "ATAS-AnXAS Joint Workshop" in Grenoble. For both events, top-class scientists could be won for keynote lectures. This also meant that the workshops were exceptionally well-attended and offered broad opportunities for scientific exchange.

Another highlight in 2022 was the success of Kristina Kvashnina who applied for a "Funding of first-time professorial appointments of excellent women scientists" of the Helmholtz Association. This funding will be combined with a professorship status at the University of Grenoble.

In addition, the young investigator group of Dr. Natalia Mayordomo Herranz "TecRad" (Interaction of Technetium with Microorganisms, Metabolites and at Mineral-Water Interfaces - Radioecological Considerations), funded by the Federal Ministry of Education and Research, started its work in July 2022.

Furthermore, Moritz Schmidt was awarded the "Fritz Straßmann Prize" of the German Chemical Society. The prize is awarded only once every four years and is the most prestigious award for radiochemists in the German-speaking world.

In retrospect of a very successful year 2022, I would like to thank the visitors, German and international ones, for their interest in our research and for their participation in the institute seminars. We will continue to strongly encourage the collaborations and visits by scientists in the future. Special thanks are due to the board of directors and the executive board of the HZDR, the Ministry of Science and Arts of the Free State Saxony (SMWK), the Federal Ministry of Education and Research (BMBF), the Federal Ministry of Economic Affairs and Energy (BMWi resp. BMWK), the Deutsche Forschungsgemeinschaft (DFG), the European Commission, and other organizations for their support.



Prof. Dr. Thorsten Stumpf
Director of the
Institute of Resource Ecology

Contents

SCIENTIFIC CONTRIBUTIONS

Part I: The Chemistry of Long-Lived Radionuclides

Encapsulating tripodal <i>N</i> -donor ligand coordinating early actinides.....	13
T. Duckworth, P. Kaden, M. Patzschke, M. Schmidt, J. März	
Actinide MOFs with 12-coordinate metal centers.....	14
K. Lv, C. Urbank, M. Patzschke, J. März, P. Kaden, S. Weiss, M. Schmidt	
Electronic structure of plutonium dioxide nanoparticles at acidic pH.....	15
K. O. Kvashnina	
Synthesis and characterization of trivalent lanthanide and actinide complexes with amidinate ligands.....	16
B. Hong, T. Bode, P. Kaden, R. Gericke, J. März	
Quantum chemical investigation of possible Np^{4+} - TM^{2+} -interactions ($TM = Ni, Pd, Pt$) in heterotrimetallic complexes of the type $[TM(\mu-PyO)_4Np(\mu-PyO)_4TM]$	17
R. Gericke, M. Swart	
The role of the atomic quadrupole moment for the prediction of paramagnetic chemical shifts in the NMR spectra of actinide complexes.....	18
M. Patzschke, J. März, P. Kaden, L. Köhler, M. Schmidt	
Modelling of polymer structures with the cheminformatics software RDKit.....	19
L. Waurick, B. Drobot, M. Patzschke	
Analysis of the reduction mechanisms of technetium in $NaClO_4$ combining spectro-electrochemical methods and electrochemical analysis.....	20
D. M. Rodríguez, N. Mayordomo, A. Parra-Puerto, D. Schild, V. Brendler, T. Stumpf, K. Müller	
Shedding light on the enigmatic $TcO_2 \cdot xH_2O$ structure with Density Functional Theory and EXAFS spectroscopy.....	21
A. F. Oliveira, A. Kuc, T. Heine, U. Abram, A. C. Scheinost	
How to determine robust and reliable thermodynamics – An exemplary approach combining NMR, TRLFS, and ITC.....	22
C. Sieber, B. Drobot, J. Kretzschmar, K. Schmeide	
2-Phosphonobutane-1,2,4,-tricarboxylic acid (PBTC): pK_a determination by multinuclear NMR spectroscopy.....	23
J. Kretzschmar, A. Wollenberg, S. Tsushima, K. Schmeide, M. Acker	
Direct determination of anomalous dispersion correction parameters from single-crystal structure data.....	24
C. Hennig, F. Meurer, O. V. Dolomanov, N. Peyerimhoff, F. Kleemiss, H. Puschmann, M. Bodensteiner	
Atomically dispersed pentacoordinated-zirconium catalyst with axial oxygen ligand for oxygen reduction reaction.....	25
X. Wang, Y. An, L. Liu, L. Fang, Y. Liu, J. Zhang, H. Qi, T. Heine, T. Li, A. Kuc, M. Yu, X. Feng	
Highly accessible and dense surface single metal FeN_4 active sites for promoting the oxygen reduction reaction.....	26
G. Chen, Y. An, S. Liu, F. Sun, H. Qi, H. Wu, T. He, P. Liu, R. Shi, J. Zhang, A. Kuc, U. Kaiser, T. Zhang, T. Heine, G. Wu, X. Feng	

Part II: Long-Lived Radionuclides & Transport Phenomena in Geological Systems

Y(III) sorption at the orthoclase (001) surface measured by X-ray reflectivity	29
J. Neumann, J. Lessing, S. S. Lee, J. E. Stubbs, P. J. Eng, M. Demnitz, P. Fenter, M. Schmidt	
EXAFS and DFT studies of competitive Am ³⁺ and Y ³⁺ sorption on corundum	30
N. Huittinen, S. Virtanen, A. Rossberg, M. Eibl, S. Lönnrot, R. Polly	
New insights into the effect of Ca(II) on U(VI) and Np(VI) retention on Ca-bentonite and clay minerals at hyperalkaline conditions – a luminescence spectroscopic study	31
T. Philipp, N. Huittinen, S. Shams Aldin Azzam, R. Stohr, J. Stietz, T. Reich, K. Schmeide	
Batch and IR spectroscopic studies of U(VI) sorption onto zirconia (ZrO ₂)	32
I. Jessat, A. Dietze, K. Heim, H. Foerstendorf, T. Stumpf, N. Jordan	
Investigation of tetragonal polymorphs in Ce(IV)-doped ZrO ₂	33
L. B. F. dos Santos, K. O. Kvashnina, V. Svitlyk, C. Hennig, N. Huittinen	
Influence of different synthesis methods on the phase purity of Ce/Nd-co-doped zirconates	34
S. Richter, S. E. Gilson, N. Huittinen	
Investigation of zirconia ceramics under high pressure conditions related to nuclear repositories	35
V. Svitlyk, S. Weiss, C. Hennig	
Influence of sintering conditions on the structure and the redox speciation of homogeneous (U,Ce)O ₂ ceramics	36
M. Massonnet, L. Claparede, J. Martinez, P. Martin, M. O. J. Y. Hunault, D. Prieur, A. Mesbah, N. Dacheux, N. Clavier	
Oxygen K-edge X-ray Absorption Spectra of ThO ₂ and CeO ₂	37
L. Amidani, T. Dumas, D. K. Shuh, S. M. Butorin, C. J. Sahle, A. Longo, K. O. Kvashnina	
Interlayer excitons in MoSe ₂ /2D perovskite hybrid heterostructures – the interplay between charge and energy transfer	38
M. Karpínska, J. Jasíński, R. Kempt, J. D. Ziegler, H. Sansom, T. Taniguchi, K. Watanabe, H. J. Snaith, A. Surrente, M. Dyksik, D. K. Maude, Ł. Kłopotowski, A. Chernikov, A. Kuc, M. Baranowski, P. Plochocka	
Structural analysis of 14 MeV Au ion-irradiated monazite targets	39
S. E. Gilson, V. Svitlyk, C. Hennig, H. Lippold, C. Fischer, G. L. Murphy, A. Bukaemski, S. Akhmadaliev, N. Huittinen	
Dissolution kinetic of soddyite	40
F. Bok, C. Cariven, N. Hoth, V. Brendler	
Improved kinetics for mineral dissolution reactions in pore-scale reactive transport modeling	41
J. Schabernack, C. Fischer	
The influence of sedimentary heterogeneity on the diffusion of radionuclides in the sandy facies of Opalinus Clay at the field scale	42
C. Chen, T. Yuan, R. Lu, C. Fischer, O. Kolditz, H. Shao	
Pore network and solute flux pattern analysis towards improved predictability of diffusive transport in argillaceous host rocks	43
T. Bollermann, T. Yuan, J. Kulenkampff, T. Stumpf, C. Fischer	
An upscaling workflow from the pore scale to the core scale to model diffusive flux	44
T. Yuan, C. Fischer	
Water uptake by cement analyzed with positron emission tomography	45
J. Kulenkampff, A. Reiss, S. Gruhne, D. Lösel	
A workflow from real rock samples to K _d values and their distribution – Combining measurements of rock heterogeneities with reactive transport modeling	46
S. Pospiech, F. Bok, V. Brendler	

Sorption Reference Database SOREDA – General principles and mineral site density calculations.....	47
S. Zechel, F. Bok	
Thermodynamic database for Europium: procedures, guidelines, and recommended values	48
N. Jordan, T. Thoenen, S. Starke, K. Spahiu, V. Brendler	

Part III: Long-Lived Radionuclides in Biological Systems

Interaction of U(VI) with <i>Nicotiana tabacum</i> cells – Endocytosis contributes to the uranium(VI) uptake under phosphorous-deficient conditions	53
W. A. John, B. Lückel, N. Matschiavelli, R. Hübner, S. Matschi, W. Hoehenwarter, S. Sachs	
Proof of microbially induced U(VI) reduction by different electron donors	54
A. M. Newman-Portela, F. Bok, A. Kassahun, M. L. Merroun, J. Raff, E. Krawczyk-Bärsch	
New insights into U binding properties of bioligands in the cell wall of Gram-negative bacterium <i>Magnetospirillum magneticum</i> AMB-1.....	55
E. Krawczyk-Bärsch, J. Ramtke, B. Drobot, R. Steudtner, J. Raff	
Interaction of U(VI) with plant cells - Impact on U(VI) immobilization and mobility	56
J. Jessat, H. Moll, W. A. John, M.-L. Bilke, R. Hübner, J. Kretzschmar, R. Steudtner, B. Drobot, T. Stumpf, S. Sachs	
FastICA vs. ITFA: tracking U(VI) reduction by <i>Desulfosporosinus hippei</i>	57
A. Rossberg, S. Hilpmann	
Eu(III) distribution and speciation in different fungal mycelium samples.....	58
A. Günther, A. Wollenberg, M. Vogel, B. Drobot, R. Steudtner, R. Hübner, J. Raff	
Plant cell interactions with potentially toxic metals: Europium(III) and <i>Daucus carota</i>	59
J. Jessat, H. Moll, W. A. John, M.-L. Bilke, R. Hübner, R. Steudtner, B. Drobot, T. Stumpf, S. Sachs	
Uptake and distribution of Eu(III) in hydroponically grown plants	60
M. Klotzsche, R. Steudtner, M. Vogel, B. Drobot	
Friend or foe? Potential microbial impacts on bentonites used for deep geological repository	61
T. S. Wei, N. Matschiavelli, V. Sushko, A. Cherkouk	
Formation of artificial multi-species bio-constructs of aerobic and anaerobic bacteria	62
S. Hilpmann, I. Jeschke, D. Deev, M. Zupan, T. Rijavec, A. Lapanje, S. Schymura, A. Cherkouk	
Spatial and temporal evolution of enzymatic degradation of PET plastics	63
H. Lippold, L. Kahle, C. Sonnendecker, J. Matysik, C. Fischer	
Quantitative assessment of metal toxicity by metabolic heat flow analysis	64
K. Fahmy	
The unexpected anion sensitivity of DNA-origami stability originates in hydration effects	65
D. Dornbusch, A. Rossberg, S. Tsushima, K. Fahmy	
Preparation of a ²³³ Pa tracer for accelerator mass spectrometry of ²³¹ Pa in environmental samples	66
J. Wolf, A. Barkleit, S. Fichter, R. Steudtner	
SURFBIO – Innovation Hub for surface and colloid biology science	67
S. Schymura, R. Barros, I. Deligiozi, C. Furlan, B. Lapuente de Ojeda, S. Martel-Martín, R. Moreno, B. Parakhonskiy, T. Rijavec, C. Rumbo, A. Skirtach, M. Suarez Diez, A. Lapanje	

Part IV: Nuclear Reactor Safety Research

Master Curve Testing of RPV steels using Mini-C(T) Specimens – Stable crack growth criteria and Censoring Statistics.....	71
A. Das, P. Chekhonin, M. Houska, F. Obermeier, E. Altstadt	
Helical dislocations and dislocation line decoration in ion-irradiated Fe-9Cr studied by scanning transmission electron microscopy	72
K. Vogel, H.-J. Engelmann, P. Chekhonin, F. Bergner, C. Kaden	
Small-angle neutron scattering applied to low-dose neutron-irradiated ferritic/martensitic steel Eurofer97	73
A. Ulbricht, F. Bergner, U. Keiderling	
A new approach to the bulk-equivalent hardness of thin ion-irradiated layers	74
F. Bergner, C. Kaden, A. Das, P. Hähner	
Characterization of brittle fracture initiation sites in reactor pressure vessel steels.....	75
P. Chekhonin, A. Das, F. Bergner, E. Altstadt	
ESFR-SIMPLE: a new Euratom project on Sodium Fast Reactor safety	76
E. Fridman	
Experimental activation determination of metal foils placed inside a German nuclear power plant for validation of neutron fluence calculations	77
A. Barkleit, R. Rachamin, J. Konheiser	
Radiological characterization of FA-centering pins irradiated during a German PWR operation.....	78
R. Rachamin, J. Konheiser	
Estimation of the number of burst fuel rods in a Large-Break Loss-of-Coolant Accident.....	79
M. Jobst, F. Schäfer	
NuScale control rod ejection transient benchmark	80
Y. Bilodid, E. Fridman	
Model validation of a VVER-440 and surrounding area	81
E. Poenitz, J. Konheiser, S. Baier	
Steam line break analysis applied to NuScale small modular reactor (SMR) with ATHLET-DYN3D in the framework of the EU H2020 McSAFER.....	82
E. Diaz-Pescador, S. Kliem	
Transverse isotropic radial core expansions by means of coordinate transformation	83
E. Nikitin, E. Fridman	

PUBLICATIONS

○ Articles (peer-reviewed).....	87
○ Further Contributions.....	94
○ Oral Presentations	95
○ Media Contributions.....	101
○ Theses	102

SCIENTIFIC ACTIVITIES

- Actinides Revisited – 2022 105
- ATAS/AnXAS 2022 – Joint Workshop
5th International Workshop on Advanced Techniques in Actinide Spectroscopy
9th Workshop on Speciation, Techniques and Facilities for Synchrotron Radiation..... 106
- Awards 107
- Seminars (Talks of Visitors) 107
- Teaching Activities..... 108

PERSONNEL 111

ACKNOWLEDGEMENTS 117

INDEX OF AUTHORS 122

SCIENTIFIC CONTRIBUTIONS (PART I)

Chemistry

The Chemistry of
**LONG-LIVED
RADIONUCLIDES**

Encapsulating tripodal N-donor ligand coordinating early actinides

T. Duckworth, P. Kaden, M. Patzschke, M. Schmidt, J. März

In this study the coordination behavior of the tripodal pure N-donor chelator tris-((1H-pyrrol-2-ylmethyl)ethane)-amine (trenpy) towards the early actinides, focusing on the tetravalent oxidation state, was explored. A series of isostructural 1:1 complexes has been synthesized and two complexes [UCl(trenpy)] and [NpCl(trenpy)] were characterized in solid state by single crystal X-ray diffraction (SC-XRD) and in solution by nuclear magnetic resonance spectroscopy (NMR). Quantum chemical calculations were performed for all complexes and the molecular structures obtained by SC-XRD served as starting points for geometry optimizations.

Studies of an isostructural series of early actinides with pure N-donor ligands are scarce and for Schiff-base systems based on pyrrole-imines functional groups as chelators, only one 1:1 complex with uranium is reported in the literature.^[1,2] Since pyrrole-imines have shown to be good chelators for early actinides exploring their reactivity, e.g., halide exchange reactions and reduction is important for gaining detailed information about their bonding properties and electronic structure.

EXPERIMENTAL. All complexation reactions were carried out under an inert atmosphere in a dedicated underpressure glovebox where radioactive materials can safely be handled. The trenpy ligand was synthesized with three equivalents of formylpyrrole and one equivalent of the corresponding tris(2-aminoethyl)amine in ethanol according to a literature procedure.^[3] For the salt metathesis reactions the actinide chloride salts Th to Pu have been used to react with one equivalent of the deprotonated trenpy ligand in methylene chloride or tetrahydrofuran as solvents to form the respective actinide complexes with Th, U, Np, and Pu (1–4). Single crystals of the uranium (2) and neptunium (3) complexes were grown by slow evaporation of the corresponding solvent.

RESULTS. Previous quantum chemical calculations on the closed shell thorium system show that a proposed 1:1 complex with C_{3v} -symmetry (Fig. 1a), in which the tren nitrogen, actinide, and chloride anion lie in a straight line is 39.5 kJ/mol less favorable than a bent conformer with C_1 -symmetry in which the anion lies at an 82° angle to the axis passing through the actinide and the tren nitrogen. In order to clarify which conformer is experimentally present SC-XRD was employed. The molecular structures reveal a seven-fold coordinated actinide center with three $An-N_{pyrrole}$ and three $An-N_{imine}$ bonds coming from the triply deprotonated ligand and one chloride ligand for charge compensation. The SC-XRD structures confirm the computa-

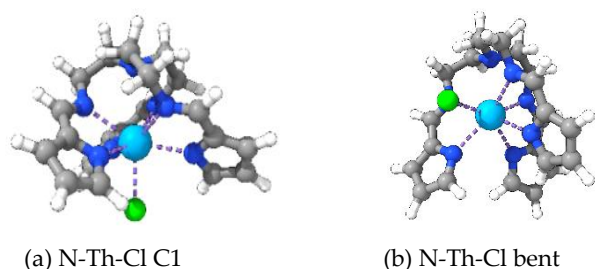


Figure 1. Comparison of the calculated conformers left (aligned, C_{3v}) and right (bent, C_1) of a 1:1 complex [ThCl(trenpy)] (1).

tional results. The nitrogen of the tren moiety at 2.72 Å (2) and 2.70 Å (3) respectively, is too far away to bind to the actinide.

Evaluation of the molecular structure data shows similar bond lengths to the N-donor functionalities of the pyrrole and imine moieties (Tab. 1). The computational results reveal comparable results for the $An-N_{pyrrole}$ and $An-N_{imine}$ overestimating however the $An-N_{tren}$ and underestimating the An-Cl bond distance. Compared with reported literature data, the An-Cl distances are in reasonable agreement.^[4]

Table 1. Intramolecular distances between metal center (An) and coordinating atoms in isostructural [AnCl(trenpy)] complexes.

d/[Å]	Th 1	U 2	Np 3	Pu 4
An-N _{imine}	2.54	2.47(3)	2.44(2)	2.44
An-N _{pyrrole}	2.52	2.47(5)	2.45(2)	2.43
An-N _{tren}	2.79	2.72(7)	2.70(2)	2.72
An-Cl	2.68	2.66(8)	2.66(7)	2.61

*: calculated bond distances in grey, experimental in black.

To compare structures in the solid state and in solution, the synthesized compounds were also studied in dichloromethane - d₂ solution by NMR.

There are 24 individual proton signals (Fig. 2) present which could be assigned with the help of 2D NMR spectra. It can be concluded that the C_1 -symmetry persists in solution. For instance, for a more symmetrical C_{3v} complex, only seven different signals would have been expected.

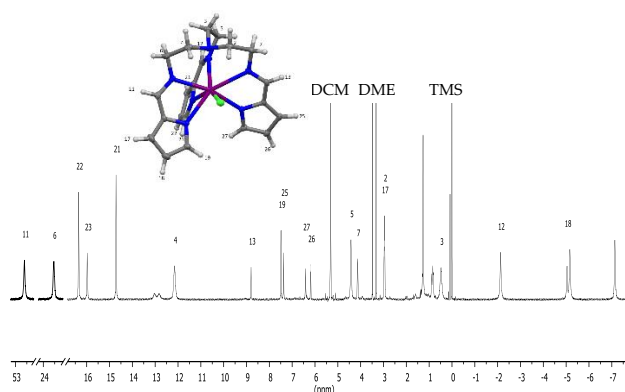


Figure 2. ¹H NMR spectrum of [NpCl(trenpy)] (3) taken at 298 K in dichloromethane-d₂ with molecular structure. Color code: neptunium (purple), chloride (green), nitrogen (blue), carbon (grey) and hydrogen (white).

In summary, the trenpy ligand is capable of complexing the early actinides Th-Pu with a 1:1 metal to ligand ratio starting from the actinide chloride salts. A C_1 -symmetrical complex is present both in solution and in the solid state.

ACKNOWLEDGEMENTS. This work was supported by the German Federal Ministry of Education and Research (BMBF) under project number 02NUK059B (f-Char).

[1] Köhler, L. et al. (2021) *Chem.-Eur. J.* **27**, 18059–18065.

[2] Köhler, L. (2022) PhD Thesis, Technische Universität Dresden.

[3] Wang, Y. et al. (2008) *Acta Crystallogr. Sect. E Struct. Rep. Online* **64**, 0629–0629.

[4] Kloditz, R. et al. (2020) *Inorg. Chem.* **59**, 15670–15680.

Actinide MOFs with 12-coordinate metal centers

K. Lv,¹ C. Urbank,² M. Patzschke, J. März, P. Kaden, S. Weiss, M. Schmidt

¹China Academy of Engineering Physics, Mianyang, China; ²Georg-August-Universität, Göttingen, Germany

A new class of actinide metal organic frameworks (An-MOFs) has been constructed for a wide range of tetravalent early actinides (Th, U, Np, and Pu). The An-MOFs are isorecticular and feature a hitherto unprecedented highly symmetrical 12-coordinate metal environment. The MOFs exhibit autoluminescence and wide band-gap semiconducting properties, which might be exploited for, e.g. radiation detection.

Metal organic frameworks (MOFs) are an underexplored category of actinide compounds that may have useful applications in catalysis, radiation detection, or as tailor-made waste form for radioactive wastes.^[1] Beyond their potential applications, they also offer a platform to study actinide properties in chemical environs not easily achieved in molecular complexes. One such property is the coordination number (CN), which will typically be in the range of 7–10 for early An(IV). Higher coordination numbers have been predicted computationally and in a few cases realized experimentally, but only with very small donor atoms such as B, H, or He.^[2,3] It is then an intriguing question what is the highest coordination number that can be realized with typical donor atoms such as O or N, and which properties would be connected with such a high coordinative saturation.^[4]

EXPERIMENTAL. The synthesis was similar for all An-MOFs. Exemplarily, Pu(IV)-ADC was produced by dissolving PuCl₄·2DME (0.0124 g, 0.022 mmol) in 1 mL DMF and 0.25 mL EtOH and transferred to a 15 mL capped vial containing 9,10-anthracenedicarboxylic acid (ADC) (0.0106 g, 0.04 mmol) and 2-fluorobenzoic acid (0.0994 g, 0.712 mmol). The mixture was hand-shaken and then heated at 100 °C for 19 hours. Slow cooling to room temperature yielded single-crystals of sufficient quality for SC-XRD.

Subsequently, the crystal structure of all materials was determined by single crystal XRD using a Bruker D8-Venture single-crystal X-ray diffractometer (Mo K α radiation) under flowing N₂ gas at 100 or 300 K.

Table 1. An(IV)–O bond length in An(IV)-ADC in Å.

Th(IV)	U(IV)	Np(IV)	Pu(IV)
2.577(3)	2.532(3)	2.515(4)	2.510(1)

RESULTS. Four isorecticular An-MOFs could be obtained including the rare transuranic MOFs Np(IV)- and Pu(IV)-ADC. In all structures the actinide is symmetrically surrounded by six equivalent, bidentate carboxylates, yielding an ideal icosahedral [AnO₁₂] primary building unit (PBU). Each ADC bridges to PBUs for a (2,6) *pcu* topology. Structure and PBU are shown in Fig. 1. The An–O bond lengths, given in Tab. 1, are on the long end of typical values for molecular An(IV) complexes and the decrease in bond length is notably smaller than the corresponding change in ionic radii from Np to Pu (0.005 and 0.02 Å, respectively), indicating a steric limitation for the high coordination number. Moreover, quantum chemical calculations at the DFT level of theory show clearly that the CN 12 can only be stabilized by enforcing high symmetry as found in the crystal structure of An-ADC. In practice, the high symmetry is enforced by the MOF scaffolding, proving that the same coordinative environment could not be isolated as a molecular complex.

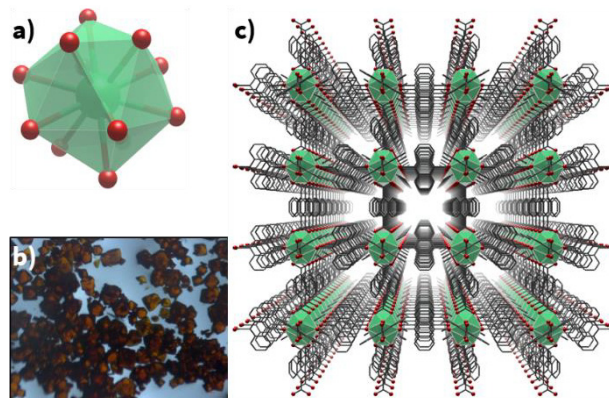


Figure 1. Structure of the PBU showing only An and O (a). Photograph of Pu(IV)-ADC single crystals (b); three-dimensional structure of the MOF lattice in An(IV)-ADC (c).

Despite the limitations imposed by working with actinides, efforts were made to characterize the chemical and physical properties of the novel materials. A BET surface area from CO₂ adsorption could be determined to 33.7 m²/g, corresponding to a median pore width of ~5.8 Å. Th(IV)-ADC is stable up to 210 °C, as well as in dilute acids, while in concentrated acid (8 M HNO₃) and 0.01 M NaOH considerable leaching is observed. In addition, UV/vis spectroscopy using a diffuse reflection setup revealed a wide band-gap of 2.84 eV for Th(IV)-ADC. The same MOF exhibits autoluminescence at a rate of 4.16 × 10⁴ cts/(s·g), more than ten times higher than Th(NO₃)₄·5H₂O.

It should be noted that La(III) and Eu(III) as well as Ce(IV), despite their equally large ionic radii, do not form isorecticular ADC-MOFs, but instead dimeric PBUs with a CN of 8 or 9 are observed. Attempts to synthesize U(III)-ADC yielded full *in situ* oxidation to again produce U(IV)-ADC. Co-crystallization in the presence of two actinides [Th(IV)/U(IV) or U(IV)/Np(IV)] leads to the selective crystallization of the MOF containing the larger actinide, which is likely related to the steric hindrance imposed by six ADC ligands.

In summary, our work has revealed a 12-coordinate MOF structure, which is unique to An(IV) and exhibits interesting properties, which may be exploitable for future applications. Here, the extraordinary CN is a consequence of the large cation radii of the tetravalent actinides in combination with the high symmetry enforced by the MOF scaffolding.

ACKNOWLEDGEMENTS. K.Lv was supported by the National Natural Science Foundation of China (No.12075214).

[1] Lv, K. *et al.* (2021) *Coord. Chem. Rev.* **446**, 214011.

[2] Kaltsoyannis, N. *et al.* (2017) *Angew. Chem. Int. Ed.* **56**, 7066–7069.

[3] Daly, S. R. *et al.* (2010) *Angew. Chem. Int. Ed.* **49**, 3379–3381.

[4] Lv, K. *et al.* (2022) *J. Am. Chem. Soc.* **144**, 2879–2884.

Electronic structure of plutonium dioxide nanoparticles at acidic pH

K. O. Kvashnina

Properties of PuO₂ nanoparticles (NPs) formed under acidic conditions (pH 1–4) are explored here at the atomic scale by high energy resolution fluorescence detected (HERFD) X-ray absorption spectroscopy at the Pu M₄ edge.^[1] The Pu(IV) oxidation state dominates in all NPs formed at pH 1–4. However, the suspension at pH 1 demonstrates the presence of Pu(III) and Pu(VI) in addition to Pu(IV), which originates from the starting solution rather than from the NPs themselves.

Plutonium (Pu) is undoubtedly one of the most puzzling elements of the periodic table. Pu may exist in oxidation states III, IV, V, VI and VII, though the latter is relatively stable only under alkaline oxidizing conditions. The most prominent peculiarity of Pu chemical complexity is the ease of redox transformations between Pu(III), Pu(IV), Pu(V) and Pu(VI), which allows Pu to exist under certain conditions in all four oxidation states simultaneously, even in natural waters. However, to determine exactly if other oxidation states of Pu are present, one needs to use a direct method of probing Pu electronic 5f-states at real state conditions. The recently developed synchrotron-based method – X-ray absorption near edge structure (XANES) in high energy resolution fluorescence detection (HERFD) mode – is a powerful technique to investigate Pu species, which allows for the determination of different oxidation state impurities with a high precision (in order of 2%). We have recently investigated PuO₂ NPs under other conditions (at pH 8 and pH >10) by the HERFD method and have found that Pu(IV) is the dominating oxidation state for all investigated NPs, synthesized under environmentally relevant and waste storage conditions.^[2–3] The aim of this study is to determine if similar PuO₂ NPs are formed under acidic conditions and to investigate Pu oxidation states in these NPs.

RESULTS. First, we have investigated structural and electronic properties of the formed PuO₂ NPs with high-resolution transmission electron microscopy (HRTEM) and HERFD methods. The HRTEM data reveal that independent from pH conditions, small crystalline NPs are formed with an average particle size of 2 nm, as reported in Fig. 1a-b. The HERFD-XANES spectra of the three investigated PuO₂ NP samples, formed at pH 1, 2 and 4 are similar (Fig. 1c). Spectra of NPs at pH 2 and 4 are identical to that of the reference while spectral features for NPs at pH 1 are broader and there is also a shoulder on the left side from the main edge (at ~3.967 eV). The characteristic spectral difference for all PuO₂ NPs compounds at various pH is shown at the bottom of Fig. 1c. The low energy shoulder in the X-ray spectroscopy process is generally attributed to a change towards a lower oxidation state and can indicate the presence of Pu(III) in the case of PuO₂ NPs formed at pH 1. The peak broadening of the absorption feature at the ~3.971.5 eV indicates the presence of higher oxidation states (probably Pu(VI)). The broadening of the main edge remains the same (as can be seen from the spectra directly or by checking the difference curve at this energy range) therefore contribution of Pu(V) can be excluded. Generally, the Pu(V) M₄ HERFD has a special energy position, which is shifted by 0.6 eV from Pu(IV).^[3] Therefore, it allows us to suggest that PuO₂ NPs formed at pH 1 contain a mixture of Pu(III), Pu(VI) and Pu(IV) oxidation states. Moreover, HRTEM shows that PuO₂ particles formed at pH 1 are less agglomerated than others. This indi-

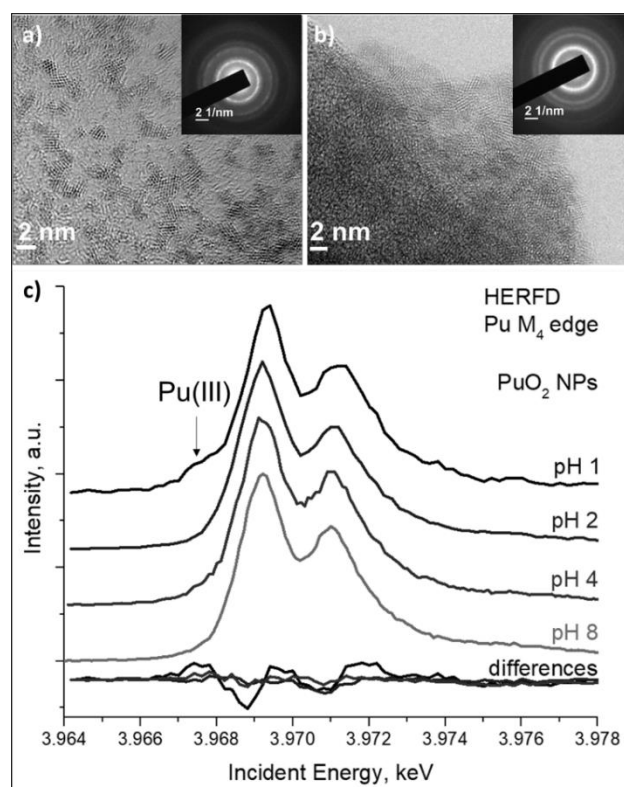


Figure 1. Solid phase characterisation: HRTEM data for NPs from Pu(IV) solution at pH 1 (a) and pH 2 (b). Inset: corresponding electron diffraction patterns. Pu M₄ HERFD spectra from NPs samples (c). Spectral difference between Pu samples and Pu reference “Pu (IV) from pH 8” are shown at the bottom.

cates the possible increase of NP stability in the solution as well and complicates the process of particle separation from the solution, requiring high-speed centrifuges or ultrafiltration. Therefore, as a next step, we have studied the evolution of the initial Pu solution over time. UV-vis spectra of the Pu solution recorded at different time intervals showed that after 20 hours of interaction (which corresponds to the time needed for the preparation of the samples for HERFD), the distribution of Pu oxidation states in solution is as follows: Pu(IV) is 1.4×10^{-4} M, Pu(III) is 0.4×10^{-4} M and Pu(VI) is 0.09×10^{-4} M. A Pu(V) contribution was not detected by UV-vis spectrometry.^[1] Therefore, we conclude that Pu oxidation states other than the Pu(IV) observed in the HERFD spectrum of the sample at pH 1 come directly from the solution. It has been detected due to the high sensitivity of the HERFD method towards the Pu concentration at these conditions.

ACKNOWLEDGEMENTS. This research was funded by European Commission Council under ERC grant N759696.

- [1] Gerber, E. et al. (2022) *Environ. Sci. Nano* **9**, 1509–1518.
- [2] Gerber, E. et al. (2020) *Nanoscale* **12**, 18039–18048.
- [3] Kvashnina, K. O. et al. (2019) *Angew. Chemie Int. Ed.* **58**, 17558–17562.

Synthesis and characterization of trivalent lanthanide and actinide complexes with amidinate ligands

B. Hong, T. Bode, P. Kaden, R. Gericke, J. März

A series of trivalent lanthanide and actinide tris-amidinate complexes $[M(iPr_2BA)_3]$ ($M = La, Nd, Eu, Yb, U, Np$; $iPr_2BA = N,N'$ -diisopropylbenzamidinate) was synthesized and characterized in solid state and in solution to gain a deeper understanding of the bonding situation between f -block elements and N -donor ligands.

Employing soft donor ligands to achieve selective actinide complexation is not limited to academic debate but is of importance for advanced nuclear industrial applications such as separation of actinides from trivalent lanthanides in spent nuclear fuel. It is believed that this selectivity originates from the subtle differences in covalent character in actinide metal-ligand interactions. Thus, covalency in f -element complexes is a topic of considerable current interest.^[1]

As part of our endeavor to elucidate this covalency in metal-ligand interaction, we recently have shown a synthesis route for the homoleptic (*S*)-PEBA complex of trivalent cerium and trivalent uranium as rare examples of chiral amidinate N -donor complexes.^[2,3] For the most part, however, amidinate complexes of trivalent actinides, especially transuranics, have remained elusive, which was our motivation for this present work.

EXPERIMENTAL. The synthesis of all trivalent tris-amidinate complexes $[M(iPr_2BA)_3]$ ($M(III) = La$ (1), Nd (2), Eu (3), Yb (4), U (5) and Np (6)) was achieved by a salt metathesis reaction of the anhydrous metal halides and three equivalents of lithium salt of the amidinate ligands (Fig. 1a). After workup procedures, the resulting compounds were obtained in good yields and were slowly evaporated from a saturated *n*-pentane solution at ambient temperature to obtain crystals suitable for SC-XRD measurement. All compounds were highly sensitive to air and moisture.

RESULTS. A schematic representation of the trivalent lanthanide and actinide complexes (1–6) is shown in Fig. 1a. The coordination geometry of the complexes can be described as distorted trigonal prismatic. For instance, the molecular structure of the Nd complex (2), represented in Fig. 1b., possesses a C_2 axis along the Nd1-C14 atoms and a pseudo C_3 axis defined by Q1 (where Q1 is the centroid of the plane spanned by N1-N2*-N3*) and Q2 (centroid of the plane spanned by N1*-N2-N3) derived from the nitrogen atoms of the three ligands.

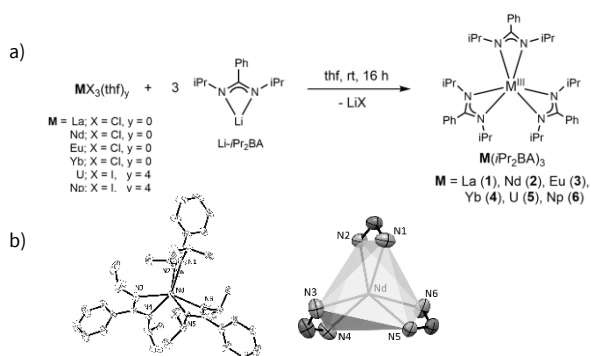


Figure 1. Synthesis of $[M(iPr_2BA)_3]$ (1–6) (a). Molecular structure and coordination polyhedron of $[Nd(iPr_2BA)_3]$ (2) with thermal ellipsoids drawn at the 30% probability level; hydrogen atoms are omitted for clarity (b).

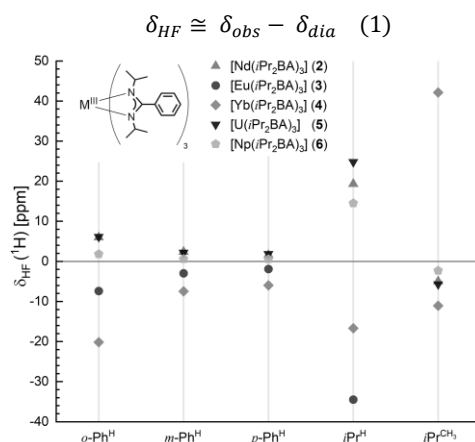


Figure 2. Plot of hyperfine chemical shift δ_{HF} for protons of $[M(iPr_2BA)_3]$ (2–6) in toluene- d_8 at 303 K.

The paramagnetic influence of the trivalent f -metal ions was investigated in solution by NMR spectroscopy. As there is no diamagnetic reference for trivalent actinide complexes, the chemical shifts of U(III) and Np(III) complexes were compared to those of the La(III) compound. The pure paramagnetic contribution was obtained by subtracting the chemical shift values of the diamagnetic reference $[La(iPr_2BA)_3]$ (1) from the measured chemical shifts of the paramagnetic complexes, and the resulting values were plotted in Fig. 2. According to the NMR studies, the electronic structures of $[U(iPr_2BA)_3]$ (5) and $[Np(iPr_2BA)_3]$ (6) are very similar to $[Nd(iPr_2BA)_3]$ (2) in solution. On the other hand, $[Eu(iPr_2BA)_3]$ (3) and $[Yb(iPr_2BA)_3]$ (4) complexes showed opposite signs of the hyperfine chemical shifts compared to Nd (2), U (5), and Np (6) complexes, as expected from literature.^[4] The CH_3 signal of the isopropyl group for $[Eu(iPr_2BA)_3]$ (3) is a very broad resonance ranging from 20 ppm to -10 ppm. For $[Yb(iPr_2BA)_3]$ complex (4), the signal for CH_3 splits into two peaks at 43 ppm and -10 ppm at 303 K. The elucidation of this behavior is part of ongoing investigations, and one possible explanation for this splitting is a hindered rotation of the CH_3 groups due to the small ionic radius (0.868 \AA) of Yb(III), causing different magnetic environments for the CH_3 protons.^[5]

Following work will focus on the synthesis and characterization of trivalent plutonium complexes to evaluate the covalency trends among the actinide series. In addition, EPR spectroscopy, superconducting quantum interference device (SQUID) magnetometry, and quantum chemical calculations will be applied to obtain in-depth knowledge of the electronic and magnetic properties of trivalent f -element complexes.

ACKNOWLEDGEMENTS. This work was supported by the German Federal Ministry of Education and Research (BMBF) under the project number 02NUK059B-f-Char.

- [1] Neidig, M. L. *et al.* (2013) *Coord. Chem. Rev.* **257**, 394–406.
- [2] Kloditz, R. *et al.* (2020) *Inorg. Chem.* **59**, 15670–15680.
- [3] Fichter, S. (2020) PhD thesis, TU Dresden.
- [4] Pintacuda, G. *et al.* (2007) *Acc. Chem. Res.* **40**, 206–212.
- [5] Shannon, R. D. (1976) *Acta Crystallogr.* **A32**, 751–767.

Quantum chemical investigation of possible Np⁴⁺-TM²⁺-interactions (TM = Ni, Pd, Pt) in heterotrimetallic complexes of the type [TM(μ -PyO)₄Np(μ -PyO)₄TM]

R. Gericke, M. Swart¹

¹Institut de Química Computacional i Catalísi, Universitat de Girona, Girona, Spain

Heterobi- or trimetallic compounds are an emerging topic due to their tunable bond characteristics and the synergistic properties arising from the heteronuclear core and the independently tunable ligand properties. Molecular heterometallic actinide-transition metal complex structures are highly underrepresented with only around 50 crystallographically characterized complexes in the literature, which are restricted to thorium and uranium with no example containing transuranic elements.^[1] However, actinides are outstanding probes for bond analysis due to their unique magnetic and electronic properties, e.g. as molecular magnets.

COMPUTATIONAL METHODS. The molecular geometry of complexes of the type [TM(μ -PyO)₄Np(μ -PyO)₄TM] (TM = Ni, Pd, Pt) have been optimized using ORCA 5.0.3 using the unrestricted PBE0 functional with a relativistically recontracted Karlsruhe basis sets ZORA-def2-TZVPP (for C, H, N, O, Ni) and SARC-ZORA-TZVPP (for Np, Pd, Pt), the scalar relativistic ZORA Hamiltonian, atom-pairwise dispersion correction with the Becke-Johnson damping scheme (D3BJ) and COSMO solvation (CH₂Cl₂: ϵ = 8.9, r_{solv} = 2.94). VeryTightSCF and slowconv options were applied and the DEFGRID3 was used with a radial integration accuracy of 10 for Np, Ni, Pd and Pt for all calculations. Further analyses have been performed using NBO 7.0 and Multiwfn 3.8.

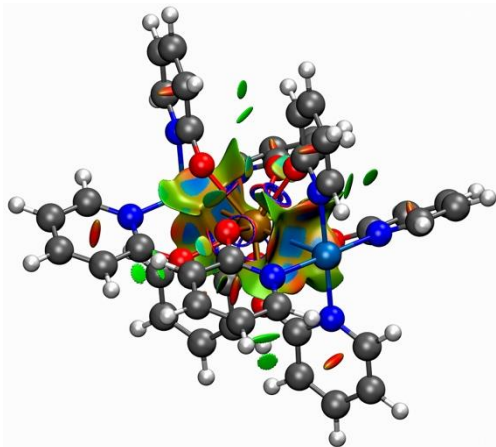


Figure 1. Non-covalent interactions descriptor (NCI) of the compound [Pt(μ -PyO)₄Np(μ -PyO)₄Pt] (Np – brown, Pt – teal, N – blue, O – red, C – grey, H – white; isovalue 0.45; blue zones indicate attractive interaction, red zones indicate repulsive interactions).

RESULTS. The abilities of d⁸-metals, such as Ni²⁺, Pd²⁺ and Pt²⁺, to act as lone-pair donors towards Lewis acids have already been demonstrated and make those elements interesting targets for the formation of An-TM complexes.^[2] The ambident 2-pyridyloxy has been proven to be an effective bridging ligand for heterobimetallic complexes.^[3] We therefore designed neutral complexes where the trans-uranic element Np is located in a double-capped square-antiprismatic coordination sphere with eight oxygen atoms and two transition metals (TM). The TM elements are square-planar coordinated by four N-donor atoms aligning the d(z²)-TM-orbitals along the TM-Np-TM axis. Geometry optimization of the symmetric complexes resulted in the following

Np-TM-distances: Np-Ni 3.36, Np-Pd 3.38, Np-Pt 3.33 Å, which are about 7%, 3% and 2% larger than the sum of the covalent radii, respectively.^[4] From pure geometric parameter, it can be assumed that Np⁴⁺-TM²⁺-interactions are present and will increase in the order Ni < Pd < Pt. The non-covalent interaction (NCI) descriptor confirms the expected trend reaching from van-der-Waals interactions for Np-Ni to increased attractive interactions in Np-Pt (Fig. 1) over Np-Pd. The natural charges obtained from natural population analyses (NPA) support a decreased ionic repulsion within the TM-Np-TM core along the series (Sum of Natural Charges of the TM-Np-TM core: TM = Ni 3.11, Pd 2.99, Pt 2.84).

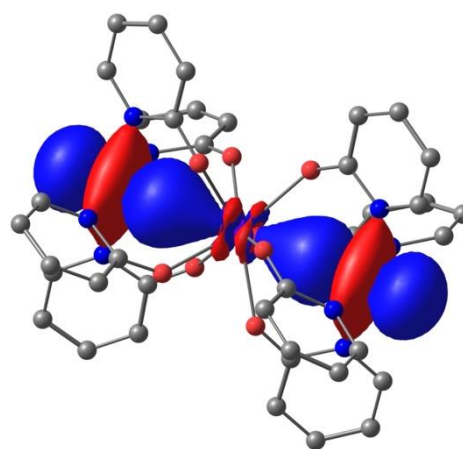


Figure 2. Visualization of two alpha spin d(z²) Pt Natural Localized Molecular Orbitals (NLMO) of the compound [Pt(μ -PyO)₄Np(μ -PyO)₄Pt] (isosurface 0.05 au). H atoms are omitted for clarity.

The delocalization index along the series is following the same order TM = Ni (0.04) < Pd (0.07) < Pt (0.12) and suggests, especially for the [Pt(μ -PyO)₄Np(μ -PyO)₄Pt] complex, some additional covalent contribution within the TM-Np-TM core. The two lone pairs observed by Natural Localized Molecular Orbital analyses of the Pt-Np-Pt complex, which are located along the heterotrimetallic core feature Pt/Np contributions of 96%/3% (Fig. 2). This clearly indicates some covalent interaction between the transition metal and actinide, respectively. The Np hybrid composition is 14% s, 45% d and 41% f. Such a high f-orbital contribution on the actinide motivates further quantum chemical and experimental investigations of these systems.

ACKNOWLEDGEMENTS. The authors are grateful to the HPC-Europa3 Transnational Access program for funding (HPC17UYKFM), the computer resources and assistance provided by the Barcelona Supercomputing Center and for computing time at the High-Performance Computing Cluster at TU Bergakademie Freiberg, which was funded by Deutsche Forschungsgemeinschaft (DFG)-397252409.

- [1] Cambridge Structure Database, ConQuest version 2021.3.0, build 333817.
- [2] Truflandier, L. A. *et al.* (2011) *Angew. Chem. Int. Ed.* **50**, 255–259.
- [3] Gericke, R. *et al.* (2021) *Inorg. Chem.* **60**, 18122–18132.
- [4] Cordero, B. *et al.* (2008) *Dalton Trans.*, 2832–2838.

The role of the atomic quadrupole moment for the prediction of paramagnetic chemical shifts in the NMR spectra of actinide complexes

M. Patzschke, J. März, P. Kaden, L. Köhler, M. Schmidt

A new tool to predict paramagnetic chemical shift patterns in ^1H -NMR spectra of actinide compounds was developed and tested. First results are presented here.^[1]

NMR spectroscopy is a valuable tool to gain structural information and insight into the electronic properties of chemical compounds. It has also proven to be very useful in actinide chemistry. Calculations of NMR parameters, especially the shielding tensor, have progressed rapidly and have reached a stage where prediction of NMR spectra is now routine, at least for closed shell systems. Many actinide compounds, however, possess unpaired electrons and therefore additional shifts are observed. Calculation of these is not straightforward and is a topic that is still under active development. For lanthanide compounds such calculations have been performed successfully, but actinides are more complicated. Due to increased relativistic effects, spin-orbit coupling leads to closer lying states, this makes the required accuracy of the involved calculations higher. Numerous of such multi-reference calculations are required to simulate a single spectrum and quite often these calculations are at the border of what is computationally feasible. A simpler computational tool to predict the typical shift pattern would therefore be valuable. The atomic quadrupole moment might be this tool. The connection between these moments and paramagnetic chemical shifts will be discussed in the following and a few results will be presented.

METHODS. Chemical shifts are sensitive to the environment. This effect is enhanced, when unpaired electrons are present. In addition to the diamagnetic shift of the closed-shell reference, one finds paramagnetic shifts that approximately comprise of δ_{con} (contact shift or FCS) and δ_{pc} (pseudocontact shift or PCS). The FCS progresses through bonds and decays rapidly, becoming irrelevant after three bonds. It is therefore not very important in the ^1H -NMR of our actinide complexes. The PCS works through space and affects nuclei farther away from the heavy metal center. The effect can be positive or negative and it is governed by Equation 1:

$$\delta_{\text{PC}} = \frac{1}{12\pi r^3} \left[\Delta\chi_{\text{ax}} (3 \cos^2(\theta) - 1) + \frac{3}{2} \Delta\chi_{\text{rh}} (\sin^2 \theta \cos 2\Omega) \right] \quad (1)$$

It is seen, that the PC shift depends on the shape of the tensor of magnetizability. This tensor consists only of real numbers and can therefore always be diagonalized. If in the diagonal form there is one large and two small values, the tensor is prolate and the system is called axial. In this case, the PC shift distribution looks like a $d(z^2)$ orbital, with the positive shifts in the dumbbell parts and negative shifts in the torus part (Fig. 1, top). Quite often the situation is not so clear cut and the shape of the PCS cones is somewhat more complex. The magnetizability has to be calculated at the NEVPT2 level and such calculations are very demanding. The problem for actinide compounds are the numerous low-lying excited states that have to be included in the calculation. Interestingly, the magnetizability is connected with another property that is easier to calculate, namely the quadrupole moment of the molecule or the quadrupole moment of the actinide in the complex, as this is the center of the unpaired electrons. Equation 2 shows the connection between the two quantities:

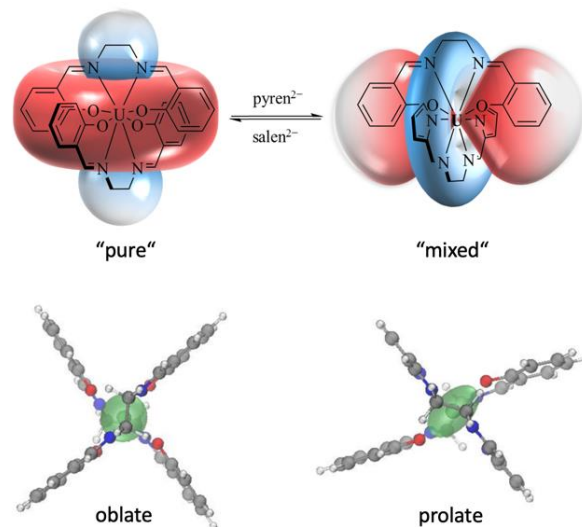


Figure 1. PCS cones for the pure U(IV) salen complex (top left) and the mixed salen/pyren complex (top-right). Red indicates regions of negative PCS contribution, blue positive PCS contributions. In the lower part the corresponding quadrupole moments of the uranium atom can be seen.

$$Q_{aa} = -\frac{\hbar|e|}{8\pi M_p} \left\{ \frac{2g_{AA}}{A} - \frac{g_{BB}}{B} - \frac{g_{CC}}{C} \right\} - \frac{2mc^2}{|e|} \{ 2\chi_{AA} - \chi_{BB} - \chi_{CC} \} \quad (2)$$

This equation also contains the g-tensor and the three rotational moments in the reference frame of the molecule (principal axis A, B and C). It should therefore be possible to gain insight into the shape of the magnetizability by calculating the quadrupole moment, a quantity that can be calculated at the DFT level. Such calculations can be performed by analyzing the multipole moment in QTAIM basins of the molecule using the software MultiWFN.^[2]

RESULTS. Our group recently managed to synthesize a U(IV) complex bearing one salen and one pyren ligand^[1]. The ^1H -NMR spectrum of this complex differs from previously synthesized pure 1:2 salen and pyren complexes. Direct calculation of the magnetizability tensor is very difficult as U(IV) is not a Kramers doublet, but has many low-lying states. We therefore tested our new tool and the effect of the change in substitution on the quadrupole moment of U(IV) is striking. In the pure salen case an oblate form is found, governed by the four U-O interactions. In the mixed system this changes to a prolate form, with the axis along the O-U-O bonds. The PCS cones and quadrupole moments can be seen in Fig. 1. Further studies are being conducted to ascertain the usefulness of this metric for other actinide complexes.

[1] Köhler, L. (2022) PhD thesis, TU Dresden.

[2] Lu, T. and Chen, F. (2012) *J. Comput. Chem.* **33**, 580–592.

Modelling of polymer structures with the cheminformatics software RDKit

L. Waurick, B. Drobot, M. Patzschke

Especially for polymer structures with different monomers, the amount of possible combinations rises fast, leading to various problems in studying the behavior of those molecules. The greater the variability of the structures, the more difficult it becomes to find a suitable screening method using an experimental approach. One way to deal with this is to take advantage of the increasing capabilities of theoretical chemistry. While Molecular Mechanics (MM) software is already fast enough to calculate a large number of different molecules with a reasonable size, generating those starting structures also needs to happen before. The cheminformatics python package RDKit provides several tools for an automated way to create polymer structures with the opportunity to freely design the python script it is used with.^[1]

WORKING WITH RDKIT. Once RDKit is imported to the python code, there are two basic options to create a molecular structure. The first one is that the structure is created from a so-called Smiles, which is a definition of a molecule as a string (e.g., "CCCCCCC" for heptane). The second option is to import the structure information from a .mol-file or a similar text in form of a .mol-file. Afterwards, the molecular coordinates are typically stored in a 2D variant of themselves without any hydrogen atoms. In case of organic polymers, this is helpful as the addition of side chains is fairly easy without first removing hydrogen atoms. In preparation for a calculation, the next step is to add hydrogens based on the potential neighbors of each atom. The Adjustment of the atom properties (e.g., charges) is also possible and needs to be done before adding those hydrogen atoms.^[2]

RDKit does also provide a method to convert the 2D structures stored in .mol-files into 3D structures. Therefore, a combination of two algorithms is included in the python package. The first one uses distance geometry to generate an initial estimate of the coordinates based on the connection table.^[3] The second is the ETKDG method of Riniker and Landrum and utilizes torsion angle preferences from the Cambridge Structural Database (CSD) as a correction to the coordinates generated by distance geometry.^[4] This normally leads to a good start structure for upcoming theoretical experiments.^[2] Figure 1 shows a scheme of the basic workflow for creating a heptane molecule with different functional groups as side chains.

For some applications it may be useful to directly change some specific coordinates within the 3D structures. To achieve this, the structure information needs to be converted to a conformer format by a built-in function. This creates a link between the corresponding .mol and conformer data. The conformer format can then be used to read and manipulate the coordinates of specific atoms of the structure on the fly.^[2]

OUTLOOK. In general, the RDKit package is a useful tool for automated structure generation in theoretical chemistry. With the polymer structures generation methods shown, it will be possible to build peptides just by the sequence of their amino acids. These can be used to accomplish a screening method for the investigation of the bonding of these biopolymers to different metal centers. Therefore, the Universal Force Field (UFF), which is also implemented in RDKit, will be used to optimize the biopolymer structures.^[5] The goal of the screening will be to filter out possible candidates for a

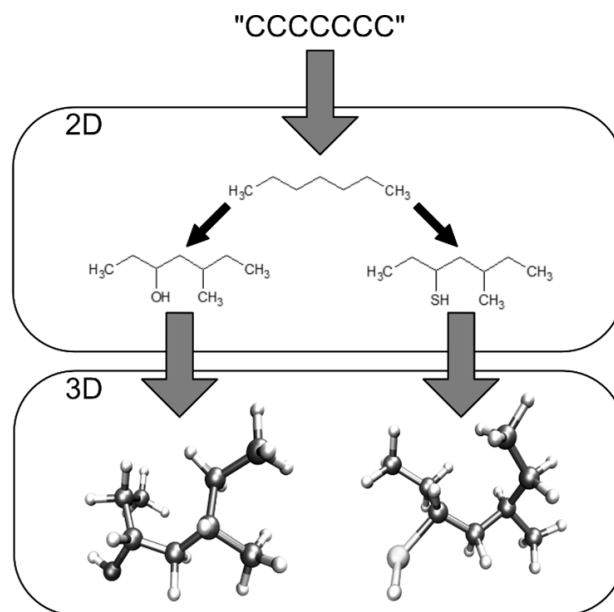


Figure 1. Workflow of building two different substituted heptane molecules in RDKit.

strong binding of the desired metal from the huge amount of different peptides. Then, when only a few amino acid sequences are available, they can be much more easily studied with experimental approaches or with a higher specification level of theoretical chemistry (e.g., DFT).

[1] RDKit: Open-source cheminformatics. <https://www.rdkit.org>.

[2] Getting Started with the RDKit in Python. <https://www.rdkit.org/docs/GettingStartedInPython.html>.

[3] Blaney, J. et al. (1994) *Reviews in Computational Chemistry*, VCH, New York.

[4] Riniker, S. et al. (2015) *J. Chem. Inf. Comp. Sci.* **55**, 2562–74.

[5] Rappe, A. et al. (1992) *J. Am. Chem. Soc.* **114**, 10024–10039.

Analysis of the reduction mechanisms of technetium in NaClO₄ combining spectro-electrochemical methods and electrochemical analysis

D. M. Rodríguez, N. Mayordomo, A. Parra-Puerto,¹ D. Schild,² V. Brendler, T. Stumpf, K. Müller

¹Imperial College London, London, United Kingdom; ²Karlsruhe Institute of Technology, Karlsruhe, Germany

The reduction of technetium (Tc) from Tc(VII) to Tc(IV) in NaClO₄ solution has been studied as a function of pH by spectro-electrochemical methods and electrochemical analysis. The results show that the reduction of Tc(VII) to Tc(IV) occurs directly at pH > 4, whereas it goes through a Tc(V) intermediary species at pH 2.

⁹⁹Tc is a long-lived fission product ($\tau_{1/2} \sim 2.14 \times 10^5$ years) of ²³⁵U and ²³⁹Pu. Tc migration in ground water is highly dependent on its oxidation state. The reduction of Tc(VII)O₄⁻ to Tc(IV) hampers Tc migration since either a low soluble solid (TcO₂) and/or cationic species ready to interact with minerals are formed. This reduction step is electrochemically induced or by reductants such as Fe(II)- or S(-II)-minerals.^[1-3] However, the molecular mechanisms of this step had not been yet fully understood. Despite the clear environmental relevance, this is important from a fundamental chemical point of view. In this work, we have explored the reduction mechanism of Tc(VII) in non-complexing NaClO₄ solutions by spectro-electrochemical methods, Raman microscopy, X-ray photoelectron spectroscopy (XPS), and electrochemical analysis.^[4]

EXPERIMENTAL. Solutions of 0.5 mM KTc(VII)O₄ solutions were analyzed. The electrodes used in the electrochemical procedures were glassy carbon electrode as working electrode (both in stationary or rotational mode), platinum as counter electrode, and Ag/AgCl (3 M KCl) as reference electrode. Tc(VII) electrochemical reduction was monitored in parallel by UV-vis spectroscopy in an N₂ glovebox.^[5] Cyclic voltammetry (CV) was performed at five different scan rates (from 5 to 25 mV/s) at pH 2.0 and pH 10.0. The current of the peaks associated to reduction processes (cathodic peaks) in a window of potential interest were scanned using a rotating disc electrode at six angular velocities (from 100 to 3,000 rpm) (884 Professional VA instrument, Metrohm). The precipitate obtained in the electrochemical reduction was analyzed by Raman spectroscopy (Aramis, Horiba), and by XPS (PHI 5000 VersaProbe II, ULVAC-PHI Inc.).

RESULTS. Figure 1 shows the CV performed in Tc solutions at pH 2.0 and pH 10.0 at different scan rates. CV carried out from pH 4.0 to 8.0 are comparable to that recorded at pH 10.0. It is observed that the number of peaks present in the CV is dependent on pH, which is related to a change in the number of electroactive species. As well, in the range from -0.9 to +1.2 V, a change is observed in the potential values related to oxidation and reduction processes. Spectro-electrochemical reduction experiments at pH 2.0 and pH 10.0 show a decrease on the intensity of the Tc(VII)O₄⁻ signals at 247 and 289 nm, but no additional bands are observed. In the electrochemical reduction experiments, the formation of a solid is observed at both pH values.^[4] XPS identified Tc(IV) in the solids, which also present two characteristic peaks in the Raman spectra (374 and 1107 cm⁻¹).^[4] Thus, with the aim to analyze the reduction mechanism of Tc(VII) at pH 2.0 and 10.0, we have measured the current for potentials in the region of interest of cathodic peaks using a rotating disc electrode. Randles-Sevcik and Levich equations were applied to the results to determine the number of

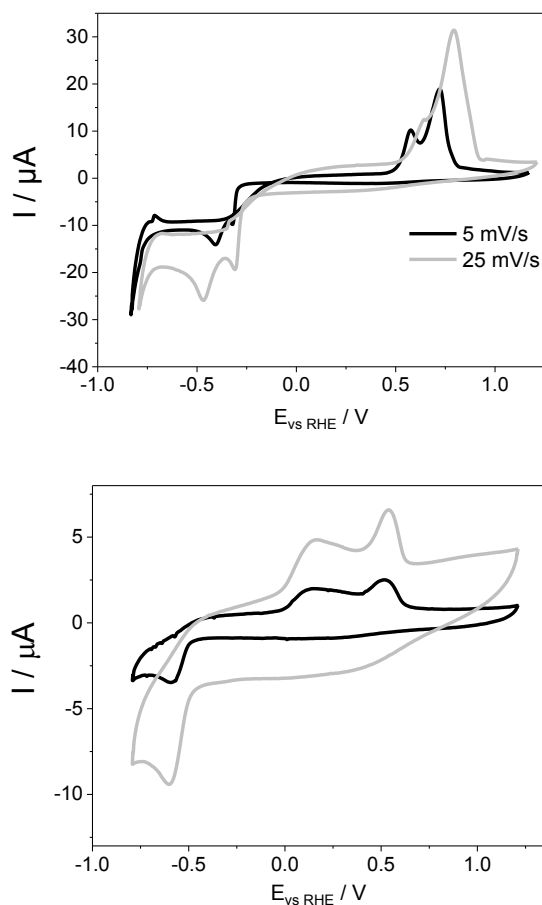


Figure 1. Cyclic voltammograms of 0.5 mM KTcO₄ solutions at pH 2.0 (top) and pH 10.0 (bottom). Potential values have been converted to those for reversible hydrogen electrode (RHE).

electrons exchanged and the diffusion coefficient of the electroactive species, respectively. Details are given elsewhere.^[4] At pH 2.0, the reduction occurs in two steps with the initial gain of 2.3 ± 0.3 electrons by Tc(VII) to obtain Tc(V), which subsequently receives 1.3 ± 0.3 electrons to form Tc(IV). At pH 10.0 Tc(VII) is directly reduced to Tc(IV) with the transfer of 3.2 ± 0.3 electrons.

These results narrow a significant gap in the fundamental knowledge of Tc aqueous chemistry and are important to understand Tc speciation. They provide basic steps on the way from non-complexing to complex media.

ACKNOWLEDGEMENTS. Funding from the Federal Ministry for Economic Affairs and Climate Action (BMWK) is acknowledged (02E11607B).

- [1] Pearce, C. *et al.* (2019) *Sci. Total Environ.* **716**, 132849.
- [2] Pearce, C. *et al.* (2018) *ACS Earth Space Chem.* **2**, 532–547.
- [3] Chotkowski, M. *et al.* (2021) *Electrochemistry of Technetium*, Springer International Publishing AG, Amsterdam, The Netherlands.
- [4] Rodríguez, D. M. *et al.* (2022) *Inorg. Chem.* **61**, 10159–10166.
- [5] Rodríguez, D. M. *et al.* (2022) *Report HZDR-119*, p. 50.

Shedding light on the enigmatic $\text{TcO}_2 \cdot x\text{H}_2\text{O}$ structure with Density Functional Theory and EXAFS spectroscopy

A. F. Oliveira, A. Kuc, T. Heine,¹ U. Abram,² A. C. Scheinost

¹Technische Universität Dresden, Dresden, Germany; ²Freie Universität Berlin, Berlin, Germany

The β -emitting ^{99}Tc isotope is a high-yield fission product in ^{235}U and ^{239}Pu nuclear reactors, raising special concern in nuclear waste management due to its long half-life and the high mobility of pertechnetate (TcO_4^-). Under the conditions of deep nuclear waste repositories, Tc is retained through biotic and abiotic reduction of TcO_4^- to compounds like amorphous $\text{TcO}_2 \cdot x\text{H}_2\text{O}$ precipitates. It is generally accepted that these precipitates consist of linear $(\text{Tc}(\mu\text{-O})_2(\text{H}_2\text{O})_2)_n$ chains, with H_2O at *trans* positions. Although corresponding Tc-Tc and Tc-O distances have been obtained from EXAFS spectroscopy, this structure is largely based on analogy with other compounds. Here, by combining DFT calculations and EXAFS measurements of fresh and aged $\text{TcO}_2 \cdot x\text{H}_2\text{O}$ samples, we show that $\text{TcO}_2 \cdot x\text{H}_2\text{O}$ forms zigzag chains with H_2O groups in *cis* configuration. Moreover, these chains undergo a very slow aging process whereby they form longer chains and, later, a tridimensional structure that could eventually result in a new TcO_2 polymorph.^[1]

EXPERIMENTAL. Assuming Re as an analogue for Tc, we took crystallographic coordinates of α -, β -, and γ - ReO_2 to construct the corresponding TcO_2 crystal structures.^[2–4] From these, α -, β -, and γ - $\text{TcO}_2 \cdot 2\text{H}_2\text{O}$ infinite chains were extracted; to balance the electric charges and to saturate dangling bonds, terminal O-atoms were converted into H_2O groups. All crystal and chain structures were fully optimized (including lattice parameters) with the PBE density functional in AMS/BAND.^[5] Experimental EXAFS spectra were collected for $\text{TcO}_2 \cdot x\text{H}_2\text{O}$ samples measured within a week from preparation (fresh) and about four years after preparation (aged).^[1,6] EXAFS shell fitting was conducted in *R*-space with WinXAS;^[7] JFEFF 9.6 was used to derive paths for the intrachain Tc-O and Tc-Tc distances from the DFT-optimized β - $\text{TcO}_2 \cdot 2\text{H}_2\text{O}$ chain structure, and paths of interchain Tc-Tc distances from the DFT-optimized β - TcO_2 crystal structure.^[8]

RESULTS. The DFT calculations clearly show the zigzag chain – β - $\text{TcO}_2 \cdot 2\text{H}_2\text{O}$ – as the most energetically favored (Fig. 1). The Tc-O bond lengths are characteristic of the O-configuration (terminal, bridged, protonated, unprotonated), while Tc-Tc distances allow to unambiguously discriminate the three chain configurations. Indeed, simulated EXAFS spectra for α -, β -, and γ - $\text{TcO}_2 \cdot 2\text{H}_2\text{O}$ chains differ considerably from each other, with β - $\text{TcO}_2 \cdot 2\text{H}_2\text{O}$ giving the best match to the experimental spectra of the fresh and aged samples. Moreover, as shown in Fig. 2, Tc-O and Tc-Tc distances obtained from EXAFS fittings are in excellent agreement with the optimized β - $\text{TcO}_2 \cdot 2\text{H}_2\text{O}$ chain, especially for the aged sample, for which high frequency signals (absent in the fresh sample) could be fitted to second and third Tc-Tc intrachain shells and to interchain distances compatible with the β - TcO_2 crystal. Therefore, our data suggest that small zigzag chain units form initially, which then continue to age, polymerizing by dehydration into a loose tridimensional network. Eventually, a new β -type TcO_2 polymorph may form.

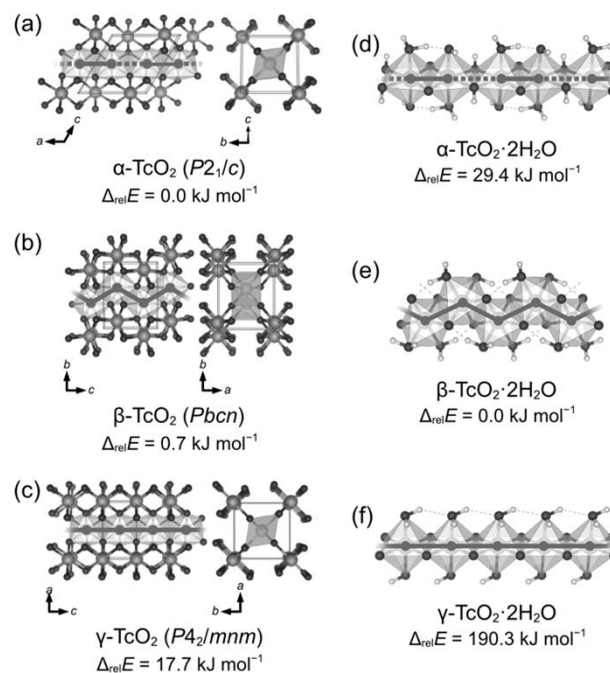


Figure 1. Optimized structures of TcO_2 crystal polymorphs and related $\text{TcO}_2 \cdot 2\text{H}_2\text{O}$ chains. Tc atoms represented as octahedra emphasize the structure of laterally interconnected chains in the TcO_2 crystals. The light grey lines emphasize the linear and zigzag paths of the chains, with dashed lines indicating the longer Tc-Tc distances. During optimization of α - $\text{TcO}_2 \cdot 2\text{H}_2\text{O}$, a few H atoms migrated from H_2O groups to μ -O bridges. The $\Delta_{\text{rel}}E$ values correspond to the relative energies per formula unit.

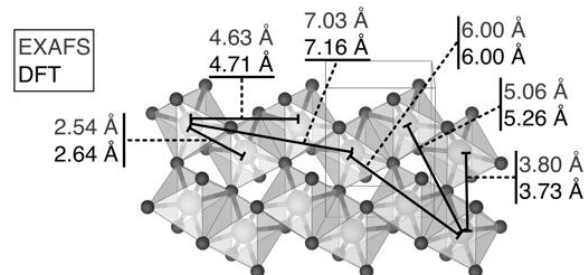


Figure 2. Tc-Tc distances for $\text{TcO}_2 \cdot x\text{H}_2\text{O}$. EXAFS values were obtained from the spectrum of the aged sample. Intra- and interchain values for DFT come from the optimized structure of the β - $\text{TcO}_2 \cdot 2\text{H}_2\text{O}$ chain and β - TcO_2 crystal. The excellent agreement between EXAFS and DFT (upper and lower digits, respectively) indicates that $\text{TcO}_2 \cdot x\text{H}_2\text{O}$ consists of zigzag chains that slowly age into longer chains, eventually forming tridimensional structures.

ACKNOWLEDGEMENTS. The research was funded by the European Commission (EC) via the EURAD FUTURE T3 project (H2020-847593) and by the German Federal Ministry of Education and Research (BMBF) via the KRIMI project (02NUK056C). The authors thank Prof. B. Grambow (SUBATECH Nantes, France) for fruitful discussions.

- [1] Oliveira, A. F. *et al.* (2022) *Chem. Eur. J.* **28**, e202202235.
- [2] Ferreira, F. F. *et al.* (2009) *J. Synchrotron Radiat.* **16**, 48.
- [3] Magnéli, A. (1957) *Acta Chem. Scand.* **11**, 28.
- [4] Ivanovskii, A. L. *et al.* (2005) *Phys. Lett. A* **348**, 66–70.
- [5] AMS 2019, SCM, Theoretical Chemistry, Vrije Universiteit, Amsterdam, The Netherlands (<https://www.scm.com/doc/BAND/index.html>).
- [6] Yalçıntaş, E. *et al.* (2016) *Dalton Trans.* **45**, 17874.
- [7] Ressler, T. (1998) *J. Synchrotron Radiat.* **5**, 118.
- [8] Rehr, J. J. *et al.* (2010) *Phys. Chem. Chem. Phys.* **12**, 5503.

How to determine robust and reliable thermodynamics – An exemplary approach combining NMR, TRLFS, and ITC

C. Sieber, B. Drobot, J. Kretschmar, K. Schmeide

Accurate literature data on thermodynamics of organic chelating ligands is scarce. Many publications lack spectroscopic evidence for all prevalent species, which is necessary for accurate data evaluation. Multi-species systems and high complex formation constants are hardly accessible for typical techniques like potentiometric titrations or spectrophotometric experiments.^[1,2] To address some of these difficulties and improve data quality, we propose a multi-method scheme (Fig. 1) to analyze dissolved metal complexes of organic ligands using nuclear magnetic resonance spectroscopy (NMR), time-resolved laser-induced fluorescence spectroscopy (TRLFS) and isothermal titration calorimetry (ITC).

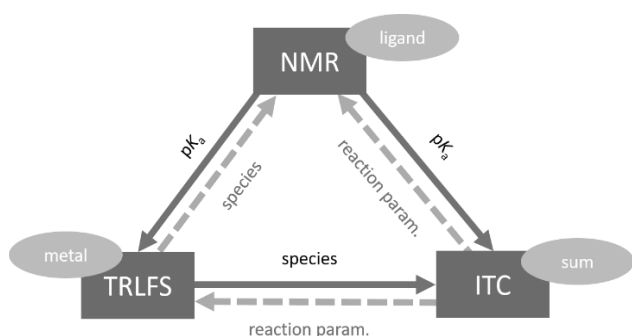


Figure 1. Schematic representation of workflow.

All three aforementioned methods have different advantages. One method alone cannot provide a comprehensive overview of the complexation, so multiple methods should be considered. The information gained with one method, however, is key for planning accurate experiments with the other two and *vice versa*.

Table 1. Methods used in this paper and the information they provide.

Provides information about:	NMR	TRLFS	ITC
pK _a	x		
log β		x	x
ΔH, (ΔS, ΔG)			x
species distribution	(x)	x	
ligand	x		
metal		x	
complex	(x)	x	
reaction			x

NMR spectroscopy is an elegant method for determining pK_a values. In contrast to, e.g., potentiometry, it also provides structural information, allowing for assignment of the respectively abstracted proton. Corresponding pH-dependent chemical shifts can be analyzed by means of sigmoidal dose-response fit functions, with the inflection point(s) representing the pK_a value(s) (Fig. 2, left).

Knowing the ligand's pK_a value(s), optimized TRLFS and ITC experiments are possible, since the pH ranges for the deprotonation of the ligand are known.

Regarding the formed complex species, TRLFS provides useful information from the metal ion's perspective upon, e.g., ligand-to-metal titrations where in case of Eu(III) corre-

sponding ⁵D₀ → ⁷F_j transitions change systematically (Fig. 2, right). Additionally, from luminescence lifetimes the number of coordinating water molecules can be determined. When multiple species are present, extraction of single component spectra is necessary, and can be achieved by using parallel factor analysis (PARAFAC).

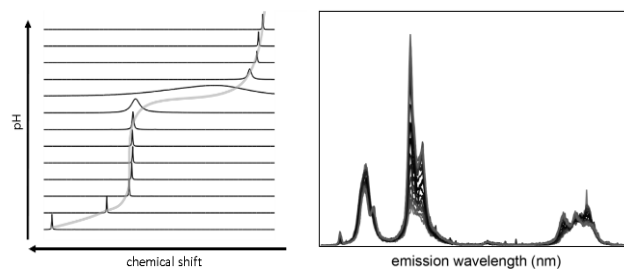


Figure 2. Exemplary pH-dependent ligand ¹H NMR spectra (left) and Eu(III) fluorescence spectra as a function of ligand concentration (right).

For ascertaining complex stoichiometries, NMR and TRLFS can respectively quantify fractions of uncomplexed ligand and metal ions in solution.

With the number of complex species and their distribution on hand, optimal experimental conditions, for instance concentration and pH range, can be set for ITC measurements, since this technique does not allow for species sensitive measurements.

ITC can be used as a complementary technique to gather thermochemical data. The observable of ITC is heat released in a chemical reaction based on its reaction enthalpy (ΔH) (Fig. 3). In addition, complex affinities (K) and reaction stoichiometries can be determined. With $-RT \ln K = \Delta_R G^0$ and $\Delta G = \Delta H - T\Delta S$ the Gibbs free energy and entropy of the reaction can be determined.

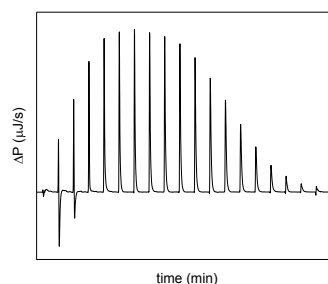


Figure 3. Exemplary ITC thermogram of a carboxylic ligand as a function of Eu(III) concentration.

CONCLUSION. Thermodynamic data play a key role in risk and safety assessment of, e.g., long-term nuclear waste repositories. Since organic ligands used for decontamination processes, such as nitrilotriacetate (NTA), are often co-disposed with the radioactive waste, their complexation behavior has to be considered when modeling such a repository. The proposed method provides accurate and reliable values for log β, ΔH and ΔS, which are essential parameters for such models.^[3]

[1] McBryde, W. *et al.* (1973) *J. Inorg. Nucl. Chem.* **35**, 4193–4197.

[2] Souaya, E. *et al.* (2000) *Molecules* **5**, 1121–1129.

[3] Sieber, C. *et al.* (2023) in preparation.

2-Phosphonobutane-1,2,4,-tricarboxylic acid (PBTC): pK_a determination by multinuclear NMR spectroscopy

J. Kretzschmar, A. Wollenberg,^{1,2} S. Tsushima,³ K. Schmeide, M. Acker^{1,2}

¹Chair for Radiochemistry and Radioecology, Technical University Dresden, Dresden, Germany; ²Central Radionuclide Laboratory and Radiation Protection, Technical University Dresden, Dresden, Germany. ³International Research Frontiers Initiative, Institute of Innovative Research, Tokyo Institute of Technology, Meguro, Tokyo, Japan

2-Phosphonobutane-1,2,4,-tricarboxylic acid, PBTC, is utilized as an efficient long-term retarder in concrete, and as a corrosion inhibitor in reinforced concrete and steel. As such, PBTC could also become a substantial component of a nuclear waste repository, and is therefore being investigated for its complexation properties towards radionuclides. Reliable pK_a values of PBTC are scarcely found in the literature. However, these data are critical parameters for ascertaining PBTC speciation, especially with regard to a sound structural and thermodynamic characterization of its metal ion complexes. A rigorous evaluation of pH-dependent ¹H, ¹³C, and ³¹P NMR spectra allowed determination of the pK_a values along with their assignment to the corresponding sites.

EXPERIMENTAL. Details of both sample preparation and quantum chemical calculation can be found in our recent paper.^[1] Briefly, PBTC solutions with background electrolyte, $I_m = 0.5\text{ m NaCl}$, were prepared in the pH range 0–11 with increments of 0.2 to 0.4 pH units, and measured by ¹H, ³¹P, and ¹³C NMR spectroscopy. Spectra were recorded at 25 °C with an Agilent DD2-600 NMR system, operating at 14.1 T with corresponding ¹H, ¹³C, and ³¹P resonance frequencies of 599.8, 150.8, and 242.8 MHz, respectively, using a 5 mm oneNMR™ probe.

RESULTS. Changes in the molecule's structure (*e.g.*, conformation) or speciation (*e.g.*, protonation and/or redox states) can be addressed by NMR. Accordingly, changes in the resonance frequencies of nuclei of (or close to) a functional group upon de-/protonation reactions allow for determination of the molecule's pH-dependent microstates. Consequently, the pH-induced shifts of NMR signals can be evaluated by means of sigmoidal dose–response fit functions, of which the inflection point(s) represent the pK_a value(s). In the case of PBTC (*cf.* Fig. 1A), five pK_a values are to be expected, *viz.* two for the dibasic phosphonate group, and three for the respective carboxyl groups.

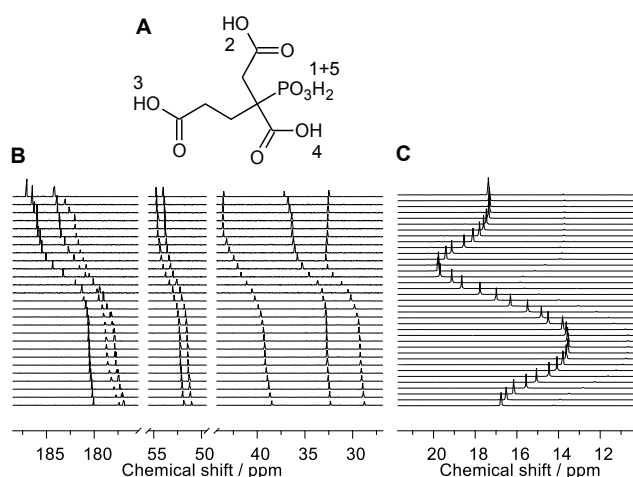


Figure 1. Generic structure of PBTC along with sequence of deprotonation (A). NMR pH-titration series of PBTC ($I_m = 0.5\text{ m NaCl}$), with pH values increasing from bottom to top: ¹³C NMR (B) and ³¹P NMR spectra (C).

Upon increasing pH, *i.e.* successive deprotonation, the ¹³C signals uniformly shift downfield (Fig. 1B), whereas the phosphonate's ³¹P NMR signal (Fig. 1C) behaves more complex. In contrast, the ¹H signals (not shown) feature special behavior as they respond to changes in both speciation and conformation, with opposing effects on the shifts. Therefore, and because of directly probing the sites of interest, ¹³C and ³¹P spectra were used to determine pK_a values.^[1] The latter are summarized in Tab. 1, and a corresponding species distribution diagram is shown in Fig. 2.

Table 1. pK_a values ($I_m = 0.5\text{ m NaCl}$) of PBTC obtained from ³¹P and ¹³C NMR pH-titration.

Site	pK_a^*
PO ₃ H ₂	0.90 ± 0.02
1-COOH	3.92 ± 0.03
4-COOH	4.76 ± 0.03
2-COOH	6.13 ± 0.03
PO ₃ H ⁻	9.79 ± 0.02

*: mean ± 2σ.

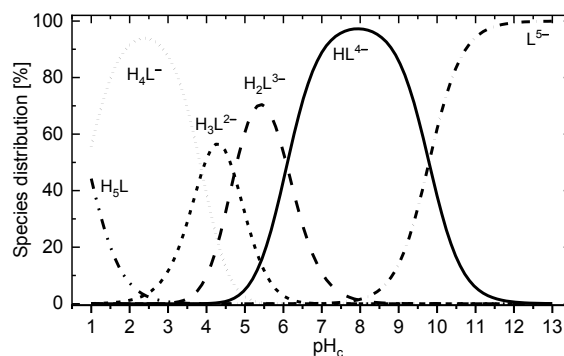


Figure 2. Species distribution diagram of PBTC (H₅L) corresponding to the pK_a values determined in this study.

In order to ascertain the mobility of a metal ion (radionuclide) of interest and hence performing a sound risk and safety assessment, robust and reliable thermodynamic data for any formed complex are essential. Hereby, the ligand's pK_a values, as determined for PBTC in this work, are critical figures for subsequent determination of thermodynamic parameters of the formed complex(es). For a more general procedure on obtaining such data set (*e.g.*, $\log \beta$, ΔH , and ΔS), refer to C. Sieber *et al.*^[2]

ACKNOWLEDGEMENTS. This research was funded by the German Federal Ministry for Economic Affairs and Energy (BMWi) within the GRaZ II projects, nos. 02E11860B and 02E11860G. The authors thank D. Goldbach for his valuable lab work.

[1] Kretzschmar, J. *et al.* (2022) *Molecules*, **27**, 4067.

[2] Sieber, C. *et al.* (2023) this report, p. 22.

Direct determination of anomalous dispersion correction parameters from single-crystal structure data

C. Hennig, F. Meurer,¹ O. V. Dolomanov,² N. Peyerimhoff,³ F. Kleemiss,¹ H. Puschmann,^{2,3} M. Bodensteiner¹

¹Faculty for Chemistry and Pharmacy, University of Regensburg, Regensburg, Germany; ²OlexSys Ltd., Chemistry Department, Durham University, Durham, U.K.; ³Department of Mathematical Sciences, Durham University, Durham, U.K.

The atomic form factor is a prerequisite to determine atomic structures with X-ray diffraction. Corrections for anomalous dispersion effects must be applied to take resonant scattering into account. The traditional way is to use tabulated values based on theoretical calculations on isolated atoms, e.g., the values of Sasaki and Henke *et al.*^[1,2] Here we show that anomalous dispersion parameters can be derived directly from experimental diffraction data.^[3]

The atomic form factor includes contributions for elastic and inelastic scattering, the latter being called anomalous dispersion parameters. The correction for anomalous dispersion based on tabulated values is only a rough approximation. Near absorption edges, these data are not correct because they contain additional fine structures resulting from electronic transitions into partially occupied orbitals and from backscattering of electrons from neighboring atoms. Thus, this correction requires significant refinement. Our aim is to determine anomalous dispersion parameters directly from single-crystal structure data. The experiment requires a tunable X-ray source, a detector for X-ray diffraction (Pilatus 2M) and a fluorescence detector (Vortex) to determine independently the X-ray absorption spectrum, which corresponds to the absorptive part of the anomalous dispersion (f''). This setup is provided by XRD2 at ROBL (see schematic representation at Fig. 1).^[4]

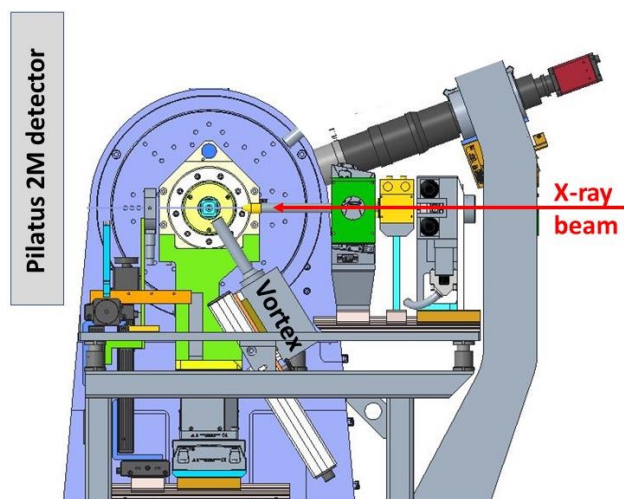


Figure 1. Schematic drawing of XRD2 / ROBL.

We determined the dispersion parameters of $\text{Mo}(\text{CO})_6$ using diffraction data.^[5] These values were compared with the absorptive part of the anomalous dispersion accessible from the Mo K edge absorption spectrum of the same sample. The related dispersive function f' was derived from f'' according to the Cromer & Liebermann equation.^[5] Seven full diffraction data sets were recorded at energies as shown in Fig. 2. Individual form factors f_0 were computed from wavefunction calculations for the respective structure model according to the Hirshfeld Atom Refinement (HAR) method.^[6] The anomalous dispersion parameters were included in the least-squares refinement. Figure 2 shows that the experimentally

obtained anomalous dispersion parameters from diffraction data follow well the independently acquired absorption spectrum, whereas the tabulated values are only rough approximation of the true function.

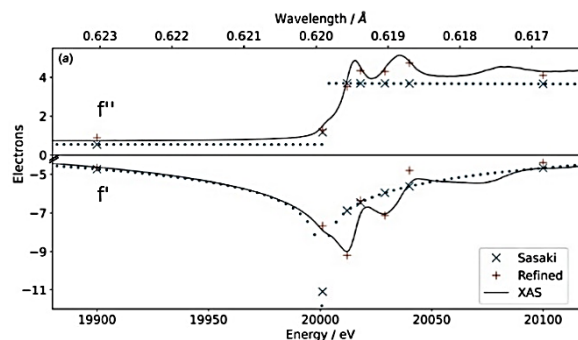


Figure 2. X-ray absorption spectrum (f'') of $\text{Mo}(\text{CO})_6$ (top solid line) and the related f' function (bottom solid line). Sasaki's tabulated (x symbols) and refined (+ symbols) values from experimental diffraction measurements for f'' and f' .

The differences between the tabulated and the refined f' and f'' are reflected in the structure models. The overall agreement factors and the residual electron density for the structure model with tabulated dispersion values is significantly larger than the agreement factors and residual electron density of the structure models obtained with refined anomalous dispersion parameters (see Fig. 3). The refinement of dispersion parameters leads to a robust structure model within the investigated energy range.

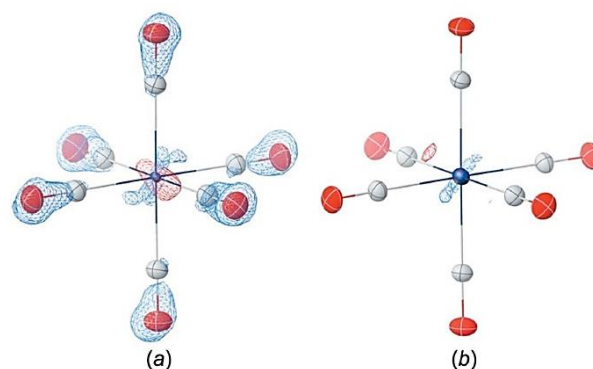


Figure 3. Negative (blue) and positive (red) residual electron density at an iso-surface level of $0.33 \text{ e } \text{Å}^{-3}$ of $\text{Mo}(\text{CO})_6$ at 20,001 eV for the HAR model using the Sasaki's tabulated (a) and refined (b) dispersion values.

- [1] Sasaki, S. (1989) *KEK Report* **88-14**, 1–136.
- [2] Henke, B. L. *et al.* (1993) *At. Data Nucl. Data Tables* **54**, 181–342.
- [3] Meurer, F. *et al.* (2022) *IUCr J* **9**, 604–609.
- [4] Scheinost, A. C. *et al.* (2021) *J. Synchr. Rad.* **28**, 333–349.
- [5] Watts, B. (2014) *Opt. Express*, **22**, 23628–23639.
- [6] Kleemiss, F. *et al.* (2021) *Chem. Sci.* **12**, 1675–1692.

Atomically dispersed pentacoordinated-zirconium catalyst with axial oxygen ligand for oxygen reduction reaction

X. Wang,¹ Y. An,² L. Liu,³ L. Fang,⁴ Y. Liu,¹ J. Zhang,¹ H. Qi,⁵ T. Heine,^{1,2} T. Li,⁴ A. Kuc,² M. Yu,¹ X. Feng¹

¹Technische Universität Dresden, Dresden, Germany; ²HZDR, Leipzig, Germany; ³International Iberian Nanotechnology Laboratory INL, Braga, Portugal; ⁴Northern Illinois University (NIU), DeKalb, U.S.A.; ⁵Universität Ulm, Ulm, Germany

Single-atom catalysts (SACs), as promising alternatives to Pt-based catalysts, suffer from the limited choice of center metals and low single-atom loading. Here, we report a pentacoordinated Zr-based SAC with nontrivial axial O ligands (denoted O-Zr-N-C) for oxygen reduction reaction (ORR). The O ligand down-shifts the d-band center of Zr and confers Zr sites with stable local structure and proper adsorption capability for intermediates. Consequently, the ORR performance of O-Zr-N-C prominently surpasses that of commercial Pt/C, achieving a half-wave potential of 0.91 V vs. reversible hydrogen electrode and outstanding durability (92% current retention after 130-hour operation). Moreover, the Zr site shows good resistance towards aggregation, enabling the synthesis of Zr-based SAC with high loading (9.1 wt-%). With the high-loading catalyst, the zinc-air battery (ZAB) delivers a record-high power density of 324 mW cm⁻² among those of SAC-based ZABs.

EXPERIMENTAL. This work is a collaboration between theoretical group from HZDR and experimentalists from various institutions. Details will be provided only from the theoretical work, information on experimental part is given elsewhere.^[1] All the calculations were carried out using AMS package. DFT with PBE exchange-correlation functional, the TZP basis sets composed of Slater-type and numerical orbitals, and D3 van der Waals correction were used. The geometries were fully optimized using 2D periodic models. Spin-polarized DFT calculations were performed for the oxygen-containing intermediates.

RESULTS. Density functional theory (DFT) calculations were performed to explore how the local coordination environment of Zr determines the catalytic mechanism. First, conventional in-plane quadra-coordinated Zr structures (*i.e.*, Zr-N_{4-n}-C_n, *n* = 0, 2 and 3) were investigated. As revealed, all Zr-N_{4-n}-C_n structures show extremely strong adsorption on O-containing intermediates (binding energy > 4 eV), which indicates the ultrahigh energy for the last step of OH* desorption from the catalysts, leading to poor ORR activity. Meanwhile, the strong adsorption energy of O-intermediates reflects high tendency of the in-plane quadra-coordinated Zr to link another axial O ligand. We, thus, calculated the formation energies of Zr-N_{4-n}-C_n and O ligand-linked Zr-N_{4-n}-C_n (denoted O-Zr-N_{4-n}-C_n). It is notable that the much lower formation energy (ΔE_f) of O-Zr-N_{4-n}-C_n (-9.22 eV of O-Zr-N₄, -6.12 eV of O-Zr-N₂-C₂, and -3.93 eV of O-Zr-N₁-C₃) than that of Zr-N_{4-n}-C_n (-3.08 eV of Zr-N₄, 0.68 eV of Zr-N₂-C₂, and 0.84 eV of Zr-N₁-C₃) manifests that the O-Zr-N_{4-n}-C_n structure is more energetically favourable than Zr-N_{4-n}-C_n motif. The low formation energy also reflects the excellent chemical stability of the pentacoordinated Zr sites in the O-Zr-N-C catalyst, which inhibits the local structure collapse of Zr sites during the ORR process and explains the ultralong ORR durability of the O-Zr-N-C catalyst. For an intuitive comparison, we further calculated the ORR Gibbs free energy profiles of O-Zr-N-C. Significantly decreased energy barriers are discovered for all O-Zr-N_{4-n}-C_n structures in comparison with the corresponding Zr-N_{4-n}-C_n

structures, again demonstrating the high preference for the former. The OH* desorption energy of O-Zr-N₁-C₃ decreases to 0.49 eV compared with 5.32 eV in Zr-N₁-C₃. The ORR activity follows the order of O-Zr-N₁-C₃ > O-Zr-N₄ > O-Zr-N₂-C₂, with the overpotential of 0.55 V, 0.62 V, and 0.87 V, respectively.

Additional insights are gained by examining the d-band electronic structures of Zr centers, as the d-band center is recognized to well correlate with the metal-adsorbate interaction. The axial O ligand is verified to greatly lower the d-band center of Zr-N₁-C₃ from -1.27 eV to -2.50 eV, thus, explaining the weakened adsorption energy of O-intermediates on O-Zr-N₁-C₃. Moreover, the downshift of d-band center is also found for other O-Zr-N_{4-n}-C_n structures in comparison with the corresponding Zr-N_{4-n}-C_n. Moreover, the Bader charge of Zr (0.41 e⁻) in O-Zr-N-C is lower than that of Zr (0.55 e⁻) in Zr-N-C, which indicates the extra charge transfer between O and Zr in O-Zr-N₁-C₃ due to the electron-withdrawing axial O ligand. From this perspective, the lower charge in O-Zr-N₁-C₃ further indicates the weaker interaction between Zr and O-containing intermediates, enabling the easier desorption of OH*. These findings provide significant guidance for the future effort in modifying or re-designing Zr-based active sites *via* diverse approaches (*e.g.*, heteroatom coordination and hetero-metal sites). All results are summarized in Fig. 1.

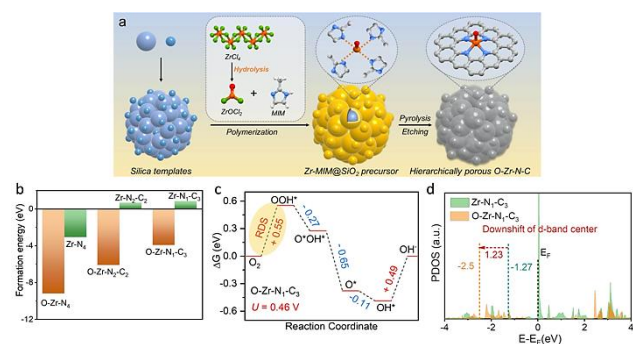


Figure 1. Schematic illustrating the synthetic route of O-Zr-N-C (a). Formation energy of O-Zr-N_{4-n}-C_n and Zr-N_{4-n}-C_n (*n* = 0, 2 and 3) (b). ORR Gibbs free energy profiles on O-Zr-N₁-C₃ at the potential bias *U* = 0.46 V (c). PDOS of Zr sites in O-Zr-N₁-C₃ and Zr-N₁-C₃ (d).

This paper resulted also in a press release prepared by HZDR.

ACKNOWLEDGEMENTS. The authors gratefully acknowledge the financial support provided by the Deutsche Forschungsgemeinschaft (CRC-1415: 417590517) and they acknowledge the Centre for Information Services and High-Performance Computing (ZIH) in Dresden.

[1] Wang, X. *et al.* (2022) *Angew. Chem. Int. Ed.* e202209746, 1–8.

Highly accessible and dense surface single metal FeN₄ active sites for promoting the oxygen reduction reaction

G. Chen,¹ Y. An,² S. Liu,³ F. Sun,⁴ H. Qi,^{1,5} H. Wu,⁶ T. He,³ P. Liu,⁶ R. Shi,⁷ J. Zhang,⁸ A. Kuc,² U. Kaiser,³ T. Zhang,⁷ T. Heine,^{1,2} G. Wu,³ X. Feng¹

¹Technische Universität Dresden, Dresden, Germany; ²HZDR, Leipzig, Germany; ³University of New York, New York, U.S.A.; ⁴Chinese Academy of Sciences, Shanghai, China; ⁵Universität Ulm, Ulm, Germany; ⁶Shanghai Jiao Tong University, Shanghai, China; ⁷Northwestern Polytechnical University, Xi'an, China

Single iron atom and nitrogen-codoped carbon (Fe–N–C) electrocatalysts, which have great potential to catalyze the kinetically sluggish oxygen reduction reaction (ORR), have been recognized as the most promising alternatives to the precious metal platinum. Unfortunately, the ORR properties of the existing Fe–N–C catalysts are significantly hampered by the inferior accessibility and intrinsic activity of FeN₄ moieties. Here, we constructed densely exposed surface FeN₄ moieties on a hierarchically porous carbon (sur-FeN₄-HPC) by Fe ion anchoring and a subsequent pyrolysis strategy using the nitrogen-doped hierarchically porous carbon (NHPC) as the scaffold.^[1] The high surface area of the NHPC with abundant surface Fe anchoring sites enabled the successful fabrication of densely accessible FeN₄ active moieties (34.7 × 10¹⁹ sites g⁻¹) on sur-FeN₄-HPC. First-principles calculations further suggested that the edge effect could regulate the electronic structure of the single Fe site, hence promoting the intrinsic ORR activity of the FeN₄ moiety. As a result, the sur-FeN₄-HPC electrocatalyst exhibited excellent ORR activity in acidic media with a high half-wave potential of 0.83 V (vs. the reversible hydrogen electrode). We further examined sur-FeN₄-HPC as a cathode catalyst in proton exchange membrane fuel cells (PEMFCs). The membrane electrode assembly delivered a high current density of 24.2 mA cm⁻² at 0.9 V_{iR-free} (internal resistance-compensated voltage) under 1.0 bar O₂ and a maximum peak power density of 0.412 W cm⁻² under 1.0 bar air. Importantly, the catalyst demonstrated promising durability during 30,000 volt-ages cycles under harsh H₂ and air conditions. The PEMFC performance of sur-FeN₄-HPC outperforms those of the previously reported Fe–N–C electrocatalysts. The engineering of highly accessible and dense surface FeN₄ sites on sur-FeN₄-HPC offers a fruitful pathway for designing high-performance electrocatalysts for different electrochemical processes.

EXPERIMENTAL. This work is a collaboration between theoretical group from HZDR and experimentalists from various institutions. Details will be provided only from the theoretical work, information on experimental part is given elsewhere.^[1] All the calculations were carried out using AMS package. DFT with PBE exchange-correlation functional, the TZP basis sets composed of Slater-type and numerical orbitals, and D3 van der Waals correction were used. The geometries were fully optimized using 1D and 2D periodic models. Spin-polarized DFT calculations were performed for the oxygen-containing intermediates. The ORR performance was explored under the theoretical framework developed by Nørskov et al.^[2]

RESULTS. We have theoretically studied three models: basal-plane (b-FeN₄), armchair-edge (e-FeN₄(A)) and zigzag-edge (e-FeN₄(Z)) carbon hosted FeN₄. The four Fe–N bond lengths in b-FeN₄ are equal and on average 1.90 Å, but are elongated in e-FeN₄(A) to 1.92 Å, and shorten in e-FeN₄(Z) to

1.88 Å. The spin moments of the Fe center, which is a critical descriptor of the electronic structure, were calculated to be 1.97 μ_B (b-FeN₄), 1.84 μ_B (e-FeN₄(A)), and 1.92 μ_B (e-FeN₄(Z)), showing a decrease when FeN₄ is introduced close to the edges. In addition, the Hirshfeld charge distribution analysis revealed a higher electron density for e-FeN₄(A) and e-FeN₄(Z).

The adsorption properties of the ORR intermediates (*i.e.*, OOH*, O* and OH*) on the catalyst models were examined next and the corresponding free energy profiles at U = 1.23 V (the equilibrium-potential) were calculated. For b-FeN₄, the O* binding energy (ΔE_{O*}) is 1.25 eV, which is much lower than that on Pt (1.57 eV), suggesting a strong adsorption strength of O* on b-FeN₄. This leads to the difficulty of removing the next formed intermediate, OH*, with a large reaction barrier of 0.76 eV, being the rate-determining step (RDS) for the ORR. In sharp contrast, the ΔE_{O*} values on e-FeN₄(Z) and e-FeN₄(A) are 1.41 eV and 1.54 eV, respectively, very close to that on Pt, indicating that the adsorption strengths of O* on e-FeN₄(A) and e-FeN₄(Z) are weakened. The weakened adsorption strength of O* efficiently lowers the ORR limiting kinetics barriers from 0.76 eV (on b-FeN₄) to 0.69 eV (e-FeN₄(Z)) and 0.53 eV (on e-FeN₄(A)). Figure 1 shows all the simulated results, including the typical volcano plot established by Nørskov *et al.*^[2] Our DFT calculations imply that the edge effect could further enhance the intrinsic ORR properties of the single FeN₄ site. Yet, the precision construction and advanced characterization of FeN₄ sites on carbon edges are still needed.

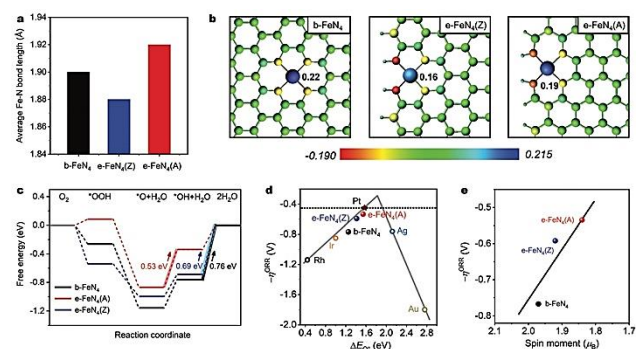


Figure 1. Average Fe–N bond lengths in b-FeN₄, e-FeN₄(Z), and e-FeN₄(A) models (a). The corresponding Hirshfeld charges distribution (b). Free-energy profiles for the ORR under the equilibrium potential (U = 1.23V) (c). The arrows indicate the RDS. Trends in ORR activity plotted as function of ΔE_{O*} on different catalyst models (d). The correlation of overpotential and spin moment of the single Fe center in each model (e).

ACKNOWLEDGEMENTS. The authors gratefully acknowledge the financial support provided by the Deutsche Forschungsgemeinschaft (CRC-1415: 417590517) and they acknowledge the Centre for Information Services and High-Performance Computing (ZIH) in Dresden.

[1] Chen, G. *et al.* (2022) *Energy Environ. Sci.* **15**, 2619–2628.

[2] Nørskov, J. K. *et al.* (2004) *J. Phys. Chem. B* **108**, 17886–17892.

SCIENTIFIC CONTRIBUTIONS (PART II)

Geological Systems

Long-Lived Radionuclides & Transport Phenomena in

GEOLOGICAL SYSTEMS

Y(III) sorption at the orthoclase (001) surface measured by X-ray reflectivity

J. Neumann,¹ J. Lessing, S. S. Lee,¹ J. E. Stubbs,² P. J. Eng,^{2,3} M. Demnitz,⁴ P. Fenter,¹ M. Schmidt

¹Argonne National Laboratory, Lemont, IL, U.S.A.; ²Center for Advanced Radiation Sources, The University of Chicago, Chicago, IL, U.S.A.; ³James Franck Institute, The University of Chicago, Chicago, IL, U.S.A.; ⁴Eindhoven University of Technology, Eindhoven, The Netherlands

Feldspars are an abundant group of natural minerals and the main constituent of crystalline rock, which is considered as a potential host rock for radioactive waste disposal. Recently, our group studied the sorption of a variety of rare earth elements (REE) and trivalent actinides (Am, Cm) on K-feldspar.^[1] We found that feldspars retain the minor actinides strongly and were able to propose a surface complexation model. This model, however, requires assuming a sorption structure, which was not accessible from our data. Here, we use Y(III), as a representative of the rare earth elements (REE) and a homologue of the trivalent actinides, to elucidate the structure of sorption complexes on the orthoclase (001) plane.

We used *in situ* high resolution X-ray reflectivity (XR), *i.e.*, crystal truncation rod (CTR) diffraction and resonant anomalous X-ray reflectivity (RAXR) to study Y sorption as a function of concentration $[Y^{3+}]$ and pH. The data reveal an inner-sphere (IS) sorption complex at a distance of ~ 1.5 Å from the surface and an outer-sphere (OS) complex at 3–4 Å. Based on these data a bidentate, binuclear binding mode can then be proposed for the IS complex.^[2]

EXPERIMENTAL. Gem-quality orthoclase single crystals were cleaved and reacted for 18h in solutions containing YCl_3 at pH 5 and 7. The pH was adjusted by adding small amounts of 0.01 and 0.1 M HCl and NaOH. Specifically, a first crystal was reacted in 0.1 mM Y^{3+} at pH 7. After XR measurements, the crystal was transferred into a solution at a higher $[Y^{3+}] = 1$ mM at the same pH and reacted for an additional 18h. To identify the impact of pH, a second crystal was reacted with a solution at fixed $[Y^{3+}] = 10$ mM first at pH 5 and subsequently at pH 7.

XR were measured at the Advanced Photon Source (APS) at Argonne National Laboratory.^[3] Specular crystal truncation rod (CTR) diffraction, measures scattering intensities along the (00L) direction, from which a total electron density (ED) profile of the mineral/water interface can be determined (lines in Fig. 1). CTR was combined with resonant anomalous X-ray reflectivity (RAXR), which yields a resonant element's distribution on the surface (area plots in Fig. 1 from modulations in the scattering intensity at its X-ray absorption edge ($Y K = 17.038$ keV)).

RESULTS. CTR and RAXR data were analyzed to obtain total and Y specific vertical electron density profile (Fig. 1), from which in turn Y coverages can be derived (Tab. 1). All samples show a well-defined peak at 1.3–1.6 Å in their total ED profiles, which can be attributed to absorbed water. Additional peaks must be related to Y adsorption. At pH 7 and $[Y^{3+}] \geq 1$ mM, an IS complex was identified at a distance of ~ 1.5 Å, which is likely identical to the IS species identified in our previous study.^[1] In addition, multiple OS species are observed at larger distances. At the highest pH and concentration their distribution becomes very broad (> 15 Å), which may indicate surface precipitation.

The OS complexes likely stem from the relatively high concentration of $[Y^{3+}]$ required for XR. The IS species should, however, be representative of the IS species found in exper-

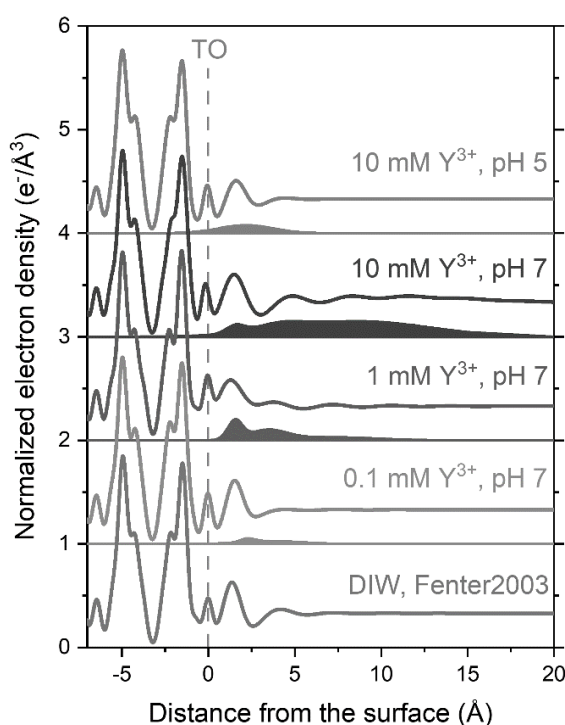


Figure 1. Total electron density (lines) and Y^{3+} contributions (filled area) out of the best fit models of CTR and RAXR data of absorbed Y^{3+} on orthoclase (001). With TO: terminal oxygen.

Table 1. Measured Y(III) coverages θ_{tot} by RAXR.

$[Y]$ (mM)	0.1	1	10	10
pH	7	7	7	5
θ_{tot} (Y/AUC*)	0.43(15)	1.82(84)	5.3(19)	0.86(22)

*: area of the unit cell.

iments with powdered samples.^[4] The distance to the surface terminating oxygens (TO) of ~ 1.5 Å can be used to propose a binding geometry. Any mono- or bidentate, mononuclear sorption complexes would require either unrealistically long bond (~ 3.8 Å) or short ~ 1.5 Å bond lengths. This leaves two bidentate, binuclear sorption sites, which can be distinguished by their Y–O bond lengths, where only binding to two TO1 yields reasonable bond lengths of 2.46 Å.

In summary, we were able to characterize the sorption structure of Y(III) on orthoclase (001) on the molecular level and verify that studies with powdered and single-crystalline samples yield comparable results.

ACKNOWLEDGEMENTS. This work was funded by the German Federal Ministry of Economics and Technology (BMWi, 02E 11668B), the U.S. Department of Energy, (DE-AC02-06CH11357; DE-SC0019108), National Science Foundation (EAR-1634415), the German Federal Ministry of Education and Research (BMBF, 02NUK053B), and the Helmholtz Association (SO-093).

[1] Neumann, J. *et al.* (2021) *J. Colloid Interface Sci.* **591**, 490–499.

[2] Neumann, J. *et al.* (2023) *Environ. Sci. Technol.* **57**, 266–276.

[3] Sutton, S. R. *et al.* (2022) *Phys. Chem. Miner.* **49**, 1–24.

[4] Demnitz, M. *et al.* (2022) *Sci. Total Environ.* **843**, 156920.

EXAFS and DFT studies of competitive Am³⁺ and Y³⁺ sorption on corundum

N. Huittinen, S. Virtanen,¹ A. Rossberg, M. Eibl, S. Lönnrot,¹ R. Polly²

¹Radiochemistry Unit, University of Helsinki, Helsinki, Finland; ²Institute for Nuclear Waste Disposal, Karlsruhe Institute of Technology, Karlsruhe, Germany

Sorption competition reactions of trivalent cations (Eu³⁺, Am³⁺, Y³⁺) on the corundum surface have been explored with a combination of experimental and computational techniques.^[1] EXAFS investigations at the Am L₃-edge indicate that the overall metal ion concentration in the samples influences the speciation of Am³⁺ on the corundum surface. A change of the complex geometry with increasing Am³⁺ + Y³⁺ concentration can be seen as a decrease of the overall Am–O coordination number from nine to eight, and the subsequent shortening of the average Am–O bond length. DFT calculations postulate the formation of tetradentate and tridentate Am³⁺ complexes at low and high surface coverages, respectively.

Adsorption reactions on mineral surfaces are often described with help of different surface sites (strong *vs.* weak ones), which are responsible for the metal-ion uptake in different concentration regimes. In the presence of multiple cations with similar redox chemistries, competition for available surface sites has been shown to occur.^[2] Very little is known, however, about the speciation of the metals in competing scenarios, *i.e.*, whether or not changes occur in the complex structures or their bonding to the surface, especially in the hypothesized strong- and weak site sorption regimes. We have thereby investigated the uptake of Am³⁺ on corundum (α -Al₂O₃) in the absence and presence of Y³⁺ as competing metal by combining extended X-ray absorption spectroscopy (EXAFS) investigations with density functional theory (DFT) calculations. Isotherm studies using the radioactive ¹⁵²Eu tracer were used to identify the sorption regimes where strong sites and weak sites contribute to the sorption reaction.

EXPERIMENTAL. The isotherm experiments were conducted in TRIS buffered solutions (pH ~8.3) over a large range of Eu³⁺ concentrations (1.3×10^{-9} – 1×10^{-4} mol/L), in the absence and presence of 10^{-6} or 10^{-4} mol/L Y³⁺. The speciation of Am³⁺ on the corundum surface was investigated *via* EXAFS at the Am L₃-edge for Am³⁺ and Am³⁺ + Y³⁺ concentrations in both strong- and weak site sorption regimes. Optimized Am³⁺ complexes on a cluster depicting the corundum (110) surface were computed using DFT. Calculations were performed for a single and two closely located Am complexes on the corundum cluster to account for low- and high-coverage scenarios on the mineral surface.

RESULTS. The Eu³⁺ sorption isotherms show a significant reduction of the Eu³⁺ uptake in the presence of Y³⁺ (Fig. 1). Moreover, a change of the slope from one to less than one occurs for Eu³⁺ concentrations of approximately 5×10^{-6} mol/L. The non-linear isotherms with a clear change of their slopes can be considered indicative for the presence of different sorption sites (strong and weak ones) on the mineral surface. The EXAFS results show a reduction of the Am³⁺ coordination number to the surrounding oxygen atoms from nine to eight when going from the strong to weak site sorption regimes. This is true for both non-competitive and competitive samples. With the reduction of the coordination number, the average Am–O distance is shortened by approximately 0.011 Å. Using DFT calculations, a plausible description for the formed surface complexes in the two sorption

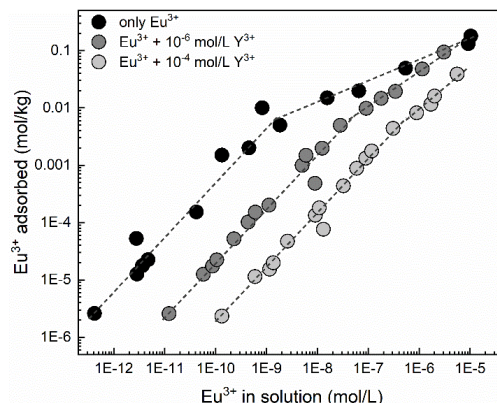


Figure 1. Sorption of Eu³⁺ in the absence and presence of Y³⁺ as competing element, investigated as a function of Eu³⁺ concentration at pH 8.3 ± 0.1.

regimes were obtained (Fig. 2). At low surface coverages, DFT predicts the formation of a tetradentate Am complex with five coordinating hydration water entities. When a second Am complex is added on the (110) cluster, the Am³⁺ surface coordination changes to tridentate, while the number of coordinating water molecules remains unchanged. Thus, the overall coordination number is reduced from nine to eight. The lower denticity to the surface allows for shorter bonds to be formed between the Am cluster and the corundum surface.

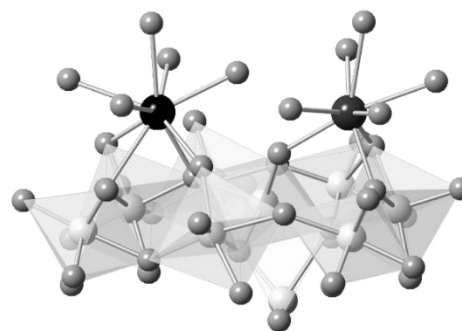


Figure 2. DFT-optimized Am-complexes on the corundum (110) surface. Atom colours are white (Al), light grey (O), dark grey (tridentate Am), and black (tetradentate Am).

The results show that strong and weak sites are not just hypothetical surface groups required for a correct description of isotherm data for surface complexation models. As adsorption on the different site types is influenced by the overall metal ion concentration in solution, the presence of chemically similar elements must be taken into account when describing the retention of actinides on mineral surfaces. Moreover, the decreasing coordination to the surface may have implications on the reversibility of the sorption reaction, which should be carefully explored in future studies.

[1] Huittinen, N. *et al.* (2022) *Minerals* **12**, 1380.

[2] Virtanen, S. *et al.* (2018) *Appl. Geochem.* **92**, 71–81.

New insights into the effect of Ca(II) on U(VI) and Np(VI) retention on Ca-bentonite and clay minerals at hyperalkaline conditions – a luminescence spectroscopic study

T. Philipp, N. Huittinen, S. Shams Aldin Azzam, R. Stohr,¹ J. Stietz,¹ T. Reich,¹ K. Schmeide

¹Johannes Gutenberg-Universität Mainz, Department of Chemistry, Mainz, Germany

The U(VI) and Np(VI) sorption on the aluminosilicate minerals kaolinite, muscovite and Ca-bentonite was strongly enhanced by Ca²⁺ at pH ≥ 10. Concerning the underlying retention mechanisms at hyperalkaline conditions, site-selective time-resolved laser-induced luminescence spectroscopy (TRLFS) provided spectroscopic proof for two dominating U(VI) species at the surfaces: (i) a ternary U(VI) complex, where U(VI) is bound to the surface via bridging Ca cations with the configuration surface ≡Ca–OH–U(VI) and, (ii) U(VI) sorption into the interlayer space of calcium (aluminum) silicate hydrates (C-(A)-S-H), which form as secondary phases in the presence of Ca due to partial dissolution of aluminosilicates at hyperalkaline conditions.^[1]

The influence of hyperalkaline pore waters, caused by cementitious materials, on U(VI) retention on Ca-bentonite, was studied in Philipp et al.^[2] It was hypothesized that the binding of anionic uranyl hydroxide complexes to negatively charged surfaces is mediated by Ca²⁺ cations. To provide spectroscopic proof for all complexes occurring at hyperalkaline pH conditions, further batch sorption and TRLFS studies were performed in the current work.

EXPERIMENTAL. U(VI) and Np(VI) sorption on Ca-bentonite (Calcigel[®]), kaolinite, and muscovite was studied using 0.1 M NaCl or 0.1 M NaCl/0.02 M CaCl₂ as background electrolytes ([U(VI)] = 5 × 10⁻⁷ M, [Np(VI)] = 1 × 10⁻⁷ M, N₂). U(VI)-containing TRLFS samples ([U(VI)] = 5 × 10⁻⁷ M) were prepared for kaolinite and muscovite in the absence (pH 10–11) and presence of 0.02 M Ca (pH 12–12.5), and those for Ca-bentonite in diluted Gipshut solution (I = 2.6 M, pH 11 and 12.5).^[3]

RESULTS. Sorption experiments and zeta potential measurements showed that Ca²⁺ sorbs strongly onto Ca-bentonite at pH 8–13, leading to a partial compensation of the negative surface charge. Thereby, potential sorption sites for anionic actinyl species are generated. The application of the two background electrolytes (0.1 M NaCl or 0.1 M NaCl/0.02 M CaCl₂) for U(VI) and Np(VI) sorption experiments with Ca-bentonite as well as the Ca-free minerals kaolinite and muscovite showed that An(VI) sorption at pH 10–12 is strongly enhanced in the presence of Ca²⁺.

All luminescence spectra point to different U(VI) speciation in mineral suspensions at the two different solution conditions (pH, Ca absence or presence). Results are shown for Ca-bentonite in Fig. 1. At pH 11, the sample shows a spectrum with pronounced luminescence line-narrowing (Fig. 1a). Two species were identified: an inner-sphere sorbed U(VI) complex (species 2) and a complex with outer-sphere character attributed to a Ca²⁺ mediated complex (species 1).

Based on X-ray absorption spectroscopic results^[2], postulated structures for the two ternary surface complexes showing the Ca-bridge between silanol surface sites of the minerals and uranyl hydroxide species are shown in Fig. 2.

At pH ≥ 12, the U(VI) emission spectra obtained for all minerals are broader, as exemplarily shown for Ca-bentonite in Fig. 1b. For decomposition of the spectra, the two species ex-

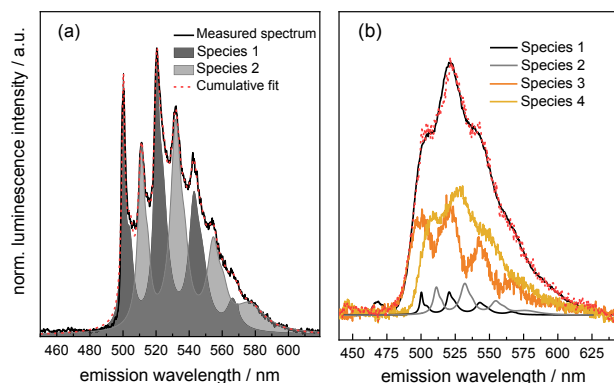


Figure 1. Extracted pure components from the decomposition of the measured U(VI) emission spectra in the Ca-bentonite suspension at pH 11 (a) and at pH 12.5 (b).

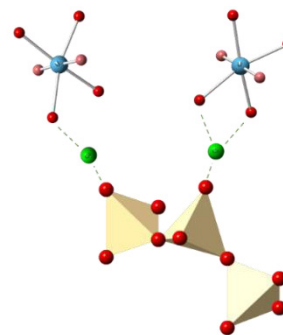


Figure 2. Proposed structures for ternary surface complexes showing a Ca-bridge between silanol surface sites of the minerals and uranyl hydroxide species predominant in the hyperalkaline pH range. Color code: uranium (blue), calcium (green), silicon (yellow), oxygen (red).

tracted from the Ca-bentonite suspension at pH 11 (see above) and two from C-S-H (C/S = 1.2, pH 12.1), namely a surface complex (species 3) and a species sorbed into the C-S-H interlayer (species 4), were applied.^[4, 5]

As exemplarily shown for Ca-bentonite in Fig. 1b, the composite emission spectra of the three different aluminosilicates at pH ≥ 12 can be reproduced with the help of the four emission spectra of single species. Although the exact percentages of the present species cannot be given due to the different luminescence quantum yields of the species, the amount of U(VI) species associated with the C-S-H phase is likely to be larger than the sorption complexes on the aluminosilicates (species 1 + 2).

The batch sorption and spectroscopic results clearly indicate that C-(A)-S-H is formed as secondary phase in all Ca-containing mineral suspensions, as a consequence of partial dissolution of aluminosilicates at hyperalkaline conditions. Such C-(A)-S-H additionally contribute to the retention of anionic actinide species in clayey systems.

ACKNOWLEDGEMENTS. This work was supported by the BMWi (no. 02E11415A, 02E11415B, 02E11860B).

- [1] Philipp, T. et al. (2022) *Sci. Tot. Environ.* **842**, 156837.
- [2] Philipp, T. et al. (2019) *Sci. Tot. Environ.* **676**, 469–481.
- [3] Lommerzheim, A., Jobmann, M. (2014) *Report DBETEC-08-2014-Z*.
- [4] Tits, J. et al. (2015) *Dalton Trans.* **44**, 966–976.
- [5] Wolter, J. et al. (2019) *Chemosphere* **218**, 241–251.

Batch and IR spectroscopic studies of U(VI) sorption onto zirconia (ZrO₂)

I. Jessat, A. Dietze, K. Heim, H. Foerstendorf, T. Stumpf, N. Jordan

The uptake of U(VI) onto zirconia (ZrO₂) was investigated by batch sorption experiments and *in situ* ATR FT-IR spectroscopy. A strong influence of the pH and solid-to-liquid ratio on the U(VI) sorption onto zirconia was observed, while the ionic strength had no significant effect. Infrared experiments showed the formation of U(VI) inner-sphere surface species.

Uranium is the most important element in the nuclear fuel cycle and its interactions with corroded phases in the near-field of a repository are crucial processes, which have to be taken into account in a safety assessment of a nuclear waste repository. Zirconia is the main corrosion product of the zircaloy cladding material of spent nuclear fuel rods and represents a first barrier against the release of dissolved radionuclides into the environment.

EXPERIMENTAL. The pH-dependent batch experiments (Tab. 1) were conducted at room temperature under inert gas (N₂) to exclude carbonate. The samples were equilibrated for three days and subsequently centrifuged (1 h; 4,020 × g). The

Table 1. Experimental parameters of the U(VI) pH-dependent batch sorption experiments onto ZrO₂.

m/V ratio (g L ⁻¹)	[U(VI)] (mol L ⁻¹)	I (NaCl) (mol L ⁻¹)
0.5	1.2 × 10 ⁻⁶	0.01 or 0.1
0.5	1.1 × 10 ⁻⁵	0.01
4.0	1.2 × 10 ⁻⁶	0.01

U(VI) concentrations in the supernatants were verified by ICP-MS. For experiments conducted at 0.01 mol L⁻¹ NaCl and 1.1 × 10⁻⁵ mol L⁻¹ U(VI), zeta potential measurements were performed before centrifugation under exclusion of CO₂. Pure ZrO₂ suspensions (0.5 g L⁻¹) were prepared at 0.01 mol L⁻¹ NaCl under inert gas conditions and the pH of the isoelectric point (pH_{IEP}) of the mineral was derived from zeta potential measurements after three days of shaking. *In situ* ATR FT-IR spectroscopy experiments were performed to study the sorption and desorption processes of U(VI) ([U]: 2 × 10⁻⁵ mol L⁻¹; 0.1 mol L⁻¹ NaCl) onto ZrO₂ under inert conditions.^[1]

RESULTS. The sorption of U(VI) onto zirconia started around pH 3 and maximum sorption was reached above pH 5 (Fig. 1 a), which is in agreement with former studies.^[2] The change of the ionic strength (0.01 or 0.1 mol L⁻¹ NaCl) had no influence on the U(VI) sorption, indicating the predominant formation of U(VI) inner-sphere surface complexes (Fig. 1 a, open and filled squares). This finding was supported by the results of the zeta potential measurements at the higher U(VI) concentration (Fig. 1 b, open and filled triangles), where a shift of the pH_{IEP} towards higher pH value in the presence of U(VI) (pH_{IEP} 8.8) was observed compared to the pristine ZrO₂ (pH_{IEP} 8.3). The decreasing influence of the sorbed U(VI) on the zeta potential shift with increasing pH was assigned to the formation of (polynuclear) U(VI) hydrolysis species, which dominate the aqueous U(VI) speciation in the absence of carbonate.^[3] At a higher solid-to-liquid ratio the sorption edge is shifted towards lower pH (Fig. 1a, open diamonds), suggesting the presence of different kinds of sorption sites.

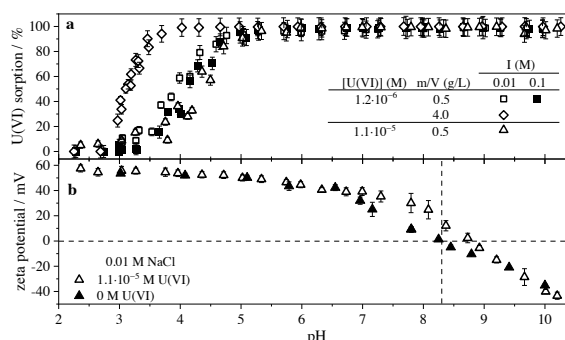


Figure 1. U(VI) sorption edges at different U(VI) concentrations, ionic strengths, and solid-to-liquid ratios (m/V) (a) and zeta potential curves of 0.5 g L⁻¹ ZrO₂ suspensions with I = 0.01 mol L⁻¹ NaCl in presence and absence of 1.1 × 10⁻⁵ mol L⁻¹ U(VI) (b).

Time-dependent IR spectra of the U(VI) sorption onto ZrO₂ under inert gas conditions at pH 5.5 are shown in Fig. 2a. A red shift of the asymmetric stretching vibration ν₃(UO₂) to 913 cm⁻¹ compared to the aqueous uranyl species at 922 cm⁻¹ was observed due to the sorption of U(VI) onto zirconia.^[4] The desorption step (Fig. 2b) revealed an only partly reversible sorption of U(VI), confirming the formation of U(VI) inner-sphere complexes on the ZrO₂ surface.

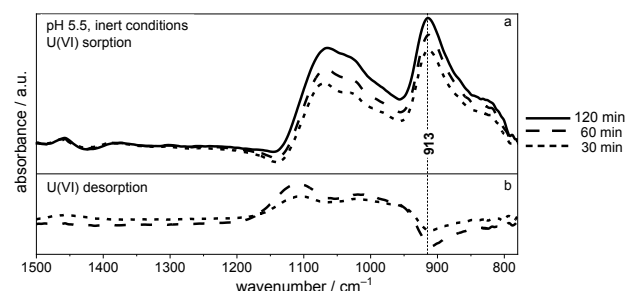


Fig. 2: *In situ* ATR FT-IR spectra of the time-dependent sorption (a) and desorption (b) of 20 μM U(VI) onto ZrO₂ at pH 5.5 and I = 0.1 mol L⁻¹ NaCl under inert conditions.

Future experiments (sorption isotherms, spectroscopic analysis, *e.g.* IR, XAS, TRLFS, at different sample conditions) will provide detailed information about the binding sites of U(VI) on ZrO₂ as well as the number and structure of the formed U(VI) surface species. This will help to constrain the parametrization of a thermodynamic surface complexation model. The results of this work will support a reliable prediction of the fate of U(VI) in the environment.

ACKNOWLEDGEMENTS. We want to acknowledge the help by Dr. M. Acker from the Central Radionuclide Laboratory at the Technische Universität Dresden, where several of the batch sorption experiments were conducted.

[1] Müller, K. *et al.* (2009) *Environ. Sci. Technol.* **43**, 7665–7670.
 [2] Lomenech, C. *et al.* (2003) *Radiochim. Acta* **91**, 453–461.
 [3] Grenthe, I. *et al.* (2020) in: *Second Update on the Chemical Thermodynamics of Uranium, Neptunium, Plutonium, Americium and Technetium Chemical Thermodynamics Volume 14* p. 171–230, Nuclear Energy Agency of the OECD (NEA).
 [4] Müller, K. *et al.* (2008) *Inorg. Chem.* **47**, 10127–10134.

Investigation of tetragonal polymorphs in Ce(IV)-doped ZrO₂

L. B. F. dos Santos, K. O. Kvashnina, V. Svitlyk, C. Hennig, N. Huittinen

A series of cerium doped zirconia samples were synthesized *via* the co-precipitation route. The crystal structures were analyzed by a combination of Raman, XANES, and synchrotron X-ray diffraction. Using a small amount of Eu³⁺ as co-dopant enabled ss-TRLFS analyses to monitor the phase transformations. No solid phase separation was detected, however, a very detailed analysis of the diffractograms and Raman data was required to understand the complex phase evolution in the samples. Strong indications for the presence of at least one metastable phase in addition to the tetragonal and cubic phases were obtained.

Safe disposal solutions for generated high-level radioactive waste will be challenging in the near future.^[1] Recent studies have suggested that crystalline ceramic matrices, such as zirconia (ZrO₂) have a high potential to be used as immobilization matrices for radioactive waste. At room temperature, zirconia has a monoclinic (*m*) structure. At higher temperatures, tetragonal (*t*) and cubic (*c*) structures can be stabilized. The stabilization can also be achieved at ambient conditions by incorporating oversized cations, such as cerium (Ce), in the crystal structure. In addition, studies have shown, that several metastable phases (*t'*, *t''*, κ , and *t**), can be formed for doped zirconia materials.^[2] Discerning the crystal structure is crucial to understand the properties of these phases, especially when the solubility limit is directly related to the tetragonal polymorphs.^[3]

EXPERIMENTAL. To investigate the phase composition of zirconium containing different Ce concentrations, four ZrO₂ solid solutions with 60 to 90 mol-% Ce were synthesized following the protocol of dos Santos *et al.*^[4] The samples were characterized by Raman microspectroscopy (HORIBA Jobin Yvon LabRAM Aramis). The site selective luminescence investigations were conducted by a Rhodamine 6G/Rhodamine B dye mixture; XANES and synchrotron X-Ray Diffraction (SXRD) measurements were done at ROBL beamline at the ESRF Facility, Grenoble, France.

RESULTS. The SXRD characterizations (Fig. 1) showed no solid phase separation (CeO₂ + ZrO₂). The pure cubic structure was stabilized in concentrations from 80 mol-% Ce, when the peak at 13.9°, typical for the tetragonal structure, disappears. With increasing cerium incorporation into zirco-

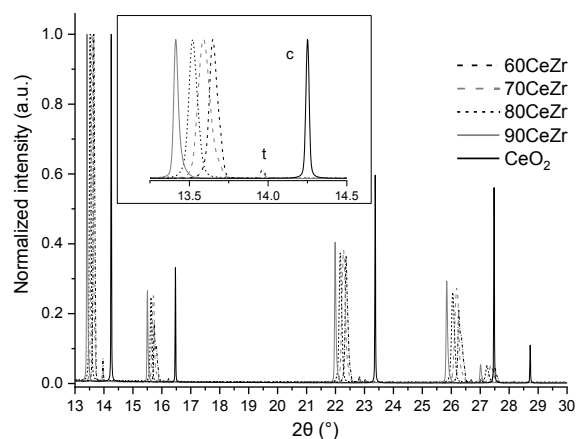


Figure 1. X-Ray diffractogram of zirconia doped with 60 to 90 mol-% of cerium and of CeO₂. Inset: enlarged region of 2θ for clarity.

nia, this diffraction peak shifts to lower 2θ, since Ce⁴⁺ is a larger cation than Zr⁴⁺, this behavior is expected. The compositions with 60 and 70 mol-% Ce, were first thought to contain a mix of tetragonal and cubic phases. However, in the Raman analysis of the 60 mol-% Ce sample (Fig. 2A), a large band around 500 cm⁻¹ was observed. This band is known as a defect band (DB).^[5] A potential reason for the appearance of this band could be the reduction of Ce(IV) to Ce(III) in the samples, and the generation of oxygen vacancies in the crystal structure. Thus, XANES investigations were conducted for selected samples, which confirm the sole presence of Ce(IV).

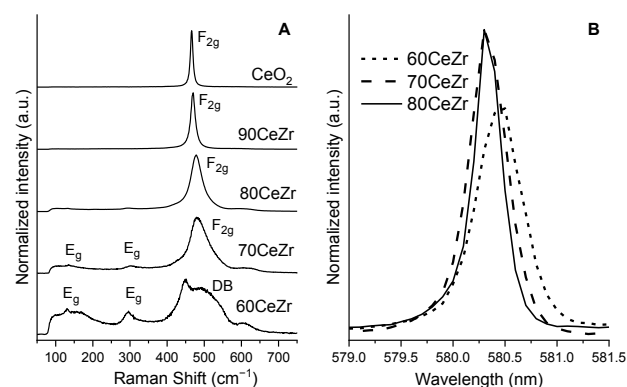


Figure 2. Raman (A) and ss-TRLFS (B) spectra of 60–90 mol-% of Ce-doped ZrO₂ and of CeO₂.

Raman is a sensitive technique to the M–O bonds, being very useful to detect defects in a crystalline structure. The DB can be related to the presence of a tetragonal double prime (*t''*) phase, with a crystallographic axial *c/a* ratio close to 1, *i.e.*, almost identical to the cubic structure. However, in this phase some oxygen ions are displaced from their crystallographic positions in a pure cubic phase along the *c* axis.^[3] Increasing the cerium concentrations this DB transforms in the prominent F_{2g} mode, meaning that a phase transformation is occurring to stabilize the cubic structure. The small bands at 145 and 300 cm⁻¹ can be assigned to the E_g mode, they are related to the tetragonal structure for the samples 60 and 70 mol-% Ce, which is consistent with the corresponding SXRD data. In the ss-TRLFS investigations (Fig. 2B), the Eu³⁺ excitation spectra can be seen to become systematically narrower with increasing Ce doping. This corroborates the occurrence of a phase transformation from a less ordered structure toward a defect-free solid. The tetragonal double prime is associated with the presence of defects caused by the displacement of oxygen ions, evident on the samples 60 mol-% Ce.

ACKNOWLEDGEMENTS. This work was supported by the German Federal Ministry of Education and Research (BMBF) under the ACE project (02NUK060A).

- [1] Alwaeli, M. *et al.* (2021) *Energies* **15**, 4275.
- [2] Varez, A. *et al.* (2007) *J. Eur. Ceram. Soc.* **27**, 3677–3682.
- [3] Lamas, D. G. *et al.* (2003) *J. Mater. Chem.* **13**, 904–910.
- [4] dos Santos, L. B. F. *et al.* (2021) *Report HZDR-119*, p. 52.
- [5] Loridant, S. (2021) *Catal.* **373**, 98–111.

Influence of different synthesis methods on the phase purity of Ce/Nd-co-doped zirconates

S. Richter, S. E. Gilson, N. Huittinen

Ce/Nd-co-doped zirconates with different dopant concentrations were synthesized via coprecipitation and solid-state synthesis. For solid-state synthesis, the influence of different mixing methods (manual, mechanical, magnetic) on the phase purity of the sintered powders was investigated. Coprecipitation yielded rather phase-pure products whereas solid-state mixing generally led to a worse phase purity. Manual mixing with a long grinding time, multiple sintering cycles, and a high Nd-dopant concentration allowed for better phase purity via solid-state synthesis.

Zirconium-bearing crystalline phases, such as zirconate pyrochlores, are currently being investigated as potential host matrices for the immobilization of radionuclides present in high level waste streams (HLW).^[1] Zirconate pyrochlores are characterized by high chemical durability and radiation resistance.^[2,3] However, upon irradiation, some zirconate pyrochlores undergo a phase transition to the defect fluorite crystal structure, inhibiting a safe matrix incorporation of radionuclide.^[3] In this work, cerium was studied as a surrogate for americium due to its similar ionic radius and oxidation state stability.^[4]

EXPERIMENTAL. Five different compositions of Ce/Nd-co-doped zirconates were investigated. The Ce-content was 5 mol-% for all the compositions; the Nd-content was varied between 0 and 50 mol-%.

For coprecipitation, solutions of CeCl_3 , $\text{Nd}(\text{NO}_3)_3 \cdot 6\text{H}_2\text{O}$, and $\text{ZrOCl}_2 \cdot 8\text{H}_2\text{O}$ in 0.01 M HNO_3 were mixed and precipitated using the reverse-dropping methods into 12.5% NH_4OH .^[5] The hydroxides were washed six times with Milli-Q water. After drying, they were calcined (4 h, 600 °C), pelletized (8 mm diameter, 5 kN), and sintered (48 h, 1500 °C).

For solid-state synthesis, the Ce-, Nd-, and Zr-solutions were precipitated, washed, dried, and calcined (4 h, 800 °C) separately to obtain pure CeO_2 , Nd_2O_3 , and ZrO_2 . Three different methods were used for mixing the oxides. Manual mixing involved hand-grinding the metal oxides with an agate mortar and pestle (grinding time: 5 or 10 min). Mechanical mixing was done by ball-milling the components (milling time: 10 or 20 min). For magnetic mixing, water was added to the metal oxides to create a slurry, which was stirred for 2 h before being dried again. The mixed metal oxide powders were pressed to pellets (8 mm diameter, 5 kN) and sintered (48 h, 1500 °C). After sintering, selected pellets were ground (2 min), re-pelletized (8 mm diameter, 5 kN), and re-sintered (48 h, 1500 °C).

Powder X-ray diffraction (PXRD) was used to characterize all samples. The measurements were carried out on a Rigaku Mini-Flex 600 diffractometer using $\text{Cu-K}\alpha$ radiation ($\lambda = 1.54 \text{ \AA}$, $2\theta = 3\text{--}90^\circ$, 0.02 step size, $2^\circ/\text{min}$ spin speed).

RESULTS. The PXRD patterns of the compositions synthesized *via* coprecipitation showed the formation of rather phase-pure monoclinic ($\text{Zr}_{0.95}\text{Ce}_{0.05}\text{O}_2$), cubic ($\text{Zr}_{0.80}\text{Ce}_{0.05}\text{Nd}_{0.15}\text{O}_{1.925}$), cubic defect fluorite ($\text{Zr}_{0.65}\text{Ce}_{0.05}\text{Nd}_{0.30}\text{O}_{1.85}$) (Fig. 1a), and cubic pyrochlore ($\text{Zr}_{0.50}\text{Ce}_{0.05}\text{Nd}_{0.45}\text{O}_{1.775}$) structures.

The PXRD patterns of the samples synthesized *via* solid-state methods, *e.g.* manual mixing (Fig. 1b) showed several overlapping peaks indicating the presence of multiple phases. Especially mechanical and magnetic mixing led to products

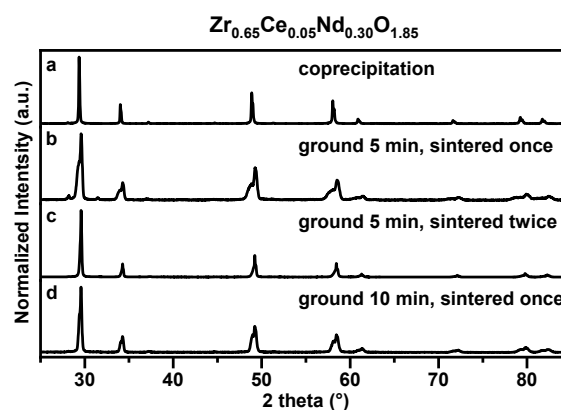


Figure 1. PXRD patterns of $\text{Zr}_{0.65}\text{Ce}_{0.05}\text{Nd}_{0.30}\text{O}_{1.85}$ synthesized *via* (a) coprecipitation; (b–d) manual solid-state mixing.

containing multiple phases. Some of the additional peaks could be attributed to ZrO_2 , CeO_2 , and Nd_2O_3 as well as Ce/Nd-zirconates of different compositions, suggesting insufficient mixing of the educts.

Following those results, attempts were made to achieve better phase purity. Of the three mixing methods, manual mixing yielded the most phase-pure products, so this method was selected for further experiments. Re-sintering the compositions (after grinding and re-pelletizing) led to significant improvement of phase purity, demonstrated by fewer and more defined peaks in the PXRD pattern (Fig. 1c). The formation of a more phase-pure product was also indicated in the PXRD pattern of another sample that was ground longer and only sintered once (Fig. 1d). However, the effect is not as pronounced as in the case of the re-sintered sample. Therefore, both re-sintering as well as longer grinding time can be seen as strategies to enhance phase purity. Furthermore, an increase of the Nd-content to 50 mol% also correlates to an improvement of phase purity (Fig. 2). Conversely, a longer milling time in mechanical mixing did not lead to significant changes in phase purity.

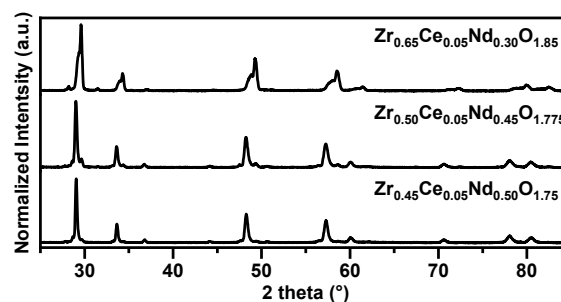


Figure 2. PXRD patterns of Ce/Nd-co-doped zirconates with different Nd content (manual solid-state mixing; ground 5 min, sintered once).

ACKNOWLEDGEMENTS. This work was funded by BMBF as part of the AcE project (02NUK060A).

- [1] Finkeldei, S. *et al.* (2017) *Acta Mater.* **125**, 166–176.
- [2] Lumpkin, G. R. *et al.* (2006) *Elements.* **2**, 365–372.
- [3] Lian, J. *et al.* (2004) *Nucl. Instrum. Meth. B.* **218**, 236–243.
- [4] Shannon, R. D. (1976) *Acta Cryst. A.* **32**, 751–767.
- [5] Chen, H. *et al.* (2009) *J. Alloys Compd.* **480**, 843–848.

Investigation of zirconia ceramics under high pressure conditions related to nuclear repositories

V. Svitlyk, S. Weiss, C. Hennig

We present here a new protocol for selecting and validating promising solid phases for the long-term immobilization of radiotoxic elements under deep geological repositories conditions. It consists of exposing materials of interest to extreme conditions of temperature and pressure combined with *in situ* structural characterization. In particular, structural and phase stabilities of corresponding systems are tracked with the help of synchrotron radiation diffraction. This approach allowed us to identify Y-stabilized ZrO₂ phases which can potentially be used as host matrices for tetravalent actinides for underground storage.

While typical depths for currently planned radioactive waste repositories are at about 500 m, depths down to 15 km have been considered.^[1] The latter would correspond to externally applied pressures of ~0.4 GPa and temperatures of ~400 °C. While a depth of 500 m provides much lower pressure and temperature, accidental conditions (like fire, tectonism, or shocks/explosions) may increase their values. Furthermore, we speculate that elevating temperature and pressure are means of accelerating time, thereby allowing to bring realistic experimental durations (hours to a few days) closer to the durations dictated by the long half-lives of key radionuclides (in the order of Ga). Thus, considering elevated temperature and pressure for the validation of phases as potential host matrices for underground storage of radiotoxic elements will increase the reliability of long-term predictions essential for the safety case.

Here we report on synthesis and *in situ* structural studies under extreme conditions of temperature (*T*) and pressure (*P*) of Y-stabilized zirconia, ZrO₂. Derivatives of zirconia are promising materials as host matrices for radiotoxic elements since these phases are known to remain geologically stable up to 10⁹ years.^[2]

EXPERIMENTAL. Series of tetragonal and cubic Y-ZrO₂ (YSZ) phases have been synthesized *via* the co-precipitation method. Ambient, *T*- and *P*-dependent *in situ* synchrotron radiation diffraction experiments were performed at ROBL.^[3] *HT* was achieved and controlled with a Cyberstar hot gas blower furnace. Temperature was calibrated on Ag diffraction lines using NIST equations and all samples were subsequently scanned in a *T* range of 300–1150 K with a typical heating rate of 6 K/min. During *P*-dependent experi-

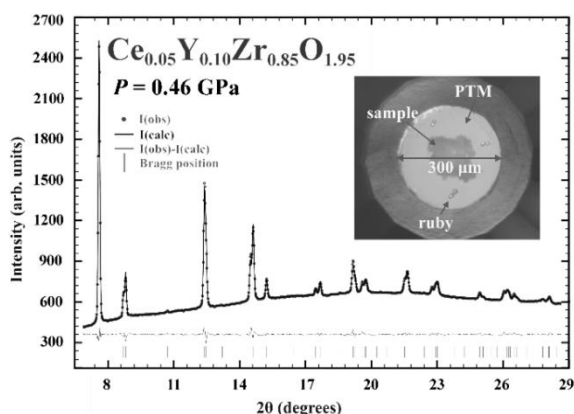


Figure 1. Typical *HP* diffractogram and a corresponding DAC assembly (inset).

ments, *HP* was generated using diamond anvil cells (DACs) using diamonds with 600- μ m culets. Samples were contained in stainless steel gaskets with holes of 300 μ m and a thickness of 95 μ m (Fig. 1, inset). Neon gas or silicon oil were used as *P*-transmitting media in order to ensure hydrostatic conditions. Diffraction data were collected on ROBL's high resolution XRD1 and multipurpose XRD2 diffractometers.

RESULTS. Cubic YSZ were found to dissolve ~20%-at. more tetravalent Th atoms than the corresponding tetragonal phases.^[4] Here, higher cubic symmetry favors incorporation of large guest atoms due to more symmetrical arrangement of coordinating O atoms compared to lower symmetry phases. Both tetragonal and cubic YSZ phases exhibit excellent stability at elevated temperatures.

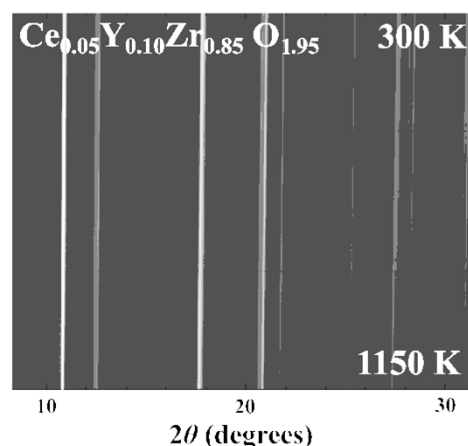


Figure 2. *T*-dependent diffraction patterns of Ce-YSZ.

In particular, no phase transitions were observed in tetragonal (Fig. 2) and cubic Ce-YSZ and no release of guest Ce⁴⁺ atoms, surrogate for tetravalent actinides, was revealed.^[5] While tetragonal Ce-YSZ phase transformed to a higher cubic symmetry around 9 GPa, no release of cerium atoms was observed as well.^[5]

The studied YSZ materials revealed remarkable stabilities under extreme conditions, they are expected to preserve integrity under conditions of underground repositories, at least with respect to elevated *T* and *P*.

We propose analogous studies under extreme conditions of temperature and pressure as a part of standard protocol for validating phases as host matrices for radiotoxic elements to be placed in underground repositories for long-term and secure storage.

ACKNOWLEDGEMENTS. This project was supported by BMBF AcE grant (02NUK060). D. Naudet, J. Exner, N. Baumann are acknowledged for technical/computing support.

- [1] Krall, L. et al. (2020) *Environ. Sci. Technol.* **54**, 629.
- [2] Heaman L. and LeCheminant, A. (1993) *Chem. Geol.* **110**, 95–126.
- [3] Scheinost, A. C. et al. (2021) *J. Synchr. Rad.* **28**, 333–49.
- [4] Svitlyk, V. et al. (2022) *J. Am. Ceram. Soc.* **105**, 5975.
- [5] Svitlyk, V. et al. (2022) *J. Am. Ceram. Soc.* **105**, 7831.

Influence of sintering conditions on the structure and the redox speciation of homogeneous (U,Ce)O₂ ceramics

M. Massonnet,¹ L. Claparede,¹ J. Martinez,² P. Martin,² M. O. J. Y. Hunault,³ D. Prieur, A. Mesbah,¹ N. Dacheux,¹ N. Clavier¹

¹ICSM, Univ Montpellier, CEA, CNRS, ENSCM, Bagnols/Cèze, France; ²CEA, DES, ISEC, DMRC, University of Montpellier, Marcoule, France, ³Synchrotron SOLEIL, L'Orme des Merisiers, Saint-Aubin, France

Although uranium-cerium dioxides are frequently used as a surrogate material for (U,Pu)O_{2-δ}, there is currently no reliable data regarding the oxygen stoichiometry and the redox speciation of the cations in such samples. In order to fill this gap, we present here results of a synchrotron study of highly homogeneous (U,Ce)O_{2±δ} sintered samples prepared by wet-chemistry route.

EXPERIMENTAL. The synthesis of the (U,Ce)O_{2±δ} starting powders is based on the precipitation and rapid ageing of mixed hydroxides. The resulting compounds were studied by Synchrotron Powder X-Ray Diffraction (SPXRD) and Extend X-ray Absorption Fine-Structure (EXAFS) spectroscopy performed on The Rossendorf Beamline (BM20). High-energy resolution fluorescence-detected XANES (HERFD-XANES) data were measured at the MARS beamline of the SOLEIL synchrotron.

RESULTS. The use of nanometric and highly reactive uranium-cerium dioxide powders prepared by wet-chemistry route led to the fabrication of homogenous and dense U_{1-x}Ce_xO_{2±δ} solid solutions after sintering at high temperature. Our main focus was on studying the impact of the operating conditions during the heat treatment (firing temperature, oxygen partial pressure), on the structure and redox speciation of the final ceramics.

We used HERFD-XANES spectroscopy to determine accurately the oxygen/metal molar ratios (*i.e.*, O/M with M = U + Ce) in all samples (Fig. 1). Under reducing atmosphere (pO₂ ~ 6 × 10⁻²⁹ atm), the oxides had an O/M close to 2.00. Even though a limited fraction (typically 5 % or less) of the uranium was found to be oxidized to U(V), we assume that this was most likely arising during storage and preparation of the samples for the synchrotron measurements. Hence, one can consider that in the furnace, the dioxide compounds were stoichiometric, with U(IV) preventing cerium from being reduced to Ce(III). In contrast, the samples prepared under argon (pO₂ ~ 2 × 10⁻⁶ atm) showed O/M ratios varying with the sintering conditions. They globally appear to be hyper-stoichiometric (*i.e.* O/M > 2.00), the departure from the dioxide stoichiometry decreasing with both the cerium content in the sample, and the sintering temperature. The reduction of the initial cerium(IV) present in the precursor into Ce(III) was then not sufficient to counter-balance the oxidation of U(IV) into U(V) under the operating conditions chosen. Nevertheless, such deviation from the ideal O/M = 2.00 ratio was found to generate only moderate structural disorder from EXAFS data at the U-L₃ edge, mainly in the coordination shell of the cations.

In fact, whatever the sintering temperature and atmosphere, all the samples retained the fluorite-type structure of the UO₂ and CeO₂ parent compounds. The determination of accurate lattice parameters by SPXRD allowed us to complete the data already reported in the literature, and to propose a mathematical equation linking the unit cell parameter, the chemical composition and the deviation from the stoichiometry. Such relation can now be used as a first approximation to estimate the O/M stoichiometry of uranium-cerium mixed oxides across a wide compositional range.

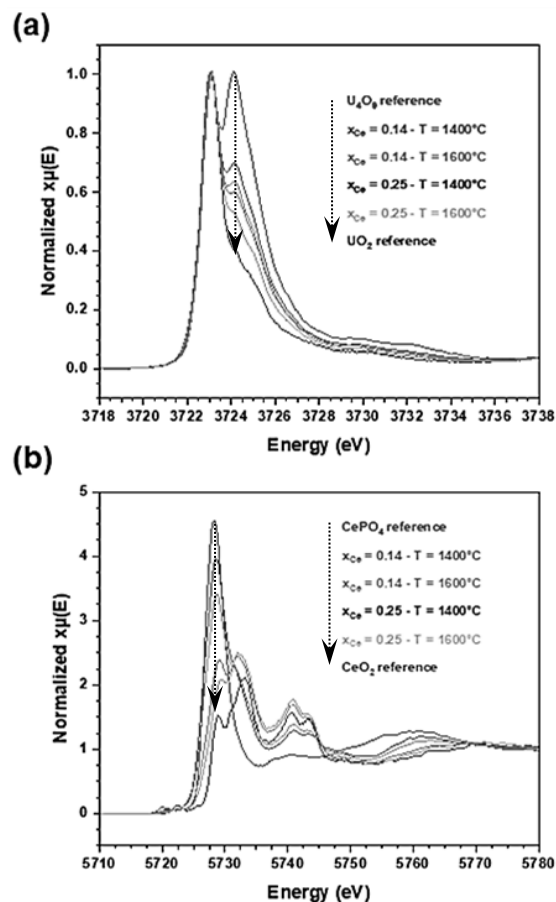


Figure 1. Normalized HERFD-XANES spectra at the U-M₄ (a) and Ce-L₃ (b) edges for various U_{1-x}Ce_xO_{2±δ} samples sintered under argon atmosphere.

The structural data also constitute a solid starting point for the evaluation of the impact of the O/M stoichiometry on several characteristics of dense uranium-cerium dioxide pellets, such as microstructure and chemical durability.^[1]

ACKNOWLEDGEMENTS. The authors thank the SOLEIL and ESRF synchrotrons for providing beamtime.

[1] Massonnet *et al.* (2023) *Inorg. Chem.*, submitted.

Oxygen K-edge X-ray Absorption Spectra of ThO₂ and CeO₂

L. Amidani, T. Dumas,¹ D. K. Shuh,² S. M. Butorin,³ C. J. Sahle,⁴ A. Longo,⁴ K. O. Kvashnina

¹CEA, DES, ISEC, DMRC, University of Montpellier, Bagnols sur Cèze, France; ²Lawrence Berkeley National Laboratory, Berkeley, California, U.S.A.;

³Uppsala University, Uppsala, Sweden; ⁴ESRF, Grenoble, France.

Measuring the ligand K-edge provides an insightful view on the electronic structure of the metal ion, if covalency plays a role in the chemical bond. In this work we compare the oxygen K-edge of CeO₂ and ThO₂ and analyze the data with *ab initio* spectral calculations. Our results reveal that the three peaks in both spectra can be ascribed to *f*- and *d*-orbitals, the latter split into *e_g* and *t_{2g}* bands. While for CeO₂ the 4*f* orbitals form a sharp band below the 5*d*-*e_g* and 5*d*-*t_{2g}*, for ThO₂ the 5*f* band spreads over a larger range located in-between the 6*d*-*e_g* and 6*d*-*t_{2g}* bands.^[1]

A chemical bond with a certain degree of covalency is described by wave-functions made by contributions from both the ligands and the metal. The X-ray absorption near-edge structure (XANES) spectrum is proportional to the projected density of states localized on the absorber. If some metal character is mixing with the ligand, ligand K-edge XANES will see this contribution. The oxygen K-edge spectra of CeO₂ and ThO₂ are a very clear and instructive example of the insight given by ligand K-edge on the electronic structure of the metal.

RESULTS. Figure 1 shows the experimental O K-edge XANES (open circles) for CeO₂ (panel a) and ThO₂ (panel b). Both edges are characterized by three peaks. CeO₂ exhibits two very sharp peaks and a third broad one. ThO₂ exhibits a very sharp peak, a second peak with substructures and a third broad one. XANES spectral calculations obtained with the FDMNES code are shown in Fig. 1 (second traces).^[2] They nicely reproduce the experimental spectra, with all features at the correct energy and with good agreement for the width and the relative intensities. To know which orbitals are contributing most to each peak, we can look at the projected densities of states (DOS) from both O, Ce and Th (Fig. 1a,b, third traces). As expected, all features belong to the O *p*-DOS, which is what we probe with the O K-edge. By looking at the Ce and Th projected DOS we can deduce if the peaks of the O *p*-DOS are due to hybridization with metal orbitals. Figure 1 reports the Ce 5*d* and Th 6*d* DOS (third traces) splitted in two bands, *e_g* (red) and *t_{2g}* (light blue), which is due to the cubic crystal field of the 8 O-ligand arranged at the corner of the cube with Ce/Th in the center. The *e_g* band is at lower energy than the *t_{2g}*, in opposite order compared to the case of an octahedral crystal field, where the 6 ligands are along the axial directions. By comparison with the O *p*-DOSs and with XANES calculations, we can assign the second sharp peak of the CeO₂ spectrum and the first sharp peak of the ThO₂ spectrum to hybridization with the *e_g* band of the metal. The third broad peaks of both CeO₂ and ThO₂ are instead due to hybridization with the *t_{2g}* metal band. Finally, inspection of the *f*-DOSs (Fig. 1, lower traces) reveals that Ce 4*f* orbitals form a very sharp band which appears as the first sharp peak of CeO₂ O K-edge XANES because of the hybridization with O 2*p* states. Differently, the 5*f* orbitals of Th form a broader and more structured band which appears in ThO₂ O K-edge XANES as the second substructured peak.

Our results shows how the O K-edge provides a nice overview of the electronic structure of the metal centers in CeO₂

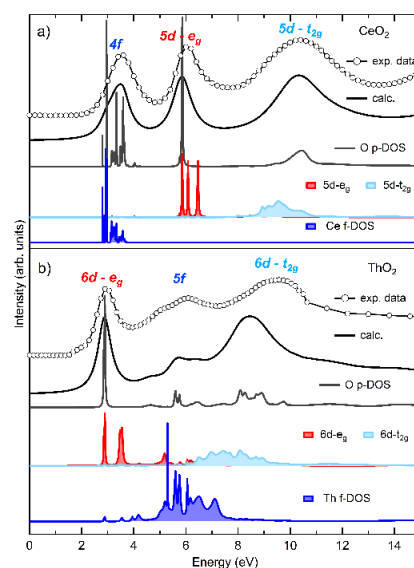


Figure 1. Experimental (empty dots) and calculated (black line) O K-edge XANES for CeO₂ (a) and ThO₂ (b). The projected DOSs are reported below the calculated spectra: O 2*p*-DOS (dark grey), Ce 5*d*/Th 6*d* *e_g* (red) and *t_{2g}* (light blue) bands, Ce 4*f*/Th 5*f* (blue).

and ThO₂. Our findings confirm that the 5*f* band lies in-between the 6*d* band in ThO₂ as predicted by DFT.^[3] To verify the sensitivity of the O K-edge to structural modifications, we calculated the O K-edge XANES of a 2.1 nm ThO₂ nanoparticles, using the same approach described in Amidani *et al.*^[4] The results are shown in Fig. 2, where the spectrum from the bulk is compared to that of the central O and of the whole nanoparticle. It is interesting to notice that surface effects are mainly affecting the first peak, which is severely lowered in the case of the nanoparticles.

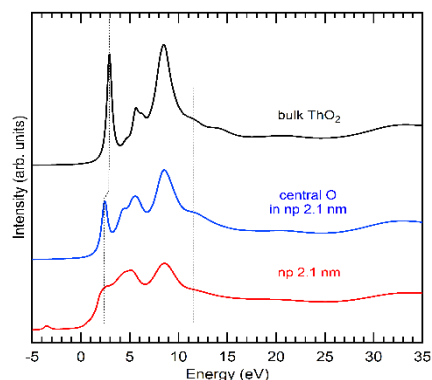


Figure 2. O K-edge XANES calculated for bulk ThO₂ (black), the central O atom of the 2.1 nm nanoparticle (blue) and the weighted average of all O absorber in the nanoparticle (red).

- [1] Amidani, L. *et al.* (2023) *J. Phys. Chem. C.*, accepted.
- [2] Bunău, O. and Joly, Y. (2009) *J. Phys.: Condens. Matter* **21**, 345501.
- [3] Prodan, I. D. *et al.* (2007) *Phys. Rev. B* **76**, 033101.
- [4] Amidani, L. *et al.* (2019) *Phys. Chem. Chem. Phys.* **21**, 10635–10643.

Interlayer excitons in MoSe₂/2D perovskite hybrid heterostructures – the interplay between charge and energy transfer

M. Karpińska,¹ J. Jasiński,² R. Kempt,³ J. D. Ziegler,⁴ H. Sansom,⁵ T. Taniguchi,⁶ K. Watanabe,⁶ H. J. Snaith,⁵ A. Surrente,² M. Dyksik,^{1,2} D. K. Maude,¹ Ł. Kłopotowski,⁷ A. Chernikov,³ A. Kuc,⁸ M. Baranowski,² P. Plochocka^{1,2}

¹CNRS, Toulouse, France; ²Wrocław University of Science and Technology, Wrocław, Poland; ³Technische Universität Dresden, Dresden, Germany; ⁴Universität Regensburg, Regensburg, Germany; ⁵University of Oxford, Oxford, U.K.; ⁶National Institute for Materials Science (NIMS), Ibaraki, Japan; ⁷Polish Academy of Sciences, Warsaw, Poland; ⁸HZDR, Leipzig, Germany

Van der Waals crystals have opened a new and exciting chapter in heterostructure research, removing the lattice matching constraint characteristics of epitaxial semiconductors. They provide unprecedented flexibility for heterostructure design. Combining 2D perovskites with other 2D materials, in particular transition metal dichalcogenides (TMDs), has recently emerged as an intriguing way to design hybrid opto-electronic devices. However, the excitation transfer mechanism between the layers (charge or energy transfer) remains to be elucidated. Here, we investigate PEA₂PbI₄/MoSe₂ and (BA)₂PbI₄/MoSe₂ heterostructures by combining optical spectroscopy and density functional theory (DFT) calculations. We show that band alignment facilitates charge transfer. Namely, holes are transferred from TMDs to 2D perovskites, while the electron transfer is blocked, resulting in the formation of interlayer excitons. Moreover, we show that the energy transfer mechanism can be turned on by an appropriate alignment of the excitonic states, providing a rule of thumb for the deterministic control of the excitation transfer mechanism in TMD/2D-perovskite heterostructures.

EXPERIMENTAL. This work is a collaboration between theoretical group from HZDR and experimentalists from various institutions. Details will be provided only from the theoretical work, information on experimental part is given elsewhere.^[1] The MoSe₂@(PEA)₂PbI₄ (PEPI/MoSe₂) and MoSe₂@(BA)₂PbI₄ (BAPI/MoSe₂) structures were relaxed using FHI-aims employing the PBE functional on tight tier 1 numeric atom-centered orbitals, including Tkatchenko–Scheffler correction for dispersion interactions, and scalar relativistic corrections (ZORA) on a 2×2×1 Γ -centered k-grid. The electronic band structure, the Mulliken projections, and the density of states were calculated including spin–orbit coupling and considering the dipole correction on a 4×4×1 Γ -centered k-grid.

RESULTS. Density functional theory simulations of electronic structures of both heterojunctions were performed. The TMD and 2DP layers in both cases are incommensurate, thus, larger heterostructures with a twist angle were necessary. To reveal the contribution of particular orbitals to the valence and conduction bands, we performed Mulliken analysis (Fig. 1). This shows that the top of the valence band is located at the Γ point in both heterostructures and is mainly composed of orbitals from the PbI₄ slab. At the same time, the conduction band edges are located between the Γ and Y points and are dominated by the TMD states, as clearly seen in the projected density of states (pDOS) plots. States related to the organic spacers are a few eV above the edges of the lowest conduction bands forming a barrier for electrons. Similarly in the valence band, the largest contributions of the organic spacer orbitals to the valence band DOS are observed at about -7 eV, significantly below the top of the MoSe₂ and PbI₄ valence bands.

A closer inspection (expanded view of the top of the valence band) reveals a non-vanishing contribution of the organic spacers to the DOS between the valence band edges of PbI₄ and MoSe₂. Consequently, a cascade-like band alignment is formed in the valence bands of both heterostructures, facilitating hole transfer from MoSe₂ to the 2DP, which represents a prerequisite for interlayer exciton formation. Therefore, our DFT calculations support the hypothesis that the low energy PL originates from interlayer exciton (IX) emission with the electrons localized in the MoSe₂ layer and the holes localized in the 2DP layer. The effective type-II band alignment between MoSe₂ and the 2DP gives rise to the formation of interlayer excitons (IX), with PL emission below the intralayer excitonic transitions. The interlayer nature of the IX transition is supported by the long PL decay time and PLE studies. Moreover, we show that charge transfer can occur simultaneously with energy transfer in the opposite direction, which depends on the excitonic state alignment. The electronic structures are shown in Fig. 1.

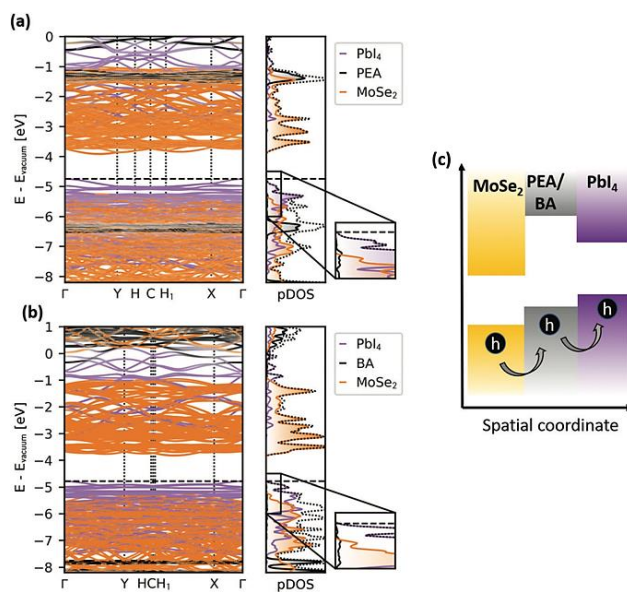


Figure 1. Mulliken-projected band structures of PEPI/MoSe₂ and BAPI/MoSe₂ heterostructures showing the majority contributions of each layer and density of states (pDOS) projected to particular building blocks (a, b). Zoom-in of pDOS shows the contribution of organic spacer states. Schematic illustration of the band alignment in both heterostructures as calculated by DFT (c).

ACKNOWLEDGEMENTS. The authors gratefully acknowledge the financial support provided by the Deutsche Forschungsgemeinschaft (CRC-1415: 417590517) and they acknowledge the Centre for Information Services and High-Performance Computing (ZIH) in Dresden and the GCS Supercomputer JUWELS at the Jülich Supercomputing Centre (JSC).

[1] Karpińska, M. et al. (2022) *Nanoscale* **14**, 8085–8095.

Structural analysis of 14 MeV Au ion-irradiated monazite targets

S. E. Gilson, V. Svitlyk, C. Hennig, H. Lippold, C. Fischer, G. L. Murphy,¹ A. Bukaemskiy,¹ S. Akhmadaliev,² N. Huittinen

¹Forschungszentrum Jülich, Institut für Energie- und Klimaforschung (IEK-6), Jülich, Germany; ²HZDR, Institute of Ion Beam Physics and Materials Research, Dresden, Germany

Polycrystalline pellets of Eu^{III}-doped LaPO₄ monazite were irradiated with 14 MeV Au ions at various fluences at the Ion Beam Center (IBC). Subsequent structural analysis involved analytical techniques to assess differences in the long- and short-range order of the samples upon irradiation. Grazing incidence diffraction (GID) reveals the presence of an amorphous contribution in the diffraction patterns of all irradiated ceramics. Raman spectra suggest disruption in the local coordination environments of the monazite structure. Vertical scanning interferometry (VSI) was used to examine the surface topographies of the pristine and irradiated sides of the ceramics.

Monazites are interesting materials with various properties that make them attractive for the immobilization of trivalent ions in nuclear waste.^[1] For instance, their high radiation resistance has been observed in natural monazite specimens over geological time scales.^[2] To assess their suitability as host forms for radionuclides in nuclear waste, thorough knowledge about their structural response to radiation is critical. In this study, 14 MeV Au ions were used to simulate the recoil of daughter products from the alpha-decay of actinides. Samples were irradiated to fluences expected to produce significant observable damage to the ceramic samples.

EXPERIMENTAL. To avoid annealing processes from occurring during irradiation, samples were secured in a cryostat at 77 K. Samples were irradiated to the fluences given in Tab. 1. To help quantify radiation damage, fluences are often related to displacements per atom (dpa). Monte Carlo simulations using the SRIM software package predicted that the Au ions penetrate approximately three micrometers into the samples.^[3] GID data of irradiated samples were collected over an omega range of 0 to 14° using the XRD-2 setup at the Rossendorf beamline at the European Synchrotron Radiation Facility in Grenoble, France. Raman spectra were recorded over a range of 70 to 1200 cm⁻¹ with an 1800 lines grating using a Horiba Jobin-Yvon Raman spectrometer equipped with a HeNe excitation source. VSI data were obtained from an SNeox 3D Optical Profiler (Sensofar, Spain) with Mirau objectives. White light was used to determine sample height and collect images.

Table 1. Sample and irradiation details.

Fluence Number	Fluence (ions/cm ²)	Displacements per atom	Rel. volume expansion ⁵
4	1 × 10 ¹⁵	4.64	10 ×
2	1 × 10 ¹⁴	0.46	–
1	5 × 10 ¹³	0.23	4.6 ×

RESULTS. GID patterns collected at an omega angle of 2.0° are given in Fig. 1A. A representative pattern of pristine ceramic is shown in black. The patterns of the three irradiated samples each display an amorphous signal that is not observed in the pristine sample. This suggests disruption in the long-range order of the monazite structure with irradiation, regardless of dose.

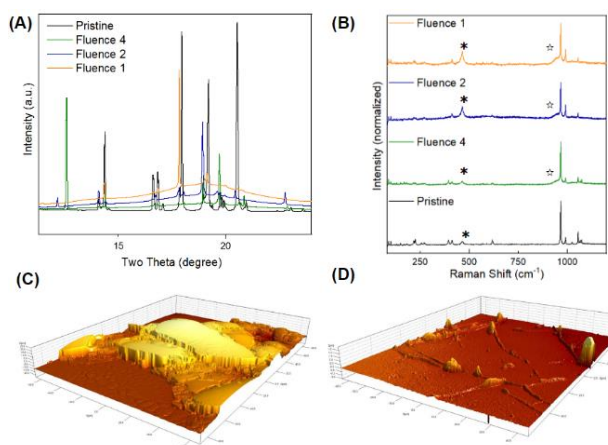


Figure 1. GID patterns (A), Raman spectra (B), and VSI images showing global swelling (C) and local swelling (D) of the irradiated LaPO₄ ceramics.

To probe local coordination environments in the samples, Raman spectra were collected (Fig. 1B). Compared to the pristine sample, spectra of irradiated samples reveal a shoulder at approximately 943 cm⁻¹ that is attributed to the symmetric stretch of the PO₄ group.^[4] Peak fitting did not show a trend in the peak center or full-width half-maximum (FWHM) of this shoulder with dose. Additionally, a change in intensity of the ν_2 peak at approximately 465 cm⁻¹ with decreasing dose was also observed. Thereby, Raman spectra confirm changes in local coordination environments of the irradiated samples.

VSI measurements of the surfaces of the irradiated ceramics allow for estimation of the volume swelling caused by ion implantation. The difference in surface topologies between pristine and irradiated sides of the ceramics was analyzed and an average difference of about 300 nm was recorded for the ceramic irradiated to fluence 4 whereas an average difference of approximately 140 nm was recorded for the ceramic irradiated to fluence 1. Using the equation from Picot *et al.*^[5] gives a volume expansion of 10 × and 4.6 × the original monazite volumes, respectively. Additionally, these measurements reveal two different types of swelling in the irradiated ceramics. Figure 1C illustrates swelling in the form of the expansion of an entire grain in the ceramic irradiated to fluence 4. Conversely, Fig. 1D illustrates swelling in the form of thin, raised ridges along grain boundaries in the ceramic irradiated to fluence 2.

Future work will involve comparison of these results to those of LaPO₄ single-crystals irradiated under identical conditions to compare their radiation response and dissolution studies of the irradiated monazite samples.

ACKNOWLEDGEMENT. BMBF funding, AcE project (02NUK060A). Beamtime at the ESRF was granted under proposal A20-1 839. Ion Beam Center, HZDR for irradiations. The authors thank the Central Radionuclide Laboratory, TU Dresden for use of their facilities.

[1] Neumeier, S. *et al.* (2017) *Radiochim. Acta* **105**, 961–984.

[2] Nasdala, L. *et al.* (2020) *Sci. Rep.* **10**, 14676.

[3] Ziegler, J. *et al.* (2010) *Nucl. Instrum. Methods Phys. Res.* **268**, 1818–1823.

[4] Begun, G. *et al.* (1981) *J. Raman. Spec.* **11**, 273–278.

[5] Picot, V. *et al.* (2008) *J. Nucl. Mater.* **381**, 290–296.

Dissolution kinetic of soddyite

F. Bok, C. Cariven,¹ N. Hoth,¹ V. Brendler

¹TU Bergakademie Freiberg, Institut für Bergbau und Spezialtiefbau, Freiberg, Germany

The geochemical modeling of radionuclide migration is mostly based on thermodynamic models describing the major processes, such as complex formation, precipitation/dissolution, sorption and incorporation as equilibria. To perform time-dependent modeling it is necessary to include kinetic data. In this work, a kinetic model for $(\text{UO}_2)_2\text{SiO}_4 \cdot 2\text{H}_2\text{O}$ (soddyite) dissolution was developed.^[1]

In contrast to various thermodynamic database projects, there is currently no internationally recognized database for kinetic data. This can be explained by the heterogeneity of the kinetic model approaches, as well as the fact that, depending on the chemical environment, different reaction pathways and thus parameters for rate laws for the reaction of a phase can exist. Furthermore, a variety of competing models with different degrees of complexity exist in the literature to describe kinetics.

The kinetic rate model by PALANDRI and KHARAKA is a simplistic but pragmatic approach for silicate minerals using only one dependency for the mineral dissolution: pH with reaction rate laws in three different ranges (acidic, neutral and alkaline) and a general surface area normalization to $1 \text{ m}^2/\text{g}$ in case of missing data.^[2]

The aim of the work presented here was the kinetic description of soddyite dissolution in the acidic range (pH = 4–6), where no precipitation of other uranyl mineral phases is expected and the effect of uranyl carbonate complexation can be neglected. For this, also the temperature-dependent solubility of the mineral had to be determined.

EXPERIMENTAL. Synthetic soddyite prepared by MOLL was used for the experiments.^[3] Batch dissolution experiments were conducted at pH 4.00, 5.00, and 5.90 (± 0.01) at the temperatures of 25 °C, 35 °C and 50 (± 1) °C (Fig. 1). The mineral was suspended in 0.1 M LiCl solution shaken for up to 104 days under pH adjustment using HCl/LiOH. Sampling at several time points were performed to determine the reaction progression over time at different conditions as well as the equilibrium concentration of U and Si as function of temperature (Fig. 1, inset).

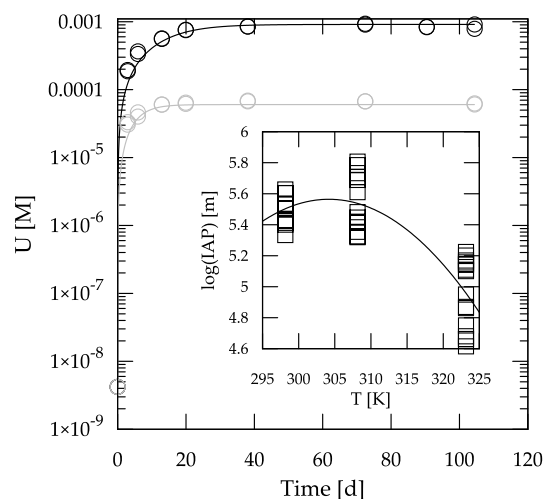


Figure 1. Dissolution kinetics of soddyite in 0.1 M LiCl solution (exemplary for the data at T = 25 °C), experimental data (o), fit (—), black: pH = 4, grey: pH = 5; Inset: Temperature dependence of the ion activity product of soddyite solution (pH = 4–5.9), experimental data (□), fit (—).

RESULTS. The temperature-dependent solubility product of soddyite was derived using the uranium concentration at the final plateau of the dissolution curves. To do so, the ion activity product (IAP) for uranyl silicate was calculated using the geochemical speciation code PHREEQC with the thermodynamic database ThermoChimie (V10d).^[4, 5] A polynomial fit then gave the parametrized solubility product's temperature function (1):

$$\log K_{sp} = -(150 \pm 37) + (1.03 \pm 0.24)T - (0.0017 \pm 0.0004)T^2 \quad (1)$$

The PHREEQC implementation skript of the kinetic rate law of PALANDRI and KHARAKA by ZHANG et al. was used for parameter fitting of the kinetic rate equation (2) in the acidic range.^[6]

$$k = A \cdot e^{-\frac{E_a}{RT}} \cdot a_{H^+}^n \quad (2)$$

For this purpose, PHREEQC was coupled with the parameter estimation software Ucode2014.^[4, 7] The results are given in Tab. 1.

Table 1. Soddyite dissolution kinetic rate parameters for equation 2.

Parameter	Value
Arrhenius pre-exponential factor (A)	$12 \pm 35 \text{ mol} \cdot \text{m}^2 \cdot \text{s}^{-1}$
Activation energy (E_a)	$39.6 \pm 3.8 \text{ kJ} \cdot \text{mol}^{-1}$
Proton activity power (n)	0.77 ± 0.24

CONCLUSIONS. The obtained thermodynamic model for the temperature-dependent solubility of the uranium silicate mineral soddyite, as well as the kinetic model for its acid dissolution, represents a robust extension of the capabilities of geochemical modeling. Incorporating kinetic data into safety calculations can help reduce conservatism. This work serves as a first step toward a kinetic database consistent with existing thermodynamic databases.

ACKNOWLEDGEMENTS. The authors thank M. Acker, S. Taut and S. Weiss for their support and the possibilities to perform the work coronationally in the laboratories of the TU Dresden. Analytical work was performed by S. Beutner (HZDR-IRE) and U. Czeslik (VKTA), the authors thank these colleagues as well.

- [1] Cariven, C. (2022) *Long-term reactions of silicate mineral phases – implementation and application of pH-dependent dissolution rates with relevance for future nuclear waste disposals*, MSc Thesis, TU Bergakademie Freiberg, Inst. f. Bergbau.
- [2] Palandri, J.L. et al. (2004) *U.S. Geological Survey report 2004–1068*, 70 pp.
- [3] Moll, H. (1996) *Radiochim. Acta* **74**, 3–7.
- [4] Parkhurst, D.L. et al. (2013) *U.S.G.S. report 6-A43*.
- [5] Giffaut, E. et al. (2014) *Appl. Geochemistry* **49**, 225–236.
- [6] Zhang, Y. et al. (2019) *Computers & Geosciences* **133**, 104316.
- [7] Poeter, E.P. et al. (2014) *IGWMC report GWWI 2014–02*.

Improved kinetics for mineral dissolution reactions in pore-scale reactive transport modeling

J. Schabernack, C. Fischer

Recent numerical investigations revealed that the heterogeneity of the dissolution rate observed in numerous experiments cannot be explained by fluid transport effects. This heterogeneity is attributed to intrinsic surface reactivity. Therefore, reactive transport models (RTM) require parameterization of the surface reactivity for accurate predictions. For this purpose, a nanotopographic parametrization based on surface slope has been recently suggested. In this study, we utilize and improve this parametrization for RTMs of pore-scale systems, from the crystal surface to the single crystal geometry, going beyond the previous reactivity parametrization.^[1,2] 2D and 3D RTMs were developed using COMSOL Multiphysics for calcite systems based on experimental measurements. We compared the results between classically parameterized RTMs, RTMs with new slope parameterization, and experimental data. The effect of flow on dissolution under conditions far-from-equilibrium is found to be negligible, highlighting the importance of surface reactivity in the dissolution reaction. For the first time, the new surface slope factor (SSF) was able to accurately reproduce the experimental results on a crystal surface with large field-of-view, large height variability of the topography, and over a long-term reaction period.^[1]

NUMERICAL. All simulations were performed at an average velocity of 1,000 mm/s similar to the estimated experimental velocity.^[3] The fluid flow in our system was simulated assuming laminar flow conditions. The Navier-Stokes equation for the flow of an incompressible viscous fluid was applied. For the simulation of species transport in the system, we applied the advection-diffusion-reaction equation for general transport. At the liquid-solid interface, calcite can dissolve and release Ca^{2+} and CO_3^{2-} into the solution. This was implemented by using a flux boundary condition. In RTMs, the dissolution of the crystalline matter is usually simulated by applying a rate law according to transition state theory. To define surface reactivity in the rate equation, we introduced the improved SSF as a prefactor dependent on the local slope values (Fig. 1).

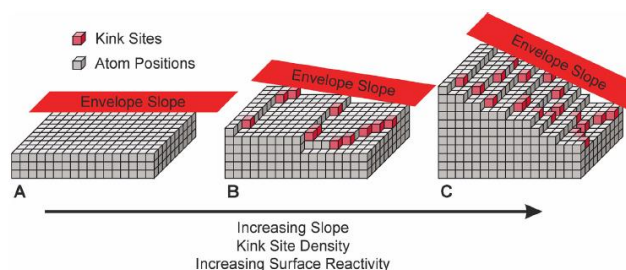


Figure 1. Schematic illustration of the correlation of surface slope and kink site density on an atomic scale using the example of a Kossel-Stranski crystal surface. An atomically flat surface with no inclination and no crystal steps (A). A crystal surface with few steps leading to an intermediate slope (B). There are highly reactive kinks in the steps (red cubes). A crystal surface with increased slope, resulting in higher step density and thus higher concentration of kink sites referring to the basal area (C). Based on this concept, the slope factor is used as a proxy parameter to describe the density distribution of steps and kinks and, consequently, the reactivity distribution on mineral surfaces.

RESULTS. The application of SSF strongly modifies the classical RTM simulation results.^[1] The resulting dissolution rate maps show largely heterogeneous rate distributions, very similar to the distribution in the experimental counterpart.^[2] High dissolution rates are concentrated in the deep etch pits and along large steps of the calcite surface. Intermediate rates are found at shallower etch pits and smaller steps on mostly flat surface areas. Surface areas without any structures show dissolution rates close to zero, similar to the experimental results.

Overall, we can conclude that the new simulation results satisfactorily reflect the rate heterogeneity, visible from the rate spectra shown in Fig. 2.

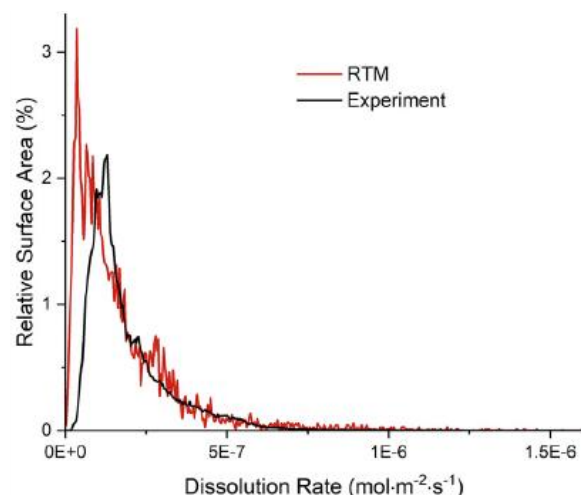


Figure 2. Dissolution rate spectra obtained in the experiment (black line) and simulated using the improved RTM approach with slope factor (red line), showing a better agreement compared to the previous RTM approach.^[2] In particular, the critical high rate contributions ($> 10^{-7}$ mol m⁻² s⁻¹) are now satisfactorily described by the model, which is very important for its predictive capability.

The new parameterization greatly improved sensitivity for intermediate to high reactivity ranges compared to the previous parameterization.^[1,2] A 3D model was used to demonstrate the general applicability of the parameterization for use in realistic geometric data sets. Thus, we also showed that neglecting heterogeneous surface reactivity in an RTM leads to incorrect predictions regarding the evolution of porosity, pore geometry, and surface topography. Our new slope factor proved to be suitable as a first-order proxy for the distribution of surface reactivity in 3D pore-scale rock systems. The description of surface reactivity is crucial for accurate long-term modeling of technical and natural systems.

ACKNOWLEDGEMENTS. The authors gratefully acknowledge funding by the German Federal Ministry of Education and Research (BMBF), grant 02NUK053B, and the Helmholtz Association, grant SO-093 (iCross).

- [1] Schabernack, J. and Fischer, C. (2022) *Geochim. Cosmochim. Acta* **334**, 99–118.
- [2] Karimzadeh, L. and Fischer, C. (2021) *ACS Earth Space Chem.* **5**, 2408–2418.
- [3] Bibi, I. et al. (2018) *Minerals* **8**, 256.

The influence of sedimentary heterogeneity on the diffusion of radionuclides in the sandy facies of Opalinus Clay at the field scale

C. Chen,¹ T. Yuan, R. Lu,¹ C. Fischer, O. Kolditz,¹ H. Shao¹

¹Helmholtz Centre for Environmental Research – UFZ, Leipzig, Germany

Radionuclide migration in clay-rich formations is typically dominated by diffusion considering the low permeability of these formations. An accurate estimation of radionuclide migration in host rocks using numerical tools plays a key role in the safety assessment of disposal concepts for nuclear waste. In the sandy facies of the Opalinus Clay (SF-OPA), the spatial variability of the pore space network and compositional heterogeneity at the pore scale (nm to μm) cause heterogeneous diffusion at the core scale (cm to dm). Such heterogeneous diffusion patterns affect the migration of radionuclides in various sedimentary layers even above the core scale (m).^[1] Here, we study the heterogeneous diffusion of cations based on a two-dimensional (2D) structural model at the m-scale. As key parameters for the diffusive transport calculation, the effective diffusion coefficients in different sedimentary layers are quantified based on our previously developed up-scaling workflow from pore- to core scale combined with the multi-scale digital rock models. The heterogeneous effective diffusivities are then implemented into the large-scale structural model for diffusive transport simulation using the FEM-based OpenGeoSys-6 simulator. The sensitivity analysis focuses on the effects of the SF-OPA bedding angle and of different layer succession layouts on the spatio-temporal evolution of the radionuclide diffusion front line.^[2]

NUMERICAL. We simulate the diffusive propagation of a Na^+ tracer from a source (canister) into an SF-OPA formation (Fig. 1). The structurally simplified 2D formation consists of four layers with different material properties (S1–S4), which will be varied for the case studies and which have an identical length of 40 m and an identical thickness of 5 m. The layers differ in the model with respect to their clay, sand and carbonate cement concentrations. As a result, the diffusion coefficients parallel to the strata vary from about 0.6 to $2.4 \times 10^{-11} \text{ m}^2 \text{ s}^{-1}$ and the coefficients perpendicular to the strata vary from 0.18 to $0.77 \times 10^{-11} \text{ m}^2 \text{ s}^{-1}$. On the length scale under consideration, the pore-scale heterogeneity has been shown to be converged and upscalable.^[1] Thus, we use each layer with a homogeneously distributed structure, resulting in homogeneous diffusivity. The canister is placed inside of a bentonite buffer. The initial concentration of the Na^+ is 0.3 mol L^{-1} . All the boundaries are no-flux conditions. The total simulation time is 2,000 years. More details are provided elsewhere.^[2]

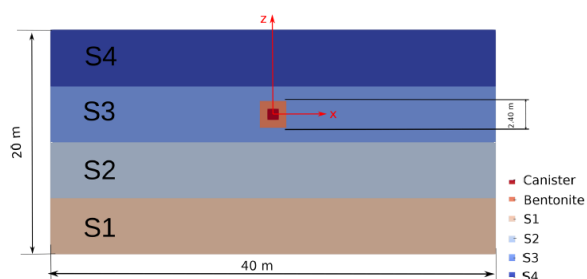


Figure 1. 2D structure model of an SF-OPA formation consisting of four different sedimentary layers. The source of diffusive flux (canister: red color) within bentonite (orange color) is placed in the center of layer S3.

RESULTS. In general, the diffusion front in this rock type migrates in the order of decimeters to meters over the period under consideration. The model configuration can be used to quantitatively study the effect of diffusion contrasts. The diffusion front can also be predicted as a function of the bedding angle of the specific sequence of sedimentary layers. In a first case study, the concentration of the studied tracer cation in the source decreases from 0.071 to 0.055 mol L^{-1} between 1,000 and 2,000 years (Fig. 2). As expected, the diffusion front in the layered system moves preferentially from the source in the direction in which the adjacent layer has a higher diffusion coefficient. After 1,000 years, the tracer has diffused about 5.80 m in the $-z$ direction, while the distance in the $+z$ direction is about 4.76 m . This is because the adjacent layer in the $-z$ direction (S2) has a higher diffusion coefficient than the adjacent layer in the $+z$ direction (S4). When analyzing the diffusion front, where the tracer concentration is equal to the standard deviation, both are still in the S3 layer after 2,000 years.

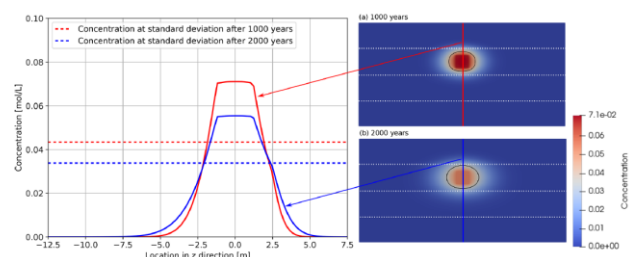


Figure 2. Na^+ concentration profiles along the z direction after 1,000 years' (red line) and 2,000 years' (blue line) diffusion. Subsets show the concentration distribution in the entire domain after 1,000 years' (a) and 2,000 years' (b) diffusion. Red line (a) and blue line (b) indicate the positioning of the concentration profiles along the z direction. The canister center is located at the position $z = 0 \text{ m}$. The white dashed lines represent boundaries between different layers. Black lines in the maps represent the diffusion fronts.

The example presented shows how the converged parameters for migration can be used in macroscopic sensitivity studies. These parameters were previously investigated in detailed laboratory studies and small-scale simulation calculations.^[1] The study presented here is an essential step in understanding the impact of small-scale heterogeneities (lamination, concretions *vs.* bedding, layers *etc.*) at the system scale. We anticipate further similar studies to quantitatively understand the system-scale phenomena.

ACKNOWLEDGEMENTS. The authors gratefully acknowledge funding by the German Federal Ministry of Education and Research (BMBF), grant 02NUK053B, and the Helmholtz Association, grant SO-093 (iCross).

[1] Bollermann, T. *et al.* (2022) *Chem. Geol.* **606**, 120997.

[2] Chen, C. *et al.* (2022) *Adv. Geosci.* **58**, 77–85.

Pore network and solute flux pattern analysis towards improved predictability of diffusive transport in argillaceous host rocks

T. Bollermann, T. Yuan, J. Kulenkampff, T. Stumpf, C. Fischer

Clay rock formations are considered as host rocks for underground radioactive waste repositories. Reliable predictions of diffusive transport heterogeneity are critical for assessing the sealing capacity of argillaceous rocks. The predictive power of numerical approaches to flow field analysis and radionuclide migration depends on the quality of the underlying pore network geometry. Both sedimentary and diagenetic complexity are controlling factors. In this study, we demonstrate a cross-scale approach to reconstruct the pore network geometries of the sandy facies of the Opalinus Clay rock, ranging from the nm to the cm scale.^[1] The resulting generalized pore network geometries are applied in digital rock models to calculate effective diffusivities.^[2] Positron emission tomography (PET) diffusion experiments confirmed the numerical approach of the pore-scale simulations. The PET analysis yielded a unique data set on the distribution of effective diffusivities in the sandy facies of the Opalinus Clay. This improves our prognostic capabilities with respect to migration properties and enhances the related transport simulations.

EXPERIMENTAL & ANALYTICAL. We identify diagenetic and sedimentary components of the sandy facies and quantify their pore size distribution and pore network geometry by using a combination of micro-computed tomography (μ -CT), focused ion beam scanning electron microscope (FIB-SEM) imaging, and mercury intrusion porosimetry (MIP) techniques. Positron emission tomography (PET) diffusion experiments using $^{22}\text{Na}^+$ as a radiotracer are applied to analyze the anisotropy of the flow (flux) field at the length scale from millimeters to centimeters. A drill core (Sample BCL-1, sandy facies OPA, Mt. Terri, diameter 80 mm, length 50 mm) was cast in epoxy resin, and an axial blind hole (diameter 4 mm, length 35 mm) was drilled perpendicular to the bedding plane. The blind hole was filled with synthetic OPA porewater. Over eight days, we measured a sequence of 30 PET datasets (cf. Fig. 1A). We used the radial standard deviations of density as a proxy for the heterogeneity of the texture of the sedimentary rock (Fig. 1B). Owing to the voxel dimensions (μ -CT voxel size: $100 \times 100 \times 100 \mu\text{m}$), clay layers show a homogeneous density distribution, resulting in a low standard deviation of density. Contrarily, the density contrast of sandy laminae caused by clay matrix, coarse grains, and diagenetic lenses leads to higher values of the standard deviation of density. To calculate effective diffusivity based on PET datasets (Fig. 1C), we performed a three-step approach. First, we defined diffusion fronts *via* the corresponding activity values [Bq/voxel] at each time step (Fig. 1A). Second, we localized the resulting activity values in each voxel layer in the z-direction and calculated their displacement [mm] over time. Third, we calculated the apparent and effective diffusion coefficients.

RESULTS. We identified diagenetic and sedimentary subfacies components based on the concentration of diagenetic carbonates and sulfides and grain size variability, and quantified their pore size distributions and pore network geometries.^[1] Figure 1A shows the radial mean quantification of the PET tracer concentration after eight days of diffusion. The μ -CT texture quantification (Fig. 1B) shows that the fast diffu-

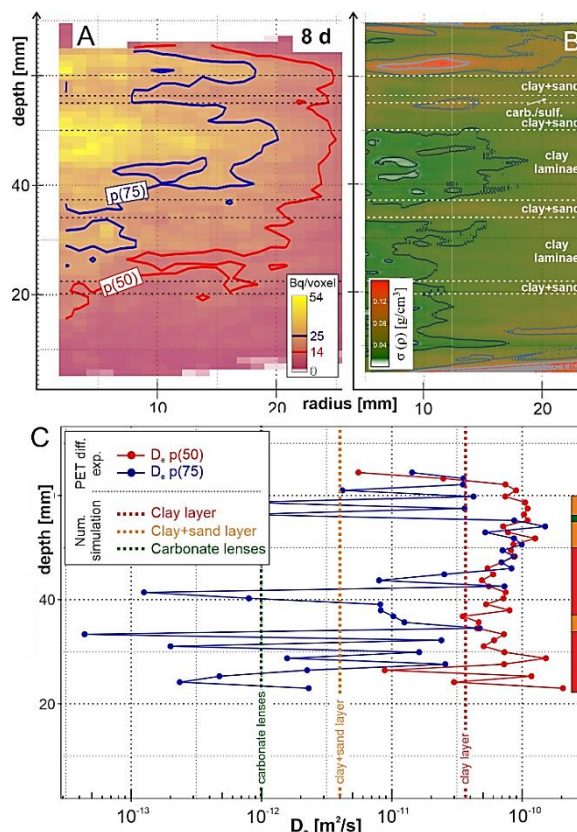


Figure 1. Radial mean values of the PET tracer concentration (A), radial mean density standard deviations (B) and effective diffusivities (C) derived from PET and μ -CT measurements along the core profile (the bar in Fig. C indicates the prevailing subfacies in the color code used for the respective calculated D_e values).

sion fronts at depth 60 mm and 40 mm to 50 mm are caused by different sedimentary and diagenetic textures. The standard deviation values between depth 40 mm and 50 mm are the lowest in the sample. This is indicative of a homogeneous clay texture. The effective diffusivities vary over three orders of magnitude at small scales (Fig. 1C). This is important for prognostic problems and the question is raised whether and on which length scale a convergence of the diffusivity occurs, which is decisive for simulations on the field scale.

This study shows how to combine three important steps for a robust migration analysis: (i) a workflow of general applicability for cross-scale identification of pore network data in argillaceous rocks, (ii) application of the pore network data for the numerical analysis of diffusive transport,^[2] and (iii) validation of numerical results *via* combined PET- μ -CT diffusion experiments.

ACKNOWLEDGEMENTS. The authors gratefully acknowledge funding by the German Federal Ministry of Education and Research (BMBF), grant 02NUK053B, and the Helmholtz Association, grant SO-093 (iCross).

[1] Bollermann, T. et al. (2022) *Chem. Geol.* **606**, 120997.

[2] Yuan, T. and Fischer, C. (2022) *Appl. Geochem.* **146**, 105478.

An upscaling workflow from the pore scale to the core scale to model diffusive flux

T. Yuan, C. Fischer

Molecular diffusion is an important transport mechanism for radionuclide migration in low-permeable argillaceous host rock such as Opalinus Clay (OPA). In this study, the influence of sedimentary and diagenetic heterogeneity on heterogeneous diffusion in sandy facies of OPA (SF-OPA) from lamina scale to drill core scale is investigated using a modeling workflow for upscaling diffusive transport from the pore scale to the core scale. Our numerical results based on a simplified structural model show fast diffusion fronts in clay laminae and slow diffusion fronts in carbonate lenses and sand laminae, demonstrating the endmembers of heterogeneous diffusion patterns in SF-OPA. Moreover, our results show that the diffusion fronts begin to homogenize after several days of diffusion with a specific influence of carbonate lenses geometry. This example illustrates how material heterogeneities affect heterogeneous diffusion on a small temporal and spatial scale.^[1]

NUMERICAL. We use the diffusion-sorption equation to describe diffusive transport of a solute in porous media. Effective diffusion coefficients of shales are determined based on multiscale digital rock models, including segmented pore network information derived from focused ion beam scanning electron microscopy (FIB-SEM) and computed tomography (CT).^[2] We simulated the heterogeneous diffusion at the core scale by applying the various effective diffusivities of different subfacies components to a simplified structural model based on the μ -CT analysis (Fig. 1). Specifically, the diffusive propagation of the $^{22}\text{Na}^+$ radiotracer has been modeled. Details of the experiments used for validation are provided elsewhere.^[3]

RESULTS. Sensitivity studies demonstrated that the dimension of sedimentary and diagenetic material at the mm to cm scale has a remarkable quantitative influence on the temporal and spatial evolution of the heterogeneous diffusion patterns in SF-OPA at the core scale. Another controlling factor affecting the homogenization time is the composition of sedimentary and diagenetic material. Using four compositional endmembers, we showed the generalized diffusion behavior in SF-OPA lithologies. Our case studies that included mm- to cm-sized carbonate concretions, the occurrence of carbonates arranged planar and parallel or transverse to the lamination, as well as the occurrence of sandy layers of different thickness within the clayey normal facies provided a first quantitative impression of the temporal and spatial diffusion contrasts. Homogenization of diffusive flow patterns occurs in the cm range after a period of tens to hundreds of days. This implies that already facies variability at the mm scale causes at least one order of magnitude difference with respect to the path length needed for homogenization. Common thick sedimentary layers and diagenetic precipitates will lead to even higher contrasts. Moreover, orders of magnitude of compositional heterogeneity still remain between the heterogeneity studied here and the field-scale consideration of large-scale stratification that is meters thick and hundreds of meters extended, which must be considered for upscaling generalized continuum-scale models.

[1] Yuan, T. and Fischer, C. (2022) *Appl. Geochem.* **146**, 105478.
 [2] Yuan, T. and Fischer, C. (2021) *Transp. Por. Med.* **138**, 245–264.
 [3] Bollermann, T. et al. (2022) *Chem. Geol.* **606**, 120997.

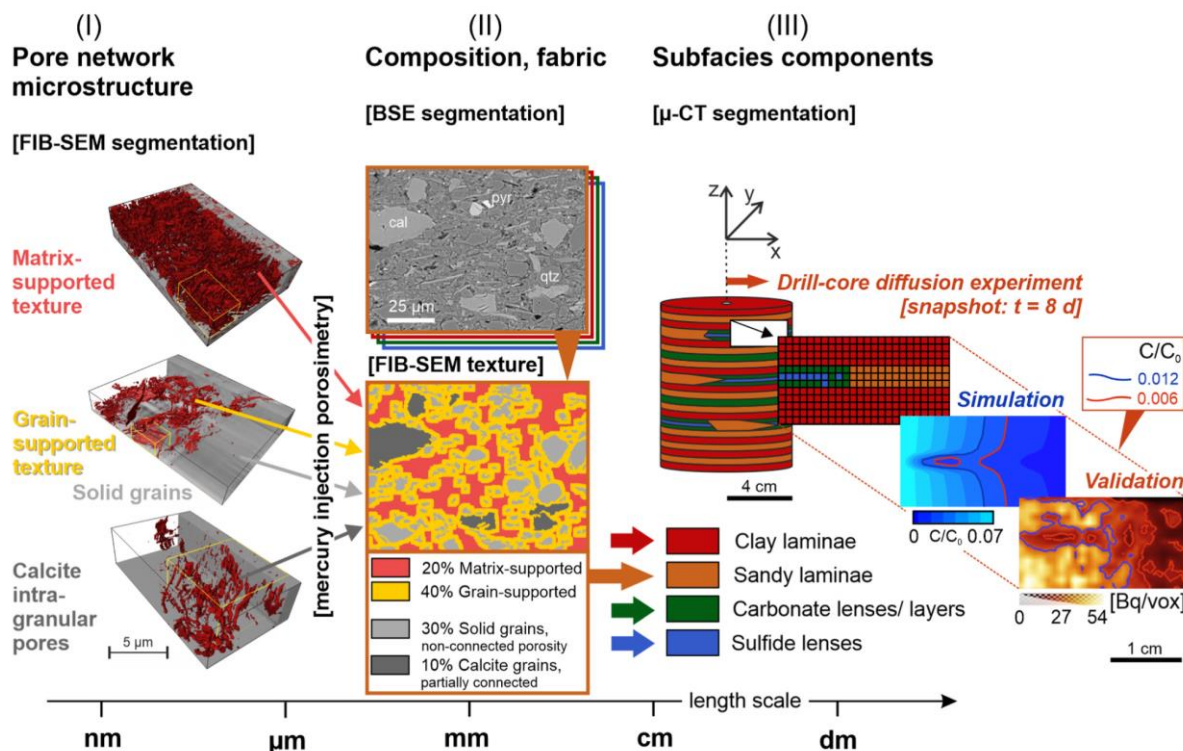


Figure 1. Schematic overview of the cross-scale approach for analysis of diffusive transport in complex rock materials. This includes analysis of the pore network and composition towards the quantification of diffusivity using multi-scale digital rock models (I and II)^[1] and core-scale modeling and validation with a PET diffusion experiment (III).^[3] To validate the numerical simulation results at the core scale, the measured activity of the positron-emitting radiotracer $^{22}\text{Na}^+$ is shown as a relative concentration (C/C_0 , C_0 is the initial concentration) and compared with the numerical results.

Water uptake by cement analyzed with positron emission tomography

J. Kulenkampff, A. Reiss,¹ S. Gruhne, D. Lösel

¹Hebrew University of Jerusalem, Israel

Dry cement paste shows rapid imbibition in contact with water. The water transport in the cement has implications for the durability of buildings and infrastructure, and for the tightness and integrity of cement-based barriers. Quantifying this rapid process requires detecting trace amounts of water in a dense and opaque material. We were able to monitor the water imbibition with a temporal resolution of 2 minutes using positron emission tomography (GeoPET). A significant portion of the water immediately penetrated into the cement during the course of the first PET-frame. The initial propagation of the front was 2 mm/min for about 30 min, followed by slow equilibration over two days. The propagation proceeded homogeneously, without significance for preferential zones.

EXPERIMENTAL. A cylindrical core (50 mm diameter and length) of Ordinary Portland cement paste (CEM 1) had been cast at BGU, Israel, and matured for about six months. Before the experiment, ~5 mm from the top of the sample was saw-cut to expose a fresh surface. Then it was oven-dried for one week at 60 °C.

A pressure container made of POM (Polyoxymethylen) and end plugs were manufactured in our machine shop. The sample was fixed between the end plugs and coated with shrinking tube. Bores in the end plugs serve as fluid reservoirs. This setup allows conducting experiments with the tracer encapsulated in the pressure container that serves as a second containment in case of leakage.

We injected 5 mL of 10^{-5} Mol $[^{124}\text{I}]\text{NaI}$ with an activity of 5.05 MBq into the top reservoir. The initial fluid level in the reservoir was ca. 5 mm.

The GeoPET scanner was started within seconds after injection and the sample was initially scanned continuously for 3 h, followed by less frequent scanning in order to record the equilibration process.

From the original PET frames with a duration of 20 min and more, we subdivided the first twenty minutes into frames with overlapping steps of 1 min and a length of 2 min, in order to resolve the initial phase. The image reconstruction applied the μCT -image of the whole setup as a reference for attenuation and scatter correction. We thus computed 17 “long” frames over a period of two days and 20 “short” frames over the initial period of 20 min.

RESULTS. The PET images show generally homogeneous propagation of the tracer into the material. This is also suggested by the homogeneity of the sample that was verified with μCT . It shows no significant density variations, only sporadic dispersed air bubbles (Fig. 1).

We thus considered for further analysis the depth profile of the tracer concentration integrated over the cylinder cross sections (activity per depth unit) (Fig. 2).

From these profiles we are able to estimate the initial propagation rate of 2 mm/min and the later equilibration time which is in the order of one day. It apparently results in a stationary decreasing humidity profile over the length of the sample.

Thus, having demonstrated the applicability of the method for the study of both fast and slow migration of tracers, it is ready now for research on cementitious material with a

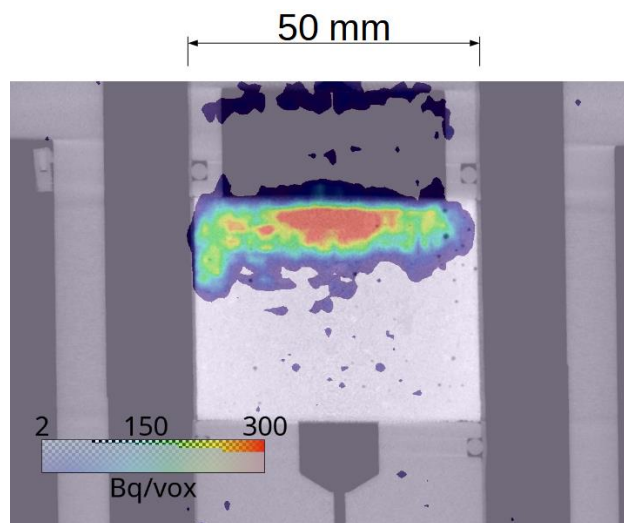


Figure 1. Cross section of the GeoPET/ μCT -Overlay of the cement sample in the pressure vessel. The PET-frame was recorded during 20 minutes after filling the chamber at the top with 5 mL $[^{124}\text{I}]\text{NaI}$, activity 5.05 MBq. Voxel size μCT : 75 μm , PET: 1.15 mm.

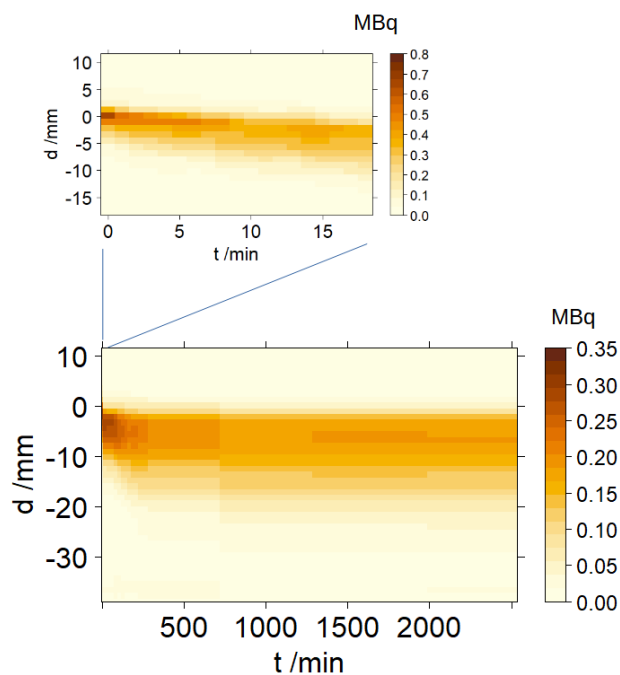


Figure 2. Activity integrated over transaxial slices vs. depth (d) and time (t). Original full-length data frames (bottom), first 20 min subdivided into 2 min frame duration (top).

broad scope of applications, like solution attack on building material, or propagation of radionuclides in nuclear waste repositories.

A workflow from real rock samples to K_d values and their distribution – Combining measurements of rock heterogeneities with reactive transport modeling

S. Pospiech, F. Bok, V. Brendler

The safety case of a nuclear waste repository in granitoid host rocks involves realistic predictions of radionuclide migration in the far-field, *i.e.*, beyond the geotechnical barrier. In crystalline rocks, fluids preferentially flow through fractures, fault systems, and open cracks, but can also migrate through weakzones in the rock, such as microcracks, calcite veins, alteration zones and mica bands. As the composition of mineral surfaces along fluid migration paths can significantly differ from the average composition of the rock as a whole, deriving the sorption properties of a geologic body requires geostatistical techniques to estimate the average composition of the mineral surface and its variability along migration paths. Here, we present a geological microstructure model based on graph theory techniques. This is the one step in the workflow that links lithology with geochemical modeling for the sorption data.

The far-field of a deep geological repository has so far been strongly simplified for the reactive transport models; among other things, the mean values for the total rock volume is used for the mineralogical composition. However, since rocks are inhomogeneous and anisotropic by nature they have a spatial variation in modal mineral composition and/or other parameters such as grain sizes, assemblages, *etc.* This can lead to under- or overestimation of the sorption properties of the rock. Incorporating the spatially varying rock composition into the reactive transport models, particularly modal mineralogy along fluid migration pathways at the various scales, would greatly improve the estimation of radionuclide retention potential. The workflow we suggest comprises two major steps: First, the rock analysis and transfer of the data into a model to retrieve modal mineralogy along migration paths, and second, the calculation of sorption as a function of fluid composition, sorption models for the respective mineral surfaces, and data like fluid/rock ratio, Eh, pH, *etc.*

METHOD. For the rock analysis eight thin section samples from several drill cores from granitic and gneissic units of the Habach series (Austrian Alps, Tauern Window) were used. These were measured using Mineral Liberation Analysis (MLA), a technique that combines high-resolution back-scattered-electron (BSE) imaging with energy-dispersive spectroscopy and machine learning (ML) algorithms to interpret the thin sections in terms of mineral phases and their spatial distribution (Fig. 1). These data are stored in databases along with all geometric properties of the mineral grains and their associations. From this databases graphs can be calculated very easily: Each vertex stores the information about the mineral phase (or void) and the grain size and each edge stores the information about the mineral grains' contact length. Migration paths can then be described by a subgraph connecting any starting grain A and any ending grain B of the path (Fig. 1). The migration path can be defined by only allowing certain types of vertices, *e.g.*, type "void", "clay mineral" or "alteration mineral", which then finds all potential pathways – even if not directly visible to the human eye – inside the rock.^[1]

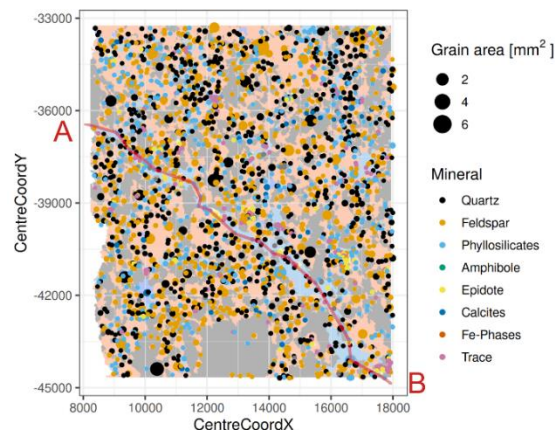


Figure 1. Detail of a thin section scan of a gneiss from the Habach series. Mineral phases were derived by the ML supported MLA software. A false colored image of the BSE constitutes the background, while the geometric data like grain coordinate and grain size are shown as points. A and B indicate the starting and end point of a subgraph, the red line is the visualization of the subgraph, spanning several vertices.

Table 1. Modal mineralogy according to Fig. 1: "Total" refers to full picture, "Path" to minerals of the subgraph connecting A and B. Qz: quartz, Fsp: feldspar, Mu: muscovite, Ep: epidote, Cc: calcite, Fe: Fe-phases.

[%]	Qz	Fsp	Mu	Ep	Cc	Fe	Trace
Total	31	59	7.6	0.63	0.98	0.26	0.52
Path	24	21	52	2.30	0	0.23	0.47

RESULTS. The modal mineralogy of the exposed surface along the fluid migration path is calculated according to information about contact length between minerals stored in the edges of each vertex along the path. In the example given in Fig. 1, the modal mineralogy along the path considerably diverts from the average composition of the selected part of the thin slice (Tab. 1).

This shows exemplarily, that the amount Illite/Muscovite – having a considerable effect on the sorption – clearly varies along this inconspicuous mica band, which is the most probable natural pathway, as opposed to the mineralogical composition of the total rock. These graph-inferred modal mineralogies and their variability can then be used as input to the geochemical models, *e.g.*, by using the sorption models of mineral surfaces provided by the RES³T database.^[2]

ACKNOWLEDGEMENTS. This work was funded by the European Union's Horizon 2020 research and innovation programme (DONUT WP within EURAD, no.847593). We thank G. van den Boogaart, R. Tolosana-Delgado, K. Bachmann, A. D. Renno and J. Krause from the Helmholtz Institute Freiberg for their great support in helping with geostatistical and analytical methods as well as providing the samples for real data. All plots and calculations where done with the programming language R.^[3]

[1] Hillier, M. *et al.* (2021) *Math Geosci* **53**, 1725–1749.
 [2] RES³T-Rosendorf Expert System for Surface and Sorption Thermodynamics, www.hzdr.de/res3t.
 [3] R Core Team. (2019) *R Foundation for Statistical Computing*. <https://www.R-project.org/>.

Sorption Reference Database SOREDA – General principles and mineral site density calculations

S. Zechel, F. Bok

In contrast to developments in the field of thermodynamic databases for aqueous species and solid phases, there are still no international database projects with respect to quality assured surface complexation data (SCM). This is due to the scattering of SCM data across a variety of incompatible surface complexation models and different sets of surface chemical species, as well as the need for a consistent logical linkage of the necessary information: Site density, protolysis and sorption reaction data. The Sorption Reference Database project SOREDA addresses these challenges by re-evaluation of published experimental sorption data in a self-consistent way to create reliable and robust sorption models.

Main goal of the SOREDA project is to create quality assured SCM datasets to describe the sorption of various radionuclides on several common mineral phases like iron(II/III)-(hydr)-oxides, clay minerals, carbonates, quartz and pyrite. To do so, raw data from published sorption experiments will be assessed and used to re-fit the reaction constants for protolysis and sorption reactions. If possible, results of spectroscopic investigations will be used to build up models on the basis of chemically validated surface species.

SITE DENSITY. The surface site density (SSD) per area is a fundamental, mineral-specific parameter of the SCM upon which all sorption reactions are based. In the literature, besides experimental methods (*e.g.*, tritium exchange), other procedures for SSD determination can be found, which vary from crystallographic calculations over estimations to treatment of SSD as a fit parameter. This caused large scattering in SSD data even for just one mineral considered. For example, SSD values ranging from 2.31 nm^{-2} up to 11.4 nm^{-2} can be found for quartz.^[1] Within this project, for each considered mineral the SSD shall be obtained using a crystallographic calculation approach being described on the example of quartz. Based on the SSD values, secured protolysis data should be generated. This approach reduces the otherwise existing strong correlation between SSD and protolysis values ($\text{p}K_{\text{a}1,2}$).

CALCULATION. Crystallographic literature data for quartz were collected and evaluated, considering only measurements at $T = 25^\circ\text{C}$ and atmospheric pressure.^[2] Surface planes were predicted by BRAVAIS-FRIEDEL-DONNAY-HARKER (BFDH) morphology calculations using the Mercury software code.^[3,4] The obtained results match with the most common surface planes for quartz which are (100), (101) and (011) as well as their symmetric equivalents.^[5] Quartz in nature, and especially within the overburden body, is not expected to form perfectly crystallized, single habits, but rather multiple intergrown crystallites. Minor crystal faces, which occur only occasionally and with small areal ratios, were omitted.

Using crystallographic data the positions of interfacial oxygen atoms were calculated for each surface plane. There, surface unit cells delimited by four crystallographically identical oxygen atoms were defined and the number of all surface oxygen atoms within the unit cell was determined. As surface oxygen positions are expected to be identical to the positions of silanolic binding groups at the quartz surface

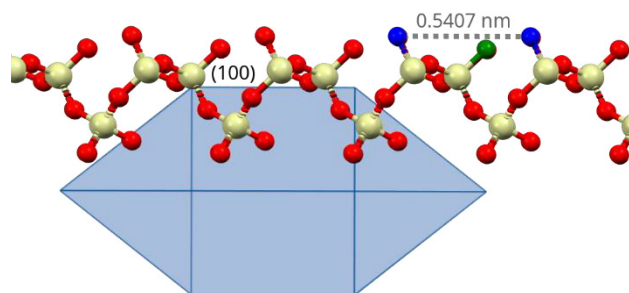


Figure 1. Calculated quartz morphology (■) and surface structure of (100) plane.^[2-4] Blue: oxygen atoms bordering the surface unit cell, Green: oxygen atoms within the surface unit cell.

(Fig. 1), the site density was calculated for each plane using the outermost singly bound oxygen atoms. For an overall SSD value the weighted mean using the relative area ratios was determined.

RESULTS. The obtained SSD for the single quartz surface planes as well as the overall SSD value are given in Tab. 1. The result is comparable with the literature data with a mean SSD value of $5.41 \pm 1.37 \text{ nm}^{-2}$.^[1] Depending on the growth-related length variation of the crystallites, different faces become dominant which results in a variation of the SSD in the range between 5.57 and 7.52 nm^{-2} .

Table 1. Quartz surface planes with relative area ratios and calculated site density.

Plane	Relative area	Site density
(100),(-100),(010),(0-10),(1-10),(-110)	6×0.082	7.52 nm^{-2}
(011),(01-1),(0-11),(0-1-1),(101),(10-1),(-101),(-10-1),(1-11),(-1-1-1),(1-1-1),(-111)	12×0.042	5.57 nm^{-2}
Weighted (by relative area) mean:		6.54 nm^{-2}

CONCLUSIONS. This approach will be conducted for all minerals relevant in SOREDA to generate SSD values with a crystal-chemical background suitable to better represent the molecular process understanding in models. Building on these SSDs, consistent thermodynamic protolysis and sorption data will then be generated and made available in a digital database. In combination with SCM data of spectroscopically evident surface species, it should be possible to build low-parameter but robust sorption models that have a high degree of extrapolability.

ACKNOWLEDGEMENTS. SOREDA is funded by the Federal Company for Radioactive Waste Disposal (BGE; contract no. E-FuE-21-03-js).

- [1] RES³T – Rossendorf Expert System for Surface and Sorption Thermodynamics, Helmholtz-Zentrum Dresden-Rossendorf, www.hzdr.de/res3t, accessed: 2022-11-01.
- [2] Nikitin, A. N. *et al.* (2007) *Crystallogr. Rep.* **52**, 428–435.
- [3] Donnay, J. H. *et al.* (1937) *Am. Mineral.* **22**, 446–467.
- [4] Macrae, D. F. *et al.* (2020) *J. Appl. Cryst.* **53**, 226–235.
- [5] Hazen, R. M. (2004) in: *Progress in biological chirality*, 137–151, Elsevier, Oxford.

Thermodynamic database for Europium: procedures, guidelines, and recommended values

N. Jordan, T. Thoenen,¹ S. Starke,² K. Spahiu,³ V. Brendler

¹Paul Scherrer Institut, Waste Management Laboratory, Switzerland; ²Computational Science Group (FWCC), Department of Information Services and Computing (FWC); ³Swedish Nuclear Fuel and Waste Management Co (SKB), Stockholm, Sweden

An extensive literature review of thermodynamic data for Europium compounds of sulphate, chloride, and phosphate has been performed. It concerns both aqueous complexes and amorphous/crystalline solid phases. The critically assessed data have been processed to obtain thermodynamic data for the standard state (1 bar, 25 °C), along with ion interaction coefficients $\epsilon(j;k)$ applicable for the Specific Ion Interaction theory (SIT) approach.

Our society is facing a steadily increasing demand for high technology products, many of them incorporating Rare Earth Elements (REE). The growing demand for these elements simultaneously meets a significant shortage on the free global market, creating the need for improved REE production and recycling. Accurate and reliable thermodynamic data are mandatory for respective optimizations. Namely for Europium, several reviews and systematic studies focusing on the aqueous chemistry are available.^[1-6] Complexation constants were determined by very different techniques such as solvent extraction, potentiometry, ion exchange, calorimetry, and spectroscopies (fluorescence, UV-vis). However, the different experimental conditions (ionic strength, temperature, europium concentration, pH range, etc.) and methodologies had negative consequences on both consistency and accuracy. Thus, a thermodynamic database project for Eu was initiated.

DATA SELECTION AND PROCESSING. An extensive data survey of more than 120 peer-reviewed publications from around 1900 until June 2021 was performed. Furthermore, technical reports, scientific books, collected editions as well as various thermodynamic databases (Nagra/PSI,^[1] Thermochemie,^[7] etc.) were surveyed to identify their original Eu(III) data sources and references used therein. Data up to 90 °C and 5M ionic strength were selected for screening, but all data dealing with hydrothermal conditions were out of the scope of this review. Thermodynamic data determined in non-aqueous solvents were explicitly not considered either. This screening provided a nominally high number of data records for the above mentioned subset of aqueous Eu complexes, (Tab. 1).

Table 1. Summary of the aqueous inorganic Eu complexation data records.

System	#total	#selected
Eu – sulphate	244	34
Eu – chloride	186	0
Eu – phosphate	40	8

However, many of them had to be discarded, mainly due to the following reasons:

- Incomplete description of experimental conditions
- Use of pH buffers acting as complexants
- Absence of corrections for pH measurements at elevated ionic strengths
- No original data but rather analogue values from other REE or compilations from secondary references
- Missing details for extrapolation to infinite dilution

- Postulation of species not independently evidenced by means of advanced spectroscopic techniques
- Too high reliance on the analogy with trivalent actinides
- For weak complexes such as chloride, inappropriate handling of changes in the activity coefficients due to the replacement of up to 100 % of the background electrolyte anion (most often ClO_4^-) by Cl^-

The remaining selected experimental data were processed adapting the Thermochemical Database Project of the Nuclear Energy Agency (NEA TDB) method to determine the $\log_{10} \beta^\circ$ value for standard conditions.^[8] First, consistency checks had to select those data records that actually could be grouped because they operated on similar species sets. Then the $\log_{10} \beta$ values for the species formation reaction were plotted as a function of ionic strength using Eq. 1 to obtain $\log_{10} \beta^\circ$ values and SIT ion interaction parameters.

$$\log_{10} \beta - \Delta z^2 D - n \log_{10} = \beta^\circ - \Delta \epsilon I_m \quad (1)$$

Before such fitting exercises reasonable errors had to be assigned, avoiding unrealistic low values given in some papers. If no experimental uncertainty was reported, an assumption had to be made to assign a reasonable value. Assigning high uncertainties above 0.6 would render respective values irrelevant for the fit within the SIT procedure. Therefore, as a pragmatic compromise, the assigned uncertainty was set to be $\log_{10} \beta \pm 0.3$, what turned out to be a practicable solution. The weighting of any data point was set to the reciprocal individual error variances $1/\sigma^2$. This setting yields the best linear unbiased estimator for the regression parameters.^[9]

If available, $\epsilon(j;k)$ values recommended by the NEA TDB at 25 °C were used.^[8] Unfortunately, the NEA TDB does not provide any specific value for $\epsilon(\text{Eu}^{3+};\text{Cl}^-)$ or $\epsilon(\text{Eu}^{3+};\text{ClO}_4^-)$. Here, we opted for a direct determination of the missing interaction coefficients based on experimental isopiestic data.^[10] The ion interaction coefficients $\epsilon(j;k)$ were kept constant in the 25 to 90 °C temperature range. We invite the readers to look at Jordan *et al.* for further details about applied procedures.^[10]

RECOMMENDED VALUES. The complexation of Eu(III) with sulphate was investigated by ion exchange, solvent extraction, spectrophotometry, electrophoresis, and time resolved laser-induced fluorescence spectroscopy.^[10] Despite the broad variety of methods used for the determination of the conditional complexation constants of the Eu(III) sulphate species in the literature, a consistent set of data was obtained for both EuSO_4^+ and $\text{Eu}(\text{SO}_4)_2^-$ aqueous complexes.^[10] The extrapolation to infinite dilution for the EuSO_4^+ complex is exemplarily shown in Fig. 1.

Chloride complexes with Eu(III) are very weak, and high chloride concentrations are needed to form them. Related experiments need to be considered with extra care because the perchlorate ion was systematically substituted by the chloride ion by more than 10%, and in some cases even completely.

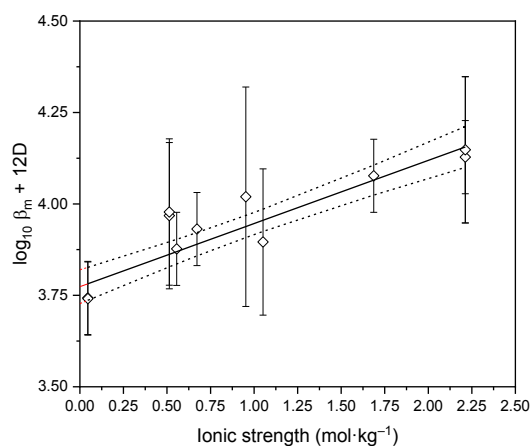


Figure 1. Linear SIT regression plot for the EuSO_4^+ complex at 25°C (in NaClO_4 medium).

However, the resulting changes in the activity coefficients due to such large compositional modifications of the background electrolyte were simply ignored. Hence, Spahiu and Puigdomènech proposed to use the pure background electrolyte (e.g. HClO_4) at an ionic strength I as a reference state, in order to obtain an expression for activity coefficient changes in mixtures (e.g. HCl-HClO_4) at the same ionic strength.^[11] This methodology enables to account for changes in the composition of the ionic medium and to treat variation in the activity coefficient in a satisfactory way. As it can be seen in Fig. 2, our recalculation based on the exclusive consideration of changes in activity coefficients without considering the formation of three Eu-chloro complexes as proposed in the original study, are able to describe the experimental data of Sekine *et al.*^[12] This means that the formation of Eu(III)-chloro complexes postulated in the experiments of Sekine *et al.* was an artefact.^[10]

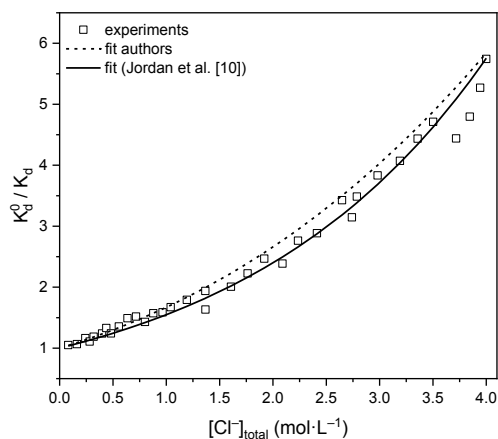


Figure 2. Experimental data obtained in $I_c = 4.0 \text{ mol L}^{-1}$ HCl/HClO_4 mixtures by Sekine *et al.* plotted against the total concentration of chloride ions.^[12] The dotted line corresponds to the fit of the original paper, with the formation of three Eu-chloro complexes but no consideration of changes in activity coefficients. The solid line was recalculated in Jordan *et al.* by considering changes in activity coefficients with no formation of Eu-chloro complexes.^[10]

Unfortunately, very little is known concerning the complexation of Eu(III) with phosphate ions. The only experimental study was performed in 2018 by Jordan *et al.* by means of laser-induced luminescence spectroscopy at 25°C and at different ionic strengths (0.6–3.1 mol L^{-1}) imposed by NaClO_4 .^[13] The impact of temperature up to 80°C on the

formation of the $\text{EuH}_2\text{PO}_4^{2+}$ complex was also investigated.^[13]

The recommended complexation constants ($\log \beta^0$) for Eu(III) aqueous complexes with sulphate and phosphate derived by Jordan *et al.* at 25°C are listed in Tab. 2.^[10]

Table 2. Recommended complexation constants ($\log \beta^0$) at 25°C derived in Jordan *et al.* [10]

Reaction	$\log_{10} \beta^0$
$\text{Eu}^{3+} + \text{SO}_4^{2-} \rightleftharpoons \text{EuSO}_4^+$	3.77 ± 0.02
$\text{Eu}^{3+} + 2 \text{SO}_4^{2-} \rightleftharpoons \text{Eu}(\text{SO}_4)_2^-$	5.38 ± 0.07
$\text{Eu}^{3+} + \text{H}_3\text{PO}_4 \rightleftharpoons \text{EuH}_2\text{PO}_4^{2+} + \text{H}^+$	0.89 ± 0.08

CONCLUSIONS. The data selection and processing methodology described here yielded the so far most comprehensive and reliable thermodynamic database for Eu complexes with sulphate, chloride, and phosphate ligands. These recommended values will be included in international thermodynamic databases, which can be used with different very commonly applied geochemical modeling software (PHREEQC, The Geochemist's Workbench, etc.). Currently, the database is expanded towards aqueous Eu(III) complexes and solid phases with hydroxides, carbonates, nitrate, and fluoride.

Eventually, a deeper understanding of the chemistry of europium provided by an increasing number of high-quality thermodynamic data will generate a large effect not only directly concerning europium itself but also e.g., for the whole REE group (alone or as part of more elaborate correlations such as linear free energy relationships), where Eu can be used as an analogue. This analogy also stretches into the realm of the chemistry of the trivalent actinides contributing considerably to the concern about the long-term safety of nuclear waste repositories.

- [1] Hummel, W. *et al.* (2002) Nagra/PSI Chemical Thermodynamic Data Base 01/01, Nagra Technical Report, NTB 02–16, Nagra, Wettingen, Switzerland.
- [2] Rard, J.A. (1985) *Chem. Rev.* **85**, 555–582.
- [3] Rard, J.A. (1987) Update of the europium data base, LLNL Internal Memo.
- [4] Spahiu, K., Bruno, J. (1995) A selected thermodynamic database for REE to be used in HLNW performance assessment exercises. Swedish Nuclear Fuel and Waste Management Co, Stockholm, 91 pp.
- [5] Wood, S.A. (1990) *Chem. Geol.* **82**, 159–186.
- [6] Brown, P. L., Ekberg, C. (2016) *Hydrolysis of Metal Ions*, Vol. 1, Wiley-VCH, Weinheim.
- [7] Giffaut, E. *et al.* (2014) *Appl. Geochem.* **49**, 225–236.
- [8] Grenthe, I. *et al.* (2020) Second Update on the Chemical Thermodynamics of Uranium, Neptunium, Plutonium, Americium and Technetium. Chemical Thermodynamics Volume 14, OECD Publications, Paris.
- [9] Rencher, A.C., Schaalje, G.B. (2008) *Linear models in statistics*, 2nd ed., Wiley.
- [10] Jordan, N. *et al.* (2022) *Coord. Chem. Rev.* **473**, 214608.
- [11] Spahiu, K., Puigdomènech, I. (1998) *Radiochim. Acta* **82**, 413–419.
- [12] Sekine, T. *et al.* (1967) *Bull. Chem. Soc. Jpn.* **40**, 251–254.
- [13] Jordan, N. *et al.* (2018) *Inorg. Chem.* **57**, 7015–7024.

SCIENTIFIC CONTRIBUTIONS (PART III)

Biological Systems

Long-Lived Radionuclides in
**BIOLOGICAL
SYSTEMS**

Interaction of U(VI) with *Nicotiana tabacum* cells – Endocytosis contributes to the uranium(VI) uptake under phosphorous-deficient conditions

W. A. John, B. Lückel, N. Matschiavelli, R. Hübner,¹ S. Matschi,² W. Hoehenwarter,² S. Sachs

¹HZDR, Institute of Ion Beam Physics and Materials Research, Dresden, Germany; ²Leibniz Institute of Plant Biochemistry, Halle/Saale, Germany

Endocytosis contributes to a considerable extent to the uranium (U) uptake in *Nicotiana tabacum* (BY-2) cells. U is likely transported to and stored in the vacuole, providing a physiologically safer pathway for the plant than U transport through the cytosol.^[1]

Radionuclides (RNs) such as uranium (U) are non-essential elements for plants. However, if present in contaminated soil, they can be taken up into plant tissue using transport mechanisms of essential nutrients. Hence, they can enter the food chain and pose a health risk to humans.

Broad-spectrum ion channel transporters, such as the iron-regulated transporter 1, regulate the influx of a variety of metals into plants, making them potential entry points for RNs.^[2] There are indications for the uptake of U into plants by calcium ion channels.^[3–5] In addition to transporter-mediated uptake, metal uptake by endocytosis has been demonstrated not only for essential but also for non-essential metals, *e.g.*, aluminum and lead.^[6,7] It has also been suggested, but not yet verified, that endocytosis may play a role in the uptake of U.^[8] We therefore studied U uptake by endocytosis in tobacco BY-2 cells by a combination of biochemical methods, microscopy and spectroscopy, complemented by proteomics.^[1] Here, we focus on the biochemical and microscopic study of endocytosis-mediated U uptake. For this purpose, endocytosis of the cells was blocked using wortmannin. The U uptake in the cells was examined using transmission electron microscopy (TEM) coupled with energy-dispersive X-ray spectroscopy (EDX).

EXPERIMENTAL. 4.5 mL of a 96-h BY-2 culture in MS medium were transferred to three Erlenmeyer flasks containing 30 mL MS_{red} medium with a reduced phosphate content. One of these cultures was exposed to 33 μM wortmannin (Sigma-Aldrich) for 30 minutes to inhibit endocytosis of the cells. After that 20 μM UO₂(NO₃)₂ were added to the wortmannin-treated cells and a second flask of MS_{red} culture. The third sample remained as control. After 6 h of incubation, the cells were separated from the culture medium and washed. Subsequently, they were digested and their U content was measured by inductively-coupled mass spectrometry. To visualize the U uptake into the cells, TEM-EDX measurements were performed. Experimental details can be found in our publication.^[1]

RESULTS. Figure 1A shows the U content of the U-exposed cells in comparison to the control. The wortmannin-treated cells exhibited a significant decrease in bioassociated U, *i.e.*, surface-bound and accumulated U, compared to the wortmannin-untreated cells, with a decrease of 14%. Applying FM4-64TM, a fluorescence dye which is able to bind to the plasma membrane and be internalized during endocytosis, we demonstrated by fluorescence microscopy that the presence of U does not inhibit endocytic processes, whereas wortmannin acts as an inhibitor. To verify this observation, the levels of proteins responsible for vesicular uptake *via* clathrin-mediated endocytosis were analyzed in U-exposed and non-exposed cells by proteomics. A U-induced change in the clathrin heavy chain variant expression was found, suggesting a shift in the type of endocytosis that occurs.

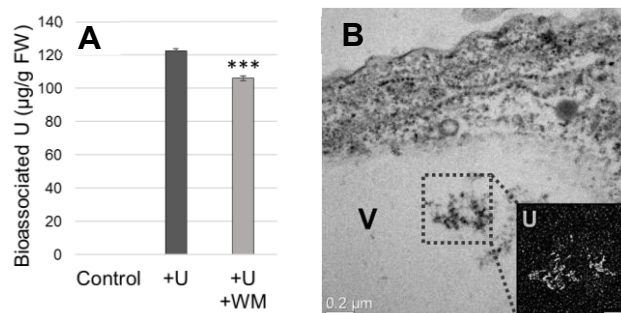


Figure 1. Bioassociated U in BY-2 cells (control, cells exposed to 20 μM U, or wortmannin (WM) and 20 μM U). Error bars represent the standard error of the mean of three measurements of one biological replicate. ***: $p < 0.001$, statistical significance between +U and +U+WM; FW: fresh weight (A). Bright-field TEM image and U-mapping of needle-like structures (EDX) of BY-2 cells exposed to 20 μM U for 24 h (B). V: vacuole; scale bar in EDX image: 100 nm.^[1]

However, the rate of endocytosis remained largely unchanged.

To localize U in the cells, conventional bright-field TEM along with scanning-TEM based EDX measurements were performed on BY-2 cells exposed to 20 μM U for 24 h. The images obtained revealed the occurrence of dense needle-like structures in most likely vacuolar/late endosomal compartments (Fig. 1B). EDX analyses showed that these objects consist of U, which is co-localized with phosphorous and oxygen. Unexpectedly, no U signals were detected at the cell surfaces (plasma membrane, cell wall), which may be due to the fact that loosely bound U was washed away by the TEM preparation process, making the adsorbed U too little to be detected. These microscopy results indicate accumulation of U in the vacuole and suggest uptake mechanisms resulting in a deposition of U in vacuoles.

The results obtained allow the conclusion that besides transporter-mediated uptake, endocytosis contributes to the uptake of U into BY-2 cells under phosphorous-deficient conditions. The accumulated U is transferred to and deposited in form of U precipitates in the vacuole.

ACKNOWLEDGEMENTS. The authors thank Prof. P. Nick (Botanical Institute, KIT) for providing the first batch of BY-2 cells, J. Seibt, S. Beutner and S. Bachmann for experimental support. We thank Dr. F. Rajabi for her contributions to wortmannin treatment of BY-2 cells. This work was funded by the BMBF (grant No. 02NUK051B). Furthermore, we acknowledge the use of the HZDR Ion Beam Center TEM facilities and the funding of TEM Talos by the BMBF (grant No. 03SF0451) in the framework of HEMCIP.

- [1] John, W. A. *et al.* (2022) *Sci. Tot. Environ.* **823**, 153700.
- [2] Nishida, S. *et al.* (2011) *Plant Cell Physiol.* **52**, 1433–1442.
- [3] Rajabi, F. *et al.* (2021) *Ecotoxicol. Environ. Saf.* **211**, 111883.
- [4] Jessat, J. *et al.* (2022) *J. Haz. Mat.* **439**, 129520.
- [5] Sarthou, M. C. M. *et al.* (2022) *J. Hazard. Mater.* **424**, 127436.
- [6] Wu, D. *et al.* (2015) *J. Exp. Bot.* **66**, 6791–6801.
- [7] Hübner, R. *et al.* (1985) *Protoplasma* **129**, 214–222.
- [8] Wheeler, H. *et al.* (1971) *Science* **171**, 68–71.

Proof of microbially induced U(VI) reduction by different electron donors

A. M. Newman-Portela,¹ F. Bok, A. Kassahun,² M. L. Merroun,¹ J. Raff, E. Krawczyk-Bärsch

¹Department of Microbiology, University of Granada, Spain; ²WISMUT GmbH, Chemnitz, Germany

Numerous anthropogenic activities have left a large legacy of radionuclide- and heavy metal-contaminated environments over the last decades. Biostimulation of the native microbial community capable to reduce soluble U(VI) to insoluble U(IV) is a promising strategy for bioremediation of contaminated waters. The aim of this study is to investigate the potential of the indigenous microbial community of U (1.05 mg/L) contaminated mine water through its biostimulation using different electron donors (gluconic acid, vanillic acid and glycerol) in different experiments. The results showed how effectively soluble U(VI) was reduced when glycerol was used as an electron donor. Fermentative bacteria and bacteria related to the biogenic sulfur and iron cycle have played a key role in the reduction of U(VI) in this study.

EXPERIMENTAL. The chemical composition of the mine water from a former U mine in Saxony (Germany) was determined by Inductively Coupled Plasma-Mass spectrometry (ICP-MS) and Ionic Chromatography (IC). A set of microcosms was designed in 1L serum bottles, each filled with fresh mine water with a U(VI) concentration of 1.05 mg/L and separately doped with glycerol, gluconic acid and vanillic acid (10 mM) as electron donor. The microcosms were incubated at 30 °C for 4 months in dark conditions. The redox potential (E_H) and the pH were monitored each week, and aliquots were taken for determination of U, Fe, As, SO_4^{2-} concentration by ICP-MS and IC. At the end of the experiment, a black precipitate was observed at the bottom of the bottle using glycerol as electron donor. The geochemical data of the mine water were used to calculate the predominance fields of uranium species using the geochemical speciation code Geochemist's Workbench, version 16.0.40/Act2, in combination with the ThermoChimie thermodynamic database.^[1, 2] To study the bacterial community, 400 µL of microcosm water was filtered through 0.44 and 0.22 µm pore size membrane (MF-Millipore®, Germany). Subsequently, filters were frozen at -20 °C up to DNA extraction. Three technical replicates per sample were analyzed. The obtained DNA was then used for bacterial 16S rRNA gene amplification and sequencing at Blue Biolabs laboratories GmbH (Berlin, Germany).

RESULTS. ICP-MS and IC results showed significant differences in the concentrations of different ions at the beginning and at the end of the experiment (Tab. 1). Especially the ICP-MS results of U revealed a U(VI) reduction of ≈90% using vanillic acid and ≈99% using glycerol as electron donors. On the other hand, no reduction was observed using gluconic acid. The pH values ranged from neutral to slightly basic values (7.00 to 8.01). However, adding glycerol, the E_H of the mine water showed a sharp drop, from 139 mV to -246 mV. Based on the experimental conditions, the calculated thermodynamic model predicted U(VI) reduction and the formation of uraninite or an amorphous U(IV) hydroxide phase, respectively. As for the bacterial community, the mine water was initially characterized by the genera *Sulfuricurvum*, *Sulfurimonas* and an unidentified genus of the family *Gallionellaceae*. At the end of the experiment in glycerol-doped microcosms, changes were observed in the microbial

Table 1. Geochemical parameters observed in the original mine water and at the end of the experiment after the electron donor biostimulation (glycerol, vanillic acid and gluconic acid). Data presented in mg/L and E_H in mV.

	Original mine water	Glycerol	Vanillic acid	Gluconic acid
pH	7.32	7.99	7.00	8.01
E_H	139	-246	218	-248
Ca	115	111	133	134
Mn	1.44	0.50	1.63	1.60
Fe	0.99	0.05	0.32	0.35
As	0.92	0.46	0.40	0.17
U	1.05	0.01	0.10	1.37
SO_4^{2-}	335	141	338	144

community, which rapidly became dominated by the genera *Paracoccus*, *Clostridium*, *Desulfovibrio* and *Chloroflexi*.

CONCLUSIONS. Biostimulation of the native microbial community is a promising alternative to conventional U remediation technologies. The addition of an electron donor such as glycerol to the mine water could enhance the biostimulation and results in an effective reduction of U(VI) by forming uraninite. Changes in the microbial community induced by the presence of glycerol have contributed to the growth of bacterial groups previously reported to be present in U-contaminated environments and to play a role in the reduction of U(VI). For instance, *Chloroflexi* sp. has already been identified in U- and heavy metal-containing environments and *Desulfovibrio* sp., a sulfate-reducing bacteria, is closely involved in the radionuclide reduction.^[3, 4] On the other hand, glycerol can be used by fermentative bacteria (*Clostridium* sp.), which are probably involved in the U(VI) reduction.^[5, 6] *Paracoccus* sp. is a bacterial genus that is metabolically versatile and has also been reported in U-containing experiments.^[7]

ACKNOWLEDGEMENTS. The authors are grateful to S.Beutner and S.Schöne for ICP-MS analyses and IC measurements, respectively.

- [1] Giffaut, E. et al. (2014) *Appl. Geochem.* **49**, 225–236.
- [2] Bethke, C. M. (2021) *Geochemical and Biogeochemical Reaction Modeling*, 3rd Ed., Cambridge University Press, Cambridge.
- [3] Harpke, M. et al (2022) *Microorganisms* **10**, 79.
- [4] Lovley, D.R. and Phillips, E. J. P. (1992) *Appl. Environ. Microbiol.* **58**, 850–856.
- [5] Newsome, L. et al. (2015) *Environ. Sci. Technol.* **49**, 11070–11078.
- [6] Gao, W. and Francis, A. J. (2013) *ISRN Biotechnol.* 657160.
- [7] Lopez-Fernandez, M. et al. (2018) *Appl. Clay Sci.* **169**, 206–216.

New insights into U binding properties of bioligands in the cell wall of Gram-negative bacterium *Magnetospirillum magneticum* AMB-1

E. Krawczyk-Bärsch, J. Ramtke, B. Drobot, R. Steudtner, J. Raff

The magnetotactic bacterium *Magnetospirillum magneticum* AMB-1 belongs to the facultative anaerobe Gram-negative bacteria. In contrast to the previously characterized binding of U to carboxyl and phosphoryl groups in the cell wall of Gram-negative bacteria, carboxylic functionalities now play the dominant role in the bioassociation of U in *Magnetospirillum magneticum* AMB-1 cells. PARAFAC analysis of TRLFS data from reference ligands highlights that peptidoglycan is the most important ligand involved, showing a stable immobilization of U over a broad pH range with the formation of three characteristic species as major binding sites.

EXPERIMENTAL. Cell suspensions of *Magnetospirillum magneticum* AMB-1 were prepared in sterile tap water at different pH (3.5, 4.5, 5.5, 6.5 and 7.5) and brought together with a 0.1 M stock solution of $\text{UO}_2(\text{NO}_3)_2$ to adjust an initial U(VI) concentration of 0.1 mM. After 24 h the suspensions were centrifuged for 5 min at $7870\times g$. Each pellet was washed twice in sterilized tap water at the defined pH, and transferred into a copper holder, shock frozen by liquid N_2 , and stored at -80°C prior to the *cryo*-TRLFS measurements. Important ligands, *e.g.*, peptidoglycan (PGN) from *Bacillus subtilis* (Sigma Aldrich), lipopolysaccharide (LPS) from *Pseudomonas aeruginosa* (Sigma Aldrich), L-rhamnose (Sigma Aldrich), D-(+) galactose (Sigma Aldrich), D-(+) mannose (Sigma Aldrich) were used as reference ligands and measured for comparison and interpretation of possible binding sites of U(VI) to *Magnetospirillum magneticum* AMB-1 cell walls. For this, each ligand was dissolved in 2 mL of sterile tap water at different pH (3.5, 4.5, 5.5, 6.5 and 7.5) with a ligand excess of 1:20. A defined volume of a 0.1 M $\text{UO}_2(\text{NO}_3)_2$ stock solution was added to achieve a final U concentration of 0.1 mM. The *cryo*-TRLFS measurements were performed at 153 K with laser pulses at 266 nm (Minilite high-energy solid-state laser; Continuum) and average pulse energy of 300 μJ . The detection of the luminescence light, emitted by the laser-induced biomass samples was recorded using an iHR550 spectrograph and an ICCD camera (both from HORIBA Jobin Yvon) in a wavelength range of 370–670 nm by averaging 100 laser pulses and using a gate time of 20 μs . The achieved data were analyzed by OriginLab2020, version 9.0 (OriginLab Corporation), including the Peak Fit module, version 4.0. Parallel factor (PARAFAC) analysis was used to extract single component spectra from the total emission spectra data sets.^[1]

RESULTS. A subsequent analysis of all emission spectra from the TRLFS data set by PARAFAC extracted the single component spectra of three dominant U(VI) species by deconvoluting the total emission spectra that were formed during the incubation of *Magnetospirillum magneticum* AMB-1 cells with U. The reference spectra of the potential ligands were used for comparison to identify and assign the extracted spectra to possible binding sites of U on the cells. The luminescence characteristics show that there is no match with LPS, L-rhamnose, D-(+) galactose and D-(+) mannose. Rather, a match was found with PGN. In Fig. 1b–d three extracted single component spectra are shown together with the appropriate reference spectra of U loaded PGN. Peak positions and ratios of the U-associated species show a very

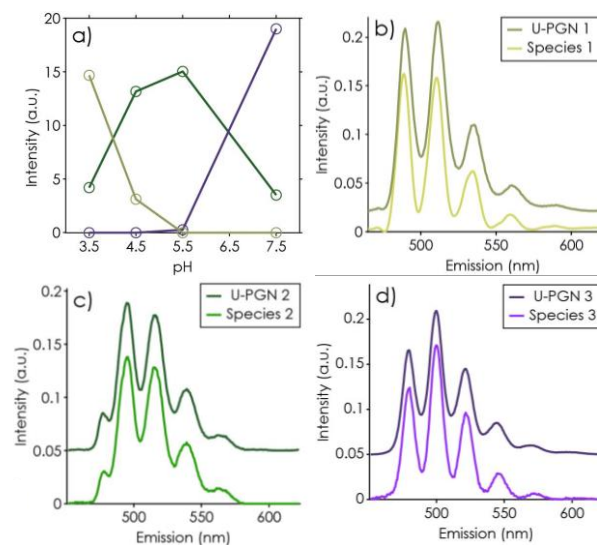


Figure 1. Relative luminescence intensity distribution of three U-PGN reference species vs. pH (a). PARAFAC extracted species (1–3) formed on *Magnetospirillum magneticum* AMB-1 cells in comparison to appropriate U-PGN reference spectra (b–d). *Magnetospirillum magneticum* AMB-1 cells were incubated with 0.1 mM U in sterilized tap water at different pH values during 24 h.

good match with the three reference spectra of U-PGN. As shown by the relative luminescence intensity distribution of the U-PGN reference species vs. pH (Fig. 1a), species 1 is mainly important in the acidic pH range. Species 2 dominates the bioassociation of U(VI) at pH 5.5. On the other hand, species 3 gains importance only in the basic pH range.^[2]

Previous studies on Gram-negative bacteria have often demonstrated the involvement of LPS and PGN in bioassociation.^[3, 4] In contrast, the present work clearly shows that phosphoryl sites could be excluded as major binding site for U in *Magnetospirillum magneticum* AMB-1 cell walls. PGN is the dominant bioligand in this sorption process.

ACKNOWLEDGEMENTS. We would like to thank S. Beutner for ICP-MS measurements and S. Kluge for the cultivation of *Magnetospirillum magneticum* AMB-1 (all HZDR, Germany).

[1] Drobot, B. *et al.* (2015) *Chem. Sci.* **6**, 964.

[2] Krawczyk-Bärsch, E. *et al.* (2022) *J. Hazard. Mater.* **437**, 129376.

[3] Kelly, S. D. *et al.* (2002) *Geochim. Cosmochim. Acta* **66**, 3855–3871.

[4] Krawczyk-Bärsch, E. *et al.* (2018) *J. Hazard. Mater.* **347**, 233–241.

Interaction of U(VI) with plant cells - Impact on U(VI) immobilization and mobility

J. Jessat, H. Moll, W. A. John, M.-L. Bilke, R. Hübner,¹ J. Kretzschmar, R. Steudtner, B. Drobot, T. Stumpf, S. Sachs

¹HZDR, Institute of Ion Beam Physics and Materials Research, Dresden, Germany

***Daucus carota* cells show a high affinity for uranium (U). In the presence of the cells, the U(VI) speciation changes depending on the exposure time. U(VI) forms complexes with malate as typical cell metabolite, which may affect U mobility and bioavailability. Microscopic results verify the immobilization of U by the cells and indicate simultaneously occurring bioaccumulation, -precipitation, and -sorption.^[1]**

Interactions of radionuclides (RNs), *e.g.*, U, with plants are of particular interest, because they can lead to an uptake of RNs into the food chain, resulting in a health hazard for humans. Besides of the immobilization of RNs by plants due to bioassociation, plants can affect their mobility through release of metabolites. Combining biochemical, spectroscopic and microscopic methods, we performed a comprehensive study on the interaction of U(VI) with *Daucus carota* cells to obtain an improved molecular understanding on the impact of plant cells on the U immobilization and mobility at the cellular level.^[1]

EXPERIMENTAL. *D. carota* suspension cells were exposed to 20 or 200 μM U(VI) for 1 to 168 h. After exposure, the amount of bioassociated U was determined and the cell vitality was assessed. The U(VI) speciation in the cell culture media was investigated by time-resolved laser-induced fluorescence spectroscopy (TRLFS) under cryogenic conditions. High performance liquid chromatography (HPLC) and nuclear magnetic resonance (NMR) spectroscopy were applied to identify cell metabolites. The U accumulation was studied by transmission electron microscopy (TEM) coupled with energy-dispersive X-ray spectroscopy (EDX). Experimental details can be found in our publication.^[1]

RESULTS. *D. carota* cells showed a high affinity towards U(VI) based on a single-step bioassociation. A strong increase of immobilized U was observed at the beginning of exposure, followed by an equilibrium after about 48 h. After one week, 88 % (20 μM) or 92 % (200 μM) of U was immobilized. In contrast to *Brassica napus* or *Nicotiana tabacum* cells, a slower U immobilization was observed.^[2,3] In addition, no remobilization of U into the solution at higher exposure times was detectable as in the case of *B. napus*.^[2] At both U(VI) concentrations, the cells exhibited increased cell vitalities, indicating an increased metabolic activity as response to the metal stress.

The U(VI) luminescence spectra of cell culture media before and after cell contact showed time-dependent changes, indicating variations of the U(VI) speciation due to bioassociation and -complexation. As a result of the parallel factor analysis (PARAFAC) of the luminescence data, three aquatic U(VI) species were identified.^[4] Their single-component spectra as well as their species distribution are depicted in Fig. 1. Species 1 dominated in the initial medium (0 h). It can be identified as the $(\text{UO}_2)_3(\text{OH})_5^+$ complex. Species 2, which occurred intermediately, can be assigned to the $\text{UO}_2(\text{CO})_3(\text{aq})$ complex, whose formation is expected under the experimental conditions. Species 3 was detected especially at the beginning of U exposure and was already observed in the presence of *B. napus* cells.^[2] It shows a significant red shift of the band positions. Investigations of the culture me-

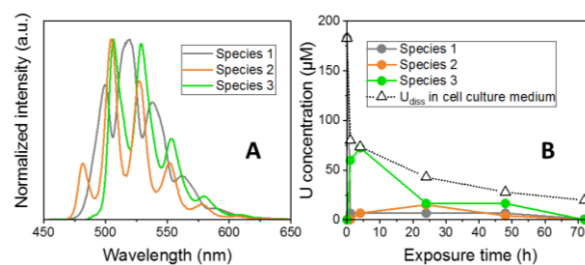


Figure 1. PARAFAC results for the U(VI) speciation in the cell culture medium after contact to *D. carota* cells. A) Extracted single-component spectra of U(VI) species. B) Time-dependent U(VI) species concentration and corresponding concentration of dissolved U in the cell culture medium (U_{diss}).^[1]

dium after cell contact by HPLC and NMR spectroscopy as well as the comparison of the luminescence spectrum with a reference spectrum led to the conclusion that species 3 is a U(VI) malate complex.

Malate is a typical cell metabolite. Whether the origin of the complexing metabolite in the medium is cell lysis or an active release cannot be stated with certainty at this point. However, the fact that species 3 specifically occurs at the beginning of exposure in the *D. carota* system with cell vitalities of 100 % or higher suggests that cell death does not contribute significantly to the metabolite release. Interestingly, there are differences in the development of species 3 between the *D. carota* and *B. napus* cell system.^[2] While species 3 occurred in the *D. carota* system at the beginning of exposure, it appeared in the presence of *B. napus* cells at longer exposure time. For the *B. napus* system, we assumed that species 3 is accompanied with a remobilization of U from the cells or a reduced bioassociation. This is confirmed by the study with *D. carota*. Here, a slower initial U bioassociation was observed, which coincides with the occurrence of species 3 (Fig. 1B). A sufficient amount of released malate in the carrot cell culture could complex U and thus hinder its bioassociation.

With respect to the U accumulation in the cells, we were able to demonstrate by TEM/EDX analyses that bioaccumulation, -sorption and -precipitation occurred simultaneously within 24 h of U exposure. A co-localization of U and P verifies that P-containing substances, *e.g.*, inorganic phosphate or phospholipids, are binding partners of U contributing to the immobilization of U.

ACKNOWLEDGEMENTS. We thank J. Seibt and S. Beutner for experimental support. This work was funded by the BMBF (grant No. 02NUK051B). Furthermore, we acknowledge the use of the HZDR Ion Beam Center TEM facilities and the funding of TEM Talos by the BMBF (grant No. 03SF0451) in the framework of HEMCP.

[1] Jessat, J. *et al.* (2022) *J. Haz. Mat.* **439**, 129520.

[2] Jessat, J. *et al.* (2021) *Environ. Sci. Technol.* **55**, 6718–6728.

[3] Rajabi, F. *et al.* (2021) *Ecotoxicol. Environ. Saf.* **211**, 111883.

[4] Drobot, B. *et al.* (2012) *Chem. Sci.* **6**, 964–972.

FastICA vs. ITFA: tracking U(VI) reduction by *Desulfosporosinus hippei*

A. Rossberg, S. Hilpmann

Iterative Target Transformation Factor Analysis (ITFA) is often used for the decomposition of spectral mixtures into the source signals (spectra), representing chemical species and their corresponding weights, *i.e.* fractions.^[1] ITFA suffers, however, from the rotational invariance of the FA model, resulting in infinite solutions for the source signals and their weights, unless a sufficient number j ($j \geq n^2 - n$) of known fractions can be supplied for the n chemical species.^[2] Since in many real world cases there is sparse $j < n^2 - n$ or no information about the fractions available, non-unique solutions and possible misinterpretations arise. The FA inherent rotational ambiguity can be removed by inclusion of well justified mathematical assumptions as covered by fast independent component analysis (FastICA).^[3] FastICA is a well-established blind source separation technique applicable to a broad spectrum of scientific and technical tasks.^[4] Here we demonstrate for the first time the successful application of FastICA to EXAFS to decipher the uranium reduction by a strictly anaerobic, sulfate-reducing bacterium, *Desulfosporosinus hippei*.

EXPERIMENTAL. For a brief introduction to FastICA consider a spectral mixture $x = a_1s_1 + a_2s_2$ where a and s are the fractions and the signals of the two sources, respectively. According to probability theory the central limit theorem postulates that when adding independent random variables, *i.e.* spectra, the resulting data distribution of such a mixture converges to a Gaussian probability distribution. Thus, the distribution of x will be more Gaussian than that of s_1 and s_2 since x shares information with s_1 and s_2 . In turn, it can be assumed that s_1 and s_2 are more non-Gaussian, since they share less information together than x with s_1 and s_2 . These strong properties result in non-linear objective contrast functions g which allow us to maximize the non-Gaussianity of the sources resulting in their minimum mutual information and maximum statistical independence, whereas the non-Gaussianity is optimized and measured by negentropy (g_1) and/or kurtosis (g_2) with:

$$g_1(s_i) = s_i \exp(-s_i^2/2), \quad g_1'(s_i) = (1 - s_i^2) \exp(-s_i^2/2)$$

$$g_2(s_i) = s_i^3, \quad g_2'(s_i) = 3s_i^2$$

while “'” stands for their derivatives. With E as the expectation value, $s_i = w_i^t z$ and z being the Eigenvectors supplied by ITFA, the iterative procedure

$$w_i = E\{zg(w_i^t z)\} - E\{g'(w_i^t z)z\}w$$

yields for each i 'th component the column vectors w_i of the matrix W so that for all source signals the maximum statistical independence is guaranteed with $s = Wz$. The fractions of the chemical species, $A = W^{-1}C_{abs}$, will reproduce together with the gained s_i the spectral mixtures $x = As$, while C_{abs} is the abstract concentration matrix supplied by ITFA. Note that in each step W needs to be symmetrically orthogonalized. Furthermore, the spectral mixtures x must be centered and whitened before calculation of z , both steps being part of the ITFA software.

The U-L_{III} spectra of *Desulfosporosinus* exposed to U(VI) were taken at different incubation times (t) (Fig. 1).^[5] Two sources were found by ITFA, hence $n = 2$. No independent information about U(IV) and U(VI) fractions is available, hence with $j < n^2 - n$ ITFA is unable to isolate the source spectra.

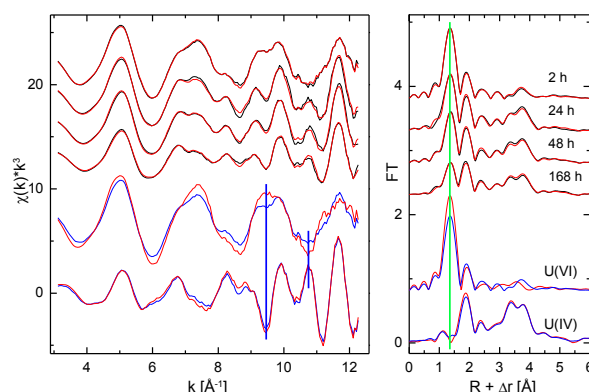


Figure 1. Experimental (black) U-L_{III}-edge EXAFS spectra (left) and corresponding Fourier transform magnitudes (FT) (right) at different incubation times and their reproduction by FastICA (red). ITFA (blue) and FastICA (red) isolated source spectra for U(VI) and U(IV). Green line shows position of axial oxygen atoms, for blue lines see text.

However, the system is a very rare case for which structural information can be exploited by ITFA in the following way: (1) Assume at each t $[U(VI) + [U(IV)] = 100\%$, and $[U(VI)]_{t=2h} = 100\%$. (2) Vary $[U(VI)]_{t=168h}$ iteratively so that the isolated U(IV) signal contains no scattering contribution of the axial oxygen atoms (O_{ax}) at 1.36 Å (green line, Fig. 1). The resulting spectra of the U(VI) and U(IV) species are shown in Fig. 1.

FastICA isolated without any further information the two source spectra (Fig. 1) just by introducing the two z supplied by ITFA, where the negentropy (g_1) was used for maximizing the non-Gaussianity of the sources.

Both methods provided very similar endmember spectra for the U(IV) species, where the contribution of O_{ax} completely vanished (which was preset in ITFA, but not in fast-ICA). For the U(VI) endmember species, however, the isolated spectra show small differences which originate probably from a U(IV) contamination of the ITFA isolated spectrum as most prominently visible in the regions marked with blue vertical lines in Fig. 1. The deviation may arise from the fact that FastICA estimated even at the shortest time step formation of already 20% U(IV), while we assumed for ITFA that the U(IV) fraction at this time was still zero.

Our example suggests that FastICA performs superior to ITFA in case that not enough constraints, like fractions of the species, are available. Furthermore, the example evidenced the role of constraints base on intuitive and/or sparse chemically information which even can lead to rotational ambiguity in the case of ITFA, hence spoiling the proper isolation of the spectra and fractions of the chemical species.

[1] Rossberg, A. *et al.* (2003) *Anal. Bioanal. Chem.* **376**, 631–638.

[2] Malinowski, E. R. (1991) in: *Factor Analysis in Chemistry*, John Wiley & Sons, New York.

[3] Hyvärinen, A. (2001) in: *Independent Component Analysis*, John Wiley & Sons, New York.

[4] Naik, R. *et al.* (2011) *Informatica* **35**, 63–81.

[5] Hilpmann, S. *et al.* (2023) *Sci. Total Environ.*, submitted.

Eu(III) distribution and speciation in different fungal mycelium samples

A. Günther, A. Wollenberg, M. Vogel,¹ B. Drobot, R. Steudtner, R. Hübner,² J. Raff

¹VKTA-Strahlenschutz, Analytik & Entsorgung Rossendorf e.V., Dresden, Germany; ²HZDR, Institute of Ion Beam Physics and Materials Research, Dresden, Germany

Detailed knowledge of the interaction mechanisms between lanthanide/actinides and different soil organisms is necessary for the characterization of the migration behavior of these elements in the environment and as basis for remediation concepts. The aim of this study was to determine the Eu(III) binding capacities of fungal mycelia of *Schizophyllum commune* (wood-inhabiting) and *Leuogogaricus naucinus* (soil-inhabiting) as well as to investigate the Eu(III) speciation and distribution in the mycelium matrix using different microscopic and spectroscopic methods.

EXPERIMENTAL. According to DSMZ recommendations, mycelium of *S. commune* was cultivated in a sterile CYM-T medium and mycelium of *L. naucinus* in the sterile medium 90. The Eu(III) binding experiments were performed in an aqueous mineral medium containing washed fresh biomass (300 mg_{bio dry weight}/L) and concentration of FeCl₃ (15 μM), MgSO₄ (160 μM), K₂HPO₄ (5 μM) and variable EuCl₃ concentration between 85 and 340 μM at pH 4, 5 or 6. High-angle annular dark-field scanning transmission electron microscopy (HAADF-STEM), energy-dispersive X-ray spectroscopy (EDXS) and chemical microscopy as combination of microscopy and high-resolution luminescence spectroscopy were applied to determine the Eu(III)-speciation and distribution in the fungal mycelium samples. More details of the experimental approach, measurements and data analysis were described earlier.^[1, 2]

RESULTS. The two-phase Eu(III)-association process by mycelium cells was not significantly affected by pH. With increasing metal concentration in the mineral medium at the same pH the bioassociated Eu(III) increased and reached values up to 500 μmol/g_{bio dry weight} in the case of *S. commune* after 48 h incubation time. In contrast, the soil-inhabiting fungi *L. naucinus* has bound only about one third of this amount at the same time. During the bioassociation process, the fungal mycelium released a metabolite into the supernatant, which formed a complex with Eu(III) still in the medium.

Figure 1 shows the different binding or deposition sites for this lanthanide in mycelium cells. *S. commune* selectively formed Eu(III) precipitates, that are deposited on the outer cell wall surface. In the case of *L. naucinus*, an accumulation of Eu(III) was observed in the cells.

Beside the binding of lanthanide in the cell wall and on the cell membranes of various organelles, Eu(III) was finely dis-

tributed in the cytoplasm. The results of EDXS analyses have demonstrated that large amounts of phosphorus, nitrogen, and in some cases sulfur (not shown here) were present in the Eu(III) accumulation areas. For this reason, it is very likely, that organic Eu(III) species, in particular organic Eu(III) phosphates are formed after interaction between Eu(III) and mycelium cells.

The spatial distribution of two different Eu(III) fungal species formed in all investigated mycelium samples after 48 h of incubation are shown in Figs. 2 and 3 (left panels). The Eu(III)-species 1 and Eu(III)-species 2 have characteristic luminescence spectra (right panels), which differ significantly in the peak shape of the F2 and F4 transitions and in the F2/F1 signal intensity ratios, indicating a different complex structure. After comparison with selected Eu(III) reference spectra, it is fairly certain and supports the HAADF-STEM result, that phosphate-containing organic ligands in particular are responsible for the immobilization of Eu(III) by fungal mycelium.^[1, 2]

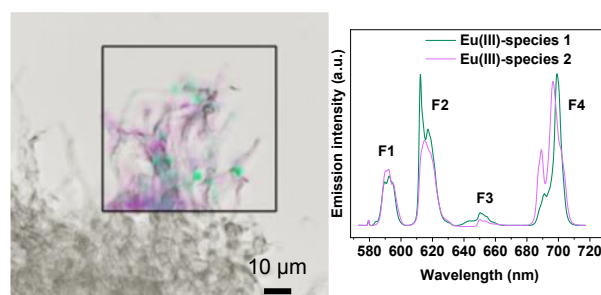


Figure 2. Microscopic image with overlay of the spectroscopic mapping analyses (left) and single component Eu(III) luminescence spectra after 48 h incubation time (right) for *S. commune*.

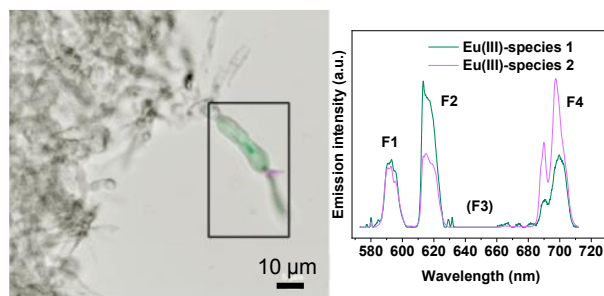


Figure 3. Microscopic image with overlay of the spectroscopic mapping analyses (left) and single component Eu(III) luminescence spectra after 48 h incubation time (right) for *L. naucinus*.

ACKNOWLEDGEMENTS. This work was supported by the German Federal Ministry of Education and Research under contract numbers 15S9276A and 03SF0451.

[1] Günther, A. et al. (2022) *Sci. Total Environ.* **850**, 158160.

[2] Vogel, M. et al. (2021) *Analyst* **146**, 6741–6745.

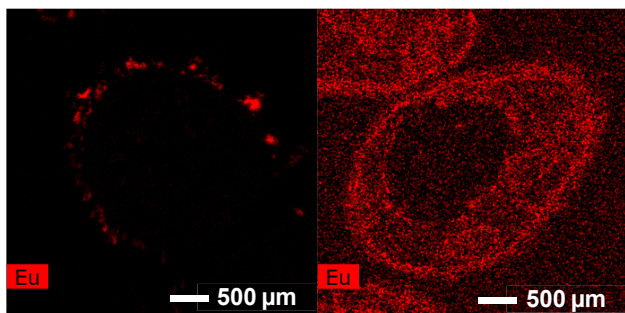


Figure 1. HAADF-STEM images of thin sections of *S. commune* (left) and *L. naucinus* (right) cells with corresponding EDXS-based distribution maps of Eu(III).

Plant cell interactions with potentially toxic metals: Europium(III) and *Daucus carota*

J. Jessat, H. Moll, W. A. John, M.-L. Bilke,¹ R. Hübner, R. Steudtner, B. Drobot, T. Stumpf, S. Sachs

¹HZDR, Institute of Ion Beam Physics and Materials Research, Dresden, Germany

A high affinity of *Daucus carota* suspension cells for Eu(III) was demonstrated. Steady-state conditions were reached in a single-step bioassociation process after 48–72 h and the cells responded with an increased metabolic activity to the Eu(III) exposure. Eu(III) species formed during carrot cell exposure were also determined.

This study is part of our investigations on the interaction of lanthanides and actinides with different plant cell lines. These experiments are a first step towards understand the physiological and biochemical mechanisms triggered in plants by stress in the presence of hazardous metals. Bioassociation of metals with plants is one way how these toxic substances can enter the food chain. This study combines biochemical, spectroscopic and microscopic techniques to gain an improved molecular process understanding of the interaction of Eu(III) with plants at the cellular level.

EXPERIMENTAL. For the experiments with Eu(III), 1.50 ± 0.03 g of *Daucus carota* (*D. carota*) cells were transferred into Erlenmeyer flasks and 10 mL of culture medium (control or containing 30 or 200 μ M Eu(III)) were added. Exposure times for bioassociation were 1, 4, 24, 48, 72, and 168 h in some cases. All details concerning cell cultivation, analytical and statistical analyses, laser-induced luminescence spectroscopy, and microscopy can be found in our publication.^[1]

RESULTS. A single-step bioassociation process was observed for Eu(III). A strong increase in immobilized Eu(III) was measured at the beginning of the exposure. 88 % (30 μ M) to 84 % (200 μ M) of Eu(III) was immobilized by *D. carota* cells after one week of exposure. Higher cell vitalities of the Eu(III)-exposed cells compared with control samples (100%) indicated high tolerance of the cells to Eu(III).

Eu(III) is an excellent probe for direct speciation analyses based on luminescence spectroscopy. By scanning the excitation wavelength around the 7F_0 -transition (565–582 nm) different Eu(III)-species can be distinguished in one sample.^[2] The measured excitation spectra of the cell culture media after cell contact (supernatants) as a function of the exposure time are depicted in Fig. 1A. The spectra are composed of comparatively broad excitation bands. This indicates poorly defined ligand fields of Eu(III) complexing ligands in the supernatants, and can be described as a continuum of similar but different binding environments. However, two distinct Eu(III) coordination environments can be seen clearly. The maximum at 579.6 nm decreases with increasing exposure time (Fig. 1A). At the same time, the more red-shifted maxi-

um at ~580.6 nm increases. The excitation maxima are strongly red-shifted compared with the maximum of the Eu^{3+} aquo ion at 578.8 nm.^[3] The areas under the individual peak can be used to determine the fraction for Eu(III)-species 1 (~579.6 nm) and 2 (~580.6 nm). This information is necessary for the iterative transformation factor analysis (ITFA) of the supernatant spectra obtained after excitation with 394 nm.^[4] Figure 1B depicts the isolated single component spectra from the sum data after excitation at 394 nm. The insert depicts the corresponding Eu(III) speciation. Eu(III)-species 1 can be interpreted as an Eu(III) complex with a medium constituent. The results for Eu(III)-species 2 indicated a Eu(III)-EDTA coordination environment. The origin of EDTA can be seen in the culture medium component ferric sodium EDTA.

Luminescence measurements (TRLFS) indicated the occurrence of two different Eu(III) species associated on the cells (Fig. 2). Eu(III)-species 1 can be described as a Eu(III) complex with carboxyl and/or phosphate groups located in the cell wall. Our TEM/EDX investigations could show a relationship between Eu(III) and phosphate groups of the cells or with released phosphate due to the cell metabolism. In contrast, a much stronger intensity of the 7F_2 -transition was measured for Eu(III)-species 2. The characteristic feature of the 7F_4 -transition of this Eu(III)-species points to a Eu(III)-coordination environment similar to that in Eu(III)-EDTA complexes, suggesting the interaction of a Eu(III)-EDTA species with the cells.

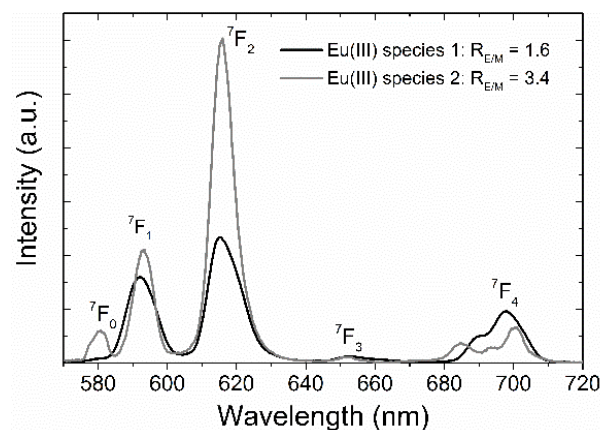


Figure 2. Results of the deconvolution of the sum spectra of the Eu(III)-loaded cells in the *D. carota* system using PARAFAC.^[5]

MISCELLANEOUS. This work is licensed under Journal of Hazardous Materials <https://doi.org/10.1016/j.jhazmat.2022.129520>.

ACKNOWLEDGEMENTS. This work was funded by the Federal Ministry of Education and Research under contract number 02NUK051B.

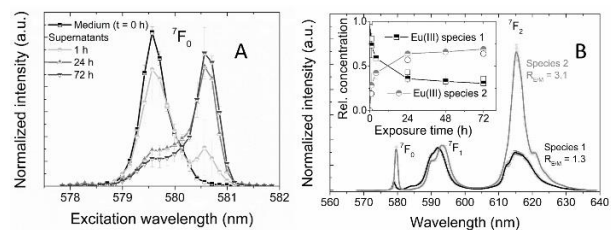


Figure 1. ${}^7F_0 \rightarrow {}^5D_0$ excitation spectra of cell culture medium and selected supernatants of the *D. carota* system (200 μ M Eu(III), $T < 10$ K) (A). Single-component spectra of Eu(III) species in the supernatants (B). Insert: Corresponding spectroscopic Eu(III) species distribution. Open symbols: values calculated from the site-selective luminescence experiments.

- [1] Jessat, J. et al. (2022) *J. Hazard. Mat.* **439**, 129520.
- [2] Binnemans, K. (2015) *Coord. Chem. Rev.* **295**, 1–45.
- [3] Carlos, L. D. et al. (2005) *Chem. Phys. Lett.* **415**, 238–242.
- [4] Roßberg, A. et al. (2003) *Anal. Bioanal. Chem.* **376**, 631–638.
- [5] Drobot, B. et al. (2015) *Chem. Sci.* **6**, 964–972.

Uptake and distribution of Eu(III) in hydroponically grown plants

M. Klotzsche, R. Steudtner, M. Vogel,¹ B. Drobot

¹VKTA – Strahlenschutz, Analytik & Entsorgung Rossendorf e.V., Dresden, Germany

Bioassociation experiments with Eu(III) and different plant species grown in hydroponic solution showed a significant uptake into the roots and a minor translocation into shoots. The speciation of Eu(III) remaining in the nutrient medium is influenced by plant-related compounds.

Minimization of the volume of contaminated soil material arising during the dismantling of nuclear facilities is crucially necessary. In this context, biological remediation processes stand out by cost-effectiveness and environmental friendliness, as plants have the ability to remove contaminants such as radionuclides and heavy metals from soil.

The aim of this work is to assess the potential of selected plants for phytoremediation and to develop a molecular process understanding of the interaction of metals with biological systems. Therefore, bioassociation experiments were conducted with Eu(III) and five plant species grown in hydroponic solutions. Particular attention was paid to spectroscopic studies of metal speciation in the growth medium upon plant contact and to the macroscopic and microscopic distribution of Eu(III) in roots and shoots.

EXPERIMENTAL. Five different plant species, namely Sand oat (*Avena strigosa*), Alfalfa (*Medicago sativa*), Flax (*Linum usitatissimum*), Crimson clover (*Trifolium incarnatum*) and Birdfoot trefoil (*Lotus corniculatus*) were cultivated in hydroponic cultivation boxes (Araponics, Belgium). Seeds were placed in agar-filled water-permeable inserts (2.5% agar in Milli-Q water). After germination, seedlings were transferred into hydroponic sponges in Araponics boxes filled with modified Hoagland solution,^[1] supplying macro- and micronutrients for growth in the aqueous nutrient medium. The boxes were placed in a phytochamber at 25 °C, 55% r.H. and a 16/8 h day/night cycle, with aquarium pumps providing oxygen supply in the medium. After 1–2 month of growth, bioassociation experiments were conducted with 200, 20 and 2 μM Eu(III) in 250 mL low phosphate Hoagland medium in Erlenmeyer flasks, each containing one single plant. Before sampling of the nutrient medium at 0, 0.1, 2.5, 24, 48, 72 and 96 h incubation time, the liquid volume was filled up to 250 mL and subsequently analyzed by pH measurement, ICP-MS and TRLFS. After 96 h, plants were washed thrice with Milli-Q water and separated into roots and shoots (*A. strigosa*, *T. incarnatum*) or roots, stems, and leaves (*M. sativa*, *L. usitatissimum*, *L. corniculatus*). Additionally, samples were branched off for TRLFS and chemical microscopy. After drying at 60 °C, individual plant parts were ashed, dissolved in concentrated HNO₃ and Eu(III) content was determined by ICP-MS. For better understanding, only the results of experiments with Birdfoot trefoil (*L. corniculatus*) are discussed below.

RESULTS. Analysis of Eu(III) concentration in the supernatant shows a stepwise bioassociation that starts with an instantaneous biosorption at the root surface upon exposing plant roots to the metal-containing medium. This initial bioassociation is followed by a slower but continuous uptake of the metal into the plant, during which up to 82% of the initial 200 μM Eu(III) (98 and 99% for 20 and 2 μM, respectively) is removed from the nutrient medium. Ashing of the in-

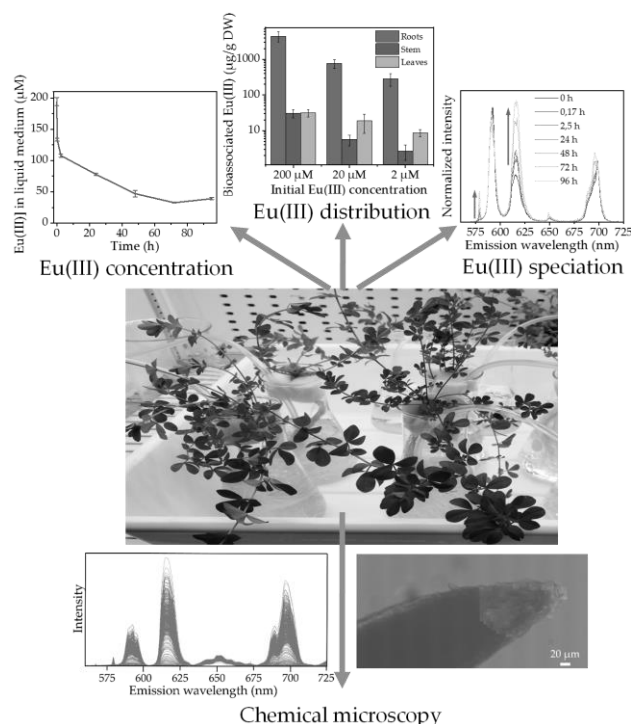


Figure 1. Hydroponic Eu(III) bioassociation experiment with *L. corniculatus* and results derived from ICP-MS of supernatant and dissolved plant ash, TRLFS of supernatant and Eu(III) distribution in a root tip.

dividual plant parts and dissolution of the residue reveals its macroscopic distribution: The majority of the assimilated metal is immobilized at/in the roots (98%), independent of the initial Eu(III) concentration, whereas < 1% is translocated in each, stem and leaves. The presence of the metal in the green parts of the plant was further confirmed by TRLFS measurements of fresh plant material.

The spectroscopic assessment of Eu(III) speciation in the liquid medium provides an insight into metal–plant interaction throughout incubation time. While the Eu(III)-aquo ion dominates at the beginning of the experiment, a speciation change already takes place within the first day. The increasing occurrence of the ⁵D₀→⁷F₀ transition and the intensity gain of the ⁵D₀→⁷F₂ band indicate a significant change in the coordination environment of Eu(III). It is very likely that metal-coordinating organic molecules are released by the roots as a response to the presence of the lanthanide. Investigations focusing on the identification of these compounds *via* HPLC are currently underway.

Furthermore, chemical microscopy was applied to detect the microscopic distribution of Eu(III) in primary and secondary roots as well as root cross sections by excitation of the metal ion with λ = 532 nm. The microspectroscopic mappings reveal a bioaccumulation in all of the aforementioned root parts, even in freshly grown root tips.

ACKNOWLEDGEMENTS. This work was funded by the BMBF under contract number 02NUK066A.

[1] Hoagland, D. *et al.* (1950) The water-culture method for growing plants without soil, Circular, Berkeley.

Friend or foe? Potential microbial impacts on bentonites used for deep geological repository

T. S. Wei, N. Matschiavelli, V. Sushko, A. Cherkouk

For a deep geological repository (DGR), a multi-barrier concept is a favorable option to store high-level nuclear waste (HLW). The natural clay formations are one of the host rocks for entire DGR due to their unique geochemical features. However, bentonite is the processed clay material in which metal HLW containers are directly embedded. The microbial impact, especially when porewater enters the DGR and H₂ gas is generated via anoxic corrosion of containers, on these clay barriers remains elusive. Based on the microbial diversity analysis, we observed that in Bavarian bentonite (B25), genera *Desulfosporosinus* and *Pelotomaculum* (both belonging to phylum Firmicutes) were enriched by H₂ gas in the presence of synthetic Opalinus clay (OPA) porewater. Interestingly, the signature of *Desulfosporosinus* was also identified in raw Calcigel bentonite (CaB). This data indicated that microbial communities in bentonites have the potential to oxidize H₂ gas and alleviate the gas pressure.

EXPERIMENTAL. The DNA of raw Calcigel (CaB) bentonite was extracted as previously described.^[1] The amplicon of the V4 region of 16S rRNA genes was subjected to next-generation sequencing using MiSeq (Illumina). Other sequence data was retrieved from anaerobic microcosm setup of B25 incubating with synthetic OPA porewater (with 14 mM of Sulfate) and 50 kPa of H₂ gas up to 305 days.^[2] All sequence data were analyzed using DADA2 to generate amplicon sequence variant (ASV).^[3] Silva v138 database was used for taxonomy assignment.^[4] The phyloseq was used for principle coordinate analysis (PCoA) to determine dissimilarity of microbial communities and data visualization for microbial diversity.^[5] The details of the samples and conditions are listed in Tab. 1.

Table 1. Sample abbreviation and microcosm conditions for B25 bentonite.

Samples	Conditions	Days
Raw CaB	Raw bentonite	-
Raw B25	Raw bentonite	-
B25 + OPA_181D	B25 + OPA porewater	181
B25 + OPA_305D	B25 + OPA porewater	305
B25 + OPA_H2_181D*	B25 + OPA porewater + H ₂	181
B25 + OPA_H2_238D*	B25 + OPA porewater + H ₂	238
B25 + OPA_H2_305D*	B25 + OPA porewater + H ₂	305

*: two biological replicates of microcosms were conducted.

RESULTS. The PCoA showed that the microbial diversity of both raw bentonites and B25 incubated with OPA porewater with or without H₂ gas was highly distinct (Fig. 1). This indicates that H₂ gas and OPA porewater are the factors that shape community structure in B25. Regarding the change in microbial community structure, Proteobacteria was dominant in raw B25; however, Firmicutes largely increased in B25 microcosm incubated with OPA porewater with/without H₂ gas, (Fig. 2A). Furthermore, the abundance of two genera in Firmicutes – *Desulfosporosinus* and *Pelotomaculum* – increased up to 80% only with supplement of H₂ gas (Fig. 2B). This suggests that they are sulfate reducers capable of oxidizing H₂ gas in B25 communities. On the other hand, raw CaB community comprised up to 6 major phyla (Fig. 2A). We noted that a signature of *Desulfosporosinus* was identified,

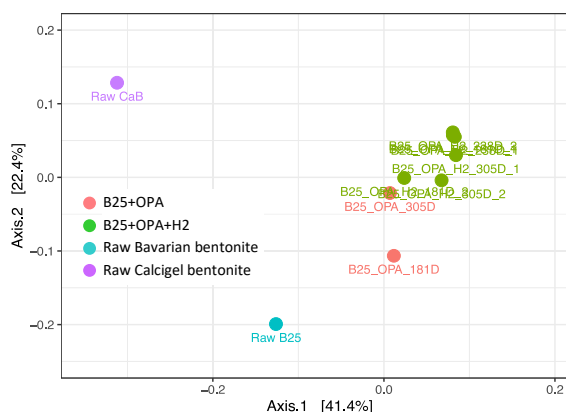


Figure 1. The PCoA for microbial community structure. Each data point is based on weighted Unifrac distance of all ASVs generated from all samples.

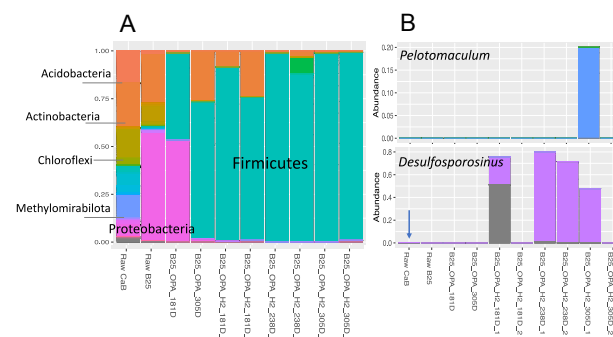


Figure 2. The community structure change at Phylum level (A) and at level of genera *Pelotomaculum* and *Desulfosporosinus* (members of Firmicutes) (B). Arrow denotes the low abundance of *Desulfosporosinus* in CaB community.

but with extremely low abundance (<0.1%), indicating that microorganisms in CaB may also have the capacity for oxidation of H₂ gas.

OUTLOOK. The 16S rRNA gene sequence analysis suggests that certain sulfate-reducing microorganisms in different bentonite communities are beneficial to DGR sites due to the potentials to alleviate H₂ pressure generated from corrosion of metal containers for HLW. However, a comprehensive investigation based on microcosm setup across different type of bentonites, metagenomic approaches and geochemical quantification should be considered because H₂S from microbial sulfate reduction may also be a corrosive agent for metals. The actual impact of indigenous microorganisms in bentonites, either beneficial or disadvantageous, on entire DGR system remains elusive.

[1] Engel, K. *et al.* (2019) *mSphere*. **4**, e00334–19.
 [2] Matschiavelli, N. *et al.* (2019) *Environ. Sci. Technol.* **53**, 10514–10524.
 [3] Callahan, B. *et al.* (2016) *Nat. Methods*. **13**, 581–583.
 [4] Quast, C. *et al.* (2013) *Nucleic Acids Res.* **41**, D590–596.
 [5] McMurdie, P.L and Holmes, S. (2031) *Plos One* **8**, E61271.

Formation of artificial multi-species bio-constructs of aerobic and anaerobic bacteria

S. Hilpmann, I. Jeschke, D. Deev,¹ M. Zupan,¹ T. Rijavec,¹ A. Lapanje,¹ S. Schymura, A. Cherkouk

¹ Jožef Stefan Institute, Department of Environmental Sciences, Ljubljana, Slovenia

In this study, we present the formation of synthetically aggregated bio-constructs composed of anaerobic *Desulfovibrio africanus* DSM 2603 or *Desulfitobacterium* sp. G1-2 together with aerobic *Cobetia marina* DSM 50416 bacterial strains. The aggregation is based on a recently described method of electrostatic modifications of the cell surfaces with polyelectrolytes (PE).^[1] This approach enables to immobilize the microorganisms and evoke synergetic interactions of different bacterial strains.

The aerobic strain *C. marina* DSM 50416, as well as the anaerobic sulfate-reducing bacteria *D. africanus* DSM 2603 and the iron-reducing isolate *Desulfitobacterium* sp. G1-2^[2], were investigated for their potential to form artificial bio-constructs with uranium(VI) reduction capabilities. The aim of this study is to combine the reduction activity of sulfate- and iron-reducing bacteria with aerobic strains to create anaerobic niches under oxygenic conditions. In this regard, new approaches for bioremediation of contaminated environments could be obtained.

EXPERIMENTAL. *Cultivation:* *C. marina* DSM 50416 was cultivated under shaking using DSMZ 79 medium at 30 °C in the dark. *D. africanus* DSM 2603 and *Desulfitobacterium* sp. G1-2 were cultivated anaerobically in iron-reduced DSMZ 63 and DSMZ 720 media (30 °C), respectively. All cells were harvested in the late exponential growth phase by centrifugation and washed in 0.9 % sodium chloride solution.

Staining: The dyes SYTO[®] 11 (green fluorescence, anaerobic strains, 50 μM) and SYTO[®] 64 (red fluorescence, aerobic strain, 50 μM) were used to stain the cells according to the manufacturer's instructions.

Formation of bio-constructs: Prior to use, the polyelectrolyte polyethylenimine (PEI) was acetylated according to Forrest *et al.*^[3] and diluted to working concentration of 0.25 %. Encapsulation was performed as reported by Deev *et al.*^[1] Stained cells of *C. marina* DSM 50416 (OD = 1, stained red) were mixed in a 1:1 ratio with acetylated polyethylenimine (Ac-PEI), incubated for 5 min and centrifuged at 1,000 rpm for 3 min. Afterwards, the cell pellet was washed in 0.9 % sodium chloride solution and resuspended. The encapsulated cells were mixed in a 2:1 ratio with anaerobic cells (stained green). The formed bio-constructs were incubated in DSMZ 720 medium for aggregates containing *Desulfitobacterium* sp. G1-2 and in DSMZ 63 medium for *D. africanus* DSM 2603 aggregates under aerobic conditions at 30 °C.

Fluorescence microscopic images: Fluorescence microscopic images of the formed bio-constructs were taken over a period of one week using the phase-contrast microscope Olympus XM11 and the software "cellSense Dimension 1.11".

RESULTS. Artificial bio-constructs of aerobic and anaerobic bacteria were formed using Ac-PEI. Fluorescence microscopic images (Fig. 1) show the distribution of aerobic *C. marina* DSM 50416 and anaerobic *Desulfitobacterium* sp. G1-2. in the aggregates.

During incubation, a redistribution of the two bacteria is observed. Initially, cells of the anaerobic bacterium are predominantly located in the outer shell of the aggregates, whereas the aerobic microorganism *C. marina* DSM 50416 is mainly observed in the interior. Due to the encapsulation of

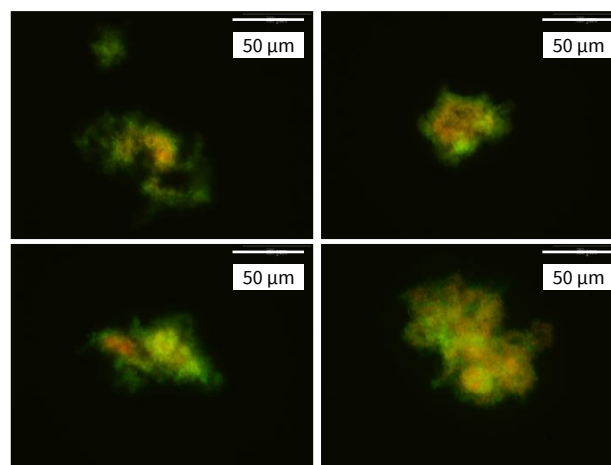


Figure 1. Distribution of *Desulfitobacterium* sp. G1-2 (green) and Ac-PEI-encapsulated *C. marina* DSM 50416 (red) in a formed artificial bio-construct over time (DSMZ 720 medium, aerobic conditions).

the cells of *C. marina* DSM 50416 with the positively charged polyelectrolyte Ac-PEI, the negatively charged cells of *Desulfitobacterium* sp. G1-2 accumulate on the outside after their addition. With increasing incubation times (168 h) no clear differentiation between *C. marina* DSM 50416 and *Desulfitobacterium* sp. G1-2 can be seen anymore. This change in bacterial arrangement is probably caused by the aerobic conditions, which are not ideal for the anaerobic bacterium *Desulfitobacterium* sp. G1-2. Therefore, cells of *Desulfitobacterium* sp. G1-2 move to the interior of the agglomerate, where less oxygen is present due to the aerobic respiration of *C. marina* DSM 50416.

The fermentative medium provides conditions for a growth of the cells, which can be seen by an increase in size of the aggregates over time. However, growth conditions are better for the aerobic bacterium, as the cells of *C. marina* DSM 50416 grow more vigorously. Nevertheless, *Desulfitobacterium* sp. G1-2 also shows some growth during the experiment, probably due to a tolerance against low oxygen concentrations.^[4]

Future work will now focus on the investigation of the potential of these bio-constructs for the reduction of uranium(VI) to less mobile uranium(IV) under anaerobic and aerobic conditions.

ACKNOWLEDGEMENTS. The SURFBIO project has received funding from the European Union's Horizon 2020 research and innovation program under the Grant Agreement No. 95237.

[1] Deev, D. *et al.* (2021) *Front. Mater.* **8**, 1–14.

[2] Bachran, M. *et al.* (2018) Report HZDR-085, p. 53

[3] Forrest, M. L. *et al.* (2004) *Pharm. Res.* **21**, 365–371.

[4] Utkin, C. *et al.* (1994) *Int. J. Syst. Bacteriol.* **44**, 612–619.

Spatial and temporal evolution of enzymatic degradation of PET plastics

H. Lippold, L. Kahle,¹ C. Sonnendecker,¹ J. Matysik,¹ C. Fischer

¹Leipzig University, Institute of Analytical Chemistry

Currently, the possibilities of biodegradation of plastics are being discussed, especially concerning the degradation kinetics, which is decisive for the viability of this strategy. Aside from the structural-chemical properties of enzyme and substrate, degradation rates are essentially determined by the evolving nanopopography. In this study, the 3-dimensional development of the surface characteristics of an amorphous PET film, reacted with a highly effective hydrolase enzyme, was explored by vertical scanning interferometry and confocal microscopy. Different stages in the mechanism of surface retreat were identified, correlating with the degradation rate.^[1]

EXPERIMENTAL. Amorphous PET film pieces (Goodfellow, Germany), partially masked with PTFE tape, were reacted with the enzyme PHL7 in potassium phosphate buffer solution, shaking at 70 °C for time periods of 0.5–24 h.^[2] The resulting surface topographies were analyzed by means of an S neox 3D optical profiler (Sensofar, Spain), operated in both VSI white-light mode using a 10x Mirau objective (Nikon) and in the mode of scanning microdisplay confocal microscopy using a 150× confocal objective (Nikon). The software SPIP (version 6.7.4) was used for visualization and data processing.

RESULTS. As shown in Fig. 1, retreat rates proved to be invariant for longer reaction times, whereas a deceleration is observed for the early stage of retreat.

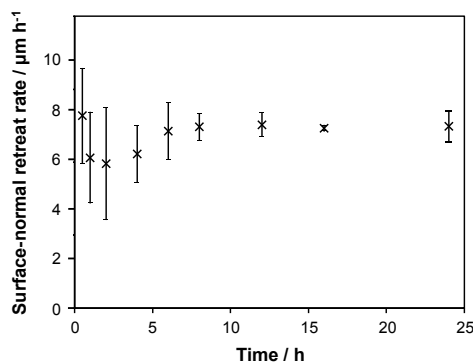


Figure 1. Average rates of surface-normal retreat as a function of reaction time. Data are given as mean values \pm SD for 3 independent experiments per time of treatment.

During this initial phase, a nano- to microscale roughness is generated, gradually eliminating the wavy topography present at the beginning (Fig. 2). However, this degradation mechanism changes fundamentally as degradation proceeds: After 4 h, the entire surface is covered by dish-like pits (Fig. 3), circular in shape and large in diameter (up to tens of μm) compared to the intermediate surface structure.

This specific progression pattern does not change significantly with increasing reaction time. In Fig. 4, the development is summarized schematically in terms of reactivity.

After a symmetric broadening until a degradation time of 2 h, asymmetric distributions are found for the long-term period until 24 h, with distribution widths varying within a limited range. Obviously, the degradation process arrives at a steady state where local reactivities both increase and decrease during retreat. Rather than a continuous “excavation”, craters appear and disappear permanently across the

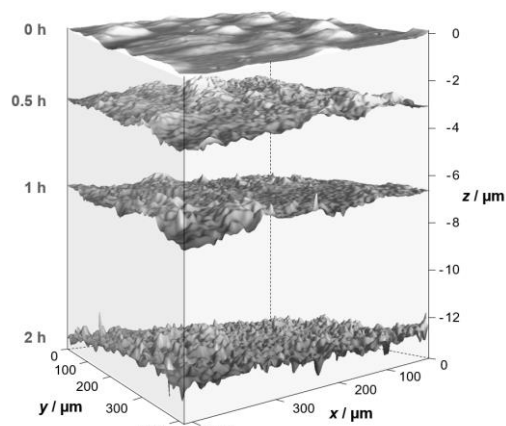


Figure 2. 3D visualization of the initial phase of degradation, characterized by an unspecific roughening process.

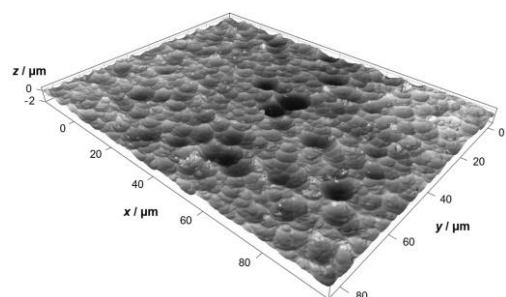


Figure 3. Circular reactivity pattern observed for the advanced phase of degradation (> 2 h).

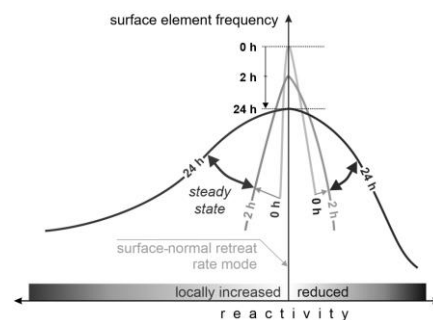


Figure 4. Schematic representation of reactivity distributions evolving during degradation. Locally excessive height loss (left from ordinate) represents locally increased surface reactivity.

surface, possibly because a certain aspect ratio (depth/radius) cannot be exceeded. Growing in diameter, the pits remain shallow and form the basis of new pits. The mechanistic background of this persistent circular degradation pattern is still in need of elucidation.

In any case, for a reliable prediction of polymer degradation, we conclude that special attention should be paid to the heterogeneous surface reactivity in future studies, particularly in view of the observed interrelation between retreat rates (Fig. 1) and rate distributions (Fig. 4).

[1] Lippold, H. et al. (2022) *npj Mater. Degrad.* **6**, 93.

[2] Sonnendecker, C. et al. (2022) *ChemSusChem* **15**, e202101062.

Quantitative assessment of metal toxicity by metabolic heat flow analysis

K. Fahmy

Quantitative analyses of cell replication address the connection between metabolism and growth. Various growth models approximate time-dependent cell numbers in culture media, but physiological implications of the parametrizations are vague. In contrast, isothermal microcalorimetry (IMC) measures with unprecedented sensitivity to heat (enthalpy) release via chemical turnover in metabolizing cells independently of modeling the time-dependence of cell numbers. IMC traces of various origins exhibit conserved patterns when expressed in the enthalpy domain rather than the time domain. The data comply extraordinarily well with a dynamic Langmuir adsorption reaction model of nutrient uptake and catalytic turnover, providing a sensitive two-parameter description of toxicity. This is exemplified here for uranium and copper toxicity during the growth of *Lactococcus lactis* cultures. The proposed formalism reproduces the “life span” of cultured microorganisms from exponential growth to metabolic decline by a succession of distinct metabolic phases following remarkably simple nutrient-metabolism relations.

EXPERIMENTAL. The strain *Lactococcus lactis* subsp. *cremoris* NZ9000/pNZ8148 (Nizo Food Research BV, The Netherlands) was grown at pH 7.2 in M17 medium containing (per liter) 5g Neopeptone, 5g Bacto Soyton, 5g beef extract, 2.5g yeast extract, 0.5g ascorbic acid, and 1g Na₂-β-glycerophosphate·5H₂O. After autoclavation, 1 mL of 1M MgSO₄ and 20 mL of 50% glucose were added from sterile-filtered solutions. IMC was performed with a TAMIII instrument (Waters GmbH, Eschborn, Germany). Calorimetric ampoules were filled with 4 mL medium and inoculated with 20 μL of a main bacterial culture which was pre-diluted with medium to OD₆₀₀ = 0.1. Thermal power was monitored continuously over 50 h at 20 °C or 25 °C as described.^[1]

RESULTS. Heat flow curves from *L. lactis* were recorded in the presence of varying concentrations of copper or uranium (Fig. 1). By transforming the data from time- to enthalpy domain, different forms of metal toxicity become readily visible. Copper merely reduces the overall metabolic activity as revealed by the conservation of the general shape of the heat flow curves. They are simply related by a scaling factor which is not visible in the time-domain. In contrast, uranium shows distinct effects, leaving the initial exponential growth unaffected but specifically reducing activity in the second metabolic phase. A software tool has been developed which employs a “dynamic adsorption reaction thermogram simulation” (dAR-TS) from which nutrient affinity Θ and maxi-

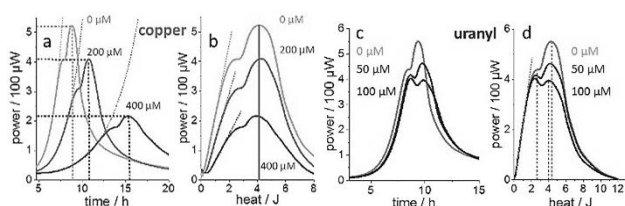


Figure 1. Time-dependent thermograms of a *L. lactis* culture grown in the presence of copper sulfate (a). The exponential growth highlighted (dotted lines). “Enthalpy plot”, the same traces plotted in dependence of totally released heat, exponential growth corresponds to a linear dependence (dotted lines) on total released heat (b). The equivalent data recorded from the same strain in the presence uranyl nitrate (b, d).

mal metabolic turnover rate r_0 are obtained as descriptors of toxicity. The initial nutrient affinity $\Theta(0)$ is called the “metabolic load” which expresses the initial growth rate r_i as a fraction of the maximal possible growth rate r_0 , such that $r_i = r_0 \Theta(0)$.

In contrast to the conventional description of a 50% inhibitory concentration of a metal, the analysis shows that toxicity is a multidimensional phenomenon because (i) different growth phases are affected differently and (ii) metals may affect maximal growth rate or metabolic load or both. Figure 2 (a, b) show that uranyl has little effect on the first growth phase but strongly affects the second phase specifically by lowering the nutrient affinity but not the maximal metabolic rate of the cells. This differs from copper toxicity which is a result of reducing predominantly maximal metabolic rate (not shown). As a control for the robustness of the fitting by dAR-TS, Fig. 2 (c, d) displays the result of the analysis of temperature-dependent growth in the absence of metals. Here, purely rate effects were expected as the increase of temperature from 20 °C to 25 °C has no effect on cell metabolism other than acceleration. The fitting procedure agrees with the biochemical prediction and clearly identifies an increase of r_0 , rather than increased nutrient affinity as the cause for higher metabolic activity.

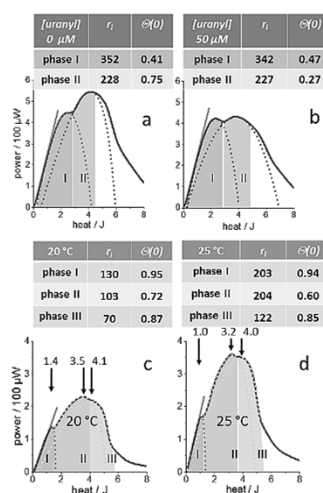


Figure 2. dAR-TS analysis reveals initial growth rate r_i and initial metabolic load $\Theta(0)$ for two metabolic phases (a, shaded areas). Culture grown from the same inoculate but in the presence of 50 μM uranyl (b). *L. lactis* culture grown at 20 °C showing the capability of dAR-TS to reproduce also the decline of metabolic activity in the third metabolic phase (c, area III). Thermogram of the same strain grown at 25 °C (d). Straight lines (solid grey, area I) mark the exponential growth phase of the initial metabolic state. Units of r_i is 10⁻³ h⁻¹.

The developed analysis tool is thus capable of describing toxicity in a highly specific manner which has become feasible only by the extremely high signal to noise ratio in modern IMC data. Calorimetry is particularly attractive for analyzing toxic effects of radionuclides since minimal handling of samples is possible. In the case of uranium toxicity studied here, the reduced nutrient affinity indicates that it is probably the complexation of substrates with the actinide which interferes with cellular nutrient uptake.

[1] Fahmy, K. (2022) *Microorganisms* **10**, 1397.

The unexpected anion sensitivity of DNA-origami stability originates in hydration effects

D. Dornbusch, A. Rossberg, S. Tsushima, K. Fahmy

The folding of DNA into rationally designed DNA origami nanostructures has been extensively studied in order to increase structural diversity and add functionality. However, the fundamental physical and chemical properties of these nanostructures remain largely unknown and unexpected counter anion effects on structure and stability have not been understood. The latter have been studied using different guanidinium (Gdm) salts to probe DNA origami stability. The statistical analysis of temperature-dependent circular dichroism (CD) spectra and atomic force microscopy (AFM) images of DNA origami triangles demonstrates that sulfate and chloride exert stabilizing and destabilizing effects, respectively, even before the DNA origami triangles melt globally. We identified structural transitions that occur during thermal denaturation and demonstrate that ion-induced variations in heat capacity (ΔC_p) determine the temperature dependence of structural damage. According to MD simulations, the different hydration shells of the anions and their ability to form Gdm⁺ ion pairs in concentrated salt solutions modulate ΔC_p via altered wetting properties of hydrophobic DNA surface regions. The underlying structural changes at the molecular level are amplified by the large number of structurally coupled DNA segments, resulting in nanoscopic correlations with AFM images.^[1]

EXPERIMENTAL. *Ex situ* AFM was used by our collaborators (A. Keller, University Paderborn) to investigate the interaction of triangular DNA origami nanostructures with the two selected Gdm⁺ salts (GdmCl, Gdm₂SO₄) at the nanostructure level. We then attempted to correlate the observed nanostructural changes with molecular features that can be addressed by CD spectroscopy and UV absorption, such as chirality and base pair opening, respectively. To handle the complex system and to account for multiple microscopic states, Principal Component Analysis was used to assess the CD-spectral signatures and relative concentrations of putative structural components underlying denaturation between 20 °C and 90 °C. In order to provide structurally interpretable results, we used an Iterative Target Transformation Factor Analysis (ITTFA).

MD simulations and data analyses were performed using AMBER 15 program package with OL15 force field applied on DNA. For Mg²⁺ ions, additional parameters were employed. MD parameters of the Gdm⁺ and SO₄²⁻ ions were obtained by means of antechamber module of AMBER package utilizing Gaussian 16 program for calculating partial charges. 50 ns MD runs were performed in a periodic boundary condition in NPT ensemble.

RESULTS. We used an Iterative Target Transformation Factor Analysis (ITTFA), to decompose the spectra into four physically meaningful principal components. Component spectra were obtained through an iterative process that satisfactorily described both data sets, allowing the effects of the two counter ions (Cl⁻ and SO₄²⁻) to be described in a common DNA-structural framework.

As a result, the observed differences in the thermal stability of Gdm⁺-bound DNA origami could be explained solely by different equilibrium constants between nearly identical structural states in both electrolytes and in accordance with CD spectra in the absence of denaturant. Importantly the

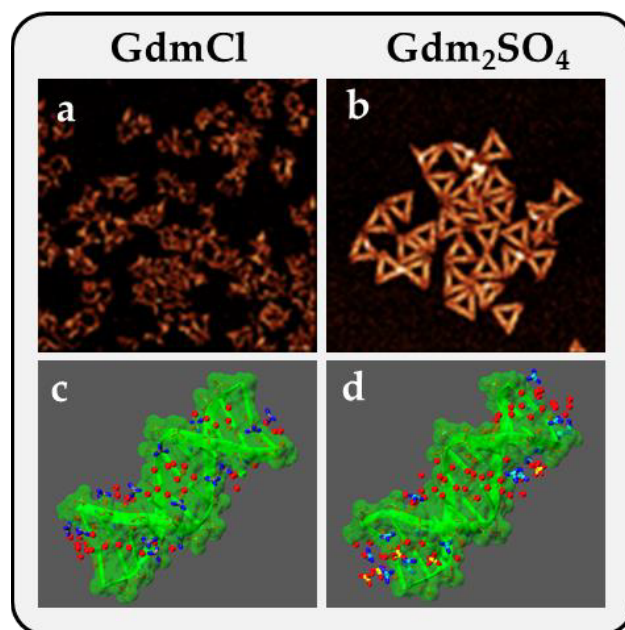


Figure 1. AFM images of DNA origami triangles deposited on mica after 1 h incubation in GdmCl (a) and Gdm₂SO₄ (b) at 6 M and 42 °C. MD simulations of DNA and solvent with Gdm⁺ salts. Representative snapshots of DNA in the presence of Gdm₂SO₄ (d), and GdmCl (c) from MD trajectories. DNA is depicted in green ribbons with green surface. Water molecules within the DNA grooves (within 5 Å from nitrogen or oxygen atoms of nucleobases) are depicted as red balls, Cl⁻ in green, Mg²⁺ in purple, S in yellow, N in blue, O in red, and C in gray.

spectroscopically derived equilibrium constants exhibit temperature-dependent enthalpy terms (heat capacity changes ΔC_p). Consequently, the free enthalpy of reaction is no longer a monotonous function of temperature, this explains the seemingly counterintuitive rise and fall of “intact” DNA origami with increasing temperature. GdmCl, but not Gdm₂SO₄, significantly increased the heat capacity change between “intact” and “damaged” structures leading to destabilisation at higher concentrations (Fig. 1a, b). MD simulations indicate that the effect is caused by a more water-like and less charged hydration shell of GdmCl and its lack of ion pairing compared to Gdm₂SO₄.

The spectral simulation reproduces the temperature dependence of structural damages solely by allowing for a ΔC_p in the transition, particularly large for GdmCl which associates more strongly with the DNA at 5–6 M Gdm⁺ (Fig. 1) leading to highly organized water cation DNA H-bond networks in the minor and major grooves of the Gdm⁺ “saturated” state. In contrast, sulfate largely preserves the natural hydration (Fig. 1c, d). The high heat capacity of Gdm⁺-bound DNA is attributed to the cation's strong water-ordering action.

[1] Hanke, M. *et al.* (2022) *Comput. Struct. Biotechnol. J.* **20**, 2611–2623.

Preparation of a ^{233}Pa tracer for accelerator mass spectrometry of ^{231}Pa in environmental samples

J. Wolf,¹ A. Barkleit, S. Fichter,¹ R. Steudtner

¹HZDR, Institute of Ion Beam Physics and Materials Research, Dresden, Germany

^{233}Pa was separated from its mother nuclide ^{237}Np using the ion-exchange resin TEVA[®]. ^{237}Np was well retained on the resin, while the ^{233}Pa could be recovered in small yields. The used plastic vial has been identified as a potential sink of ^{233}Pa . Further investigations are in progress to establish a reliable ^{233}Pa source for ^{231}Pa AMS measurements of environmental samples.

Accelerator mass spectrometry (AMS) is an ultra-sensitive method for the detection of low concentrations of trace isotopes. It allows counting of single atoms, which are filtered according to their mass. This is advantageous to decay counting as even low abundance radionuclides with long half-lives can be detected.

The detection of isotopes of the actinides U, Np, Pu and Am are well established procedures at multiple AMS facilities. However, Pa is not yet routinely measured, and procedures for the preparation and detection of ^{231}Pa in environmental samples are currently being developed.^[1,2]

AMS is a relative detection method. To determine the concentration of ^{231}Pa ($t_{1/2} = 3.28 \cdot 10^4$ a), it is necessary to add a well-known amount of the isotope ^{233}Pa ($t_{1/2} = 26.98$ days) to samples. The ^{233}Pa also allows the determination of the efficiency of the entire measurement procedure and the monitoring of Pa losses during sample preparation. It can be easily detected by γ counting.

EXPERIMENTAL. The ^{233}Pa solution is typically prepared by separating ^{233}Pa from a stock solution of its mother nuclide ^{237}Np ($t_{1/2} = 2.14 \times 10^6$ a). Following the procedure developed by Medley *et al.*^[1] a column setup has been constructed. To 1 mL of a ^{237}Np stock solution in 3M HNO_3 , 1.5M sulfamic acid, 1.5M ascorbic acid, and Fe were added to adjust the oxidation state of Np to tetravalent, whereas Pa should stay in its pentavalent oxidation state. This solution was loaded onto a column containing the ion-exchange resin TEVA[®], which retains tetravalent Np in 3M HNO_3 . The Pa(V) was rinsed (“milked”) from this column using 50 mL of 3M HNO_3 . The ^{233}Pa and ^{237}Np activities were monitored *via* γ -detection of the 311.9 keV ^{233}Pa and the 29.4 keV ^{237}Np γ -rays in 5 mL sub-samples on an Ortec HPGe γ -ray detector (30% rel. efficiency).

RESULTS. The activities of ^{233}Pa and ^{237}Np in 1 mL of the ^{237}Np stock solution were (1.99 ± 0.06) kBq and (1.93 ± 0.04) kBq, respectively, indicating a secular equilibrium in this solution. For this activity measurement, 1 mL of the stock solution was put into a liquid scintillation counting (LSC) vial. After transferring the solution to the column and rinsing the vial with 3M HNO_3 , a γ -measurement of the empty vial was conducted to check for residues of the two radionuclides. While less than 0.05% of the original ^{237}Np activity was detected in the empty vial, a ^{233}Pa activity of (54.6 ± 1.7) Bq was detected, which corresponds to 2.8% of the original ^{233}Pa activity.

To rinse the ^{233}Pa from the column, 5 mL of 3M HNO_3 have been subsequently added to the column. A γ -measurement has been conducted for each 5 mL fraction. Previously, Medley *et al.* observed that the first 5 mL rinse contained large amounts of ^{237}Np bleed-through.^[1] This has been confirmed

by our measurement, where the first rinse contained ^{237}Np activities as high as (422 ± 9) Bq, while only (2.57 ± 0.36) Bq of ^{233}Pa were eluted from the column (not shown in Fig. 1). This fraction was reloaded onto the column. No ^{237}Np above the detection limit of 0.1 Bq was detected in the next 5 mL that was rinsed from the column.

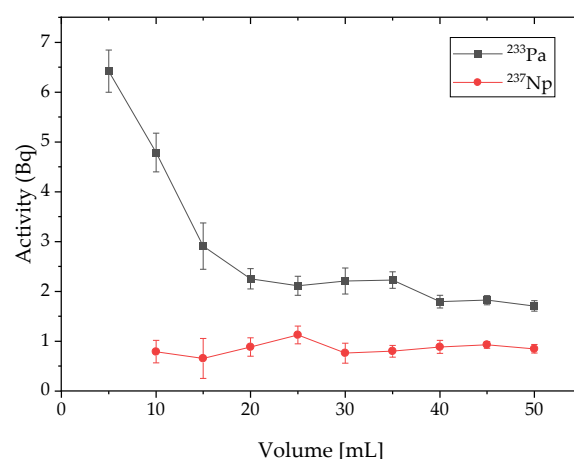


Figure 1. The activity of ^{233}Pa and ^{237}Np in each 5 mL fraction of 3M HNO_3 eluted from the column. The activity was determined by measuring the 311.9 keV and 29.4 keV γ -rays of ^{233}Pa and ^{237}Np , respectively.

The ^{233}Pa and ^{237}Np activities detected in the 50 mL rinsed from the column are shown in Fig. 1. The activity of ^{237}Np rinsed from the column is constant and below 1 Bq in all fractions. Most ^{233}Pa is eluted from the column in the first 15 mL. The amount of ^{233}Pa gradually decreases in each further 5 mL fraction rinsed from the column. While 99.6% of the ^{237}Np is retained on the column, only 1.4% of the ^{233}Pa has been eluted from the column. This is much less than the 95% recovery that has been reported recently.^[1]

CONCLUSION. As Pa is well known to adhere to most materials and the residue of ^{233}Pa in the LSC vial amounted to 2.8% of the total ^{233}Pa , it is feasible to assume that the ^{233}Pa is not retained by the resin but is attached to the column itself. To test this theory, separate γ measurements of the column and resin used in this experiment will be conducted to investigate the sink of ^{233}Pa . The development of a reliable procedure for the production of a ^{233}Pa solution is essential for future measurements of environmental ^{231}Pa .

[1] Medley, P. *et al.* (2019) *Nucl. Instrum. Methods Phys. Res. Sect. B-Beam Interact. Mater. Atoms* **438**, 66–69.

[2] Christl, M. *et al.* (2007) *Nucl. Instrum. Methods Phys. Res. Sect. B-Beam Interact. Mater. Atoms* **262**, 379–384.

SURFBIO – Innovation Hub for surface and colloid biology science

S. Schymura, R. Barros,¹ I. Deligiozi,² C. Furlan,³ B. Lapuente de Ojeda,¹ S. Martel-Martín,¹ R. Moreno,² B. Parakhonskiy,³ T. Rijavec,⁵ C. Rumbo,¹ A. Skirtach,³ M. Suarez Diez,⁴ A. Lapanje⁵

¹University of Burgos, Burgos, Spain; ²Axia Innovation, Munich, Germany; ³Wageningen University, Wageningen, The Netherlands; ⁴Ghent University, Ghent, Belgium; ⁵Jožef Stefan Institute, Ljubljana, Slovenia

Centered at Jožef Stefan Institute six top research and innovation partners across Europe are creating an innovation hub to study microbe-surface interactions using high-tech methodologies and equipment. The SURFBIO Innovation Hub aims to provide biotechnology researchers, academic institutions, industry and policy makers with training services and assessments to optimize novel materials for a variety of applications and will offer new, industry-oriented, research services opened to industry and institutions, covering all the needs in only one Hub, and collecting the activities together.

Understanding the interactions of colloids (microorganisms, nanoparticles and biomolecules) with surfaces and between themselves is a key factor that can lead to improvements in several fields, such as the biotechnology industry or the development of nano-carriers for drug delivery. As such the emerging field of Colloid Biology is positioned on the intersection between material science and molecular microbiology. The colloid-biological interactions can be studied and analyzed by applying different tools and techniques (Tab. 1). The SURFBIO Innovation Hub will give members of academia, industry and politics access to these techniques and/or training actions and assessments by establishing a European network hub centered at the Jožef Stefan Institute linking the different stakeholders.

Table 1. SurfBio project partners and expertise.

Institution	Field	Techniques
Axia Innovation	Innovation Management, Consulting	FAIR Data management
Ghent University	Nanobiotechnology	Raman-AFM, microfluidics
HZDR - IRE	Radioecology, Nanosafety	Interferometry, NP radiolabeling
Jožef Stefan Institute	Colloid Biology	LEGO-microbes
University of Burgos – ICCRAM	Materials biotechnology	Material synthesis, MultiOMICS
Wageningen University	Microbial systems biology	MultiOMICS data analysis

RESULTS. Within the SURFBIO project different innovative techniques for studying colloid biology-related structures (Fig. 1), such as artificial multispecies bio-aggregates, biofilms and bio-nano-constructs of bacteria and nanoparticles have been developed. These were compiled into a specialized “Handbook on the procedures for culturing and spectrometry techniques application in cell aggregation and biofilm development studies” and a “Handbook of good practices for FAIR data management” available to the public via the SURFBIO website.^[1] Additionally, training actions on “Wet-dry methodologies for studying cell-surface and cell-cell interactions” and “Analytical methods for the study of microbial cell- surface and surface-colloid interactions” have been devised and carried out in the form of publicly accessible webinar series (see SURFBIO YouTube channel^[2]) achiev-

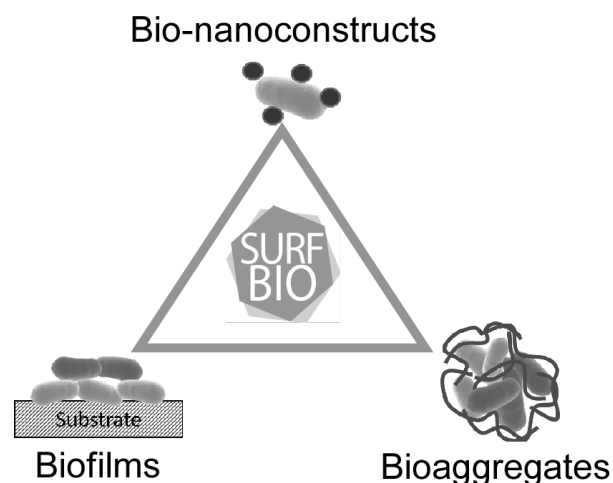


Figure 1. Research subjects of the SurfBio Innovation Hub concerning artificially constructed biostructures for applications. From biofilms (bottom, left), over multispecies bioaggregates (bottom, right) to complementary combinations of bacteria and nanoparticles (top).^[4–6]

ing a knowledge transfer from international experts to interested participants from all educational levels and across many academic fields. Furthermore, the “Week of Microbial Technologies” brought together experts from academia and industry representatives to present current research activities via invited talks and a poster session and to derive the chances, risks and needs for future hub activities in open round table discussions, as well as provide knowledge transfer via a hands-on training in “Experimental and computational approaches to study cell-cell interactions and cell-surface interactions”.^[3]

FUTURE IMPACTS. The SURFBIO project will lead to the establishment of a professional SURFBIO society to act as a network center with the goal of fostering microbial applications throughout Europe. Impacts will be:

- high-impact research results on surface and colloid biology
- improved knowledge transfer
- increased patenting
- increased peer-reviewed publications on the topic
- expanded range of testable samples
- contract research for industry
- boosted interest on surface and colloid biology
- standardization of methodologies
- new possibilities in analytical testing

ACKNOWLEDGEMENTS. The SURFBIO project has received funding from the European Union’s Horizon 2020 research and innovation program under the Grant Agreement No. 95237.

[1] <https://surfbio.eu/>.

[2] <https://www.youtube.com/channel/UCOHAecHyaknDdvnXui7QxEA>.

[3] <https://www.microtechweek.com/>.

[4] Deev, D. et al. (2021) *Front. Mater.* **8**, 624631.

[5] Verdel, N. et al. (2021) *Front. Microbiol.* **12**, 758702.

[6] Rybkin, I. et al. (2023) *Front. Bioeng. Biotechnol.* **10**, 1–11.

SCIENTIFIC CONTRIBUTIONS (PART IV)

Safety

Nuclear Reactor

**SAFETY
RESEARCH**

Research

Master Curve Testing of RPV steels using Mini-C(T) Specimens – Stable crack growth criteria and Censoring Statistics

A. Das,¹ P. Chekhonin, M. Houska, F. Obermeier,² E. Altstadt

¹Chair of Radiochemistry/Radioecology, Technische Universität Dresden, Dresden, Germany; ²Framatome GmbH, Erlangen, Germany

Neutron irradiation-induced embrittlement of the reactor pressure vessel (RPV) leads to the reduction of operating lifetime of nuclear reactors. Fracture mechanics testing of RPV steels reveals the shift in T_0 , which is related to the embrittlement of a material. To simplify the testing procedure, based on statistical data, we studied the impact of the slow stable crack growth censoring criterion of the ASTM E1921-21 standard on the determination of T_0 . We also present a statistically based strategy for an optimized test temperature selection. We found that the stable crack growth-censoring criterion did not influence T_0 significantly. We also successfully applied the new concept for selection of testing temperatures.

The selection of testing temperature in Master Curve testing is delicate as testing temperatures close to T_0 may lead to censoring due to the fracture toughness K_{Jc} exceeding the $K_{Jc,limit}$ and/or violating the $K_{Jc,\Delta a}$ stable crack growth criteria of ASTM E1921-21.^[1] On the other hand, testing at too low temperatures $T - T_0 < -50$ K also leads to test results being invalid. In this study, we develop a strategy to optimize the determination of the next test temperature to fulfill the validity criterion of $\sum r_i \cdot n_i \geq 1$. We also check the effect of the violation of the $K_{Jc,\Delta a}$ stable crack growth criterion (section 8.9.2 and 10.2.1 of ASTM E1921-21) on the determination of T_0 to simplify the Master Curve analysis procedure. With the help of a large number of Master Curve testing results of 0.16T mini-C(T) specimens we investigated the optimum test temperature selection as well as the stable crack growth criteria.

EXPERIMENTAL. For the censoring statistics a total number of 381 mini-CT tests from 11 different materials were considered (300 unirradiated, 81 irradiated). For the verification of the $K_{Jc,\Delta a}$ censoring criterion, we selected 156 tests from the 381 tests (89 unirradiated, 67 irradiated).

RESULTS. The number of censored and uncensored tests can be seen in Fig. 1 where the weighting factor n_i is highlighted for various temperature intervals as bars on top. The probability, that a test datum at a certain temperature will be censored (*i.e.*, $K_{Jc} > K_{Jc,limit}$ or $K_{Jc} > K_{Jc,\Delta a}$), can empirically be approximated by a tanh-fit (Eq. 1). The obtained fitting parameters are $c = 0.056$ and $T_{sh} = 7.9$ K.

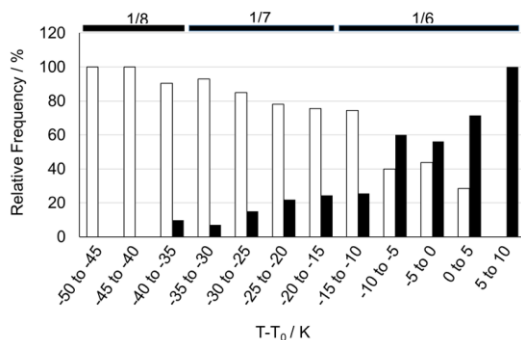


Figure 1. Relative frequencies of uncensored and censored data for various materials. The weighting factors (n) are shown for the different temperature ranges (bars on top).

$$P_c = 0.5 + 0.5 \cdot \tanh[c \cdot (T - T_0 + T_{sh})] \quad (1)$$

After the determination of a preliminary T_0 , the next test temperature (Eq. 2) is determined based on a target censoring probability defined by Eq. 3. Here the parameters $p = 0.7$ and $q = 1.1$ ensure $P_{c,trg} < 0.5 \forall s_m < 1$ and $r/N < 0.5$. The target censoring probability is shown in Fig. 2. This concept quantifies the balance between the two competing aspects of temperature selection: testing close to T_0 and avoidance of censoring.

$$T = T_0 - T_{sh} + \frac{1}{c} \cdot \arctan\left[\frac{P_{c,trg}-0.5}{0.5}\right] \quad (2)$$

$$P_{c,trg} = 0.05 + 0.9 \cdot \left[\min\left(\frac{s_m}{3}, 1\right)\right]^p \cdot \left[\frac{r}{N}\right]^q \quad (3)$$

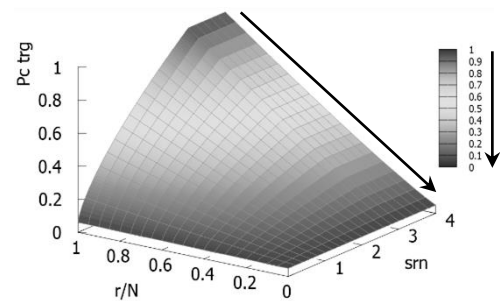


Figure 2. Target censoring probability as function of s_m and r/N .

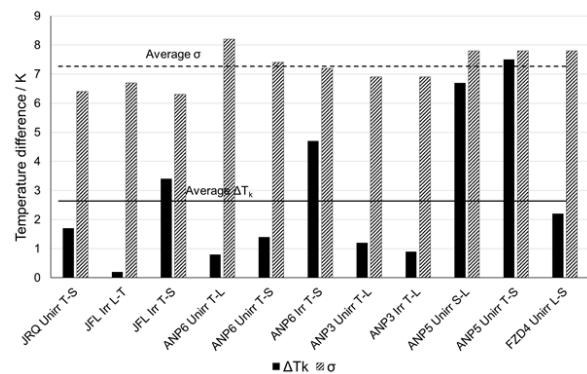


Figure 3. Reference temperatures for JRQ and JFL comparing the standard Charpy SE(B) and 0.16T C(T) specimens.

The inclusion of $K_{Jc,\Delta a}$ censoring criterion results in a small increase in T_0 as compared to the case when only the $K_{Jc,limit}$ censoring criterion is considered. Since this increase (ΔT_k) falls below the standard deviation (σ) of individual Master Curve tests (Fig. 3), it is reasonable to say that the impact of the slow stable crack growth censoring criterion on T_0 is insignificant. Therefore, to make the determination of T_0 simpler and to avoid additional analysis of the fracture surface, the $K_{Jc,\Delta a}$ censoring criterion could be removed.

ACKNOWLEDGEMENTS. We acknowledge the German BMWi project “Kleinproben” (FKZ 1501598A/B) and the EU-Euratom project “Fractesus” (contract no. 900014) for the financial support. We thank W. Webersinke, M. Roßner, V. Reinke, J. Pietzsch, and T. Welz for their valuable support.

[1] Test Method for Determination of Reference Temperature, T_0 , for Ferritic Steels in the Transition Range ASTM E1921-2021.

Helical dislocations and dislocation line decoration in ion-irradiated Fe-9Cr studied by scanning transmission electron microscopy

K. Vogel, H.-J. Engelmann,¹ P. Chekhonin, F. Bergner, C. Kaden

¹HZDR, Institute of Ion Beam Physics and Materials Research, Dresden, Germany

Irradiation-induced defects in an ion-irradiated Fe-9Cr model alloy were investigated by means of cross-sectional scanning transmission electron microscopy (STEM). Helical dislocations, which have been formed from pre-existing screw dislocations, are observed within the irradiated layer. These helices are decorated with small irradiation-induced dislocation loops. The presence of helical dislocations and their decoration by small loops resembles observations reported for neutron-irradiated Fe-9Cr.^[1] Hence we conclude that ion irradiations can produce similar defect configurations like neutron irradiations when the arrangement of pre-existing dislocations is comparable.

Fe-9Cr is a model alloy for investigating irradiation effects relevant for potential applications of high-chromium ferritic/martensitic steels in nuclear energy devices. Ion irradiation is a tool extensively used with the aim to emulate neutron damage that is characteristic for irradiation environments in fission or fusion reactors. Here we report on STEM studies of the microstructure of ion-irradiated Fe-9Cr with special emphasis on the effects of pre-existing dislocations.

EXPERIMENTAL. Irradiations with 8 MeV Fe³⁺ ions were performed with the 3 MV tandetron accelerator at the HZDR Ion Beam Center. Profiles of displacement damage and implanted ions were calculated using the binary collision code SRIM. Cross-sectional TEM specimens were prepared by focused ion beam (FIB) lift-out technique from <100> oriented grains after orientation mapping by means of electron backscatter diffraction. The microstructure was studied in a FEI Talos F200X (scanning) transmission electron microscope. Pre-existing dislocations and irradiation-induced defects were imaged in STEM mode using different diffraction vectors g . Dislocation Burgers vectors b were analyzed by means of the $g \cdot b$ invisibility criterion.^[2]

RESULTS. The most striking feature of the irradiated microstructure is the presence of helical dislocations. Figure 1 displays a STEM overview image of the irradiated layer and the non-irradiated substrate (Fig. 1a) together with the depth profiles of displacement damage and implanted ions calculated by SRIM (Fig. 1b). In the depth range of highest concentration of implanted ions, a dark band is visible similar to the bands with high concentrations of small dislocation loops observed in previous studies.^[3] In the area above the dark band, where the level of displacement damage is high, but the concentration of implanted ions is low, helical dislocations are observed (see Figs. 1c and 1d for higher magnification). These helices are aligned at an angle of approximately -45° with respect to the [100] direction of the body centered cubic crystal lattice. No helices are present in the non-irradiated substrate. Here we observe straight line dislocations that show the same alignment as the helices. From the results of the Burgers vector analyses, we conclude that the straight dislocations have a dominating screw component and that the helices have been formed from this type of pre-existing dislocations.

The higher magnified images in Figs. 1c and 1d reveal large numbers of small dislocation loops that are decorating the

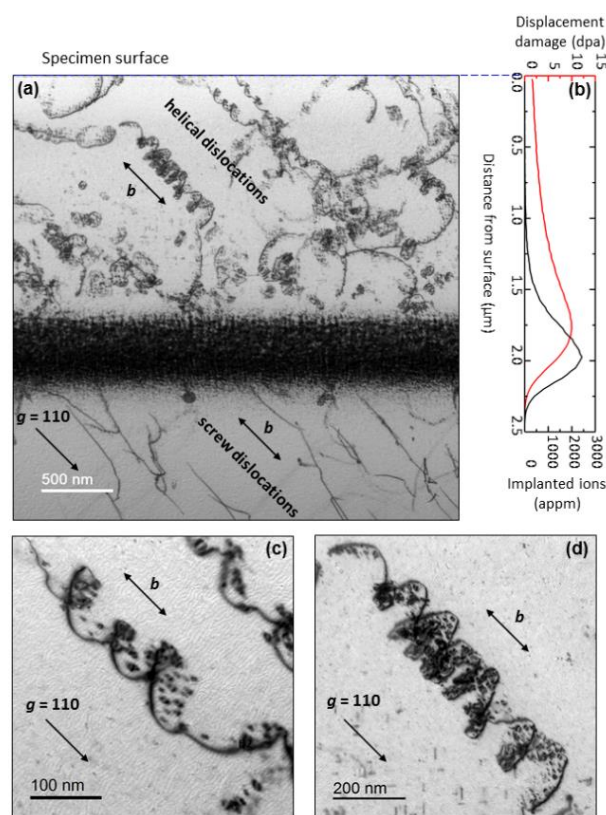


Figure 1. STEM images and damage profiles of Fe-9Cr irradiated with 8 MeV Fe³⁺ ions. Overview image (a), higher magnified images of helical dislocations (c), (d). Profiles of displacement damage and concentration of implanted ions (b).

helical dislocations. The loops, which appear as black dots or in so-called coffee bean contrast, are located within the helices mostly following the dislocation line.

A presence of helical dislocations and their decoration by small dislocation loops was reported by Haley *et al.* for neutron-irradiated Fe-9Cr.^[1] Hence we conclude that ion-irradiations can produce similar defect configurations within the depth range of low concentration of implanted ions, provided that the arrangement of pre-existing dislocations is comparable.

ACKNOWLEDGEMENTS. This work received funding from the European Commission within the project M4F (Euratom research and training programme 2014-2018 under grant agreement No 755039). The irradiations were carried out at the Ion Beam Center (IBC) at HZDR by Dr. S. Akhmalaliev. The use of the IBC TEM facilities and support by its staff is gratefully acknowledged. In particular, we thank Dr. R. Hübner for support during the STEM investigations.

[1] Haley, J. C. *et al.* (2019) *Acta Mater.* **181**, 173.

[2] Williams, D. B., Carter, C. B (2009) *Transmission Electron Microscopy*, Springer, New York.

[3] Vogel, K. *et al.* (2021) *Nucl. Mater. Energy* **27**, 101007.

Small-angle neutron scattering applied to low-dose neutron-irradiated ferritic/martensitic steel Eurofer97

A. Ulbricht, F. Bergner, U. Keiderling¹

¹Helmholtz-Zentrum Berlin, Berlin, Germany

Ferritic/martensitic (F/M) Cr steels are candidates for nuclear fission and fusion applications. The reduced-activation F/M 9%Cr steel Eurofer97 (E97) was developed and qualified as a structural fusion material resisting neutron irradiations up to 100 dpa (displacements per atom).^[1] The effect of low neutron doses in the range 0.1–0.6 dpa on the radiation-induced microstructural changes of E97 was studied by means of small-angle neutron scattering (SANS). We have found that E97 exhibits an even weaker irradiation effect than a high-purity binary Fe9Cr model alloy.

EXPERIMENTAL. Samples of the 9%Cr steel Eurofer97 (E97) and the binary Fe9Cr model alloy were exposed to neutron irradiation at 290 °C in the BR2 materials testing reactor of SCK-CEN. The SANS experiment was conducted at the beamline V4 of Helmholtz-Zentrum Berlin. Saturation magnetic fields of 1.5 T oriented perpendicular to the neutron beam were applied to the samples to separate magnetic and nuclear scattering components. The measured magnetic SANS cross section can be expressed as

$$\frac{d\Sigma_{\text{mag}}}{d\Omega}(Q) = \Delta\eta_{\text{mag}}^2 c_R V(R) |F(Q, R)|^2 dR \quad (1)$$

with the scattering vector $Q = (4\pi/\lambda)\sin(\theta/2)$. θ is the scattering angle, $\lambda = 0.45$ nm the neutron wavelength, F the form factor of spherical scatterers of radius R and V the volume of the sphere. c_R and $\Delta\eta_{\text{mag}}^2$ are the volume fraction of scatterers per size increment and the magnetic scattering contrast, respectively. Eq. (1) was solved by way of fitting the measured magnetic scattering curves to obtain the size distribution of scatterers $c_R(R)$. More details of the procedure are given in the published literature.^[2]

RESULTS. Figure 1(a) summarizes the measured magnetic difference scattering curves (with the unirradiated reference condition subtracted) along with the best fits derived according to Eq. (1) for the 0.1 and 0.6 dpa irradiations of E97. The SANS data for a binary Fe9Cr alloy irradiated in the same irradiation experiment as E97 up to 0.1 dpa are also included.^[3] The size distributions of irradiation-induced scatterers obtained for E97 and Fe9Cr are plotted in Fig. 1(b). We have found that nanostructures of radii smaller than 2 nm formed as a result of neutron irradiation of all considered materials. The total volume fraction of scatterers depends on both the neutron fluence and the alloy composition.

The measured ratios between magnetic and nuclear scattering contributions (so-called A-ratio) and the total volume fractions of irradiation-induced scatterers are listed in Tab. 1. The A-ratio is an indicator of the composition of the scatterers. Values of 1.4 and 2.0 are expected for nanovoids and Cr-rich α' -phase particles, respectively. The results indicate that nanovoids are the dominant type of scatterers in 0.1 dpa Fe9Cr, but are absent or play a minor role in 0.6 dpa E97. A candidate type of scatterers in E97 are α' -phase particles. As the solubility limit of Cr in α -Fe at 290 °C (irradiation temperature) is close to 9%, the formation of a small amount of α' in E97 is indeed possible. However, solute rich clusters of unknown composition cannot be excluded.

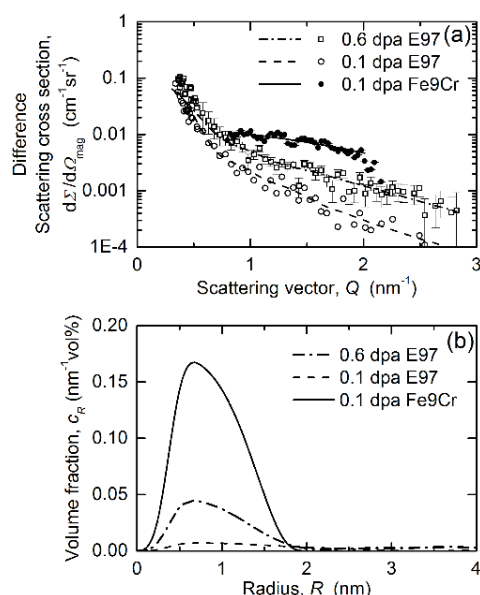


Figure 1. Magnetic difference scattering curves of Eurofer97 along with fits (a) and reconstructed size distribution of irradiation-induced scatterers for neutron-irradiated Eurofer97 (b). Results obtained for a binary Fe9Cr alloy are included for comparison.

Table 1. Characteristics of irradiation-induced scatterers.

Material/condition	Volume fraction (%)	A-ratio
E97 0.6 dpa	0.055 ± 0.005	2.2 ± 0.5
E97 0.1 dpa	0.019 ± 0.003	–
Fe9Cr 0.1 dpa ^[3]	0.15 ± 0.01	1.45 ± 0.1

The total volume fraction of scatterers deduced from magnetic SANS for irradiated E97 increases by a factor of about 3 at increasing neutron fluence by a factor of 6. For the 0.1 dpa irradiation of E97, the volume fraction is about eight times smaller than for the binary Fe9Cr alloy irradiated under the same condition. This confirms the exceptionally high irradiation resistance of E97 at low neutron fluences.

The major reason of the good irradiation resistance of E97 is the high dislocation density (10^{14} m^{-2} for E97 as compared to 10^{13} m^{-2} for Fe9Cr) in combination with a smaller grain size (2 μm for E97 as compared to 25 μm for Fe9Cr), the latter meaning a larger specific grain boundary area. Both, the dislocations and the grain boundaries act as efficient sinks for irradiation-induced point defects. The loss of point defects in turn gives rise to slower diffusion of solute atoms and lower concentrations of irradiation-induced point-defect clusters, hence good radiation resistance.

ACKNOWLEDGEMENTS. Delivery of neutron-irradiated samples from SCK-CEN is gratefully acknowledged.

[1] Ehrlich, K. et al. (2000) *J. Nucl. Mater.* **283–287**, 79–88.

[2] Ulbricht, A. et al. (2022) *J. Appl. Cryst.* **55**, 702–712.

[3] Konstantinovic, M. et al. (2020) *J. Nucl. Mater.* **540**, 152341.

A new approach to the bulk-equivalent hardness of thin ion-irradiated layers

F. Bergner, C. Kaden, A. Das, P. Hähner¹

¹JRC Petten, The Netherlands

Ion irradiation is a beneficial tool to emulate the damage of nuclear structural materials exposed to neutron irradiation. However, the small penetration depth of ions (~1 μm) poses a challenge for the derivation of bulk-equivalent properties. Nanoindentation was applied to study the effect of 5 MeV Fe ions on the indentation response of an Fe-9Cr model alloy. The combination of a modified Nix-Gao model of the indentation size effect with a composite hardness of the layer-substrate system was found to be vital for the determination of the bulk-equivalent hardness of the layer.

EXPERIMENT. Samples of dimensions 10 × 10 × 1 mm were prepared by way of mechanical and subsequent electrolytic polishing and irradiated at the Ion Beam Center of HZDR with Fe²⁺ ions of 5 MeV energy (temperature 300 °C). The depth profile of ion damage in units of displacements per atom (dpa) was calculated using the binary collision code SRIM and approximated as a box-like profile (effective layer) of 1.36 dpa ranging to a depth of 1.65 μm.

Nanoindentation was done on top of the irradiated surface using a UNAT-type device (ASMEC) equipped with a Berkovich diamond indenter and operated in the quasi-continuous stiffness mode. The indentation hardness H_{IT} was calculated as function of the indentation contact depth h_c by averaging over 20 to 30 indentation tests. The applied procedures are reported in more detail elsewhere.^[1]

RESULTS. The experimental results are shown in the format of Nix-Gao plots in Figs. 1 and 2 for unirradiated and ion-irradiated Fe-9Cr, respectively. Figure 1 indicates an indentation size effect, that is, H_{IT} increases at decreasing h_c ("smaller is harder"). This effect was originally substantiated by Nix and Gao (ONG model) in terms of geometrically necessary dislocations (GNDs) formed during the indentation process, thus introducing a characteristic length h^* and a bulk-equivalent hardness H_0 , Eq. (1).^[2]

$$H_{IT} = H_0 \sqrt{1 + \frac{h^*}{h_c}} \quad (1)$$

The ONG model (dashed straight line) fits the data well at lower values of $1/h_c$. However, there are systematic deviations from a straight line at higher values of $1/h_c$, which are assumed to be due to the unbounded growth of the density of GNDs according to Eq. (1). A better description of the da-

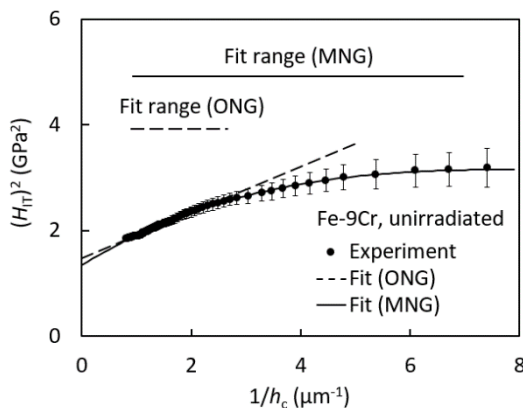


Figure 1. Nix-Gao plot of indentation hardness for unirradiated Fe-9Cr.

ta is achieved by introducing a maximum allowable density ρ_m of GNDs, resulting in a modified Nix-Gao (MNG) model, Eq. (2).^[1] The new length parameter \bar{h} is related to ρ_m . Indeed, the MNG model (solid line in Fig. 1) results in a good fit of the experimental data in a wider range of h_c .

$$H_{IT} = H_0 \sqrt{1 + \frac{h^*}{h_c} \exp\left(-\frac{\bar{h}}{h_c}\right)} \quad (2)$$

For ion-irradiated Fe-9Cr, the situation is more complex. The indentation plastic zone, which is assumed here to be a half-sphere of radius proportional to h_c , partly reaches into the unirradiated substrate, see inset in Fig. 2. Hence a composite hardness has to be considered. Here we assume linear superposition and weights given by the volume fractions f_i and f_u of the plastic zone occupied by the irradiated layer and the unirradiated substrate, respectively, Eq. (3):

$$H_{IT} = f_i H_i + f_u H_u \quad (3)$$

H_i and H_u can then be introduced according to Eq. (1) (original Nix-Gao model, ONG-2) or Eq. (2) (modified Nix-Gao model, MNG-2) with generally different sets of parameters H_0 , h^* and \bar{h} . The resulting fit curves are included in Fig. 2. We have found that the model MNG-2 provides a good fit in a wider range of h_c as compared to ONG-2, in particular toward smaller values of h_c . For a comprehensive discussion of the fit parameters we refer to the published literature.^[1] The focus here is on the bulk-equivalent hardness H_0 , which was found to be 1.97 GPa for the irradiated layer (model MNG-2) as compared to 1.16 GPa for the unirradiated substrate (model MNG). The irradiation-induced increase of H_0 of 0.81 GPa for the 1.36 dpa ion irradiation is approximately three times larger than the increase of 0.27 GPa reported for a sample of Fe-9Cr neutron-irradiated up to 0.11 dpa.^[1] This is indeed reasonable.

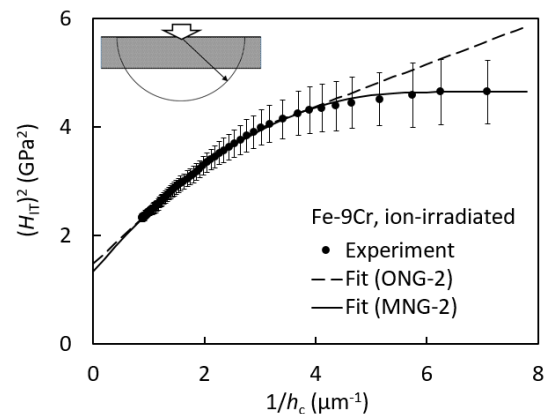


Figure 2. Nix-Gao plot of indentation hardness for ion-irradiated Fe-9Cr.

ACKNOWLEDGEMENT. This work has received funding from the Euratom research and training program 2014-2018 under grant agreement No. 755039 (M4F project). The ion irradiation was performed at the Ion Beam Center of HZDR. Many thanks to S. Akhmadaliev for support.

[1] Bergner, F. et al. (2022) *J. Appl. Phys.* **132**, 045101.

[2] Nix, W.D. and Gao, H. (1998) *J. Mech. Phys. Solids* **46**, 411–425.

Characterization of brittle fracture initiation sites in reactor pressure vessel steels

P. Chekhonin, A. Das, F. Bergner, E. Altstadt

Neutron embrittlement of reactor pressure vessel (RPV) steels limits the safe operational time of nuclear reactors. Microcracks in RPV steels which may lead to brittle fracture are known to originate from cleaved precipitates, inclusions or grain boundaries, which eventually lead to brittle fracture. So far, very little work has been dedicated to detailed fractography, which revealed the size and type of the feature found in the crack nucleation center. Additionally, the effect of neutron irradiation on microcrack nucleation is unknown. In the present work, detailed fractography and metallography is performed on a RPV steel in both its unirradiated as well as neutron irradiated state.

EXPERIMENTAL. The IAEA reference RPV base metal steel JFL available in the unirradiated as well as neutron-irradiated state ($8.67 \times 10^{19} \text{ n/cm}^2$ ($E > 1 \text{ MeV}$); $T_{\text{irradiation}} = 255^\circ\text{C}$). Master Curve testing was performed on 41 unirradiated and 36 neutron-irradiated 0.16T mini-C(T) samples extracted from standard Charpy SE(B) specimens. The unirradiated samples have been tested at temperatures between -142°C and -125°C , while the temperature range for neutron irradiated samples was between -80°C and -50°C .^[1] Dedicated fractography in combination with energy dispersive X-ray spectroscopy (EDX) were carried out in a Zeiss EVO 50 scanning electron microscope (SEM).

RESULTS. For more than one third of all samples, the presence of a large particle at the fracture initiation site could be excluded and the microcrack nucleated at a grain boundary. In the majority of all cases, a particle in the center of the initiation site has been identified.^[2] Those particles are either Mo-rich carbides (Fig. 1) or Al-rich inclusions (Fig. 2). In comparison, the metallographic analysis of the bulk steel reveals Mo-rich and Mn-rich carbides. Larger Mo-rich carbides occur less frequent than the Mn-rich carbides by at least two orders of magnitude, while larger Al-rich inclusions were not observable on a polished sample at all. Only a small fraction of observable carbides is Mo-rich which are responsible for fracture. Thus, the present work demonstrates a discrepancy between particles found in brittle fracture initiation sites and particles that are directly observable in bulk steel. Some of the initiating particles are extremely rare in the bulk.

Disregarding a few exceptions, the cleavage fracture stress obtained from finite element modeling calculations does not depend on the type of initiation, nor on the particle size. Therefore, the critical event that leads to global failure of the sample, is the propagation of a microcrack across a grain boundary. The cleavage fracture stress does not depend on the estimated size of the grain involved at the initiation site, while the size of the identified grains varies by one order of magnitude. Consequently, the required stress for the transmission of a microcrack through a grain boundary has to strongly depend on the type of the grain boundary, rather than on a stress based upon a Griffith criterion.

There are no major differences between unirradiated and neutron irradiated steel with respect to fracture initiation sites. While Al-rich particles were more frequently found in neutron irradiated samples, the authors suspect material inhomogeneities as the primary reason.

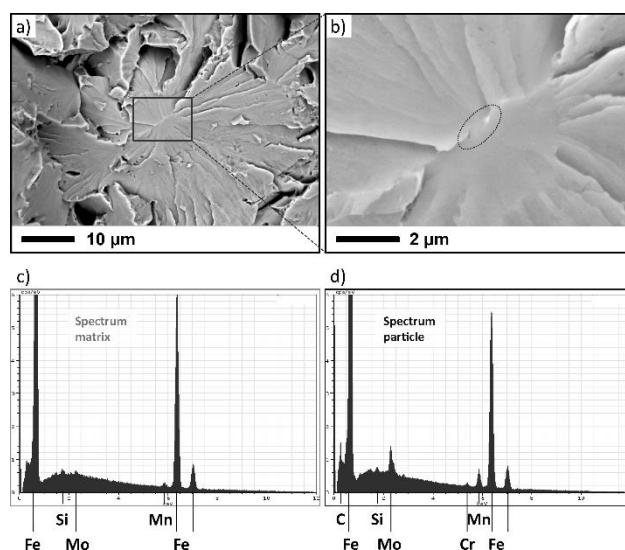


Figure 1. SEM backscatter electron micrographs of an initiation site containing a Mo-rich carbide (unirradiated sample) (a), the framed section is shown at higher magnification in (b). EDX spectrum of the metal matrix (c) and EDX spectrum of the Mo-rich carbide (d).

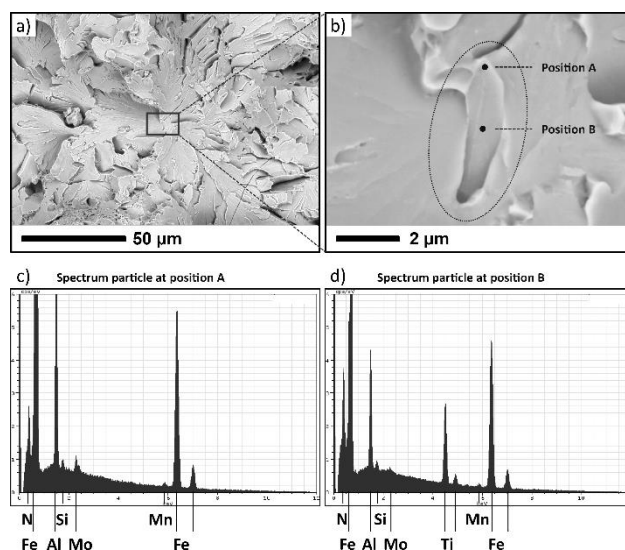


Figure 2. SEM backscatter electron micrographs of an initiation site containing an Al-rich inclusion (unirradiated sample) (a), the framed section is shown at higher magnification in (b). EDX spectra of two different positions of the Al-rich inclusion (c, d).

ACKNOWLEDGEMENTS. The authors acknowledge the financial support of this research by the German BMWi project “Kleinproben” (FKZ 1501598A/B) and express their gratitude to M.Houska, W.Webersinke, V.Reinke, J.Pietzsch, and T.Welz for their valuable technical support. Support by the Structural Characterization Facilities Rossendorf at IBC is gratefully acknowledged.

[1] Das, A. et al. (2023) Nucl. Mater. Energy, submitted.

[2] Chekhonin, P. et al. (2023) Nucl. Mater. Energy, submitted.

ESFR-SIMPLE: a new Euratom project on Sodium Fast Reactor safety

E. Fridman

The new Euratom project ESFR-SIMPLE is briefly presented here.

European Sodium Fast Reactor – Safety by Innovative Monitoring, Power Level flexibility and Experimental research (ESFR-SIMPLE) is a 4-year project launched on October 1st, 2022 in the frame of Euratom Research and Training Programme 2021–2022. The total project budget is around 8 Mio EUR of which 3 Mio EUR is the EU contribution. The ESFR-SIMPLE consortium comprises 15 partners in total:

- Eleven beneficiaries from EU states, namely University of Liege (Belgium), HZDR, KIT (Germany), CEA, EDF, Framatome, University of Lorraine (France), ENEA, POLIMI (Italy), University of Latvia (Latvia), and Slovak University of Technology (Slovakia).
- Four associated partners from EPFL, PSI (Switzerland), University of Cambridge (UK), and ANL (USA).

PROJECT OBJECTIVES. ESFR-SIMPLE is a follow-up of two European projects (FP7 CP-ESFR and H2020 ESFR-SMART) dedicated to design and safety studies on European Sodium Fast Reactor (ESFR).^[1,2] The goal of ESFR-SIMPLE is to improve safety and economics of the current ESFR design through adaptation of alternative or/and innovative technologies. The specific objectives include:

- Exploration of the impact of transition to alternative fuel form (*i.e.* metallic instead of mixed-oxide) and utilization of compact secondary system design on economics and safety.
- Development of a Small Modular Reactor (SMR) version of ESFR and assessment of its potential for simplification of the reactor design and increasing its economic competitiveness. Typical SMR features such as transportability, modularization, and standardization to be considered.
- Development and assessment of advanced methods for monitoring and processing of operational data using Artificial Intelligence (AI).
- Generation of new experimental data for assessment of innovative reactor components.
- Dissemination, education, and training activities com-

– bined with investigation of social aspects and assessment of public perception.

PROJECT STRUCTURE. The structure of ESFR-SIMPLE is shown in Fig. 1. The project contains 8 technical, 1 educational, and 1 administrative Work Packages (WP). Educational WP1 to WP8 are grouped into three sub-projects (SP):

- SP1 (WP1-WP2): “Advanced components and innovative monitoring for large ESFR”. This includes assessment of the metallic fuel option, optimization of the secondary system design, and development of the AI-based engine dedicated to preventive maintenance.
- SP2 (WP3-WP5): “Opportunities and challenges of ESFR-SMR”. This SP covers core and system design of ESFR-SMR, its safety assessment, and studies related to ESFR-SMR integration into future electrical grids.
- SP3 (WP6-WP8): “Experiments in support of technological developments”. This SP is dedicated to development and assessment of critical components related to reactor passive safety, development and testing of various measuring techniques for the detection and characterization of gas bubbles in sodium, as well as new experiments and analytical studies related to characterization of MOX fuel.

HZDR PARTICIPATION. At HZDR, two different Departments participate in the project, namely Department of Reactor Safety (FWOR) from Institute of Resource Ecology and Department of Magneto-Hydro-Dynamics (FWDH) from Institute of Fluid Dynamics. FWOR leads WP3 and contributes to WP1, WP4, WP5, and WP9 while FWDH leads WP7 and contributes to WP2 and WP9.

[1] Fiorini, G. L. *et al.* (2011) Nucl. Eng. Des. **241**, 3461–3469.
 [2] Mikityuk, K. (2022) ASME J. Nuclear Rad. Sci. **8**, 010305.

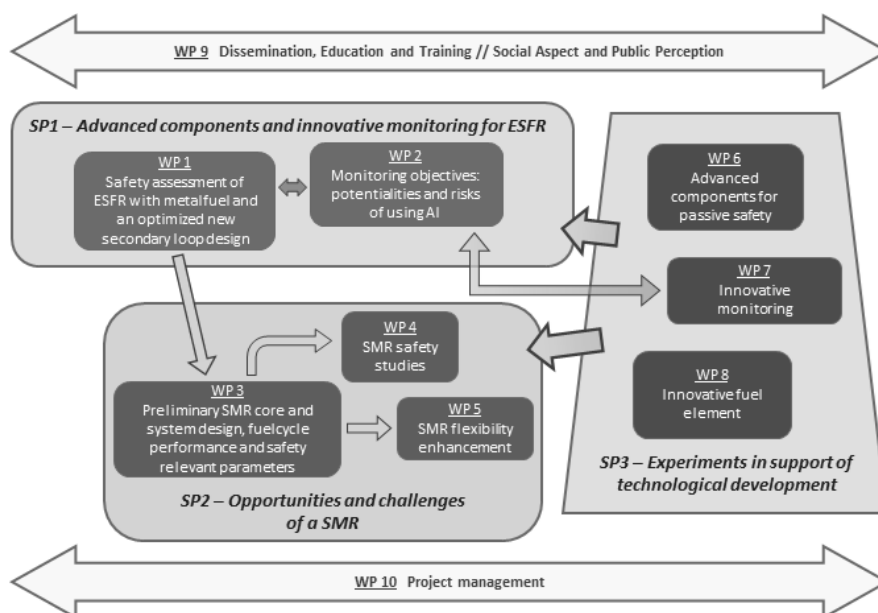


Figure 1. Project structure.

Experimental activation determination of metal foils placed inside a German nuclear power plant for validation of neutron fluence calculations

A. Barkleit, R. Rachamin, J. Konheiser

Different metal foils were placed at various positions in a nuclear power plant (NPP) for monitoring the neutron fluence during one working cycle. The activation was determined using gamma spectrometry. Activation products resulting from high-energy neutrons could only be determined near the reactor pressure vessel (RPV), whereas activation by thermal neutrons was detected even outside the exterior biological shielding.

After the final shutdown of a nuclear power plant (NPP), the dismantling and decommissioning of the NPP has to be prepared very carefully. One of the important tasks is to require precise knowledge about the activation of the reactor pressure vessel (RPV), the biological shielding, and other internal components of the NPP. The specific activities can be calculated with Monte-Carlo codes. To validate the results of such calculations, experimental determination of the neutron fluence using appropriate activation monitors is crucial. Here, the experience of reactor dosimetry was used.

EXPERIMENTAL. Metal foils (listed in Tab. 1) of variable dimensions (thickness of 0.1–2 mm and size of 8 mm diameter or 10×10 mm to 30×30 mm), corresponding to masses from 0.02–13 g, were packed in Kapton tape and stored in aluminum boxes.^[1] These neutron flux monitors were placed and recovered during the annual revision of the NPP. The smallest samples were placed at positions with very high neutron flux, *e.g.*, near the reactor pressure vessel. The biggest samples were placed at positions with a very low neutron flux, *e.g.*, behind the exterior biological shielding (Fig. 1). The samples were irradiated during one reactor working cycle (approximately one year) and after recovery analyzed by gamma spectrometry.

Table 1. Metals used as activation monitors, activation reactions and respective characteristic data*.

Metal	Activation reaction	Effective neutron energy	t _{1/2} *
Ti	⁴⁶ Ti (n,p) ⁴⁶ Sc	> 1.5 MeV	84 d
Fe	⁵⁴ Fe (n,p) ⁵⁴ Mn	> 1.0 MeV	312 d
	⁵⁸ Fe (n,γ) ⁵⁹ Fe	Thermal	45 d
Ni	⁵⁸ Ni (n,np) ⁵⁷ Co	> 8.5 MeV	272 d
	⁵⁸ Ni (n,p) ⁵⁸ Co	> 0.5 MeV	71 d
Cu	⁶³ Cu (n,α) ⁶⁰ Co	> 2.5 MeV	5.3 y
Zn	⁶⁴ Zn (n,γ) ⁶⁵ Zn	Thermal	244 d
In	¹¹³ In (n,γ) ^{114m} In	Thermal	50 d
Sn	¹¹² Sn (n,γ) ¹¹³ Sn	Thermal	115 d
Ta	¹⁸¹ Ta (n,γ) ¹⁸² Ta	Thermal	14 d

*: half-life of the activation product.

Metal foils were measured with an HPGe Gamma detector (Ortec, 30% efficiency). To avoid interfering overlap of gamma emissions or masking of low activities by very high ones, the samples were measured in different packages: (Ti + Cu), (Ni + Fe), (In + Sn + Zn) and (Ta). Measuring time was varied depending on the activation between 15 min (high activated In, Sn, Zn, and Ta) and 16 h or up to 65 h (Ti + Cu).

RESULTS. The activation reactions of the used metals cover a broad range of neutron energy (Tab. 1). This is important

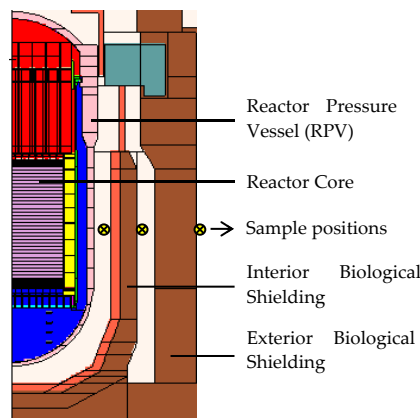


Figure 1. 3D MCNP (Monte-Carlo N-Particle transport code) model of a German PWR (Power Water Reactor) and respective sample positions.

Table 2. Measured activities of neutron flux monitors at different horizontal positions at the level of the reactor core centre (see Fig. 1).

Nuclide*	Activities (Bq/g)		
	near RPV	behind biological shielding Interior	Exterior
⁴⁶ Sc	4.0×10 ²	< DL	< DL
⁵⁴ Mn	7.4×10 ²	5.0	< DL
⁵⁹ Fe	2.0×10 ³	5.7×10 ²	< DL
⁵⁷ Co	3.2×10 ²	1.3	< DL
⁵⁸ Co	2.1×10 ⁴	1.9×10 ²	< DL
⁶⁰ Co	2.0×10 ¹	< DL	< DL
⁶⁵ Zn	2.0×10 ⁵	2.5×10 ⁴	1.6
^{114m} In	8.5×10 ⁵	1.2×10 ⁵	6.2
¹¹³ Sn	2.4×10 ⁴	2.5×10 ³	1.1×10 ⁻¹
¹⁸² Ta	2.2×10 ⁷	1.1×10 ⁵	8.9×10 ¹

*: pristine metals and isotopes see Tab. 1.

for a comprehensive picture comparing measurements and calculations. The activation quantity of the chosen metals depends on the neutron cross-section, the effective neutron energy range, and the position in the NPP. Under consideration that thermal neutrons in combination with a high cross-section provoke the highest activation (*i.e.*, Zn, In, Sn, Ta), we could measure the activation of these metals even outside the biological shielding. In contrast, activation with high energy neutrons (*e.g.*, ⁴⁶Sc from Ti, ^{57/58}Co from Ni, ⁶⁰Co from Cu) could only be measured near the RPV or partly behind the interior biological shielding (see Tab. 2) due to the effective protection capability of the biological shielding. As recently shown, the computational results agree very well with the experimental ones.^[2]

ACKNOWLEDGEMENTS. We kindly thank the TUD Central Radionuclide Laboratory for their support with the gamma measurements. This work is funded by the German Federal Ministry of Education and Research (BMBF) under contract number 15S9409A and supported by PreussenElektra GmbH.

[1] Rachamin, R. *et al.* (2020) Report HZDR-110, p. 65.
[2] Rachamin, R. *et al.* (2021) Report HZDR-113, p. 78.

Radiological characterization of FA-centering pins irradiated during a German PWR operation

R. Rachamin, J. Konheiser

In a German PWR, the fuel assemblies (FAs) positions in the reactor core are centralized by FA-centering pins. The FA-centering pins are mounted on the grid plate placed above the core. Each FA is centralized by two pins immersed in designated bores in the FA's head. During the reactor operation, the pins are irradiated by the neutron fluence streaming from the core. Due to the short distance to the core, these are particularly strongly activated. Therefore, knowledge of the activation level in the pins removed from the reactor is essential for better planning their disposal. In this study, the specific activity of the pins was calculated with a novel method based on the combined use of two Monte-Carlo codes, MCNP and FLUKA. The results of the calculations were obtained with great accuracy and can be used as guidelines for the planning of the discharged pins disposal and storage.

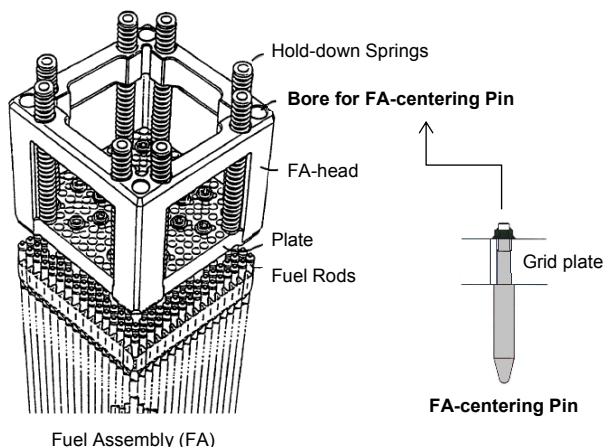


Figure 1. Illustration of the FA-centering pin and its location inside the FA.

ACTIVATION EVALUATION. The FA-centering pin illustrated in Fig. 1 has a total height of about 10 cm. It comprises a cylindrical part and a truncated cone part. The specific activity of each FA-centering pin in the reactor was calculated using the MCNP-FLUKA codes sequence.^[1] In the first step, the MCNP code was used to calculate the neutron fluence rate characteristics (spectrum, distribution, and current entering the pin surfaces) in the studied pin segment using a 3D detailed model of a German PWR.^[2] A schematic view of the reactor model (with a highlight on the FA-centering pins) is shown in Fig. 2. The neutron fluence rate prediction capability of the MCNP model was validated using neutron fluence monitors placed inside two German PWRs. The validation studies showed that the MCNP model is reliable and suitable for evaluating the neutron radiation field in the reactor for the ensuing activation calculations.^[3,4] In the second step, the FLUKA code was used to calculate the specific activity in the studied pin segment using a 3D exact model of the pin and complex source terms built based on the neutron fluence rate parameters computed using the MCNP code.^[5] The specific activity of the pins at the reactor's end of life (EOL) is shown in Fig. 3. As can be noted, the pin activation map is proportional to the neutron fluence distribution in the core, where the highest activity is in the central pins, and the lowest is in the peripheral pins. With respect to the pin activation map at the reactor's EOL, after 1, 5, and 10 years

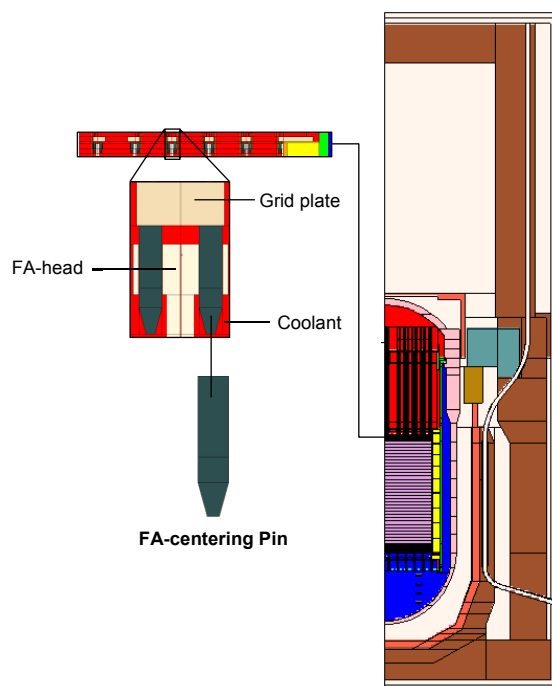


Figure 2. MCNP model of a German PWR.

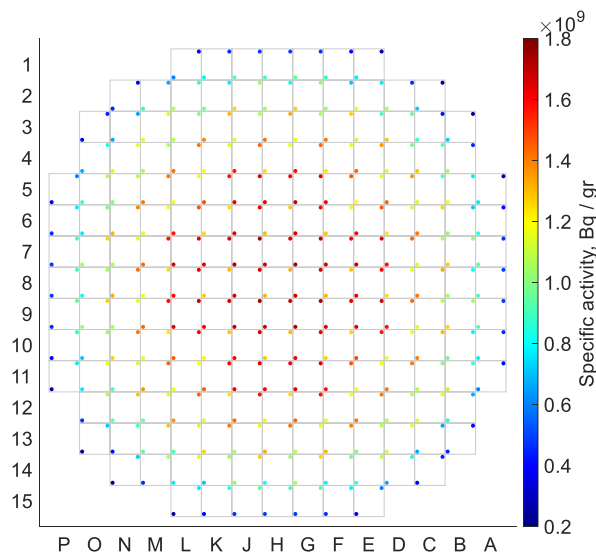


Figure 3. Specific activity of the FA-centering pins at the EOL.

of cooling time, the activation level of the pins drops by about a magnitude of 1, 2, and 7, respectively.

ACKNOWLEDGEMENTS. This work is funded as part of the PreussenElektra GmbH project "Activity calculation".

- [1] Rachamin, R. *et al.* (2022) SATIF-15.
- [2] Goorley, T. *et al.* (2012) *Nucl. Technol.* **180**, 298–315.
- [3] Rachamin, R. *et al.* (2021) KONTEC 2021.
- [4] Rachamin, R. *et al.* (2022) ICRS 14 / RPSD-2022.
- [5] Battistoni, G. *et al.* (2015) *Ann. Nucl. Energy*, **82**, 10–18.

Estimation of the number of burst fuel rods in a Large-Break Loss-of-Coolant Accident

M. Jobst, F. Schäfer

In the framework of the R2CA project, a 3D model of the reactor pressure vessel (RPV) and reactor core has been combined with a rod behavior model including deformation and burst of fuel rods, taking also into account the feedback from thermo-mechanics to the thermo-hydraulic model. With the new model, simulations of the Large-Break Loss-of-Coolant Accident (LB-LOCA) have been performed and the number of burst fuel rods has been estimated. It has been found that the 10% criterion defined by German licensing guidelines for PWR might be exceeded if conservative initial and boundary conditions are applied. Furthermore, an asymmetric distribution of the burst rods has been observed.

An important goal to be reached in the framework of the R2CA project are new methodologies to estimate the number of burst rods during LOCA more accurately. This is a necessary prerequisite for quantifying the source term, *i.e.*, the amount of fission products released from the core into the containment and further to the environment. According to German licensing guidelines for PWR, the emergency core cooling system (ECCS) has to be designed such that at maximum 10% of the fuel rods burst during the LB-LOCA accident (to limit the source term).^[1] To estimate that number, a detailed core model has been developed for the system code ATHLET-CD. The code provides a fuel rod behavior model which includes among other phenomena the deformation and burst of fuel rods.^[2]

During a LB-LOCA transient, strong asymmetric conditions can be observed. Therefore, the modelling of local distribution of thermal-hydraulic phenomena is essential. This is reached by application of a multi-channel approach for the RPV and the reactor core, which is modelled by 193 parallel inter-connected thermal-hydraulic channels (one channel for each fuel assembly). The 57,900 fuel rods of the core are grouped among each assembly according to their power level and modelled by 772 representative fuel rods (4 per assembly). Beside analyses with a realistic power distribution taken directly from core simulator results obtained for a generic German PWR, additional simulations have been performed with a top-peaked power profile (more unfavorable conditions). The LB-LOCA transient is initiated at full power with double-ended guillotine break of the cold-leg of the loop connected to the pressurizer.

RESULTS. The maximum cladding temperatures of the 772 representative fuel rods are shown by Fig. 1 (case with conservative top-peaked power profile). After a first temperature peak observed during the discharge phase of the LOCA transient, a second temperature rise occurs during the re-flooding of the reactor core until approx. 75 s all rods are quenched. From the detailed temperature evolutions, peak cladding temperatures (PCT) have been derived (red trace Fig. 1, right). Due to elevated cladding temperatures, decreasing pressure in the RPV but still high pressure inside the fuel rods, the cladding starts to creep after 20 s, which leads to burst of rods within a few seconds (38% hoop strain is applied as burst criterion in the model). In total 105 representative fuel rods burst ($\hat{=} 7875$ real rods = 13.6%), *i.e.*, the 10% criterion is exceeded for this case with conservative power profile. The rod deformation leads to reduction of the flow cross-sections in the core with reduction of core cooling capabilities. Neglecting this effect in the simulation leads to

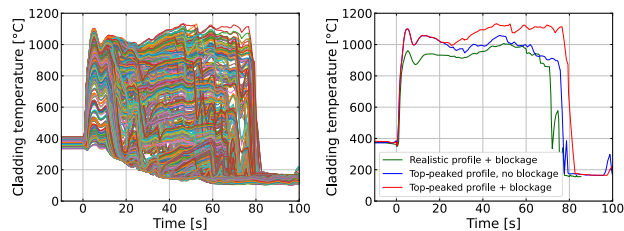


Figure 1. Cladding temperatures of all 772 representative fuel rods (left) and comparison of peak cladding temperatures for selected cases (right).

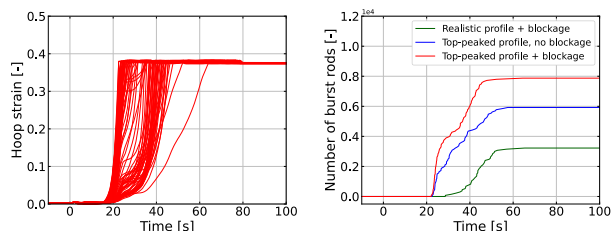


Figure 2. Hoop strain of those rods that reach the burst criterion (left). Comparison of number of burst rods (right).

reduced PCT and a lower number of burst rods (10.2%). If a realistic power profile is applied instead of conservative one, lower PCT and lower number of burst rods are found (green curves in Fig. 1/2).

The distribution of burst rods across the core has been determined (Fig. 3) with the max. hoop strain reached during the transient for the realistic power profile case. Dark red color indicates those rods that exceed the burst criterion. An asymmetric distribution of the burst rods is observed, with no burst rods in the core quadrant close to the broken loop (loop 2). That is explained by the higher mass flow rates in that region directed downwards to the downcomer connected to the broken loop, which leads to reduced cladding temperatures. This observation is in contrast to previously published core damage extent analyses with symmetrical distribution of failed rods.^[3,4] That emphasizes the importance of the application of a 3D model for realistic LOCA analysis.

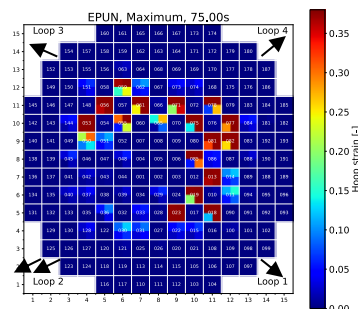


Figure 3. Distribution of hoop strain at the end of the LOCA transient.

ACKNOWLEDGEMENTS. This project has received funding from the Euratom research and training program 2014–2018 under grant agreement No 847656.

- [1] RSK (1998) RSK guidelines for pressurized water reactors, 3rd Ed.
- [2] Lovasz, L. *et al.* (2021) ATHLET-CD 3.3 User's Manual.
- [3] Heins, L. (2004) Core Damage Extent Analysis.
- [4] Pettersson, K. *et al.* (2009) OECD NEA report No. 6846.

NuScale control rod ejection transient benchmark

Y. Bilodid, E. Fridman

The EU Horizon 2020 project McSAFER is dedicated to evaluation of safety assessment methods for Small Modular Reactors (SMR). This paper proposes a transient multiphysics benchmark based on the NuScale SMR design and show results obtained with standard PWR methods.

The McSAFER is a 3-year H2020 Euratom project launched in September 2020.^[1] The project aims at improving safety analysis methodologies for small modular reactors (SMRs) by employing high-fidelity Monte Carlo (MC) based multiphysics reactor analysis tools developed in the preceding European projects NURESAFE, HPMC and McSAFE.^[2-4] One of the important tasks of McSAFER is to compare the performance of these high-fidelity tools and “traditional” diffusion-based methods as applied to transient analysis of different light water-cooled SMRs.

The comparison between different computational chains is performed in a stepwise manner by gradually increasing the complexity of the simulated cases. The performance assessment comprises static neutronic calculations, steady-state coupled neutronics/TH analyses, and finally, coupled neutron-kinetics/thermal-hydraulic (TH) simulations of selected reactivity-initiated transients (RIA).

BENCHMARK. NuScale is an integrated Pressurized Water Reactor (PWR) SMR concept with reactor vessel, pressurizer, and helical steam generators placed inside a compact containment vessel. The primary coolant system is a pump-free with a coolant flow driven by natural circulation. The expected power output is equal to 160MWth or 50MWe (Fig. 1).

The transient type chosen for the NuScale concept is the accidental ejection of control rod assembly (CRA) from the core. The NuScale control system comprises two regulating CRA banks (RE1 and RE2) and two shutdown banks (SH3 and SH4). The selected scenario considers ejection of a single regulating CRA from approx. Power Dependent Insertion Limit (PDEL) at 75% power level. The scenario is “realistic” and is analyzed in the Safety Analysis Report.

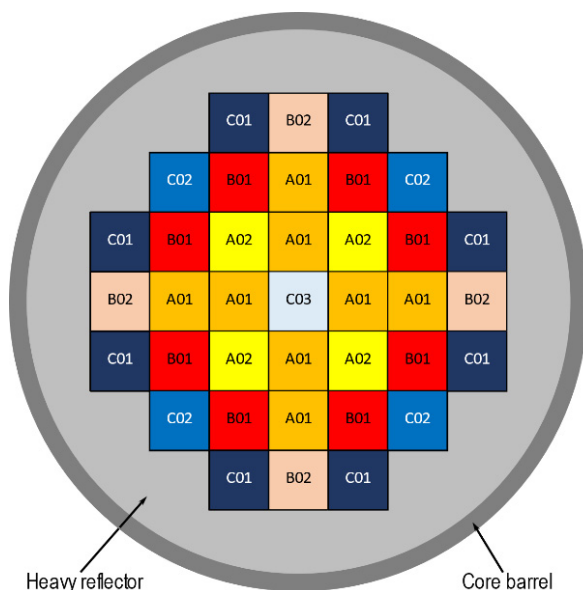


Figure 1. NuScale core.

RESULTS. Transient calculation of NuScale were performed by HZDR and other McSAFER partners using 4 different 3D full core simulators namely, DYN3D, ANTS, PANTHER, and SIMULATE5/S3K.

All codes predicted similar maximum power of 102.0%, 101.9%, 100.0%, and 102.4% for DYN3D, Ants, Panther, and SIMULATE respectively (upper panel of Figure 2). SIMULATE slightly overestimated the ejected reactivity which is in line with the steady state results. The ejected reactivity estimated *via* steady state and dynamic calculations are in very good agreement *i.e.* 169 *vs.* 170 pcm for DYN3D, 160 *vs.* 165 pcm for Panther, and 182 *vs.* 186 pcm for SIMULATE (middle panels of Fig. 2). It should be noted that currently the Ants code is not capable of calculating dynamic reactivity. Lower panel of Fig. 2 compares 3D core power peaking factor (Fq). From 0 to 2 s within the transient (before SCRAM), the difference in Fq between the codes does not exceed 0.1%. After SCRAM, the differences between the codes noticeably increased, especially for SIMULATE. Nevertheless, the importance of Fq is also reduced due to the fast drop in the core power after SCRAM.

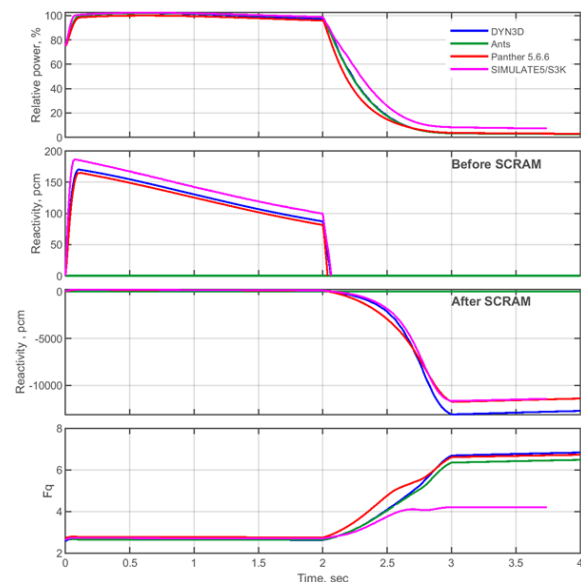


Figure 2. Transient results.

ACKNOWLEDGEMENTS. This project has received funding from the European Union’s Horizon 2020 research and innovation program under grant agreement No 945063.

- [1] Sanchez-Espinoza, V. H. *et al.* (2021) *Energies* **14**, 6348.
- [2] Chanaron, B. (2017) *Nucl. Eng. Des.* **312**, 1–7.
- [3] Demazière, C. *et al.* (2020) *EPJ Nuclear Sci. Technol.* **6**.
- [4] Sanchez-Espinoza, V. H. *et al.* (2021) *EPJ Web Conf.* **247**.

Model validation of a VVER-440 and surrounding area

E. Poenitz, J. Konheiser, S. Baier

For the validation of geometry models of the units 1 to 4 of the Greifswald NPP, spectral neutron fluences, reaction rates and specific activities were calculated for increasing distances to the fission zone. Calculations were carried out with the radiation transport codes MCNP and TRAMO. In addition to last year's article, the results of an experiment from the 7th cycle of unit 3 of the Greifswald NPP are now presented. The measurement of ex-vessel activation detectors allows the comparison of reaction rates for positions as far as 1 meter below the lower edge of the fission zone. As in the earlier validation, a considerable height shift is required to achieve a good agreement between calculations and measurement. The comparison of MCNP and TRAMO results also provided helpful insights.

In 1984/85, an ex-vessel activation detector measurement was carried out during the 7th cycle of unit 3 of the Greifswald NPP.^[1] Activation detectors were positioned at five angles for 10 height positions each. In contrast to an earlier investigated measurement for the 12th cycle of unit 1, not all of the positions were provided with a complete set of activation detectors.^[2, 3] Even with a less comprehensive data set, 192 data points are available. Moreover, the activation detectors cover a height region from the center of the fission zone to approx. 1 m below the lower edge of the fission zone. Prior to the activity measurements of reactor pressure vessel (RPV) samples in the scope of the research project WERREBA, these measured data were the ones with the largest distance to the fission zone.^[4] They are therefore especially valuable for the validation of the extended radiation transport model which is developed for the decommissioning of the Greifswald NPP. Reaction rates were calculated with the radiation transport codes MCNP and TRAMO. Additional simulations for RPV samples of several units served a comparison of spectral neutron fluences and specific activities.

RESULTS. Measured and calculated $^{54}\text{Fe}(n,p)^{54}\text{Mn}$ reaction rates are shown in Fig. 1. For the height positions 1 to 5 adjacent to the fission zone, a good agreement of measurements and calculations can be seen. For the height positions 6 (lower edge of the fission zone) to 8, increasing deviations are observed. For the two lowest height positions 9 and 10, the overestimation of the measured reaction rates becomes smaller again. This strange behavior is observed for all reactions. It can be best explained by the assumption of a vertical shift of the data points. In Fig. 2, ratios of calculated and ex-

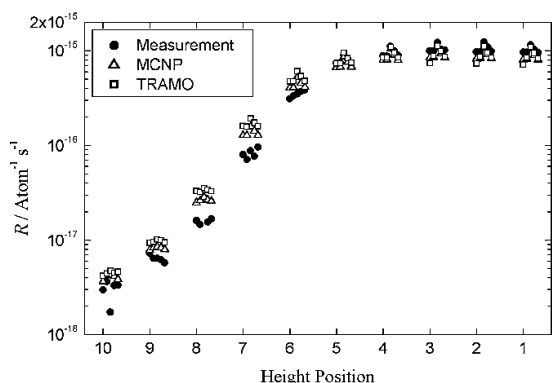


Figure 1. Measured and calculated $^{54}\text{Fe}(n,p)^{54}\text{Mn}$ reaction rates. For better visibility, the data points for different angles have small offsets.

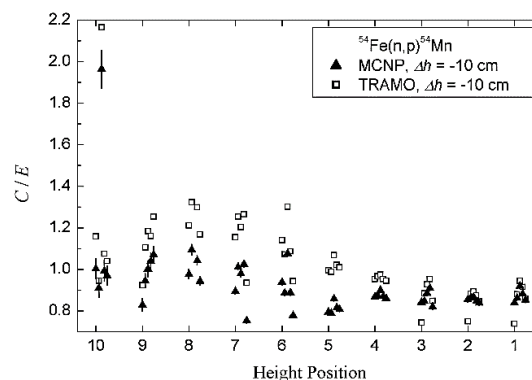


Figure 2. Ratio of calculated and experimental $^{54}\text{Fe}(n,p)^{54}\text{Mn}$ reaction rates. A vertical shift of 10 cm is assumed.

perimental reaction rates are shown. Here, an assumed height shift of 10 cm leads to a better agreement of measurements and calculations. Due to the strong scatter of the C/E ratios for the lowest height positions, the shift is somewhat ambiguous. A decrease of the reaction rates by more than 2 orders of magnitude with increasing distance to the fission zone can be recognized. Compared to the threshold reactions, the decrease is less steep for (n,γ) reactions like $^{59}\text{Co}(n,\gamma)^{60}\text{Co}$. However, it strengthens the expectation that the neutron activation in regions of the RPV distant from the fission zone is much smaller and might even go below the specific clearance/exemption levels of the Radiation Protection Ordinance. Additional simulations using MCNP's cell flagging capability reveal that essentially all neutrons in the lowest height positions were backscattered by the annular water tank. It indicates that neutrons are primarily transported through the small gap between RPV and annular water tank. This so-called streaming effect is regarded as especially challenging for Monte-Carlo neutron transport calculations.

CONCLUSIONS. In spite of the improved C/E ratios and the good agreement of the reaction rates obtained with both radiation transport codes, some comparisons remained inconclusive. Fast neutron fluences of RPV samples of unit 2 of the Greifswald NPP calculated with MCNP and TRAMO showed a good agreement for positions adjacent to the fission zone but deviate for a position 1.6 m below the lower edge of the fission zone. The comparison with measured specific activities of RPV samples of several units lead to mixed results and pointed to improvements of the radiation transport model.

ACKNOWLEDGEMENTS. This work is supported within the research framework FORKA, German Federal Ministry of Research and Education (WERREBA project: Grant Number 1559412).

- [1] Mehner, H.-C. *et al.* (1987) Report ZfK-623.
- [2] Mehner, H.-C. *et al.* (1988) Report ZfK-RPM 6/88.
- [3] Poenitz, E. *et al.* (2022) Report HZDR-119, p. 86.
- [4] Yassin, G. *et al.* (2022) Report HZDR-119, p. 85.

Steam line break analysis applied to NuScale small modular reactor (SMR) with ATHLET-DYN3D in the framework of the EU H2020 McSAFER

E. Diaz-Pescador, S. Kliem

NuScale SMR is modelled by HZDR in the framework of the EU H2020 McSAFER project. This contribution summarizes the modelling approach and simulation results applied to a steam line break sequence with the coupled thermohydraulic/neutronic system code ATHLET-DYN3D. The results at steady state show agreement with the design certification application (DCA) report. The transient results demonstrate the inherent safety of the reactor design provided by the compact steam generators, which enhance flow mixing along the downcomer and force coolant temperature homogenization at the core inlet boundary, thereby preventing a core re-criticality.

MODELLING APPROACH. NuScale is a SMR of integral pressurized water reactor (iPWR) type, operated with light water driven by natural circulation in all operation modes, with a nominal rated core thermal power of 160 MWt.^[1] One of the most prominent features of NuScale are the two compact helical coil steam generators (HCSG) embedded in the upper downcomer region. The curved geometry of the 1,380 HCSG tubes ensures symmetry in the reactor coolant system (RCS) by enhancing fluid mixing along the flow field towards the reactor core. The presented work corresponds to Task 5.1, which is based on multi-physics calculations by the coupled system code ATHLET-DYN3D applied to a reactor topology built upon traditional methods or single channel approach.^[2] The layout of the integral vessel computational model is displayed in Fig. 1.

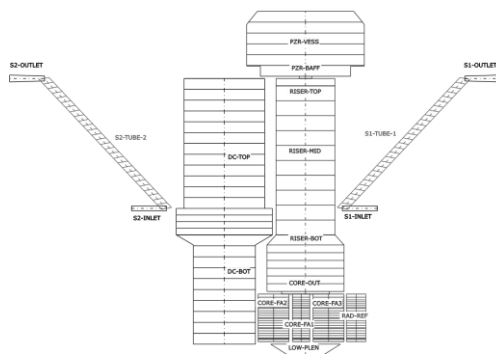


Figure 1. NuScale integral vessel layout with ATHLET-DYN3D.

ACCIDENT SCENARIO. The postulated initiating event is a non-isolable double-ended break in one of the two steam lines. The 3-D neutronic calculation by DYN3D is performed with a XS-library developed with Serpent based on a 4-neutron group homogenized nuclear constants for UO₂ fuel assemblies, control rod banks and heavy reflector. The transient calculation is started with fresh fuel (no decay heat) at hot full power and beginning of cycle.

SIMULATION RESULTS. The results at steady state show overall agreement with the DCA report (Tab. 1), with a deviation on the secondary-side pressure. The authors are currently working to improve this issue by the implementation of heat transfer and friction correlations for curved ducts. In any case, the influence of this deviation on the transient calculation will be rather limited.

Table 1. Results at Steady State Calculation.

Parameter	Unit	DCA	HZDR	Error (%)
Reactor Power	MW	160.00	160.00	0.00
RCS Pressure	MPa	12.75	13.08	2.61
Core average temperature	K	563.71	557.97	-1.01
Core mass flow	kg/s	496.17	494.53	-0.33
Pressurizer level	%	60.00	58.35	-2.75
HCSG outlet temperature	K	–	584.31	–
HCSG outlet pressure	MPa	3.689	3.424	-7.18
Main steam line mass flow	kg/s	67.06	67.06	0.00

The transient calculation shows that the affected HCSG boils-off and undergoes a rapid depressurization shortly after the two break valves are opened (200 % flow area), leading to reactor trip upon “low main steam pressure” at 2.17 s. The reactor symmetry imposed by the arrangement of the two HCSGs and the single channel modelling approach limit the coolant temperature decrease at the core inlet due to flow mixing, mostly in the downcomer lower region. The positive reactivity introduced by the Doppler and moderator temperature feedbacks is rapidly offset by the insertion of the control rods after reactor scram, with a reactivity balance of approximately -24\$ at 100 s. The temporal evolution of the primary and secondary side pressures and core mass flow rate is depicted in Fig. 2. The affected HCSG undergoes a rapid depressurization down to atmospheric pressure (1 bar), whereas the pressure inside the intact HCSG increases shortly after isolation. Pressure inside the RCS decreases progressively after reactor scram and from 50 s onwards, the decrease is controlled by the actuation of the decay heat removal system. The primary loop flow drops dramatically shortly after reactor scram since burnup is not credited in the simulation (WP5.1 specifications).

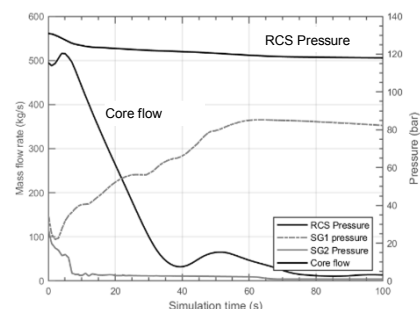


Figure 2. System pressures vs. core mass flow rate.

ACKNOWLEDGEMENTS. McSAFER has received funding from the Euratom research and training programme 2019-2020 under grant agreement No 945063.

- [1] NuScale Power LLC (2018) NuScale Standard Plant Design Certification Application, U.S. Nuclear Regulatory Commission (NRC).
- [2] Sanchez-Espinoza, V. *et al.* (2021) *Energies* **14**, 6348.

Transverse isotropic radial core expansions by means of coordinate transformation

E. Nikitin, E. Fridman

The Coordinate Transformation Method (CTM) is a tool to simulate small structural deformations that typically happen in Sodium cooled Fast Reactor (SFR) cores while having high impact on the reactor behavior. The nodal diffusion code DYN3D already contained such method in order to model uniform radial core expansions.^[1,2] Recently, the applicability of the CTM was extended to model transverse isotropic radial core expansions, i.e. symmetrical core flowerings. In this report, the first verification phase is presented using a simplified representation of a non-uniformly expanded SFR core.

BRIEF OUTLINE OF THE METHOD. With CTM, the coordinate system (x, y, z) of the radially expanded grid is transformed to another coordinate system (ξ, η, z) such that the mesh becomes equivalent to the initial unperturbed hexagonal mesh. Consequently, the differential equation of neutron diffusion has to be transformed. In the previous papers, the mathematical formulation of CTM was described in detail, showing that radial expansion leads to a simple correction of the diffusion coefficient D for the radial direction:

$$D' = \left(\frac{d}{d_0}\right)^{-2} D, \quad (1)$$

where d and d_0 are the expanded and unperturbed assembly pitch size.^[2,3] The implementation of CTM into DYN3D was tested for simplified cases in order to verify the functionality of the method itself. These tests were performed with the rectangular solver since it has the freedom of using a mixture of fine and coarse horizontal meshing as opposed to the hexagonal solver.

MODELLING APPROACH. An ad-hoc homogeneous SFR reactor core was constructed for the testing. It contains only square homogenized fuel assemblies of one type derived from the outer region of the large oxide SFR core of the OECD/NEA benchmark.^[4] The homogenized cross sections (XSs), parametrized by diagrid radial expansion, were generated using the Serpent code.^[5,6] The fissile XSs were filled into a rectangular mesh consisting of 17×17 assemblies with ten axial layers. The initial quadratic pitch was set to 20 cm and the nodal height to 10 cm. The 3D full core was radially expanded using two methods:

- *Direct approach:* An extra layers of thin nodes are added in x and y directions as seen in Fig. 1, left. At initial (unexpanded) state, the fuel material is filled in every node but in the extra nodes on the rim. During the calculation of this state, the rim-nodes has to behave as transparent medium for neutrons. When the core expands, the excess fuel material fills these rim-nodes completely.
- *CTM:* The coordinate system (x, y, z) of the radially expanded core is transformed to another coordinate system (ξ, η, z) such that the radial mesh becomes equivalent to the initial unperturbed mesh (Fig. 1, right).

VERIFICATION METHODOLOGY. The verification of CTM for non-uniform core expansions was done against the direct approach as reference in three stages:

1. *Initial state:* Calculation of the initial not expanded states.
2. *Uniform expansion:* Calculation of the uniformly expanded core to demonstrate equivalence of the methods.

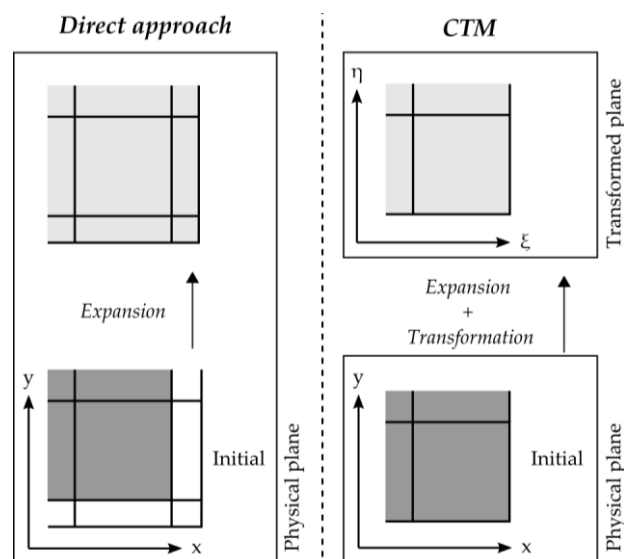


Figure 1. Radial expansion with direct approach (left) and CTM (right).

3. *Non-uniform expansion:* Comparison in case of a non-uniformly expanded core. The upper half of the core was radially expanded by 1%, while the lower half remained in the initial state.

RESULTS. The results are summarized in Tab. 1. The solutions of the initial state are identical. In case of uniform expansion, the calculated reactivity effect of 1% uniform core expansion is -579 pcm. The agreement between CTM and the reference is very good, as the difference in k_{eff} is -0.8 pcm. The calculated reactivity effect of 1% radial expansion only in the upper half of the core is about -285 pcm. Here, the obtained k_{eff} values are also in a very good agreement, as the difference is -0.9 pcm.

Table 1. Comparison of k_{eff} values between CTM and the direct approach.

Case	Direct approach	CTM	Δ (pcm)
Initial state	1.00915 6	1.00915 6	0.0
Uniform exp.	1.00329 7	1.00328 9	-0.8
Non-uniform exp.	1.00626 3	1.00625 4	-0.9

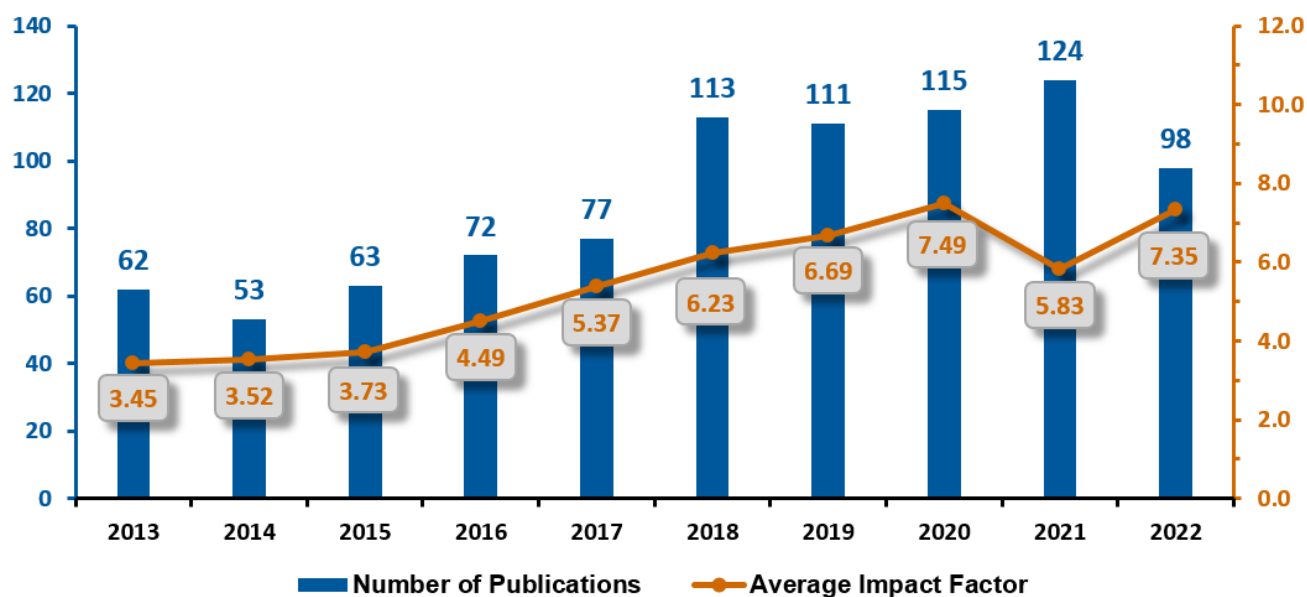
CONCLUSIONS. As a proof of concept, simple radial core expansions were modeled on a simplified homogenous SFR core. The simplifications allowed to create reference solutions with DYN3D by using the direct expansion approach. The CTM matched the reference solution within 1 pcm of the effective multiplication factor and proved its function to model symmetrical flowering.

ACKNOWLEDGEMENTS. The research leading to these results was partially funded by the Euratom research and training programme 2014-2018 under grant agreement No 754501.

- [1] Rohde, U. et al. (2016) *Prog. Nucl. Energy*, **89**, 170–190.
- [2] Nikitin, E. et al. (2019) *M&C 2019 Proc.*, 1624–1631.
- [3] Azekura, K. et al. (1989) *J. Nucl. Sci. Technol.* **26**, 374–378.
- [4] Blanchet, D. et al. (2011) *AEN – WPRS Sodium Fast Reactor Core Definitions (version 1.2)*, OECD/NEA.
- [5] Leppänen, J. et al. (2015) *Ann. Nucl. Energy* **82**, 142–150.
- [6] Nikitin, E. et al. (2015) *Ann. Nucl. Energy* **75**, 492–497.

- ARTICLES (PEER-REVIEWED)
- FURTHER CONTRIBUTIONS
 - ORAL PRESENTATIONS
 - MEDIA CONTRIBUTIONS
 - THESES

ARTICLES (PEER-REVIEWED)



Statistics on the publication activity of the Institute of Resource Ecology (IRE) within the last 10 years. The diagram considers peer-reviewed articles that were published under primary responsibility of the institute. Note that the given impact factors are based on data from 2022. The annual update might change the statistics retrospectively.

The following compilation provides peer-reviewed articles and further publications published in 2022 (online first) representing any contribution of members of the Institute of Resource Ecology.

Alcalde, J.; Carbonell, R.; Pospiech, S.; Gil, A.; Bullock, L. A.; Tornos, F.

Preface: State of the art in mineral exploration

Solid Earth 13, 1161–1168 (2022).

Doi: 10.5194/se-13-1161-2022.

Al Danaf, N.; Kretzschmar, J.; Jahn, B.; Singer, H.; Pol, A.; Camp, H. J. M. O. D.; Steudtner, R.; Lamb, D. C.; Drobot, B.; Daumann, L. J.

Studies of Pyrroloquinoline Quinone Species in Solution and in Lanthanide-dependent Methanol Dehydrogenases

Physical Chemistry Chemical Physics 24, 15397–15405 (2022).

Doi: 10.1039/D2CP00311B.

Arnold, F. M.; Liu, T. J.; Kuc, A. B.; Heine, T.

Structure-imposed electronic topology in covered graphene nanoribbons

Physical Review Letters 129, Article No. 216401 (2022).

Doi: 10.1103/PhysRevLett.129.216401.

Bansal, D.; Kaden, P.; Patzschke, M.; März, J.; Schmidt, M.

Comparative Analysis of Mononuclear 1:1 and 2:1 Tetravalent Actinide (U, Th, Np) Complexes: Crystal Structure, Spectroscopy, and Electrochemistry

Inorganic Chemistry 61, 10509–10520 (2022).

Doi: 10.1021/acs.inorgchem.2c01405.

Bazarkina, E.; Laskar, C.; Kokh, M. A.; Hazemann, J. L.;

Foulon, S.; Leynaud, O.; Desmaele, E.; Pokrovski, G. S.

Contribution of X-ray Spectroscopy to Mineralogy: Exploring Platinum Using High-Energy Resolution Fluorescence Detection X-ray Absorption Spectroscopy, HERFD-XAS

Minerals 12, 1602 (2022).

Doi: 10.3390/min12121602.

Bergner, F.; Kaden, C.; Das, A.; Merino, S.; Diego, G.; Hähner, P.

Nanoindentation applied to ion-irradiated and neutron-irradiated Fe-9Cr and Fe-9Cr-NiSiP model alloys

Journal of Applied Physics 132, Article No. 045101 (2022).

Doi: 10.1063/5.0098807.

Bezzina, J. P.; Neumann, J.; Brendler, V.; Schmidt, M.

Combining Batch Experiments and Spectroscopy for realistic Surface Complexation Modelling of the Sorption of Americium, Curium, and Europium onto Muscovite

Water Research 223, Article No. 119032 (2022).

Doi: 10.1016/j.watres.2022.119032.

Bodi, J.; Ponomarev, A.; Mikityuk, K.

Analysis of sodium boiling initiated by unprotected loss of flow in European sodium fast reactor core with different subassembly designs

Nuclear Engineering and Design 399, Article No. 112014 (2022).

Doi: 10.1016/j.nucengdes.2022.112014.

- Boelens, P.; Bobeth, C.; Hinman, N.; Weiß, S.; Zhou, S.; Vogel, M.; Drobot, B.; Azzam, S. S. A.; Pollmann, K.; Lederer, F.
Peptide functionalized Dynabeads for the magnetic carrier separation of rare-earth fluorescent lamp phosphors
Journal of Magnetism and Magnetic Materials 563, Article No. 169956 (2022).
Doi: 10.1016/j.jmmm.2022.169956.
- Bollermann, T.; Yuan, T.; Kulenkampff, J.; Stumpf, T.; Fischer, C.
Pore network and solute flux pattern analysis towards improved predictability of diffusive transport in argillaceous host rocks
Chemical Geology 606, Article No. 120997 (2022).
Doi: 10.1016/j.chemgeo.2022.120997.
- de Bona, E.; Popa, K.; Walter, O.; Cologna, M.; Hennig, C.; Scheinost, A. C.; Prieur, D.
Oxidation of Micro- and Nanograined UO₂ Pellets by in Situ Synchrotron X-ray Diffraction
Inorganic Chemistry 64, 1843–1850 (2022).
Doi: 10.1021/acs.inorgchem.1c02652.
- Boulangier, N.; Kuzenkova, A. S.; Iakunkov, A.; Nordenström, A.; Romanchuk, A. Y.; Trigub, A. L.; Zashimov, P. V.; Podana, M.; Enachescu, M.; Bauters, S.; Amidani, L.; Kvashnina, K. O.; Kalmykov, S. N.; Talyzin, A. V.
High surface area “3D Graphene Oxide” for enhanced sorption of radionuclides
Advanced Materials Interfaces 9, Article No. 2200510 (2022).
Doi: 10.1002/admi.202200510.
- Butorin, S. M.; Bauters, S.; Amidani, L.; Beck, A.; Weiss, S.; Vitova, T.; Tougaite, O.
X-ray spectroscopic study of chemical state in uranium carbides
Journal of Synchrotron Radiation 29, 295–302 (2022).
Doi: 10.1107/S160057752101314X.
- Cametti, G.; Roos, D. P.; Churakov, S. V.; Prieur, D.; Scheinost, A. C.
Pb_x(OH)_y cluster formation in STI framework-type zeolites: anomalous thermal behaviour and increased thermal stability
Scientific Reports 12, Article No. 15934 (2022).
Doi: 10.1038/s41598-022-20317-1.
- Castin, N.; Bonny, G.; Konstantinović, M. J.; Bakaev, A.; Bergner, F.; Courilleau, C.; Domain, C.; Gómez-Ferrer, B.; Hyde, J. M.; Messina, L.; Monnet, G.; Pascuet, M. I.; Radiguet, B.; Serrano, M.; Malerba, L.
Multiscale modelling in nuclear ferritic steels: from nano-sized defects to embrittlement
Materials Today Physics 27, Article No. 100802 (2022).
Doi: 10.1016/j.mtphys.2022.100802.
- Ceppatelli, M.; Scelta, D.; Serrano-Ruiz, M.; Dziubek, K.; Izquierdo-Ruiz, F.; Recio, J. M.; Garbarino, G.; Svitlyk, V.; Mezouar, M.; Peruzzini, M.; Bini, R.
High-Pressure and High-Temperature Chemistry of Phosphorus and Nitrogen: Synthesis and Characterization of α - and γ -P₃N₅
Inorganic Chemistry 61, 12165–12180, (2022).
Doi: 10.1021/acs.inorgchem.2c01190.
- Cevirim-Papaioannou, N.; Jo, Y.; Franke, K.; Fuss, M.; Blochouse, B. d.; Altmaier, M.; Gaona, X.
Uptake of niobium by cement systems relevant for nuclear waste disposal: impact of ISA and chloride
Cement and Concrete Research 153, 106690 (2022).
Doi: 10.1016/j.cemconres.2021.106690.
- Chen, C.; Yuan, T.; Lu, R.; Fischer, C.; Kolditz, O.; Shao, H.
The influence of sedimentary heterogeneity on the diffusion of radionuclides in the sandy facies of Opalinus Clay at the field scale
Advances in Geosciences 58, 77–85 (2022).
Doi: 10.5194/adgeo-58-77-2022.
- Chen, G.; An, Y.; Liu, S.; Sun, F.; Qi, H.; Wu, H.; He, Y.; Liu, P.; Shi, R.; Zhang, J.; Kuc, A. B.; Kaiser, U.; Zhang, T.; Heine, T.; Wu, G.; Feng, X.
Highly accessible and dense surface single metal FeN₄ active sites for promoting the oxygen reduction reaction
Energy & Environmental Science 15, 2619–2628 (2022).
Doi: 10.1039/d2ee00542e.
- Chulist, R.; Pukenas, A.; Chekhonin, P.; Hohenwarter, A.; Pippan, R.; Schell, N.; Skrotzki, W.
Phase Transformation Induced by High Pressure Torsion in the High-Entropy Alloy CrMnFeCoNi
Materials 15, Article No. 8407 (2022).
Doi: 10.3390/ma15238407.
- Das, A.; Altstadt, E.; Kaden, C.; Kapoor, G.; Akhmadaliev, S.; Bergner, F.
Nanoindentation response of ion-irradiated Fe, Fe-Cr alloys and ferritic-martensitic steel Eurofer 97: The effect of ion energy
Frontiers in Materials 8, Article No. 811851 (2022).
Doi: 10.3389/fmats.2021.811851.
- Demnitz, M.; Schymura, S.; Neumann, J.; Schmidt, M.; Schäfer, T.; Stumpf, T.; Müller, K.
Mechanistic understanding of Curium(III) sorption on natural K feldspar surfaces
Science of the Total Environment 843, Article No. 156920 (2022).
Doi: 10.1016/j.scitotenv.2022.156920.
- Diaz Pescador, E.; Schäfer, F.; Kliem, S.
On the validation of ATHLET 3-D features for the simulation of multidimensional flows in horizontal geometries under single-phase subcooled conditions
Nuclear Engineering and Technology 54, 3567–3579 (2022).
Doi: 10.1016/j.net.2022.04.017.

- Dzuga, J.; Seifi, M.; Rzepa, S.; Rund, M.; Koukolikova, M.; Viehrig, H. W.; Liu, Z. H.; Lewandowski, J. J.
The effects of post-processing on the local fracture toughness properties of electron beam powder bed fusion Ti-6Al-4V alloy
Engineering Fracture Mechanics 273, Article No. 108697 (2022).
 Doi: 10.1016/j.engfracmech.2022.108697.
- Ehrlich, L.; Gericke, R.; Brendler, E.; Wagler, J.
P-Ru-Complexes with a Chelate-Bridge-Switch: A Comparison of 2-Picolyl and 2-Pyridyloxy Moieties as Bridging Ligands
Molecules 27, Article No. 2778 (2022).
 Doi: 10.3390/molecules27092778.
- Fahmy, K.
Simple Growth–Metabolism Relations Are Revealed by Conserved Patterns of Heat Flow from Cultured Microorganisms
Microorganisms 10, 1397 (2022).
 Doi: 10.3390/microorganisms10071397.
- Fahmy, K.; Sakmar, T.
Interdisciplinary biophysical studies of membrane proteins bacteriorhodopsin and rhodopsin
Biophysical Reviews (2022).
 Doi: 10.1007/s12551-022-01003-y.
- Feig, M.; Carrillo-Cabrera, W.; Bobnar, M.; Simon, P.; Curfs, C.; Levytskyi, V.; Tsirlin, A. A.; Leithe-Jasper, A.; Gumeniuk, R.
Composition dependent polymorphism and superconductivity in $Y_{3+x}(Rh, Ir)_4Ge_{13-x}$
Dalton Transactions 51, 4734–4748 (2022).
 Doi: 10.1039/d2dt00167e.
- Fridman, E.; Nikitin, E.; Ponomarev, A.; Nora, A. D.; Kliem, S.; Mikityuk, K.
Extension of the DYN3D/ATHLET code system to SFR applications: models description and initial validation
Annals of Nuclear Energy 182, Article No. 109619 (2023).
 Doi: 10.1016/j.anucene.2022.109619.
- Gerber, E.; Romanchuk, A. Y.; Weiss, S.; Kuzenkova, A.; Hynault, M.; Bauters, S.; Egorov, A.; Butorin, S. M.; Kalmykov, S. N.; Kvashnina, K. O.
To form or not to form: PuO_2 nanoparticles at acidic pH
Environmental Science: Nano 9, 1509–1518 (2022).
 Doi: 10.1039/d1en00666e.
- Gueye, P. M.; Gómez-Ferrer, B.; Kaden, C.; Pareige, C.
Role of Ni, Si and P on the formation of solute-rich clusters under irradiation in Fe-Cr alloys
Journal of Nuclear Materials 570, Article No. 153958 (2022).
 Doi: 10.1016/j.jnucmat.2022.153958.
- Günther, A.; Wollenberg, A.; Vogel, M.; Drobot, B.; Steudtner, R.; Freitag, L.; Hübner, R.; Stumpf, T.; Raff, J.
Speciation and spatial distribution of Eu(III) in fungal mycelium
Science of the Total Environment 851, Article No. 158160 (2022).
 Doi: 10.1016/j.scitotenv.2022.158160.
- Gutenthaler, S. M.; Tsushima, S.; Steudtner, R.; Gailer, M.; Hoffmann-Röder, A.; Drobot, B.; Daumann, L. J.
Lanmodulin peptides – unravelling the binding of the EF-Hand loop sequences stripped from the structural corset
Inorganic Chemistry Frontiers 9, 4009–4021 (2022).
 Doi: 10.1039/d2qi00933a.
- Haldar, S.; Wang, M.; Bhauriyal, P.; Hazra, A.; Khan, A. H.; Bon, V.; Isaacs, M. A.; Ankita, L. S. d.; Boenke, T.; Grothe, J.; Heine, T.; Brunner, E.; Feng, X.; Dong, R.; Schneemann, A.; Kaskel, S.
Porous Dithiine-Linked Covalent Organic Framework as a Dynamic Platform for Covalent Polysulfide Anchoring in Lithium–Sulfur Battery Cathodes
Journal of the American Chemical Society 144, 9101–9112 (2022).
 Doi: 10.1021/jacs.2c02346.
- Hanke, M.; Dornbusch, D.; Hadlich, C.; Roßberg, A.; Hansen, N.; Grundmeier, G.; Tsushima, S.; Keller, A.; Fahmy, K.
Anion-specific structure and stability of guanidinium-bound DNA origami
Computational and Structural Biotechnology Journal 20, 2611–2623 (2022).
 Doi: 10.1016/j.csbj.2022.05.037.
- Hanke, M.; Hansen, N.; Ruiping, C.; Grundmeier, G.; Fahmy, K.; Keller, A.
Salting-Out of DNA Origami Nanostructures by Ammonium Sulfate
International Journal of Molecular Sciences 23, Article No. 2817 (2022).
 Doi: 10.3390/ijms23052817.
- Hilpmann, S.; Bader, M.; Steudtner, R.; Müller, K.; Stumpf, T.; Cherkouk, A.
Microscopic and spectroscopic bioassociation study of uranium(VI) with an archaeal Halobacterium isolate
Plos One 17, Article No. e0262275 (2022).
 Doi: 10.1371/journal.pone.0262275.
- Höhne, T.; Kliem, S.
Numerical Analysis Related to the ROCOM Pressurized Thermal Shock Benchmark
Fluids 8, Article No. 4 (2023).
 Doi: 10.3390/fluids8010004.

- Huang, W.; Wang, L.; Chen, J.; Chen, Y. C.; Wei, T. S.; Chiang, Y. C.; Wang, P.; Lee, T.; Lin, S.; Huang, L.; Shieh, W. Y. S.
***Vibrio salinus* sp. nov., a marine nitrogen-fixing bacterium isolated from the lagoon sediment of an islet inside an atoll in the western Pacific Ocean**
Antonie van Leeuwenhoek 115, 1203–1214 (2022).
Doi: 10.1007/s10482-022-01768-y.
- Huittinen, N. M.; Virtanen, S.; Roßberg, A.; Eibl, M.; Lönnrot, S.; Polly, R.
A combined extended X-ray absorption fine structure spectroscopy and density functional theory study of americium vs. yttrium adsorption on corundum (α -Al₂O₃)
Minerals 12, Article No. 1380 (2022).
Doi: 10.3390/min12111380.
- Iakunkov, A.; Nordenström, A.; Boulanger, N.; Hennig, C.; Baburin, I.; Talyzin, A.
Temperature dependent swelling transitions in MXene Ti₃C₂T_x
Nanoscale 14, 10940–10949 (2022).
Doi: 10.1039/d2nr03075f.
- Iglesias-Artola, J. M.; Drobot, B.; Kar, M.; Fritsch, A. W.; Mutschler, H.; Tang, T. Y. D.; Kreysing, M.
Charge-density reduction promotes ribozyme activity in RNA-peptide coacervates via RNA fluidization and magnesium partitioning
Nature Chemistry 14, 407–416 (2022).
Doi: 10.1038/s41557-022-00890-8.
- Jessat, J.; Moll, H.; John, W. A.; Bilke, M. L.; Hübner, R.; Kretzschmar, J.; Steudtner, R.; Drobot, B.; Stumpf, T.; Sachs, S.
A comprehensive study on the interaction of Eu(III) and U(VI) with plant cells (*Daucus carota*) in suspension
Journal of Hazardous Materials 439, Art. No. 129520 (2022).
Doi: 10.1016/j.jhazmat.2022.129520.
- Jiao, Y.; Ma, F.; Zhang, X.; Heine, T.
A perfect match between borophene and aluminium in the AlB₃ heterostructure with covalent Al-B bonds, multiple Dirac points and a high Fermi velocity
Chemical Science 13, Article No. 1016 (2022).
Doi: 10.1039/d1sc05207a.
- John, W. A.; Lückel, B.; Matschiavelli, N.; Hübner, R.; Matschi, S.; Hoehenwarter, W.; Sachs, S.
Endocytosis is a significant contributor to uranium(VI) uptake in tobacco (*Nicotiana tabacum*) BY-2 cells in phosphate-deficient culture
Science of the Total Environment 823, Article No. 153700 (2022).
Doi: 10.1016/j.scitotenv.2022.153700.
- Johnstone, E. V.; Mayordomo, N.; Mausolf, E. J.
Discovery, nuclear properties, synthesis and applications of technetium-101
Communications Chemistry 5, 1–16 Article No. 131 (2022).
Doi: 10.1038/s42004-022-00746-9.
- Jordan, N.; Thoenen, T.; Starke, S.; Spahiu, K.; Brendler, V.
A critical review of the solution chemistry, solubility, and thermodynamics of europium: recent advances on the Eu³⁺ aqua ion and the Eu(III) aqueous complexes and solid phases with the sulphate, chloride, and phosphate inorganic ligands
Coordination Chemistry Reviews 473, Article No. 214608 (2022).
Doi: 10.1016/j.ccr.2022.214608.
- Karpińska, M.; Jasiński, J.; Kempt, R.; Ziegler, J. D.; Sansom, H.; Snaith, H. J.; Taniguchi, T.; Watanabe, K.; Surrente, A.; Dyksik, M.; Maude, D. K.; Ł, K.; Chernikov, A.; Kuc, A. B.; Baranowski, M.; Plochocka, P.
Interlayer excitons in MoSe₂/2D perovskite hybrid heterostructures – the interplay between charge and energy transfer
Nanoscale 14, 8085–8094 (2022).
Doi: 10.1039/D2NR00877G.
- Kempt, R.; Lukas, S.; Hartwig, O.; Prechtel, M.; Kuc, A. B.; Brumme, T.; Li, S.; Neumaier, D.; Lemme, M. C.; Duesberg, G. S.; Heine, T.
Stacking polymorphism in PtSe₂ drastically affects its electromechanical properties
Advanced Science 9, Article No. 2201272 (2022).
Doi: 10.1002/advs.202201272.
- Khabirova, S. Y.; Aleshin, G. Y.; Plakhova, T. V.; Zubenko, A. D.; Shchukina, A. A.; Fedorova, O. A.; Averin, A. A.; Belova, E. V.; Bazarkina, E. F.; Kvashnina, K. O.; Kalmykov, S. N.
CeO₂-azacrown conjugate as a nanopatform for combined radiopharmaceuticals
Nanomaterials 12, 4484 (2022).
Doi: 10.3390/nano12244484
- Klein, J.; Wierzbowski, J.; Soubelet, P.; Brumme, T.; Maschio, L.; Kuc, A. B.; Müller, K.; Stier, A. V.; Finley, J. J.
Electrical control of orbital and vibrational interlayer coupling in bi- and trilayer 2H-MoS₂
Physical Review Materials 6, Article No. 024002 (2022).
Doi: 10.1103/PhysRevMaterials.6.024002.
- Köhler, L.; Patzschke, M.; Bauters, S.; Vitova, T.; Butorin, S. M.; Kvashnina, K. O.; Schmidt, M.; März, J.; Stumpf, T.
Insights into the Electronic Structure of a U(IV) Amido and U(V) Imido Complex
Chemistry - A European Journal 28, Article No. e202200119 (2022).
Doi: 10.1002/chem.202200119.
- Krawczyk-Bärsch, E.; Ramtke, J.; Drobot, B.; Müller, K.; Steudtner, R.; Kluge, S.; Hübner, R.; Raff, J.
Peptidoglycan as major binding motif for Uranium bioassociation on *Magnetospirillum magneticum* AMB-1 in contaminated waters
Journal of Hazardous Materials 437, Article No. 129376 (2022).
Doi: 10.1016/j.jhazmat.2022.129376.

- Kretzschmar, J.; Brendler, E.; Wagler, J.
Phenylarsonic acid–DMPS redox reaction and conjugation investigated by NMR spectroscopy and X-ray diffraction
Environmental Toxicology and Pharmacology 92, 103837–103844 (2022).
 Doi: 10.1016/j.etap.2022.103837.
- Kretzschmar, J.; Wollenberg, A.; Tsushima, S.; Schmeide, K.; Acker, M.
2-Phosphonobutane-1,2,4,-Tricarboxylic Acid (PBTC): pH-Dependent Behavior Studied by Means of Multinuclear NMR Spectroscopy
Molecules 27, 4067 (2022).
 Doi: 10.3390/molecules27134067.
- Kvashnina, K. O.
Rare radioisotopes at the ready
Nature Chemistry 14, 1337–1338 (2022).
 Doi: 10.1038/s41557-022-01086-w.
- Lagrange, T.; Pan, Z.; Bártová, B.; Butorin, S. M.; Hyatt, N. C.; Stennett, M. C.; Kvashnina, K. O.; Bernier-Latmani, R.
Uranium reduction by magnetite – mechanism of UO₂ formation monitored by STEM, SAED and EELS
Microscopy and Microanalysis 28, 2444–2446 (2022).
 Doi: 10.1017/S1431927622009370.
- Laskar, C.; Bazarkina, E.; Kokh, M.; Hazemann, J. L.; Vuilleumier, R.; Desmale, E.; Pokrovski, G. S.
Stability and structure of platinum sulfide complexes in hydrothermal fluids
Geochimica et Cosmochimica Acta 336, 407–422 (2022).
 Doi: 10.1016/j.gca.2022.08.015.
- Lippold, H.; Kahle, L.; Sonnendecker, C.; Matysik, J.; Fischer, C.
Temporal and spatial evolution of enzymatic degradation of amorphous PET plastics
npj Materials Degradation 6, Article No. 93 (2022).
 Doi: 10.1038/s41529-022-00305-6.
- Lv, K.; Urbank, C.; Patzschke, M.; März, J.; Kaden, P.; Weiß, S.; Schmidt, M.
MOFs with 12-coordinate 5f-block metal centers
Journal of the American Chemical Society 144, 2879–2884 (2022).
 Doi: 10.1021/jacs.1c13127.
- Mandal, P.; Kretzschmar, J.; Drobot, B.
Not just a background: pH buffers do interact with lanthanide ions – a Europium(III) case study
Journal of Biological Inorganic Chemistry 27, 249–260 (2022).
 Doi: 10.1007/s00775-022-01930-x.
- Meurer, F.; Dolomanov, O. V.; Hennig, C.; Peyrerimhoff, N.; Kleemiss, F.; Puschmann, H.; Bodensteiner, M.
“X-ray diffraction spectroscopy” – Refinement of dispersion correction parameters for XRD measurements of Mo(CO)₆ at the Mo K-edge
IUCrJ 9, 604–609 (2022).
 Doi: 10.1107/S205225222006844.
- Meza, A.; Macía, E.; Chekhonin, P.; Altstadt, E.; Rabanal, M. E.; Torralba, J. M.; Campos, M.
The effect of composition and microstructure on the creep behaviour of 14 Cr ODS steels consolidated by SPS
Materials Science and Engineering A 849, Article No. 143441 (2022).
 Doi: 10.1016/j.msea.2022.143441.
- Mizumachi, T.; Sato, M.; Kaneko, M.; Takeyama, T.; Tsushima, S.; Takao, K.
Fully Chelating N₃O₂-Pentadentate Planar Ligands Designed for Strongest and Selective Capture of Uranium from Seawater
Inorganic Chemistry 61, 6175–6181 (2022).
 Doi: 10.1021/acs.inorgchem.2c00306.
- Munoz, A.; Weiß, S.
Kinetic Aspects of the Electrochemical Reduction of Uranyl in HCl Solutions
Journal of the Electrochemical Society 169, Article No. 016510 (2022).
 Doi: 10.1149/1945-7111/ac3e7c.
- Neumann, J.; Lee, S. S.; Brinkmann, H.; Eng, P.; Stubbs, J.; Stumpf, T.; Schmidt, M.
Impact of Ion-Ion Correlations on the Adsorption of M(III) (M = Am, Eu, Y) onto Muscovite (001) in the Presence of Sulfate
Journal of Physical Chemistry C 126, 1400–1410 (2022).
 Doi: 10.1021/acs.jpcc.1c09561.
- Neumann, J.; Lessing, J.; Lee, S. S.; Stubbs, J. E.; Eng, P. J.; Demnitz, M.; Fenter, P.; Schmidt, M.
Y(III) sorption at the orthoclase (001) surface measured by X-ray reflectivity
Environmental Science & Technology 57, 266–276 (2022).
 Doi: 10.1021/acs.est.2c06703.
- Nordenström, A.; Iakunkov, A.; Boulanger, N.; Li, G.; Hennig, C.; Baburin, I.; Jørgensen, M.; Kantor, I.; Talyzin, A. V.
Temperature dependent intercalation of molten 1-hexadecanol into Brodie graphite oxide
Carbon 203, 770–784 (2023).
 Doi: 10.1016/j.carbon.2022.12.030.
- Oliveira, A. F.; Kuc, A. B.; Heine, T.; Abram, U.; Scheinost, A. C.
Shedding light on the enigmatic TcO₂·xH₂O structure with density functional theory and EXAFS spectroscopy
Chemistry - A European Journal 28, Article No. e202202235 (2022).
 Doi: 10.1002/chem.202202235.
- Ono, R.; Kazama, H.; März, J.; Tsushima, S.; Takao, K.
Crystal Structures of Ce(IV) Nitrates with Bis(2-pyrrolidone) Linker Molecules Deposited from Aqueous Solutions with Different HNO₃ Concentrations
Inorganic Chemistry 62, 454–463 (2023).
 Doi: 10.1021/acs.inorgchem.2c03554.

- Pareige, C.; Etienne, A.; Gueye, P. M.; Medvedev, A.; Kaden, C.; Konstantinovic, M.; Malerba, L.
Solute rich cluster formation and Cr precipitation in irradiated Fe-Cr-(Ni,Si,P) alloys: Ion and neutron irradiation
Journal of Nuclear Materials 572, Article No. 154060 (2022).
Doi: 10.1016/j.jnucmat.2022.154060.
- Philipp, T.; Huittinen, N. M.; Shams Aldin Azzam, S.; Stohr, R.; Stietz, J.; Reich, T.; Schmeide, K.
Effect of Ca(II) on U(VI) and Np(VI) retention on Ca-bentonite and clay minerals at hyperalkaline conditions – New insights from batch sorption experiments and luminescence spectroscopy
Science of the Total Environment 842, Article No. 156837 (2022).
Doi: 10.1016/j.scitotenv.2022.156837.
- Poulain, A.; Fernandez-Martinez, A.; Greneche, J. M.; Prieur, D.; Scheinost, A. C.; Menguy, N.; Bureau, S.; Magnin, V.; Findling, N.; Drnec, J.; Martens, I.; Mirolo, M.; Charlet, L.
Selenium nanowire formation by reaction of selenate with magnetite
Environmental Science & Technology 56, 14817–14827 (2022).
Doi: 10.1021/acs.est.1c08377.
- Ramzan, M. S.; Han, S. K.; Kuc, A. B.
Electronic fingerprint mechanism of NO_x sensor based on single-material SnP₃ logical junction
npj Computational Materials 8, Article No. 220 (2022).
Doi: 10.1038/s41524-022-00903-7.
- Ritschel, T.; Stahl, Q.; Kusch, M.; Trinckauf, J.; Garbarino, G.; Svitlyk, V.; Mezouar, M.; Yang, J.; Cheong, S. W.; Geck, J.
Stabilization mechanism of molecular orbital crystals in IrTe₂
Communications Physics 5, 325 (2022).
Doi: 10.1038/s42005-022-01094-9.
- Rodriguez Hernandez, D. M.; Mayordomo, N.; Parra-Puerto, A.; Schild, D.; Brendler, V.; Stumpf, T.; Müller, K.
Exploring the Reduction Mechanism of ⁹⁹Tc(VII) in NaClO₄: A Spectro-Electrochemical Approach
Inorganic Chemistry 61, 10159–10166 (2022).
Doi: 10.1021/acs.inorgchem.2c01278.
- Romanchuk, A.; Trigub, A.; Plakhova, T.; Kuzenkova, A.; Svetogorov, R.; Kvashnina, K.; Kalmykov, S.
Effective coordination numbers from EXAFS: General approaches for dioxides
Journal of Synchrotron Radiation 29, 288–294 (2022).
Doi: 10.1107/S160057752101300X.
- Rosa, A. D.; Dewaele, A.; Garbarino, G.; Svitlyk, V.; Morard, G.; Angelis, F. d.; Krstulovic, M.; Briggs, R.; Irifune, T.; Mathon, O.; Bouhifd, M. A.
Martensitic fcc-hcp transformation pathway in solid krypton and xenon and its effect on their equations of state
Physical Review B 105, 144103 (2022).
Doi: 10.1103/PhysRevB.105.144103.
- Schabernack, J.; Fischer, C.
Improved Kinetics for Mineral Dissolution Reactions in Pore-Scale Reactive Transport Modeling
Geochimica et Cosmochimica Acta 334, 99–118 (2022).
Doi: 10.1016/j.gca.2022.08.003.
- Seidel, A.; Gericke, R.; Brendler, E.; Wagler, J.
Copper Complexes of Silicon Pyridine-2-olates RSi(pyO)₃ (R = Me, Ph, Bn, Allyl) and Ph₂Si(pyO)₂
Inorganics 11, Article No. 2 (2023).
Doi: 10.3390/inorganics11010002.
- Seidel, A.; Weigel, M.; Ehrlich, L.; Gericke, R.; Brendler, E.; Wagler, J.
Molecular Structures of the Silicon Pyridine-2-(thi)olates Me₃Si(pyX), Me₂Si(pyX)₂ and Ph₂Si(pyX)₂ (py = 2-Pyridyl, X = O, S), and Their Intra- and Intermolecular Ligand Exchange in Solution
Crystals 12, 1054 (2022).
Doi: 10.3390/cryst12081054.
- Smith, H.; Townsend, L. T.; Mohun, R.; Cordara, T.; Stennett, M.; Mosselmans, F.; Kvashnina, K.; Hyatt, N.; Corkhill, C.
Direct evidence for Cr²⁺ solid solution in UO₂
Communications Chemistry 5, 163 (2022).
- Stadler, J.; Vogel, M.; Steudtner, R.; Drobot, B.; Kogiomtzigis, A.; Weiss, M.; Walther, C.
The Chemical Journey of Europium(III) through Winter Rye (*Secale cereale* L.) – Understanding through Mass Spectrometry and Chemical Microscopy
Chemosphere 313, Article No. 137252 (2022).
Doi: 10.1016/j.chemosphere.2022.137252.
- Stagg, O.; Morris, K.; Townsend, L. T.; Kvashnina, K. O.; Baker, M. L.; Dempsey, R.; Abrahamsen-Mills, L.; Shaw, S.
Sulfidation and Reoxidation of U(VI)-Incorporated Goethite: Implications for U Retention during Sub-Surface Redox Cycling
Environmental Science & Technology 56, 17643–17652 (2022).
Doi: 10.1021/acs.est.2c05314.
- Svitlyk, V.; Weiß, S.; Hennig, C.
Immobilization of radiotoxic elements with Y-stabilized zirconia: the Thorium case
Journal of the American Ceramic Society 105, 5975–5983 (2022).
Doi: 10.1111/jace.18543.

- Svitlyk, V.; Weiß, S.; Hennig, C.
Stability of doped zirconia under extreme conditions: towards long-term and secure storage of radioactive waste
Journal of the American Ceramic Society 105, 7831–7839 (2022).
 Doi: 10.1111/jace.18735.
- Takeyama, T.; Iwatsuki, S.; Tsushima, S.; Takao, K.
Synthesis and characterization of a uranyl(VI) complex with 2,6-pyridine-bis(methylaminophenolato) and its ligand-centred aerobic oxidation mechanism to a diimino derivative
Dalton Transactions 51, 6576–6585 (2022).
 Doi: 10.1039/D2DT00325B.
- Tsushima, S.; Takao, K.
Hydrophobic Core Formation and Secondary Structure Elements in Uranyl(VI)-Binding Peptides
Physical Chemistry Chemical Physics 24, 4455–4461 (2022).
 Doi: 10.1039/D1CP05401E.
- Ulbricht, A.; Heinemann, A.; Bergner, F.
Small-angle neutron scattering applied to low-dose neutron-irradiated Fe–Cr alloys and ferritic martensitic steel Eurofer97
Journal of Applied Crystallography 55, 702–712 (2022).
 Doi: 10.1107/S1600576722004800.
- Ulbricht, A.; Hernández-Mayoral, M.; Oñorbe, E.; Etienne, A.; Radiguet, B.; Hirschmann, E.; Wagner, A.; Hein, H.; Bergner, F.
Effect of neutron flux on irradiation-induced microstructure and hardening of reactor pressure vessel steel
Metals 12, Article No. 369 (2022).
 Doi: 10.3390/met12030369.
- Vivas, J.; De-Castro, D.; Poplawsky, J. D.; Altstadt, E.; Houska, M.; Urones-Garrote, E.; San-Martín, D.; Caballero, F. G.; Serrano, M.; Capdevila, C.
Creep strength boosted by a high-density of stable nanoprecipitates in high-chromium steels
European Journal of Materials (2023).
 Doi: 10.1080/26889277.2022.2118082.
- Wang, X.; An, Y.; Liu, L.; Fang, L.; Liu, Y.; Zhang, J.; Qi, H.; Li, T.; Heine, T.; Kuc, A. B.; Yu, M.; Feng, X.
Atomically Dispersed Pentacoordinated-Zirconium Catalyst with Axial Oxygen Ligand for Oxygen Reduction Reaction
Angewandte Chemie – International Edition 61, Article No. e202209746 (2022).
 Doi: 10.1002/anie.202209746.
- Yuan, T.; Fischer, C.
The influence of sedimentary and diagenetic heterogeneity on the radionuclide diffusion in the sandy facies of the Opalinus Clay at the core scale
Applied Geochemistry 146 (2022).
 Doi: 10.1016/j.apgeochem.2022.105478.
- Yuan, T.; Yang, Y.; Ait-Mouheb, N.; Deissmann, G.; Fischer, C.; Stumpf, T.; Bosbach, D.
A comparative study on heterogeneity of clay rocks using pore - scale diffusion simulations and experiments
Journal of Geophysical Research - Solid Earth (2022).
 Doi: 10.1029/2022JB025428.
- Zasimov, P. V.; Amidani, L.; Retegan, M.; Walter, O.; Caciuffo, R.; Kvashnina, K. O.
HERFD-XANES and RIXS study on the electronic structure of trivalent lanthanides across a series of isostructural compounds
Inorganic Chemistry 61, 1817–1830 (2022).
 Doi: 10.1021/acs.inorgchem.1c01525.
- Zavarin, M.; Chang, E.; Wainwright, H.; Parham, N.; Kaukuntla, R.; Zouabe, J.; Deinhart, A.; Genetti, V.; Shipman, S.; Bok, F.; Brendler, V.
A community data mining approach for surface complexation database development
Environmental Science & Technology 56, 2827–2838 (2022).
 Doi: 10.1021/acs.est.1c07109.
- Zuniga-Puelles, E.; Cardoso-Gil, R.; Ozden, A.; Bulut, N.; Himcinschi, C.; Kortus, J.; Svitlyk, V.; Gumenuik, R.
Low thermal conductivity in bournonite PbCuSbS₃: A comprehensive study
Physical Review B 106, 195201 (2022).
 Doi: 10.1103/PhysRevB.106.195201.
- Zurita, C.; Tsushima, S.; Solari, P. L.; Jeanson, A.; Creff, G.; Auwer, C. D.
Interaction of Th(IV), Pu(IV) and iron(III) with ferritin protein : how similar ?
Journal of Synchrotron Radiation 29, 45–52 (2022).
 Doi: 10.1107/S1600577521012340.

○ FURTHER CONTRIBUTIONS

- Byrum, K.; Corrodi, S.; Oksuzian, Y.; Winter, P.; Xia, L.; Edmonds, A. W. J.; Miller, J. P.; Mott, J.; Marciano, W. J.; Szafron, R.; Bonventre, R.; Brown, D. N.; Kolomensky, Y. G.; Ning, O.; Singh, V.; Prebys, E.; Borrel, L.; Echenard, B.; Hitlin, D. G.; Hu, C.; Lin, D. X.; Middleton, S.; Porter, F. C.; Zhang, L.; Zhu, R. Y.; Ambrose, D.; Badgley, K.; Bernstein, R. H.; Boi, S.; Casey, B. C. K.; Culbertson, R.; Gaponenko, A.; Glass, H. D.; Glenzinski, D.; Goodenough, L.; Hocker, A.; Kargiantoulakis, M.; Kashikhin, V.; Kiburg, B.; Kutschke, R. K.; Murat, P. A.; Neuffer, D.; Pronskikh, V. S.; Pushka, D.; Rakness, G.; Strauss, T.; Yucel, M.; Bloise, C.; Diociaiuti, E.; Giovannella, S.; Happacher, F.; Miscetti, S.; Sarra, I.; Martini, M.; Ferrari, A.; Müller, S.; Rachamin, R.; Barlas-Yucel, E.; Artikov, A.; Atanov, N.; Davydov, Y. I.; Glagolev, V.; Vasilyev, I. I.; Brown, D. N.; Uesaka, Y.; Denisov, S. P.; Evdokimov, V.; Kozelov, A. V.; Popov, A. V.; Vasilyev, I. A.; Tassielli, G.; Teubner, T.; Chislett, R. T.; Hesketh, G. G.; Lancaster, M.; Campbell, M.; Ciampa, K.; Heller, K.; Messerly, B.; Cummings, M. A. C.; Calibbi, L.; Blazey, G. C.; Syphers, M. J.; Zutshi, V.; Kampa, C.; Mackenzie, M.; Di Falco, S.; Donati, S.; Gioiosa, A.; Giusti, V.; Morescalchi, L.; Pasciuto, D.; Pedreschi, E.; Spinella, F.; Hedges, M. T.; Jones, M.; You, Z. Y.; Zanetti, A. M.; Valetov, E. V.; Dukes, E. C.; Ehrlich, R.; Group, R. C.; Heck, J.; Hung, P. Q.; Demers, S. M.; Pezzullo, G.; Lynch, K. R.; Popp, J. L.
Mu2e-II: Muon to electron conversion with PIP-II
Particle Physics Community Planning Exercise (SNOWMASS), July 17–26, 2022, Seattle, U.S.A. (2022).
Doi: 10.48550/arXiv.2203.07569.
- Diaz Pescador, E.; Jobst, M.; Kliem, S.
NuScale SMR 3-D modelling and analysis of boron dilution with the system code ATHLET in the framework of McSAFER
KERNTECHNIK 2022, 21.06.2022, Leipzig, Germany, (2022).
- Diaz Pescador, E.; Jobst, M.; Kliem, S.
NuScale SMR 3-D Modelling and Applied Safety Analyses with the System Code ATHLET in the Framework of the EU H2020 McSAFER
13th International Topical Meeting on Nuclear Reactor Thermal-Hydraulics, Operation and Safety, 06.09.2022, Hsinchu, Taiwan, (2022).
- Hurel, C.; Jordan, N.; Gerber, U.; Weiß, S.; Kubier, B.; Kleeberg, R.
Surface reactivity of anatase and rutile samples - relationship with toxicity on aquatic organisms
in: Toxicology of Ambient Ultrafine Particulate Matter, Nanoparticles and Nanomaterials in Terrestrial and Aquatic Environments (Ed.: Marc A. Williams), Wiley, Weinheim (2022).
- Kaden, P.
Nuclear Magnetic Resonance of Actinides
The Lanthanides and Actinides Synthesis, Reactivity, Properties and Applications (Eds.: S. T. Liddle, D. P. Mills, L. S. Natrajan), 617–631, World Scientific Europe, London, U.K. (2022).
- Kvashnina, K. O.; Butorin, S. M.; Wang, S.; Shi, W.
Actinide physics and chemistry with synchrotron radiation
Journal of Synchrotron Radiation 29, 1131–1132 (2022).
Doi: 10.1107/S1600577522007019
- Kulenkampff, J.
Direct tomographic observation of brine percolation into MgO-shotcrete drill cores
10th Conference on the Mechanical Behavior of Salt (SaltMech X), July 06–08, 2022, Utrecht, The Netherlands.
Doi: 10.1201/9781003295808.
- Scheinost, A. C.; Singh, B.
Metal Oxides
Daniel Hillel: Encyclopedia of Soils in the Environment, 2nd edition, Elsevier, New York, U.S.A. (2022).
- Schmeide, K.; Rossberg, A.; Bok, F.; Shams Aldin Azzam, S.; Weiss, S.; Scheinost, A. C.
Neural network analysis of EXAFS spectra to identify technetium chukanovite species.
ESRF Highlights 2021, p. 122–123. The European Synchrotron, Grenoble, France (2022).
- Smeddinck, U.; Röhlig, K. J.; Mbah, M.; Brendler, V.
Das „lernende“ Standortauswahlverfahren für ein Endlager radioaktiver Abfälle – Interdisziplinäre Beiträge
BWV–Berliner Wissenschafts-Verlag, ISBN Print 978-3-8305-5182-9, Berlin, Germany (2022).
Doi: 10.35998/9783830555124.
- Yadav, P.; Rachamin, R.; Konheiser, J.
Weight values for MCNP calculations based on Recursive Monte-Carlo method
14th International Conference on Radiation Shielding and 21st Topical Meeting of the Radiation Protection and Shielding Division, 11.06.2022, Seattle, WA, U.S.A.

ORAL PRESENTATIONS

INVITED LECTURES

- Blei, M. K.; Patzschke, M.; Kvashnina, K. O.; Waurick, L.; Schmidt, M.; Stumpf, T.; März, J.
In Search of Covalency in Tetravalent Actinide (Th - Pu) Monosalen Complex Series
Plutonium Futures -The Science 2022, September 26–29, 2022, Avignon, France (2022).
- Bok, F.
Development of Thermodynamic Sorption Databases
OECD/NEA Management Board Meeting, November 08, 2022, Paris, France (2022).
- Bok, F.; Moog, H. C.; Gaona, X.; Freyer, D.; Wissmeier, L.
Quality assurance for chemical databases using the example of the thermodynamic reference database THEREDA
BASE-Workshop „Trust in Models“ (TiM 2022), November 17–18, 2022, Berlin, Germany (2022).
- Fichter, S.
Synthesis and Characterization of Tri- and Tetravalent Actinide Amidinates
Jahrestagung der Fachgruppe Nuklearchemie 2022, October 06, 2022, Bergisch Gladbach, Germany (2022).
- Gericke, R.; März, J.; Kaden, P.; Patzschke, M.; Radoske, T.; Fichter, S.; Blei, M. K.; Schmidt, M.; Stumpf, T.
Bonding Trends in Tetravalent Actinide (Th - Pu) Complex Series
Terrae Rarae - Tage der Seltenen Erden, September 27–29, 2022, Leipzig, Germany, (2022).
- Hennig, C.
Identification of color pigments in wall paintings of Oscar Schlemmer
Das Raumbauwerk Wohnraum Adolf Meyer in Weimar im Kontext der Entwicklung des Bauhauses, April 20, 2022, Weimar, Germany, (2022).
- Kaden, C.; Bergner, F.
Nanoindentation as a tool to assess mechanical property changes under ion irradiation
NUMAT2022 - The Nuclear Materials Conference, October 24–28, 2022, Gent, Belgium (2022).
- Köhler, L.; Patzschke, M.; Kaden, P.; Kvashnina, K. O.; Schmidt, M.; Stumpf, T.; März, J.
Bonding trends in full early actinide (Th-Pu) pyren complex series
19th Radiochemical Conference, May 16–20, 2022, Mariánské Lázně, Czechia (2022).
- Köhler, L.; Patzschke, M.; März, J.; Schmidt, M.; Stumpf, T.
N-Donor Ligands as Versatile Actinide Complexation Agents
Angular Momentum - Symposium on f-Element Chemistry, March 29, 2022, Dresden, Germany (2022).
- Kuc, A. B.
Modelling 2D materials for experimental collaborations
2D-Mat School, July 24–29, 2022, Bad Honnef, Germany, (2022).
- Kuc, A. B.
Modelling van der Waals heterostructures for experimental collaborations
Semiconductor Materials Engineering Seminar, February 25, 2022, Wrocław, Poland (2022).
- Kvashnina, K. O.
High Energy Resolution X-ray Spectroscopy for Actinide Science
18th International Conference on X-Ray Absorption and Fine Structure (XAFS2022), July 10–15, 2022, Sydney, Australia (2022).
- Kvashnina, K. O.
Plutonium Chemistry by Innovative Synchrotron Methods
Plutonium Futures -The Science 2022, September 26–29, 2022, Avignon, France (2022).
- März, J.
Fundamental research on f-elements and fission products at the Institute of Resource Ecology at HZDR
The 9th ZC Colloquium in FY2022, November 11, 2022, Tokyo, Japan (2022).
- Matschiavelli, N.
Deutschlands Ausstieg aus der Atomkraft - Was passiert mit dem Müll und welche Rolle spielen Mikroorganismen?
Tag der Wissenschaften, November 24, 2022, Dresden, Germany (2022).
- Mayordomo, N.
A brief summary about technetium: Origin, medical applications, and environmental immobilization strategies
Week of science at Universidad de Alcalá, November 23, 2022, Alcalá de Henares, Spain (2022).
- Schmidt, M.
Actinide Chemistry - From Small Molecules To Real Rock
GDCh Fachtagung Nuklearchemie 2022, October 04–06, 2022, Bergisch Gladbach, Germany (2022).
- Schymura, S.; Schneider, E.; Messerschmidt, J.; Lechner, B. D.
Ca-Caseinate-enhanced remineralisation of dental apatite
Week of Microbial Technologies, November 07–11, 2022, Ljubljana, Slovenia (2022).

CONFERENCE LECTURES

- Abbasova, D.; Hoefler, G.; Arnold, T.; Wanka, S.; Franzen, C.; Wellmann
Knowledge Management (KM) In Radioactive Waste Management (RWM)
17th International Conference on Knowledge Management 2022, June 23–24, 2022, Potsdam, Germany (2022).
- Amidani, L.; Kvashnina, K.
The M4,5 edges HERFD XANES: approaches to calculations
Actinides Revisited 2022, September 21–23, 2022, Dresden, Germany (2022).
- Amidani, L.; Kvashnina, K.
XANES calculations of actinide-based materials
ATAS-AnXAS 2022 – 5th International Workshop on Advanced Techniques in Actinide Spectroscopy & 9th Workshop on Speciation, Techniques and Facilities for Synchrotron Radiation, October 17–21, 2022, Grenoble, France (2022).
- Amidani, L.; Volkova, A.; Retegan, M.; Popa, K.; Martin, P.; Kvashnina, K.
Understanding the M4 edge HERFD XANES of U⁶⁺
JdA 51 – Journées des Actinides, April 10–14, 2022, Santa Margherita, Italy (2022).
- Arnold, T.; Bok, F.; Cazala, C.; Coppin, F.; Fevrier, L.; Katz, A.; Krawczyk-Bärsch, E.; Landesman, C.; Mangeret, A.; Marsal, F.; Merroun, M. L.; Montavon, G.; Nivresse, A. L.; Pelkonen, M.; Pérez-Sánchez, D.; Rigol, A.; Sachs, S.; Skipperud, L.; Urso, L.; Veilly, E.; Vidal, M.
Identification of geochemical and biological processes controlling naturally occurring radionuclides (NOR) mobility to derive more robust solid/liquid distribution coefficients (Kd)
European Radiation Protection Week 2022, October 09–14, 2022, Estoril, Portugal (2022).
- Barkleit, A.; Rachamin, R.; Yassin, G.; Pönitz, E.; Konheiser, J.
Activation determination for decommissioning of nuclear power plants
5th International Conference on Radioecology & Environmental Radioactivity (ICRER), September 04–09, 2022, Oslo, Norway (2022).
- Barkleit, A.; Rachamin, R.; Yassin, G.; Pönitz, E.; Konheiser, J.
Experimental activation determination in and on components of nuclear power plants and comparison with activity calculations
RadChem 2022 – 19th Radiochemical Conference, May 16–20, 2022, Mariánské Lázně, Czechia (2022).
- Becker, A.; Lippold, H.; Fischer, C.
Establishment of experimental possibilities for separation experiments on gaseous H-isotope mixtures
RadChem 2022 – 19th Radiochemical Conference, May 16–20, 2022, Mariánské Lázně, Czechia (2022).
- Bernard, E.; Kulenkampff, J.; Jenni, A.; Mäder, U.
Coupled processes across a 10-year-old clayrock/concrete interface: results of a combined X-ray CT and PET transport experiment
Clay Conference, June 13–16, 2022, Nancy, France, (2022).
- Braga Ferreira Dos Santos, L.; Huittinen, N. M.; Svitlyk, V.; Hennig, C.; Stumpf, T.; Marquardt, J.
Diffraction and Raman spectroscopy studies of zirconia solid phases containing cerium
RadChem 2022 – 19th Radiochemical Conference, May 16–20, 2022, Mariánské Lázně, Czechia (2022).
- Butscher, D.; Barkleit, A.; Stumpf, T.
Spectroscopic investigation of the speciation of uranium(VI) in the biofluids of the human digestive system
RadChem 2022 – 19th Radiochemical Conference, May 16–20, 2022, Mariánské Lázně, Czechia (2022).
- Butscher, D.; Steudtner, R.; Stumpf, T.; Barkleit, A.
Investigation of the interaction of uranium(VI) with the biofluids of the human digestive system
ATAS-AnXAS 2022 – 5th International Workshop on Advanced Techniques in Actinide Spectroscopy & 9th Workshop on Speciation, Techniques and Facilities for Synchrotron Radiation, October 17–21, 2022, Grenoble, France (2022).
- Claus, G.; Lederer, F.; Boelens, P.; Drobot, B.
Identification, characterization and optimization of lanthanide ion binding peptides for the recovery of rare earth elements
International Conference on Metal-Binding Peptides: Methodologies and Applications, July 05–08, 2022, Nancy, France (2022).
- Das, A.; Chekhonin, P.; Houska, M.; Obermeier, F.; Altstadt, E.
Fracture Mechanics Testing of Neutron Irradiated RPV Steels using Mini-C(T) Specimens
The Nuclear Materials Conference 2022, October 24–28, 2022, Gent, Belgium (2022).
- Demnitz, M.; Schymura, S.; Neumann, J.; Müller, K.; Schmidt, M.
Influence of surface roughness on the sorption of Cm(III) on crystalline-water interfaces
28. Tagung der Fachsektion Hydrogeologie e.V. in der DGGV e.V., March 23–25, 2022, Jena, Germany (2022).
- Di Lorenzo, F.; Stotskyi, V.; Scheinost, A. C.; Lanson, M.; Lanson, B.; Churakov, S. V.; Marques Fernandes, M.
Metal sorption on clay minerals aiming at the geological storage of nuclear wastes
Goldschmidt 2022, July 10–15, 2022, Honolulu, Hawaii, U.S.A. (2022).

- Diaz Pescador, E.; Jobst, M.; Kliem, S.
NuScale SMR 3-D modelling and analysis of boron dilution with the system code ATHLET in the framework of McSAFER
 KERNTECHNIK 2022, June 21, 2022, Leipzig, Germany (2022).
- Diaz Pescador, E.; Jobst, M.; Kliem, S.
NuScale SMR 3-D Modelling and Applied Safety Analyses with the System Code ATHLET in the Framework of the EU H2020 McSAFER
 13th International Topical Meeting on Nuclear Reactor Thermal-Hydraulics, Operation and Safety, September 06, 2022, Hsinchu, Taiwan (2022).
- Duckworth, T.; Schwarz, N.; März, J.; Patzschke, M.; Schmidt, M.; Stumpf, T.
Synthesis and complexation of nitrogen donor ligands with tetravalent uranium
 RadChem 2022 – 19th Radiochemical Conference, May 16–20, 2022, Mariánské Lázně, Czechia (2022).
- Faria Oliveira, A.; Kuc, A. B.; Heine, T.; Abram, U.; Scheinost, A. C.
Shedding light on the enigmatic $TcO_2 \cdot xH_2O$ structure with density functional theory and EXAFS spectroscopy
 ATAS-AnXAS 2022 – 5th International Workshop on Advanced Techniques in Actinide Spectroscopy & 9th Workshop on Speciation, Techniques and Facilities for Synchrotron Radiation, October 17–21, 2022, Grenoble, France (2022).
- Faria Oliveira, A.; Kuc, A. B.; Heine, T.; Scheinost, A. C.
Insights into the Enigmatic $TcO_2 \cdot xH_2O$ Structure via Atomistic Simulations
 Goldschmidt 2022, July 10–15, 2022, Honolulu, Hawaii, U.S.A. (2022).
- Friedrich, S.; Holtmann, L.; Kretzschmar, J.; Barkleit, A.; Stumpf, T.
Complexation of Eu(III) in artificial digestive media by aminopolycarboxylic acid EGTA
 RadChem 2022 – 19th Radiochemical Conference, May 16–20, 2022, Mariánské Lázně, Czechia (2022).
- Friedrich, S.; Kretzschmar, J.; Drobot, B.; Stumpf, T.; Barkleit, A.
Complexation of Eu(III) and Cm(III) by EGTA related aminopolycarboxylic acids
 ATAS-AnXAS 2022 – 5th International Workshop on Advanced Techniques in Actinide Spectroscopy & 9th Workshop on Speciation, Techniques and Facilities for Synchrotron Radiation, October 17–21, 2022, Grenoble, France (2022).
- Gericke, R.; Kaden, P.
[An(acac)₄] - complexes revisited
 Actinides Revisited 2022, September 21–23, 2022, Dresden, Germany (2022).
- Günther, A.; Wollenberg, A.; Vogel, M.; Drobot, B.; Steudtner, R.; Hübner, R.; Stumpf, T.; Raff, J.
U(VI)- und Eu(III)-Immobilisierung durch Pilzmyzel
 GDCh Fachtagung Nuklearchemie 2022, October 04–06, 2022, Bergisch Gladbach, Germany (2022).
- Helbig, T.; Tasker, P.; Kaden, P.; Foerstendorf, H.; Lehmann, F.; Kelly, N.
Selektive Extraktion von Molybdän mit Cyanex 272 und Cyanex 600: Charakterisierung der organischen Phase zur optimierten Prozessführung
 Jahrestreffen der ProcessNet Fachgruppen Extraktion, Phytoextrakte und Membrantechnik, May 23–24, 2022, Frankfurt, Germany (2022).
- Hennig, C.; Svitlyk, V.
Linking Diffraction Techniques with XRF and XAS Spectroscopy at the German CRG Beamline ROBL / ESRF
 30th Annual Meeting of the German Crystallographic Society, March 14–17, 2022, Munich, Germany (2022).
- Hilpmann, S.; Jeschke, I.; Steudtner, R.; Hübner, R.; Stumpf, T.; Cherkouk, A.
Comparative analysis of uranium(VI) reduction by a sulfate- and an iron-reducing bacterium
 14th International Symposium on Nuclear and Environmental Radiochemical Analysis: ERA14, September 12–15, 2022, York, U.K. (2022).
- Hilpmann, S.; Steudtner, R.; Roßberg, A.; Hübner, R.; Prieur, D.; Bauters, S.; Kvashnina, K. O.; Stumpf, T.; Cherkouk, A.
Microscopic and spectroscopic insights into uranium(VI) association-reduction processes by a sulfate-reducing microorganism
 Goldschmidt 2022, July 10–15, 2022, Honolulu, Hawaii, U.S.A. (2022).
- Hilpmann, S.; Steudtner, R.; Roßberg, A.; Kvashnina, K. O.; Prieur, D.; Bauters, S.; Hübner, R.; Stumpf, T.; Cherkouk, A.
New insights into uranium(VI) reduction by a sulfate-reducing bacterium relevant to nuclear waste disposal
 DECAY Days 2022, September 21–23, 2022, St. Ursanne, Switzerland (2022).
- Hong, B.; Fichter, S.; März, J.; Kaden, P.; Patzschke, M.; Schmidt, M.; Stumpf, T.
Synthesis and Characterization of Tetravalent Actinide Amidinate Halide Complexes
 RadChem 2022 – 19th Radiochemical Conference, May 16–20, 2022, Mariánské Lázně, Czechia (2022).
- Hoving, A. L.; Qian, Y.; Marques Fernandes, J. M.; Griffioen, J.; Behrends, T.; Scheinost, A. C.
Redox-active iron in different types of clay minerals – mediated electrochemical characterization and reactivity towards Se(IV)
 Clay Conference 2022, June 13–16, 2022, Nancy, France (2022).

- Huittinen, N. M.; Opitz, L.; Eibl, M.
Aqueous vs. high-temperature syntheses of crystalline zirconia (ZrO₂) containing Cm³⁺
GDCh Fachtagung Nuklearchemie 2022, October 04–06, 2022, Bergisch Gladbach, Germany (2022).
- Jessat, I.; Roßberg, A.; Scheinost, A. C.; Lützenkirchen, J.; Foerstendorf, H.; Jordan, N.
Np(V) uptake by the cladding corrosion product zirconia: a combined batch, spectroscopic, and modeling approach
Goldschmidt Conference, July 10–15, 2022, Honolulu, Hawaii, U.S.A. (2022).
- Jessat, I.; Roßberg, A.; Scheinost, A.; Lützenkirchen, J.; Foerstendorf, H.; Jordan, N.
Uptake of Np(V) by zirconia: a combined batch, spectroscopic, and surface complexation modeling study
RadChem 2022 – 19th Radiochemical Conference, May 16–20, 2022, Mariánské Lázně, Czechia (2022).
- Jessat, I.; Roßberg, A.; Scheinost, A. C.; Lützenkirchen, J.; Foerstendorf, H.; Stumpf, T.; Jordan, N.
Np(V) sorption onto zirconia: a combined spectroscopy, batch and modeling study
ATAS-AnXAS 2022 – 5th International Workshop on Advanced Techniques in Actinide Spectroscopy & 9th Workshop on Speciation, Techniques and Facilities for Synchrotron Radiation, October 17–21, 2022, Grenoble, France (2022).
- Jordan, N.; Huittinen, N.; Jessat, I.; Réal, F.; Vallet, V.
Complexation of Cm(III) with aqueous phosphates at elevated temperatures: a luminescence, thermodynamic, and ab initio study
Plutonium Futures -The Science 2022, September 26–29, 2022, Avignon, France (2022).
- Jordan, N.; Thoenen, T.; Starke, S.; Spahiu, K.; Brendler, V.
A critical review of the solution chemistry, solubility, and thermodynamics of Eu(III)
Goldschmidt 2022, July 10–15, 2022, Honolulu, Hawaii, U.S.A. (2022).
- Katheras, A.; Karalis, K.; Bucher, A.; Krack, M.; Scheinost, A. C.; Churakov, S. V.
Ab initio modelling of magnetite surfaces for radionuclide retention
Clay Conference 2022, June 13–16, 2022, Nancy, France. Goldschmidt 2022, July 10–15, 2022, Honolulu, Hawaii, U.S.A. Actinides Revisited 2022, September 21–23, 2022, Dresden, Germany. ATAS-AnXAS 2022, October 17–21, 2022, Grenoble, France (2022).
- Klotzsche, M.
Investigation of Eu³⁺ uptake and spatial distribution in tobacco BY-2 cells
ChemTUgether 2022 - Graduate Exchange To Enhance Excellent Research, May 13–14, 2022, Dresden, Germany (2022).
- Kretzschmar, J.; Stumpf, T.
NMR spectroscopy of selected aqueous systems investigated at HZDR-IRE
Actinides Revisited 2022, September 21–23, 2022, Dresden, Germany (2022).
- Kuc, A. B.
Modelling TMDC/2D perovskite heterostructures for charge and energy transfer
Midterm meeting of SPP2244, March 21–23, 2022, Dresden, Germany (2022).
- Kuc, A. B.
Nonradiative Energy Transfer and Selective Charge Transfer in TMDC/2D perovskite Heterostructures
Psi-k conference 2022, August 22–25, 2022, Lausanne, Switzerland (2022).
- Kuc, A. B.
Simulation of hydrogen species diffusion and transport between and through layers of 2D materials
Casuscon 2022, July 11–14, 2022, Wroclaw, Poland (2022).
- Kulenkampff, J.
Direct tomographic observation of brine percolation into MgO-shotcrete drill cores
10th Conference on the Mechanical Behavior of Salt (SaltMech X), July 06–08, 2022, Utrecht, The Netherlands (2022).
- Kvashnina, K. O.
High-energy resolution X-ray spectroscopy at actinide M_{4,5} edges: what we know, what we want to know, what we can know
JdA 51 - Journées des Actinides, April 10–14, 2022, Santa Margherita Ligure (Genova), Italy (2022).
- Kvashnina, K. O.
High Energy Resolution X-ray Spectroscopy for Actinide Science
Actinides Revisited 2022, September 21–23, 2022, Dresden, Germany (2022).
- März, J.; Fichter, S.; Patzschke, M.; Kaden, P.; Köhler, L.; Schmidt, M.; Stumpf, T.
Early An(IV) complexes with N-donor ligands
Actinides Revisited 2022, September 21, 2022, Dresden, Germany (2022).
- Mayordomo, N.; Mausolf, E. J.; Johnstone, E.; Williams, D. L.; Guan, E. Y. Z.; Gary, C. K.; Davis, J.
Cans production of technetium-99m and technetium-101
International Conference on Accelerators for Research and Sustainable Development: From Good Practices Towards Socioeconomic Impact, May 23–27, 2022, Vienna, Austria (2022).

- Mayordomo, N.; Rodríguez, D. M.; Roßberg, A.; Scheinost, A. C.; Müller, K.
Tc(VII) reductive immobilization by Sn(II) pre-sorbed on alumina nanoparticles
RadChem 2022 – 19th Radiochemical Conference, May 16–20, 2022, Mariánské Lázně, Czechia (2022).
- Mayordomo, N.; Roßberg, A.; Prieur, D.; Scheinost, A. C.; Kvashnina, K. O.; Müller, K.
Tc(VII) reductive immobilization by Sn(II) pre-sorbed on alumina nanoparticles
ATAS-AnXAS 2022 – 5th International Workshop on Advanced Techniques in Actinide Spectroscopy & 9th Workshop on Speciation, Techniques and Facilities for Synchrotron Radiation, October 17–21, 2022, Grenoble, France (2022).
- Middleton, M.; Pospiech, S.; Kinnunen, J.; Tolosana Delgado, R.
Impacts of environmental variables on biogeochemical results – orientation survey in the Peräpohja Belt, Northern Finland
29th International Applied Geochemistry Symposium IAGS2022 – Facing the challenges of today using applied geochemistry, October 23–28, 2022, Viña del Mar, Chile (2022).
- Müller, S.; Ferrari, A.; Knodel, O.; Rachamin, R.
Probing charged lepton flavor violation with the Mu2e experiment
DPG Spring meeting 2022, Section “Hadrons & Nuclei”, March 28–April 01, 2022, virtual, Germany (2022).
- Müller, S.; Ferrari, A.; Mackenzie, M.; Pronskikh, V. S.; Rachamin, R.
Simulation studies of a pion production target for the Mu2e-II experiment
15th workshop on Shielding aspects of Accelerators, Targets, and Irradiation Facilities (SATIF-15), September 20–23, 2022, East Lansing, U.S.A. (2022).
- Newman Portela, A.; Krawczyk-Bärsch, E.; Lopez-Fernandez, M.; Bok, F.; Kassahun, A.; Merroun, M. L.; Raff, J.
Biostimulation of uranium reducing bacteria in contaminated mine water for bioremediation purposes: multidisciplinary approach study
Goldschmidt 2022, July 10–15, 2022, Honolulu, Hawaii, U.S.A. (2022).
- Newman Portela, A.; Krawczyk-Bärsch, E.; Lopez-Fernandez, M.; Kassahun, A.; Roßberg, A.; Kvashnina, K. O.; Bazarkina, E.; Raff, J.; Merroun, M. L.
Microbially induced reduction of Uranium in contaminated mine water for bioremediation purposes: A multidisciplinary approach study
Symposium on Remediation, September 29–30, 2022, Jena, Germany (2022).
- Pareige, C.; Gupta, J.; Vrellou, M.; Kaden, C.; Moldovan, S.; Nomoto, A.; Pareige, P.; Radiguet, B.
Understanding of the evolution of mechanical properties of steels under irradiation: micromechanics and microstructure
26th International Conference on the Application of Accelerators in Research & Industry (CAARI-SNEAP 2022), October 30–November 03, 2022, Denton, Texas, U.S.A. (2022).
- Pospiech, S.
Steps towards Reliable Data – Basic Tools and Concepts
Geoanalysis 2022, August 06–12, 2022, Freiberg, Germany (2022).
- Pospiech, S.; Tolosana Delgado, R.; Brendler, V.; Bachmann, K.; Krause, J.; van den Boogaart, K. G.
From data to model: microstructure aware models for uncertainty estimation of reactive transport in granitoid rocks
21st Annual Conference of the International Association for Mathematical Geosciences, August 29–September 03, 2022, Nancy, France (2022).
- Pospiech, S.; van den Boogaart, K. G.; Renno, A.; Möckel, R.; Fahlbusch, W.
Estimating individual uncertainties – making use of all your replicate analysis
Geoanalysis 2022, August 06–12, 2022, Freiberg, Germany (2022).
- Poulain, A.; Fernandez-Martinez, A.; Greneche, J. M.; Prieur, D.; Scheinost, A. C.; Menguy, N.; Bureau, S.; Magnin, V.; Findling, N.; Drnec, J.; Martens, I.; Mirolo, M.; Charlet, L.
Selenium nanowire formation by reaction of selenate with magnetite
ACS Spring Meeting, March 20–24, 2022, San Diego, U.S.A. (2022).
- Qian, Y.; Grangeon, S.; Scheinost, A. C.; Hoving, A.; Greneche, J. M.; Marques Fernandes, M.
Retention of redox-sensitive Tc(VII) and Se(IV) on Fe(II)/Fe(III) bearing clay minerals
Clay Conference 2022, June 13–16, 2022, Nancy, France (2022).
- Qian, Y.; Grangeon, S.; Scheinost, A. C.; Hoving, A.; Greneche, J. M.; Marques Fernandes, M.
Retention of redox-sensitive Tc(VII) and Se(IV) on Fe(II)/Fe(III) bearing clay minerals
ATAS-AnXAS 2022 – 5th International Workshop on Advanced Techniques in Actinide Spectroscopy & 9th Workshop on Speciation, Techniques and Facilities for Synchrotron Radiation, October 17–21, 2022, Grenoble, France (2022).
- Rachamin, R.; Konheiser, J.; Barkleit, A.; Seidl, M.
Dosimetry for Decommissioning of Nuclear Power Plants
14th International Conference on Radiation Shielding and 21st Topical Meeting of the Radiation Protection and Shielding Division (ICRS 14/RPSD 2022), September 25–29, 2022, Seattle, U.S.A. (2022).

- Rachamin, R.; Konheiser, J.; Seidl, M.
Activation calculations of selected RPV internal components for optimal decommissioning of nuclear power plants
15th workshop on Shielding aspects of Accelerators, Targets, and Irradiation Facilities (SATIF-15), September 20–23, 2022, East Lansing, U.S.A. (2022).
- Roode-Gutzmer, Q. I.; Barkleit, A.; Rachamin, R.; Hennig, C.; Weiß, S.; Paasch, S.; Konheiser, J.; Stumpf, T.
Neutron-irradiated concrete: Structural characterisation and gamma dosimetry
RadChem 2022 – 19th Radiochemical Conference, May 16–20, 2022, Mariánské Lázně, Czechia (2022).
- Roode-Gutzmer, Q. I.; Rössler, C.; Akhmadaliev, S.; Schymura, S.; Barkleit, A.; Stumpf, T.
Examining alkali silica reaction of radiation-damaged quartz and feldspar minerals
20th International Conference on Environmental Degradation of Materials in Nuclear Power Systems -- Water Reactors, July 17–21, 2022, Snowmass Village, Colorado, U.S.A. (2022).
- Schabernack, J.; Faria Oliveira, A.; Heine, T.; Fischer, C.
Influence of Muscovite (001) Surface Sites on Europium Adsorption
GDCh Fachtagung Nuklearchemie 2022, October 04–06, 2022, Bergisch Gladbach, Germany (2022).
- Schabernack, J.; Faria Oliveira, A.; Heine, T.; Fischer, C.
Influence of Surface Nanotopography on the Adsorption of Europium on Muscovite (001)
RadChem 2022 – 19th Radiochemical Conference, May 16–20, 2022, Mariánské Lázně, Czechia (2022).
- Schabernack, J.; Faria Oliveira, A.; Heine, T.; Fischer, C.
Site-Specific Europium Adsorption on Muscovite (001) Surfaces
Goldschmidt 2022, July 10–15, 2022, Honolulu, Hawaii, U.S.A. (2022).
- Schmeide, K.; Huittinen, N. M.; Shams Aldin Azzam, S.; Brendler, E.; Kretzschmar, J.
Uranium(VI) retention by calcium aluminosilicate hydrates (C-A-S-H) – Impact of temperature, ionic strength, and organic ligands
RadChem 2022 – 19th Radiochemical Conference, May 16–20, 2022, Mariánské Lázně, Czechia (2022).
- Stockmann, M.; Lu, R.; Gehrke, A.; Montoya, V.; Noseck, U.; Brendler, V.
Smart Ka-concept as efficient approach to improve geochemistry in reactive transport modelling
Tagung der Fachsektion Hydrogeologie der Deutschen Geologischen Gesellschaft (FH-DGGV-Tagung), March 23–26, 2022, Jena, Germany (2022).
- Sushko, V.; Dressler, M.; Wei, T. S.; Neubert, T.; Kühn, L.; Cherkouk, A.; Matschiavelli, N.
The microbial inventory of bentonite – how does it affect the long-term integrity of repository for high-level radioactive waste?
ISME Microbes, August 14–19, 2022, Lausanne, Switzerland (2022).
- Svitlyk, V.; Weiss, S.; Hennig, C.
Experimental simulation of phase evolution in conditions of underground storage: from million years to one day
Goldschmidt 2022, July 10–15, 2022, Honolulu, Hawaii, U.S.A. (2022).
- Svitlyk, V.; Weiss, S.; Hennig, C.
Extreme conditions: towards secure and long-term storage of nuclear waste
New opportunities for High Pressure Science at the ESRF-EBS, February 07–09, 2022, ESRF, Grenoble, France (2022).
- Taivalkoski, A.; Pospiech, S.; Middleton, M.; Lahaye, Y.; Kinnunen, J.
The Influence of Surface Cover and Bedrock Geology on the Snow Geochemistry – An Example from Northern Finland
Nordic Geological Winter Meeting, Reykjavik, May 11–13, 2022, Reykjavik, Iceland (2022).
- Tsushima, S.
Japan-Germany Research Network on Actinide Chemistry
Virtual Humboldt Colloquium "Top Global Research" and the Humboldt Network: New Frontiers of German-Japanese Scientific Cooperation, November 17–18, 2022, Bonn, Germany (2022).
- Tsushima, S.; Takao, K.
Hydrophobic Core Formation and Secondary Structure Elements in Uranyl(VI)-Binding Peptides
ATAS-AnXAS 2022 – 5th International Workshop on Advanced Techniques in Actinide Spectroscopy & 9th Workshop on Speciation, Techniques and Facilities for Synchrotron Radiation, October 17–21, 2022, Grenoble, France (2022).
- Wozniak, T.; Faria Junior, P. E.; Chaves, A.; Kunstmann, J.; Kuc, A. B.
Engineering of excitonic g-factors in van der Waals structures
Psi-k conference 2022, August 22–25, 2022, Lausanne, Switzerland (2022).

FURTHER LECTURES

Bergner, F.

Neutron scattering methods

European School on Nuclear Materials Science, November 07–11, 2022, Cargèse, France (2022).

Bergner, F.

X-ray and electron diffraction methods

European School on Nuclear Materials Science, November 07–11, 2022, Cargèse, France (2022).

Jessat, I.

Neptunium(V) and uranium(VI) sorption onto the zircaloy corrosion product zirconia (ZrO₂)

Presentation PhD topic, November 09, 2022, Veldhoven, The Netherlands (2022).

Kuc, A. B.

Optoelectronic properties of 2D perovskites and other inorganic-organic hybrid materials

Retreat of CRC1415 project, June 15–17, 2022, Lichtenwalde, Germany (2022).

Matschiavelli, N.

Die Rolle von Mikroorganismen bei der Lagerung von hoch-radioaktiven Abfällen - Mikrobiologie am HZDR - (2022)

Girl's & Boy's day 2022, April 28, 2022, HZDR, Germany (2022).

Matschiavelli, N.

Microbial influence on cast iron corrosion under repository-relevant conditions

UMB-II 3rd workshop, March 09–10, 2022, Greifswald, Germany (2022).

UMB-II 4th project meeting, October 26, 2022, Brunswick, Germany (2022).

Mayordomo, N.

The importance of understanding Technetium environmental behaviour

Seminar at Freie Universität Berlin, February 07, 2022, Berlin, Germany (2022).

○ MEDIA CONTRIBUTIONS

Lederer, F.; Boelens, P.; Vogel, M.; Bobeth, C.; Kießlich, T.; Bloß, C.; Wei, T.-S.; Drobot, B.

“Elektroschrott-Recycling mit Viren“ im ZDF Leschs Kosmos Beitrag “Der Schatz in der Mülltonne“

Television documentary “Leschs Kosmos”, September 06, 2022, Germany (2022)

URL: <https://www.zdf.de/wissen/leschs-kosmos/der-schatz-in-der-muelltonne-das-recycling-versprechen-100.html>
(Accessed on February 22, 2023).

Woschni, U.; Foerstendorf, H.

Abendschule: Radioaktivität

Radio broadcast, coloRadio, September 06, 2022, Dresden, Germany (2022).

URL: <https://hearthis.at/ulrike-woschni/34radioaktivitatcoloradio2022september>
(Accessed on: February 22, 2023).

DOCTORAL THESES

Demnitz, M.

Mechanistic models for the interaction of Cm(III) and Eu(III) with crystalline rocks

Fischer, S.

Understanding the role of microorganisms in determining the fate of biogenic elemental selenium nanomaterial

Jessat, J.

Wechselwirkung von Radionukliden mit Pflanzen: Identifizierung von Metaboliten und deren Einfluss auf Bioverfügbarkeit und Transport von Actiniden in der Umwelt

Köhler, L.

Komplexierung von Actiniden in unterschiedlichen Oxidationsstufen mit Hilfe organischer N-Donor Liganden

Neumann, J.

Strukturelle Untersuchung der Rückhaltung von Actiniden und ihrer Übergangsmetallhomologe an ausgewählten Alumosilikat-Phasen

MASTER THESES

Cariven, C.

Long-term reactions of silicate mineral phases - implementation and application of pH-dependent dissolution rates with relevance for future nuclear waste disposals

TU Bergakademie Freiberg (2022)

Jeschke, I.

U(VI) Reduktion durch Sulfat und Eisen reduzierende Bakterien

Waurick, L.

Berechnung des Einflusses von Halogensubstituenten auf die Elektronenstruktur von An(IV)-Salen Komplexen

Näder, A.

Computergestützte Studien der Elektronenstruktur von An(IV)-Amidinat-Systemen und Berechnung spektroskopisch relevanter Parameter

Hadlich, C.

Spectral correlation analysis of the thermal unfolding of DNA nanostructures under the influence of gadolinium salts

- CONFERENCES, WORKSHOPS
- AWARDS
- SEMINARS
- TEACHING ACTIVITIES

○ ACTINIDES REVISITED – 2022

September 21–23, 2022, Penck Hotel, Dresden, Germany

After a series of cancellations of important conferences and workshops due to the CoViD-19 pandemic, IRE decided to host a conference dedicated to actinide science together with colleagues from Erlangen, Marburg, and Göttingen, entitled “Actinides Revisited – 2022”.

The conference was held at the Penck Hotel in Dresden with 86 participants from 35 institutions in 11 nations. The participants presented exciting scientific results in 44 oral presentations and an additional 27 poster contributions. The conference covered the topics coordination chemistry, theoretical chemistry, transuranium elements, solid state chemistry, as well as spectroscopy and electronic structure.

We gratefully acknowledge the support we received from the German Federal Ministry of Education and Research *via* funding for the project “f-Char” (02NUK059B). Special thanks are also due the scientific committee consisting of Lisa Vondung, Karsten Meyer, Florian Kraus and Thorsten Stumpf for putting together this event and our five plenary speakers Suzanne Bart, Thomas Albrecht-Schönzart, David L. Clark, Steve Liddle, and Hans-Conrad zur Loye.

Plenary speaker contributions:

Liddle, Steve

The University of Manchester, Manchester, U.K.

Recent Advances in Actinide-Ligand Multiple Bonding

Albrecht-Schönzart, Thomas

Florida State University, Tallahassee, FL, U.S.A. / Colorado School of Mines, Golden, CO, U.S.A.

Enhancing Frontier Orbital Interactions in the f-Block Through Applications of Pressure and Electric Fields

zur Loye, Hans-Conrad

University of South Carolina, Columbia, SC, U.S.A.

From Mild Hydrothermal to High Temperature Solutions: Crystal Growth of New Uranium and Transuranium Phases

Bart, Suzanne

Purdue University, West Lafayette, IN, U.S.A.

Harnessing Multi-Electron Redox Chemistry to Access Unprecedented Actinide Moieties

Clark, David L.

Los Alamos National Laboratory, Santa Fe, NM, U.S.A.

Applications of ^{238}Pu are Out of this World



○ ATAS/ANXAS 2022 – JOINT WORKSHOP

5TH INTERNATIONAL WORKSHOP ON ADVANCED TECHNIQUES IN ACTINIDE SPECTROSCOPY

9TH WORKSHOP ON SPECIATION, TECHNIQUES AND FACILITIES FOR SYNCHROTRON RADIATION

October 17–21, 2022, ESRF, Grenoble, France



AnXAS is a series of unique international workshops, which focus on basic and applied research of radioactive materials using synchrotron-based techniques. The workshops have been previously held in France, U.S.A., Germany, Japan, Switzerland, and the U.K. In 2022, the workshop came back to where it started in 1998, the ESRF in Grenoble, where the EBS along with the new ROBL-II provided an excellent meeting background.

AnXAS was combined for the first time with ATAS, an International Workshop on Advanced Techniques in Actinide Spectroscopy, which has been held since 2012 in Germany, U.S.A., and France. ATAS is particularly focusing on complementary application of various spectroscopic techniques and their combination with theoretical approaches for a profound understanding of structures, thermodynamics and kinetics of f-elements complex formation.

Both workshops have been delayed due to CoVid from their usual tri- (AnXAS) and bi-annual patterns, and were now combined for the first time to improve synergistic effects and foster the scientific discussion between spectroscopists and theoreticians.

More than 90 participants from 12 countries, including the U.S.A. and Japan, gathered for a program of 52 talks and 16 posters. Sessions on Radioactive Waste Disposal, Bio-Geochemistry, Nuclear Materials, Emerging Techniques, Aqueous & Coordination Chemistry and Electronic Structure of actinides presented the current state of the art in these fields; in addition, facility reports provided a comprehensive overview on synchrotron beamlines able to perform actinide research. On the last day, several beamlines at ESRF, including ROBL-II, were visited.

The workshop was a great success and well received by all participants. The scientific community expressed a strong

interest and excitement in the continuation of this series of workshops, with a more frequent biannual pattern. The next joint ATAS-AnXAS Workshop will hence take place 2024, at ALS and Lawrence Berkeley Lab, CA, U.S.A.

Invited lecture were given by:

Corkhill, Claire

University of Sheffield, Sheffield, U.K.

Boyanov, Maxim

Bulgarian Academy of Science, Sofia, Bulgaria

Dumas, Thomas

CEA/Marcoule, Bagnols-sur-Cèze, France

Takao, Koichiro

Tokyo Institute of Technology, Tokyo, Japan

Walter, Olaf

European Commission JRC-KA, Karlsruhe, Germany

Minasian, Stefan

Ernest Orlando Lawrence Berkeley National Laboratory (LBNL), Berkely, CA, U.S.A.

Butorin, Sergei

Uppsala University, Uppsala, Sweden

Vallet, Valerie

University of Lille, Lille, France

Severing, Andrea
*Max Planck Institute for Chemical Physics and Solids,
 Dresden, and University of Cologne, Cologne, Germany*

Bernier-Latmani, Rizlan
*École Polytechnique Fédérale de Lausanne (EPFL),
 Lausanne, Switzerland*

Shaw, Sam
University of Manchester, Manchester, U.K.

In addition to beamline scientists representing all synchrotron facilities suited for actinide research.

The Young Scientist Award went to Rafael Caprani (CEA, France), the Best Poster Award was shared by Anita Kateras (University of Bern, Bern, Switzerland) and Thomas Zimmermann (HZDR, Institute of Resource Ecology, Dresden, Germany).

Further information can be found at the conference webpage: <https://www.esrf.fr/ATAS-AnXAS>.

○ AWARDS

Diaz Pescador, Eduard
Best paper awards (3rd place)
KERNTECHNIK 2022, June 21, 2022, Leipzig, Germany (2022).

Fichter, Sebastian
Promotionspreis – 2022
*GDCh, Fachgruppe Nuklearchemie
 October 6, 2022*

Friedrich, Sebastian
Poster award
*Actinides Revisited 2022, September 21–23, 2022,
 Dresden, Germany (2022).*

Schmidt, Moritz
Fritz-Straßmann-Preis – 2022
*GDCh, Fachgruppe Nuklearchemie
 October 6, 2022*

Sieber, Claudia
Poster award
*RadChem 2022 – 19th Radiochemical Conference, May 16–
 20, 2022, Mariánské Lázně, Czechia (2022).*

Steuertner, Robin
Postdoc Award for Best Oral Contribution
*Terrae Rarae - Tage der Seltenen Erden, September 27–
 29, 2022, Leipzig, Germany (2022).*

Zimmermann, Thomas
Best Poster Award from RSC Advances
**“Investigating the complex interaction of
 technetium with magnetite nanoparticles”**
*ATAS-AnXAS 2022 – 5th International Workshop on
 Advanced Techniques in Actinide Spectroscopy & 9th
 Workshop on Speciation, Techniques and Facilities for
 Synchrotron Radiation, October 17–21, 2022, Grenoble,
 France (2022).*

○ SEMINARS (TALKS OF VISITORS)

Zeler, Justyna
*Faculty of Chemistry, University of Wrocław, Wrocław,
 Poland*
**Luminescence thermometry in biological
 applications**
September 16, 2022

Zych, Eugeniusz
*Faculty of Chemistry, University of Wrocław, Wrocław,
 Poland*
**Non-Boltzmann Luminescent Thermometers for
 Wide Operating Ranges**
September 16, 2022

Kaskel, Stefan
*Technische Universität Dresden / Fraunhofer-Institut für
 Werkstoff- und Strahltechnik, Dresden, Germany*
**Porous Energy Materials: From Fundamentals to
 Applications**
October 7, 2022

Düllmann, Christoph
*GSI Helmholtzzentrum für Schwerionenforschung /
 Johannes Gutenberg-Universität Mainz / Helmholtz-
 Institut Mainz, Germany*
**The superheavy elements – a journey to the end of
 the periodic table**
November 29, 2022

TEACHING ACTIVITIES

(Winter term: WT; summer term: ST)

Lectures

Bok, F.

Friedrich-Schiller-Universität, Jena

ST 2022

Geochemische Modellierung mit Geochemist's Workbench®

Brendler, V.

Dresden University of Applied Sciences

ST 2022

Radiochemistry

Fahmy, K.

Technische Universität Dresden

WT 2021/2022, WT 2022/2023

Molecular Biophysic: Concepts and Methods

ST 2022

Biological Thermodynamics

Fischer, C.

Universität Bremen

ST 2022

Diagenese

Universität Leipzig

WT 2021/2022, WT 2022/2023

Moderne Methoden in der Materialwissenschaft

Heine, T.

Technische Universität Dresden

WT 2021/2022, WT 2022/2023

PC II (Theorie der Chemischen Bindung)

PC III (Einführung in die Computerchemie)

Theoretische Chemie

Computational Spectroscopy

WT 2021/2022

Quantum Chemistry

Yonsei University Seoul, Korea

ST 2022

Artificial Intelligence and Machine Learning

Huittinen, N.

Technische Universität Dresden

ST 2022

Radioecology

WT 2022/2023

Allgemeine und Anorganische Chemie

Kuc, A. B.

Universität Leipzig

WT 2021/2022

Computational Chemistry of Solids

WT 2022/2023

Computational Spectroscopy

Lippold, H.

Universität Leipzig

ST 2022

Entstehung und Eigenschaften ionisierender Strahlung

WT 2021/2022, WT 2022/2023

Radioanalytik

Radiochemische Analysemethoden

Mayordomo Herranz, N.

Technische Universität Dresden

WT 2022/2023

Radioecology

Raff, J.

Dresden University of Applied Sciences

WT 2021/2022, WT 2022/2023

Mikrobiologie

Technische Universität Dresden

WT 2021/2022, WT 2022/2023

Mikrobielle Laugung

Schmidt, M.

Technische Universität Dresden

ST 2022, WT 2022/2023

Chemistry of the f-elements

Schymura, S.

Universität Leipzig

WT 2021/2022, WT 2022/2023

Radioanalytik

Stumpf, T.

Technische Universität Dresden

WT 2021/2022

Radiochemistry

Courses

☞ The laboratory course “Radiochemistry” was provided from August 29–September 09, 2022, as a part of a module of the chemistry master degree program at the Technische Universität Dresden.

Advisers:

Braga Ferreira dos Santos, L.	Klotzsche, M.
Butscher, D.	Lessing, J.
Dornbusch, D.	Mayordomo Herranz, N.
Duckworth, T.	Patzschke, M.
Friedrich, S.	Sachs, S.
Hong, B.	Sieber, C.
Jessat, I.	Sushko, V.
Jordan, N.	Waurick, L.
Kaden, P.	Zimmermann, T.

☞ Biophysics course of the Dresden-International-Graduate School (WT 2021/2022 & WT 2022/2023).

Advisers:

Fahmy, K.	Oertel, J.	Philipp, J.
-----------	------------	-------------

☞ Courses and seminars were held referring to the following lectures:

Fahmy, K.
Technische Universität Dresden,
 WT 2021/2022, WT 2022/2023
Biophysics course of the Dresden-International-Graduate School

Faria Oliveira, A.
Technische Universität Dresden,
 WT 2021/2022
Spektroskopie mit dem Computer
 WT 2022/2023
Theorie der chemischen Bindung

Kuc, A. B.
Universität Leipzig,
 WT 2021/2022
Spektroskopie (PC)
 WT 2021/2022
Computational Chemistry for Solids
 WT 2022/2023
Computational Spektroskopie

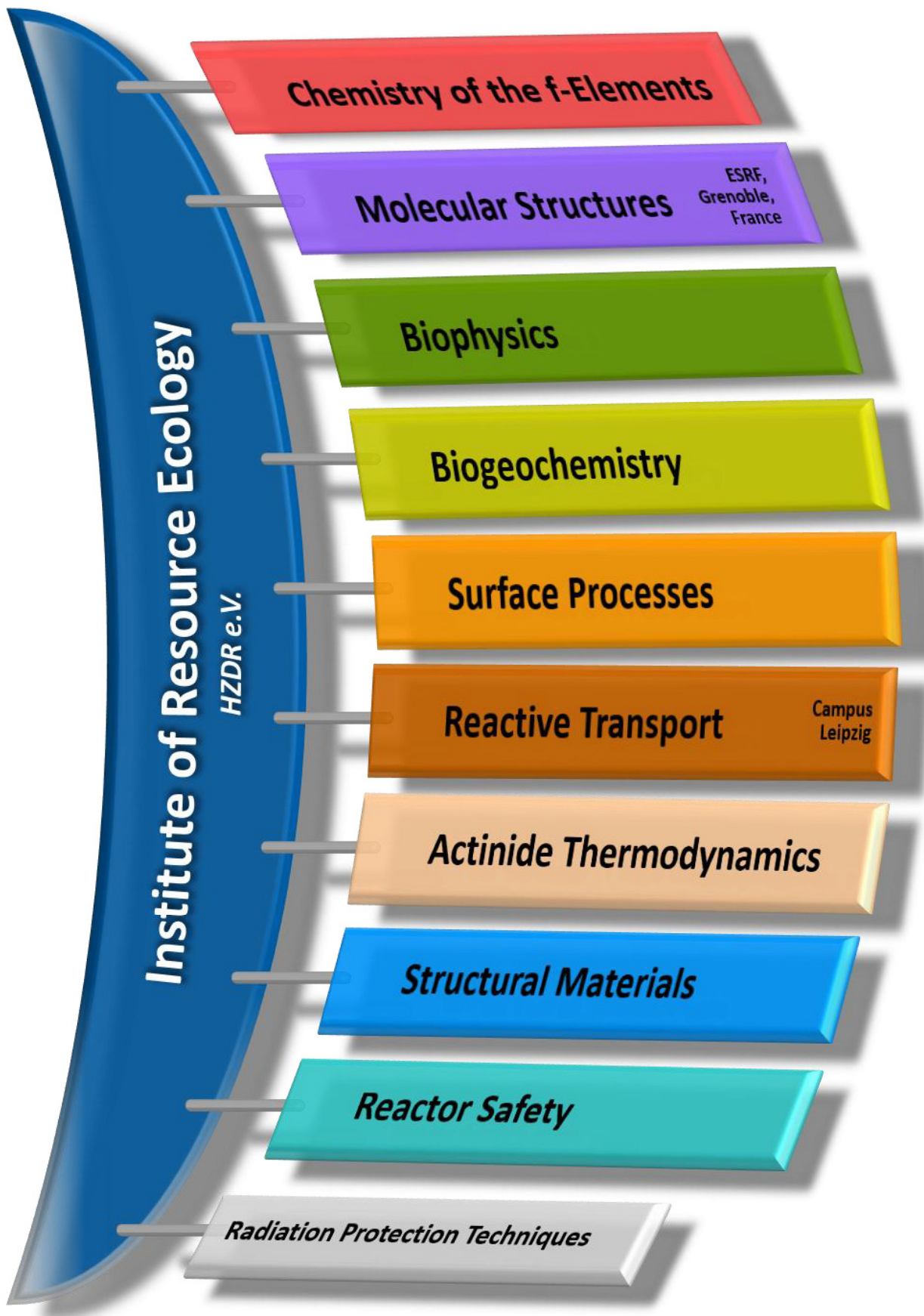
Springer, M.
Technische Universität Dresden,
 WT 2021/2022, WT 2022/2023
Theorie der chemischen Bindung

Following page:

Impressions of further activities of the IRE in 2022. Photos were taken during the annual PhD seminar of the institute at Scheffau,



PERSONNEL



HEAD OF INSTITUTE: Prof. Dr. Thorsten Stumpf

ADMINISTRATION:

Office Dresden: Goritzke, Jana; Theunert, Bettina;
Kovacs, Jenny; Kurde, Kerstin; Rott, Sonja
Office Leipzig: Gerstner, Katrin; Meinken, Roswitha; Pedrosa Gil, Nadja

PROJECT COORDINATION:

Dr. Arnold, Thuro

RADIATION PROTECTION TECHNIQUES:

Bachmann, Stefanie; Dräger, Eric; Eisold, Silke; Falkenberg, Dirk;
Henke, Stefan; Jimenez Hernandez, Susana; Nebe, Kathrin
Sysad (IT): Berndt, Ronny

ACTINIDE THERMODYNAMICS

PROF. DR. BRENDLER, VINZENZ

Dr. Abbasova, Dinara
Dr. Bok, Frank
Düick, Viktor*
Fankhänel, Tobias*
Dr. Kretzschmar, Jérôme
Dr. Richter, Anke
Dr. Pospiech, Solweig
Dr. Schierz, Ariette
Dr. Schneide, Katja
Shams Aldin Azzam, Salim

Sieber, Claudia*
Dr. Stockmann, Madlen
Zechel, Susanne

ANALYTICS
Dr. Foerstendorf, Harald
Beutner, Sabrina
Goldbach, Dominik
Heim, Karsten
Schöne, Sylvia

SURFACE PROCESSES

DR. MÜLLER, KATHARINA

Butscher, Daniel*
Chlupka, Alina
Dennitz, Maximilian*
Dietze, Alexandra
Friedrich, Sebastian*
Jessat, Isabelle*
Dr. Jordan, Norbert
Müller, Christa
Dr. Rodriguez Hernandez, Diana M.
Weiss, Stephan

INCORP. INTO SOLID PHASES
Dr. Huitfenn, Nina
Dr. Barkeit, Astrid
Braga Ferreira dos Santos, Luiza*
Dr. Gilson, Sara
Roode-Gutzmer, Quirina
Dr. Yassin, Ghada

TECRAD – YOUNG INV. GROUP
Dr. Mayordomo Herranz, Natalia
Bureika, Arkadz
Cardaió, Irene*

REACTIVE TRANSPORT

PDD DR. FISCHER, CORNELIUS

Becker, Alexandra*
Cadenas Rivera, Maria Alejandra*
Costa Guedes, Beatriz*
Dr. Franke, Karsten
Grubne, Stefan
Hilpmann, Stephan
Dr. Kulenkampff, Johannes
Dr. Lippold, Holger
Lösel, Dagmar
Dr. Mansel, Alexander

Raj, Abhishek*
Schabernack, Jonas*
Schögliger, Claudia
Schöngart, Jan*
Dr. Yuan, Tao
Zhou, Wenyu*

NANOSAFETY
Dr. Schymura, Stefan
Uygan, Senha Simale Su*

Campus Leipzig

STRUCTURAL MATERIALS

DR. ALTSTADT, EBERHARD

Dr. Bergner, Frank
Dr. Brandenburg, Jann-Erik
Dr. Cheknonin, Paul
Dr. Das, Aniruddh
Houska, Mario
Dr. Kaden, Cornelia
Dr. Kapoor, Garima
Lai, Libang*

Pietzsch, Jens
Reinke, Vanessa
Richter, Tony
Röfner, Michaela
Dr. Ulbricht, Andreas
Dr. Vogel, Karin
Webersünke, Wolfgang
Weiz, Tilo

BIOGEOCHEMISTRY

DR. RAFF, JOHANNES

Bertheau, Rahel
Dr. Drobot, Björn
Flemming, Katrin
Dr. Günther, Alix
Dr. Jessat, Jenny
Fabrega-Puentes, Alejandro*
Dr. John, Warren
Klotzsche, Max*
Dr. Krawczyk-Bärsch, Evelyn
Dr. Mandall, Poullami
Dr. Moll, Henry
Dr. Sachs, Susanne

Seibt, Jana
Stalke, Sebastian
Dr. Stedtner, Robin
Waurick, Lukas*

MICRONUC
Dr. Cherkouk, Andrea
Hilpmann, Stephan*
Kluge, Sindy
Dr. Malschiavelli, Nicole
Sushko, Vladyslav*
Dr. Wei, Ting-Slyang

CHEMISTRY OF THE F-ELEMENTS

PDD DR. SCHMIDT, MORITZ

Dr. Gericke, Robert
Dr. Kaden, Peter
Dr. Neumann, Julia
Lessing, Jessica*
Dr. Patzschke, Michael
Ramakrishnan, Sreenivas

METALLOORGANIC ACTINIDE
CHEMISTRY
Dr. März, Juliane
Duckworth, Tamara*
Hong, Boseok*
Köhler, Luisa*

Dr. An, Yun

Eren, Ismail*

Gouatieu Dongmo, Elvira*

Lurz, Christian*

Iha, Gautam*

Springer, Maximilian*

Dr. Yang, Li

MOLECULAR STRUCTURES

DR. HABIL. SCHENOST, ANDREAS C.

Dr. Baumann, Nils
Exner, Jörg
Dr. Faria Oliveira, Augusto
Dr. Hennig, Christoph
Naudet, Damien
Dr. Prieur, Damien
Dr. Rossberg, André
Dr. Svitlyk, Volodymyr

Zimmermann, Thomas*

ELECTRONIC STRUCTURES:
Dr. Kvashnina, Kristina O.
Dr. Amidani, Lucia
Dr. Bazantkná, Elena
Dr. Ote, Florian

ESRF, Grenoble

REACTOR SAFETY

DR. KLIEEM, SÖREN

Dr. Baier, Silvio
Bastrakova, Ksenia*
Dr. Bilodid, Yuri
Diaz, Rescador Eduard*
Dr. Fridman, Emil
Gommlich, André
Dr. Grab, Alexander
Jobst, Matthias

Konheiser, Jörg
Dr. Nikitin, Evgeny
Dr. Pönitz, Erik
Dr. Ponomarev, Alexander
Dr. Rachamin, Reuven
Dr. Schäfer, Frank
Yadav, Pratibha*

BIOPHYSICS

PROF. DR. FAHMY, KARIM

Dornbusch, Daniel*
Dr. Kieler, Charlotte
Nucke, Lisa*

Dr. Oertel, Jana
Philipp, Jenny
Prof. Dr. Tsumihama, Satoru

PHYS. CHEM. OF BIOLOGICAL CONDENSATES
Dr. Adams, Ellen

*: Ph.D. student (as of 2022/12/31)

GUEST SCIENTISTS

Brumme, Thomas	<i>Technische Universität Dresden, Germany</i>
Dykas, Jakob	<i>Technische Universität Dresden, Germany</i>
Garcia Gómez, Sonia	<i>Universitat Polytechnica de Catalunya, Barcelona, Spain</i>
Heller, Anne	<i>Technische Universität Dresden, Germany</i>
Lender, Theresa	<i>RWTH Aachen, Germany</i>
Reiss, Amit	<i>Hebrew University of Jerusalem, Israel</i>
Sayed, Ahmed M. T.	<i>Technische Universität Dresden, Germany</i>
Takeyama, Tomoyuki	<i>Tokyo Institute of Technology, Japan</i>
Thai, Quang Minh	<i>Technische Universität Dresden, Germany</i>

CO-FUNDED PH.D. STUDENTS

Böhm, Wendelin	<i>Technische Universität Dresden, Germany</i>
Caprani, Rafael	<i>Université Nantes, France</i>
Diksha, Saini	<i>Université Grenoble Alpes, France</i>
He, Yihua	<i>Laboratoire de physique subatomique et des technologies associées (Subatech), Nantes, France</i>
Kempton, Roman	<i>Technische Universität Dresden, Germany</i>
Kirsch, Klemens	<i>Bundesanstalt für Materialforschung und -prüfung (BAM), Berlin, Germany</i>
Newman Portela, Antonio	<i>UGR Granada, Spain</i>
Raj, Mantan	<i>Technische Universität Dresden, Germany</i>
Umm-e-Hani	<i>Jacobs University Bremen gGmbH, Germany</i>

MASTER/DIPLOMA/BACHELOR

Balas, Johannes	Hadlich, Christoph	Näder, Adrian	Uhlitzsch, Lucie
Cariven, Claire	Jeschke, Isabelle	Richter, Selina	Zscheile, Amelie

GRADUATE ASSISTANTS, STUDENT ASSISTANTS, TRAINEES

Blei, Magdalena Kerstin	E Silva, Clara Lisa	Renningholtz, Tim
Bode, Tobias	Kola, Naga Suresh	Uhlitzsch, Lucie

ACKNOWLEDGEMENTS

The Institute of Resource Ecology is one of the ten institutes of the Helmholtz-Zentrum Dresden–Rossendorf e.V. (HZDR). As registered, non-profit institution, the HZDR is supported by the authorities of the Federal Government and the Free State of Saxony. In addition to the basic funding, the financial support of the projects listed below by the given organizations and companies is gratefully acknowledged.

FUNDING ORGANIZATION / COMPANY	PROJECT TITLE	CONTRACT NO. (if applicable)
Commission of the European Communities (EU)	COMET – Two dimensional lattices of covalent- and metal-organic frameworks for the Quantum Hall resistance standard	20FUN03
	ENTENTE – European Database for Multiscale Modelling of Radiation Damage	H2020-900018
	ESFR-SIMPLE - European Sodium Fast Reactor - Safety by Innovative Monitoring, Power Level flexibility and Experimental research	HEU-101059543
	ESFR-SMART – European SFR – Safety Measures Assessment and Research Tools	H2020-754501
	EURAD – European Joint Programme on Radioactive Waste Management ConCorD, CORI, DONUT, FUTURE T2 + T3, MAGIC, SFC, UMAN, KMSoK	H2020-847593
	FRACTESUS – Fracture mechanics testing of irradiated RPV steels by means of sub-sized specimens	H2020-900014
	INNUMAT – Innovative Structural Materials for Fission and Fusion	HEU-101061241
	McSAFER – High-Performance Advanced Methods and Experimental Investigations for the Safety Evaluation of Generic Small Modular Reactors	H2020-945063
	PIANOFORTE – Partnership for European research in radiation protection and detection of ionising radiation : towards a safer use and improved protection of the environment and human health	HEU-101061037
	R2CA: Reduction of Radiological Consequences of Design Basis and Design Extension Accidents	H2020-847656
	RadoNorm – Towards effective radiation protection based on improved scientific evidence and social considerations – focus on radon and NORM + RadoNorm Open Call Grant	H2020-900009
	Sol2H2 – Computational Design of Materials for Photocatalytic Hydrogen Generation and Separation	H2020-101031846
	STRUMAT-LTO – STRUctural MATerials research for safe Long Term Operation of LWR NPPs	H2020-945272
	SurfBio – Innovation hub for surface and colloid biology research	H2020-952379
	TOP – ERC Starting Grant – Towards the Bottom of the Periodic Table	H2020-759696
Federal Ministry for Economic Affairs and Climate Action (BMWK) & Federal Ministry of Education and Research (BMBF) & Federal Ministry for the Environment, Nature Conservation, Nuclear Safety and Consumer Protection (BMUV)	AcE – Grundlegende Untersuchungen zur Immobilisierung von Actiniden mittels Einbau in endlagerrelevante Festphasen	02NUK060A
	EMPRADO – Entwicklung einer Methode zur Pre-Aktivitäts- und Dosisleistungsberechnung von reaktornahen Bauteilen auf Basis von Neutronenflussverteilungen Berechnung der Neutronenflussverteilung in reaktornahen Bauteilen und deren Validierung an Experimenten als Basis der Aktivitätsrechnungen	15S9409A

FUNDING ORGANIZATION / COMPANY	PROJECT TITLE	CONTRACT NO. (if applicable)
	f-Char – Verbundprojekt – Spektroskopische Charakterisierung von f-Element-Komplexen mit soft donor-Liganden	02NUK059B
	GRaZ II – Verbundvorhaben Geochemische Radionuklidrückhaltung an Zementalterationsphasen	02E11860B
	iCross – Verbundprojekt iCross Integrität von Endlagersystemen für radioaktive Abfälle – Skalenübergreifendes Systemverständnis und Systemanalyse	02NUK053B
	KRIMI Verbundprojekt Kinetik der Radionuklidimmobilisierung	02NUK056C
	MgO-S3 Spritzbeton für Streckenverschlüsse für HAW-Endlager im Steinsalz	02E11769B
	MgO-C3 Verbundprojekt: MgO-Beton C3 als langzeitbeständiges und schnellwirksames Verschlusselement für Schachtverschlüsse zukünftiger HAW-Endlager im Salinar; Teilprojekt: Untersuchung der Kontakte innerhalb der Zuschlagskörnung	02E12072B
	PANAS – Verbundvorhaben Untersuchungen zu passiven Nachzerfallswärme-Abfuhrsystemen; Teilprojekt B: Untersuchungen zu Kondensationsprozessen im Notkondensator und numerische Simulation einer passiven Wärmeabfuhrkette	02NUK041B
	PepTight – Lasst die Biologie ran – Peptide umgarnen entscheidende Rohstoffe: die „natürliche“ Trennung von Lanthaniden, Teilprojekt A	031B1122A
	RADEKOR – Verbundprojekt Speziation und Transfer von Radionukliden im Menschen unter besonderer Berücksichtigung von Dekorporationsmitteln	02NUK057A
	RENA – Biologische Radionuklidentfernung durch Nutzung natürlicher Assoziationsprozesse, Teilprojekt A	02NUK066A
	ResKin_Move – Geschwindigkeitsfeld-Analyse mit Positronen-Emissions-Tomografie (PET): Parametrisierung und Validierung von Transportmodellen (Plug-Skala)	03G0900A
	SMILE – Smart-K _a in der Langzeitsicherheitsanalyse – Anwendungen, Teilprojekt B	02E11668B
	STROEFUN III – Strömungstechnischer Funktionsnachweis für Verschlussbauwerke und flüssigkeitsgestützte Abdichtung des Kontaktbereiches Phase III: Vertiefung Kenntnisstand Kontaktbereich & Injektionsmittel, <i>in situ</i> -Versuche	02E11748B
	TecRad – Wechselwirkung von Technetium mit Mikroorganismen, Metaboliten und an Mineral-Wasser Grenzflächen - Radioökologische Betrachtungen	02NUK072
	TRAVARIS Verbundvorhaben: Transfer langlebiger Radionuklide aus der vadosen Zone in die Rhizosphäre und deren Aufnahme in Pflanzen unter Berücksichtigung mikrobiologischer Prozesse - Teilprojekt C: Einfluss der Bodenmikrobiologie auf den RN-Transfer und Verifizierung von Aufnahmemechanismen für RN in Pflanzen	15S9437C
	UMB II – Umwandlungsmechanismen in Bentonitbarrieren II	02E11870B

FUNDING ORGANIZATION / COMPANY	PROJECT TITLE	CONTRACT NO. (if applicable)
	VESPA II – Verbundprojekt Verhalten langlebiger Spalt- und Aktivierungsprodukte im Nahfeld eines Endlagers und Möglichkeiten ihrer Rückhaltung	02E11607B
	WERREBA – Wege zum effizienten Rückbau von Reaktorkomponenten und Betonabschirmung: Berechnung des Aktivitätsinventars und deren Validierung an Bohrkernen sowie Mobilitätsuntersuchungen von Radionukliden	15S9412
	WTZ-Granit – Vorhersage der heterogenen Radionuklidsorption auf Kluff- und Störungsflächen in granitischen Gesteinen: Parametrisierung und Validierung verbesserter reaktiver Transportmodelle	02E11911A
Deutsche Forschungsgemeinschaft (DFG, German Research Foundation)	DFG-Programmpauschalen ab 2014 – Verwaltung von 25 % der ab 2014 zu den DFG-Projekten bewilligten Programmpauschalen	
	DNA-Struktur Molekulare Mechanismen der Interaktion chaotroper Salze mit natürlichen und künstlichen DNA-Strukturen	FA 248/8-1
	Graduiertenkolleg „Wasserstoff-Isotope 1,2,3H“	GRK 2721/1
	SFB 1415 – Sonderforschungsbereich 1415 „Chemie der synthetischen zweidimensionalen Materialien“	SFB 1415/1 2020
ANDRA	REDOX - Redox reactivity of selenium in environmental geomeia	n20087095HZDR
Framatome, SAS	DYN3D Support Service Framatome	
Bundesgesellschaft für Endlagerung mbH (BGE)	THEREDA IV Datenbank SOREDA – Entwicklung von Oberflächenkomplexierungsmodellen und Erstellung einer Referenz-Datenbasis	
Helmholtz-Gemeinschaft Deutscher Forschungszentren e.V. (HGF, Helmholtz Association)	HEP CROSSING – Crossing borders and scales – an interdisciplinary approach	PIE-0007
	LiqCounter – New Liquid Scintillation Counter	HE-2021-06-FSF
	NUSAFE / iCross	SO-093
ITD	Berechnungen MCNP und FLUKA	
PreussenElektra GmbH	Berechnung hochaufgelöste Neutronenspektren an ausgesuchten Positionen des Reaktordruckbehälters und der daraus resultierenden Aktivitäten	4500355585
	Gekoppelte Dyn3D/Athlet-Analysen	4500355625/PME/0701
	Monitoring – Rekursive Berechnung von Neutronenfeldern in Räumen außerhalb der biologischen Abschirmung	4500353697
South African Medical Research Council (SAMRC), Johannesburg, South Africa	Haarproben – Analyse von Uran in Haarproben von Kindern und Jugendlichen, die in der Nähe von Minenhalden in Südafrika leben	
TÜV NORD	Prüfung geologischer Fragen	M.ASS.06.015.01.F70

FUNDING ORGANIZATION / COMPANY	PROJECT TITLE	CONTRACT NO. (if applicable)
TÜV SÜD	DYN3D Wartung TÜV S 2020/2021 ff- FWOR TÜV VVER 1200 code 1 – Support and consulting services WVER AP03	500603389
ÚJV Řež, a.s., Czech Republic	DYN3D für UJV Wartung 2021/2022, 2022/2023	VT1100028
VW Stiftung	VW Stipendium Iarmosh	9C097

INDEX OF AUTHORS

AUTHOR.....	PAGE
Abram, U.	21
Acker, M.	23
Akhmadaliev, S.	39
Altstadt, E.	71, 75
Amidani, L.	37
An, Y.	25, 26
Baier, S.	81
Baranowski, M.	38
Barkleit, A.	66, 77
Barros, R.	67
Bergner, F.	72, 73, 74, 75
Bilke, M.-L.	56, 59
Bilodid, Y.	80
Bode, T.	16
Bodensteiner, M.	24
Bok, F.	40, 46, 47, 54
Bollermann, T.	43
Brendler, V.	20, 40, 46, 48
Bukaemskiy, A.	39
Butorin, S. M.	37
Cariven, C.	40
Chekhonin, P.	71, 72, 75
Chen, C.	42
Chen, G.	26
Cherkouk, A.	61, 62
Chernikov, A.	38
Claparede, L.	36
Clavier, N.	36
Dacheux, N.	36
Das, A.	71, 74, 75
Deev, D.	62
Deligiozi, I.	67
Demnitz, M.	29
Diaz-Pescador, E.	82
Dietze, A.	32
Dolomanov, O. V.	24
Dornbusch, D.	65
dos Santos, L. B. F.	33
Drobot, B.	19, 22, 55, 56, 58, 59, 60
Duckworth, T.	13
Dumas, T.	37
Dyksik, M.	38
Eibl, M.	30
Eng, P. J.	29
Engelmann, H.-J.	72
Fahmy, K.	64, 65
Fang, L.	25
Feng, X.	25, 26
Fenter, P.	29
Fichter, S.	66
Fischer, C.	39, 41, 42, 43, 44, 63
Foerstendorf, H.	32
Fridman, E.	76, 80, 83
Furlan, C.	67
Gericke, R.	16, 17
Gilson, S. E.	34, 39

AUTHOR.....	PAGE
Gruhne, S.	45
Günther, A.	58
Hähner, P.	74
He, T.	26
Heim, K.	32
Heine, T.	21, 25, 26
Hennig, C.	24, 33, 35, 39
Hilpmann, S.	57, 62
Hoehenwarter, W.	53
Hong, B.	16
Hoth, N.	40
Houska, M.	71
Hübner, R.	53, 56, 58, 59
Huittinen, N.	30, 31, 33, 34, 39
Hunault, M. O. J. Y.	36
Jasiński, J.	38
Jeschke, I.	62
Jessat, I.	32
Jessat, J.	56, 59
Jobst, M.	79
John, W. A.	53, 56, 59
Jordan, N.	32, 48
Kaden, C.	72, 74
Kaden, P.	13, 14, 16, 18
Kahle, L.	63
Kaiser, U.	26
Karpińska, M.	38
Kassahun, A.	54
Keiderling, U.	73
Kempt, R.	38
Kleemiss, F.	24
Kliem, S.	82
Kłopotowski, Ł.	38
Klotzsche, M.	60
Köhler, L.	18
Kolditz, O.	42
Konheiser, J.	77, 78, 81
Krawczyk-Bärsch, E.	54, 55
Kretzschmar, J.	22, 23, 56
Kuc, A.	21, 25, 26, 38
Kulenkampff, J.	43, 45
Kvashnina, K. O.	15, 33, 37
Lapanje, A.	62, 67
Lapuenta de Ojeda, B.	67
Lee, S. S.	29
Lessing, J.	29
Li, T.	25
Lippold, H.	39, 63
Liu, L.	25
Liu, P.	26
Liu, S.	26
Liu, Y.	25
Longo, A.	37
Lönnrot, S.	30
Lösel, D.	45
Lu, R.	42
Lückel, B.	53
Lv, K.	14

AUTHOR..... PAGE

Martel-Martin, S.....67
 Martin, P.36
 Martinez, J.....36
 März, J. 13, 14, 16, 18
 Massonnet, M.36
 Matschi, S.....53
 Matschiavelli, N.53, 61
 Matysik, J.63
 Maude, D. K.....38
 Mayordomo, N.....20
 Merroun, M. L.54
 Mesbah, A.36
 Meurer, F.....24
 Moll, H.56, 59
 Moreno, R.67
 Müller, K.20
 Murphy, G. L.39

 Neumann, J.....29
 Newman-Portela, A. M.54
 Nikitin, E.83

 Obermeier, F.71
 Oliveira, A. F.....21

 Parakhonskiy, B.67
 Parra-Puerto, A.20
 Patzschke, M..... 13, 14, 18, 19
 Peyerimhoff, N.....24
 Philipp, T.....31
 Plochocka, P.....38
 Poenitz, E.81
 Polly, R.30
 Pospiech, S.46
 Prieur, D.....36
 Puschmann, H.24

 Qi, H.25, 26

 Rachamin, R.....77, 78
 Raff, J.54, 55, 58
 Ramtke, J.....55
 Reich, T.....31
 Reiss, A.....45
 Richter, S.34
 Rijavec, T.....62, 67
 Rodríguez, D. M.....20
 Rossberg, A.....30, 57, 65
 Rumbo, C.67

 Sachs, S.53, 56, 59
 Sahle, C. J.....37
 Sansom, H.38
 Schabernack, J.....41
 Schäfer, F.....79
 Scheinost, A. C.....21

AUTHOR.....PAGE

Schild, D.....20
 Schmeide, K..... 22, 23, 31
 Schmidt, M. 13, 14, 18, 29
 Schymura, S.....62, 67
 Shams Aldin Azzam, S.31
 Shao, H.42
 Shi, R.26
 Shuh, D. K.....37
 Sieber, C.....22, 23
 Skirtach, A.67
 Snaith, H. J.38
 Sonnendecker, C.63
 Spahiu, K.48
 Starke, S.....48
 Steudtner, R..... 55, 56, 58, 59, 60, 66
 Stietz, J.....31
 Stohr, R.....31
 Stubbs, J. E.29
 Stumpf, T. 20, 32, 43, 56, 59
 Suarez Diez, M.....67
 Sun, F.....26
 Surrente, A.....38
 Sushko, V.61
 Svitlyk, V. 33, 35, 39
 Swart, M.....17

 Taniguchi, T.....38
 Thoenen, T.....48
 Tsushima, S.23, 65

 Ulbricht, A.73
 Urbank, C.14

 Virtanen, S.30
 Vogel, K.72
 Vogel, M.....58, 60

 Wang, X.....25
 Watanabe, K.38
 Waurick, L.19
 Wei, T. S.61
 Weiss, S. 14, 35
 Wolf, J.....66
 Wollenberg, A.23, 58
 Wu, G.26
 Wu, H.26

 Yu, M.25
 Yuan, T.....42, 43, 44

 Zechel, S.47
 Zhang, J.....25, 26
 Zhang, T.26
 Ziegler, J. D.....38
 Zugan, M.62



Institute of Resource Ecology
Bautzner Landstrasse 400
01328 Dresden/Germany
Phone +49 351 260-3210
Fax +49 351 260-3553
Email contact.resourceecology@hzdr.de
<http://www.hzdr.de>

Member of the Helmholtz Association